2011

HIGH PERFORMANCE PIEZOELECTRIC MATERIALS AND DEVICES FOR MULTILAYER LOW TEMPERATURE CO-FIRED CERAMIC BASED MICROFLUIDIC SYSTEMS

Wenli Zhang
University of Kentucky, alex_zhang2006@hotmail.com

Recommended Citation

Zhang, Wenli, "HIGH PERFORMANCE PIEZOELECTRIC MATERIALS AND DEVICES FOR MULTILAYER LOW TEMPERATURE CO-FIRED CERAMIC BASED MICROFLUIDIC SYSTEMS" (2011). *University of Kentucky Doctoral Dissertations*. 200.
https://uknowledge.uky.edu/gradschool_diss/200

ABSTRACT OF DISSERTATION

Wenli Zhang

The Graduate School

University of Kentucky

2011

HIGH PERFORMANCE PIEZOELECTRIC MATERIALS AND DEVICES FOR MULTILAYER LOW TEMPERATURE CO-FIRED CERAMIC BASED MICROFLUIDIC SYSTEMS

ABSTRACT OF DISSERTATION

A dissertation submitted in partial fulfillment of the
requirements for the degree of Doctor of Philosophy in the
College of Engineering
at the University of Kentucky

By
Wenli Zhang

Lexington, Kentucky

Co-Director: Dr. Richard E. Eitel, Professor of Department of Chemical and Materials Engineering
and Dr. Fuqian Yang, Professor of Department of Chemical and Materials Engineering

Lexington, Kentucky

2011

ABSTRACT OF DISSERTATION

HIGH PERFORMANCE PIEZOELECTRIC MATERIALS AND DEVICES FOR MULTILAYER LOW TEMPERATURE CO-FIRED CERAMIC BASED MICROFLUIDIC SYSTEMS

The incorporation of active piezoelectric elements and fluidic components into micro-electromechanical systems (MEMS) is of great interest for the development of sensors, actuators, and integrated systems used in microfluidics. Low temperature co-fired ceramics (LTCC), widely used as electronic packaging materials, offer the possibility of manufacturing highly integrated microfluidic systems with complex 3-D features and various co-firable functional materials in a multilayer module. It would be desirable to integrate high performance lead zirconate titanate (PZT) based ceramics into LTCC-based MEMS using modern thick film and 3-D packaging technologies. The challenges for fabricating functional LTCC/PZT devices are: 1) formulating piezoelectric compositions which have similar sintering conditions to LTCC materials; 2) reducing elemental inter-diffusion between the LTCC package and PZT materials in co-firing process; and 3) developing active piezoelectric layers with desirable electric properties.

The goal of present work was to develop low temperature fired PZT-based materials and compatible processing methods which enable integration of piezoelectric elements with LTCC materials and production of high performance integrated multilayer devices for microfluidics. First, the low temperature sintering behavior of piezoelectric ceramics in the solid solution of $Pb(Zr_{0.53}, Ti_{0.47})O_3$-$Sr(K_{0.25}, Nb_{0.75})O_3$ (PZT-SKN) with sintering aids has been investigated. 1 wt% $LiBiO_2$ + 1 wt% CuO fluxed PZT-SKN ceramics sintered at 900^{o}C for 1 h exhibited desirable piezoelectric and dielectric properties with a reduction of sintering temperature by 350^{o}C. Next, the fluxed PZT-SKN tapes were successfully laminated and co-fired with LTCC materials to build the hybrid multilayer structures. HL2000/PZT-SKN multilayer ceramics co-fired at 900^{o}C for 0.5 h exhibited the optimal properties with high field d_{33} piezoelectric coefficient of 356 pm/V. A potential application of the developed LTCC/PZT-SKN multilayer ceramics as a microbalance was demonstrated. The final research focus was the fabrication of an HL2000/PZT-SKN multilayer piezoelectric micropump and the characterization of pumping performance. The measured maximum flow rate and backpressure were 450 μl/min and 1.4 kPa respectively. Use of different microchannel geometries has been studied to improve the pumping performance. It is believed that the high performance multilayer piezoelectric devices implemented in this work will enable the development of highly integrated LTCC-based microfluidic systems for many future applications.

KEYWORDS: Low temperature co-fired ceramics (LTCC),
Piezoelectric ceramics, Multilayer structure,
Microfluidics, Micropump

Wenli Zhang
Student's signature

Date

HIGH PERFORMANCE PIEZOELECTRIC MATERIALS AND DEVICES FOR MULTILAYER LOW TEMPERATURE CO-FIRED CERAMIC BASED MICROFLUIDIC SYSTEMS

By

Wenli Zhang

Richard E. Eitel
Co-Director of Dissertation

Fuqian Yang
Co-Director of Dissertation

Stephen E. Rankin
Director of Graduate Studies

Date

DISSERTATION

Wenli Zhang

The Graduate School

University of Kentucky

2011

HIGH PERFORMANCE PIEZOELECTRIC MATERIALS AND DEVICES FOR MULTILAYER LOW TEMPERATURE CO-FIRED CERAMIC BASED MICROFLUIDIC SYSTEMS

DISSERTATION

A dissertation submitted in partial fulfillment of the
requirements for the degree of Doctor of Philosophy in the
College of Engineering
at the University of Kentucky

By
Wenli Zhang

Lexington, Kentucky

Co-Director: Dr. Richard E. Eitel, Professor of Department of Chemical and Materials Engineering
and Dr. Fuqian Yang, Professor of Department of Chemical and Materials Engineering

Lexington, Kentucky

2011

To my wife, Jing Yang,

for her understanding, support, and endless love

ACKNOWLEDGMENTS

My sincerest thanks and gratefulness are dedicated to all the people without whom this work would not have been possible.

First and foremost, I would like to express my deepest gratitude to my advisor and friend, Dr. Richard E. Eitel, for his guidance and patience during the entire course of my Ph.D. study at University of Kentucky. His constant support and invaluable advice help me develop various skills and encourage me to strive for more originality and the best. I also would like to acknowledge the valuable opportunities he provided for me to participate in diverse exciting multidisciplinary projects and inspiring conferences.

I would like to thank my committee members for their precious time, insightful comments, and inspiring questions on my dissertation. My special thanks go to each of them, Dr. Fuqian Yang, for his valuable suggestions, beneficial discussions, and continuous encouragement through the years, Dr. John Balk, for his willingness to participate in my defense committee at the last moment, and Dr. Janet K. Lumpp, for her continued support from the very beginning of my study at UK and admirable effort for attending my defense at the very end. I also want to acknowledge Dr. Christine Trinkle for serving on my dissertation defense and providing thoughtful suggestions for improving the quality of my work.

I gratefully acknowledge Dr. Bruce J. Hinds for serving on my Ph.D. qualifying exam and providing insightful comments and constructive criticisms on

my research, especially for his understanding and indulgence for my request of modifying doctoral advisory committee at short notice. I also would like to give my thanks to Dr. Tongguang (Tony) Zhai for his help, advice, and encouragement over the years.

I am indebted to my talented and dedicated group members in Dr. Eitel's lab who have helped me complete this work by sharing their expertise and comments, especially Dr. Serhiy Leontsev for helping me set up various measurement platforms and providing helpful advice on many aspects of my research and Mr. Sunil Gotmare for sharing his experience and knowledge as well as providing his prompt and unreserved support whenever I need it. My thanks also go to Ms. Jin Luo and Mr. Brian M. Ray for their useful and generous support during the last year of my study.

I am grateful to Dr. Thomas Dziubla for providing research guidance and access to equipment and resources needed for my research during the first couple of years. Thanks to Mr. Paritosh Wattamwar for helping me get familiar with the instruments in Dr. Dziubla's lab and providing necessary assistance on our collaborative project. I also wish to acknowledge Dr. J. Zach Hilt and Dr. Nitin Satarkar for the challenging and fruitful cooperation on the project of integrating polymers with ceramics.

I would like to acknowledge my current and previous colleagues and friends at UK for their support and friendship, Dr. Jianhui Xu, Dr. Rong Chen, Mr. Wei Wen, Mr. Juchuan Li, Dr. Ding (Vivian) Li, Dr. Ye Sun, Ms. Whitney

Epperson, Dr. Yang-Tse Cheng, Dr. Matthew J. Beck, Mr. Yan Li, Dr. Qingliu Wu, Dr. Reynold A. Frimpong, Mr. William Mercke, Dr. Stephen E. Rankin, Dr. Barbara L. Knutson, Dr. Kimberly W. Anderson, Mr. Bruce Cole, Mr. Jerry Vice, and Ms. Nancy Miller from CME department, Dr. Xin Xu, Dr. Ning Ma, Ms. Jin Cheng, Mr. Xiaoji Ma, Mr. Bo Zhao, Mr. Ming Yan, and Dr. J. Todd Hastings from ECE department. I'm sure I forgot to mention many important persons but please know that your names are written in my heart.

In addition, I want to appreciate the financial support from DEPSCoR and KSEF for the work presented in this dissertation. I would also like to thank Heraeus Inc. Thick Film Division for providing the LTCC materials used in this work.

I would like to extend my deepest thanks to my parents, Weichang Zhang and Shujuan Li, and other family members for their constant support, encouragement, and confidence in me all these years. I also would like to express my heartfelt gratitude to my mother-in-law, Xiulan Dong, who had sacrificed a lot in her own life and accompanied my wife and me during the hardest time in our lives. Finally, but most importantly, I would like to thank my wife, Jing Yang and baby daughter, Jingchun, for all the meaning and happiness you brought into my life.

TABLE OF CONTENTS

Acknowledgments iii

List of Tables ix

List of Figures xii

Chapter 1. Introduction 1
    1. 1 Motivation 1
    1. 2 Organization of the thesis 4

Chapter 2. Background 7
    2. 1 Low temperature co-fired ceramics (LTCC) 7
        2. 1. 1 Introduction to thick-film technology 8
        2. 1. 2 LTCC materials and technology 10
        2. 1. 3 LTCC applications 15
    2. 2 Lead zirconate titanate Pb(Zr, Ti)O_3 (PZT) ceramics 24
        2. 2. 1 Piezoelectric and ferroelectric ceramics 24
        2. 2. 2 Pb(Zr, Ti)O_3 solid solutions 32
        2. 2. 3 PZT ceramics for piezoelectric devices 38
    2. 3 Integration of LTCC with PZT ceramics 44
        2. 3. 1 Ceramic micro-electromechanical systems (C-MEMS) 44
        2. 3. 2 Compatibility between LTCC and PZT 46
        2. 3. 3 Current development in LTCC and PZT materials 50
    2. 4 Sintering of ceramics 56
        2. 4. 1 Driving force for sintering 56
        2. 4. 2 Solid-state sintering 58
        2. 4. 3 Liquid-phase sintering 67
        2. 4. 4 Viscous sintering 72
        2. 4. 5 Constrained sintering 76
    2. 5 Micropumps for lab-on-chip microfluidic systems 79
        2. 5. 1 Micropumps for microfluidics 79
        2. 5. 2 Peristaltic micropump 86
        2. 5. 3 Piezoelectric actuation 89
        2. 5. 4 Integration of micropumps in microfluidic systems 91

Chapter 3. Low temperature sintering and properties of Pb($Zr_{0.53}$, $Ti_{0.47}$)O_3-Sr($K_{0.25}$, $Nb_{0.75}$)O_3 (PZT-SKN) ceramics with $LiBiO_2$ and CuO addition......... 95
    3. 1 Introduction 95
    3. 2 Experimental methods and materials preparation 96
    3. 3 Results and discussion 99
        3. 3. 1 Effectiveness of fluxes 99
        3. 3. 2 Phase and microstructure 100
        3. 3. 3 Dielectric and piezoelectric properties 107

3. 3. 4 Compatibility for integration with LTCC 113
3. 4 Conclusions 116

Chapter 4. Sintering behavior, properties, and applications of co-fired LTCC/PZT-SKN multilayer ceramics 117
4. 1 Introduction 117
4. 2 Master sintering curve (MSC) model.. 118
4. 3 Tape casting technique 121
4. 4 Experimental procedures 124
4. 4. 1 Tape casting 124
4. 4. 2 Construction of MSC 127
4. 4. 3 Fabrication of LTCC/PZT-SKN multilayer ceramics 129
4. 4. 4 Characterization of microstructures and properties 129
4. 4. 5 Microbalance fabrication and testing 130
4. 5 Results and discussion 131
4. 5. 1 Master sintering curve analysis 131
4. 5. 2 Microstructure and chemical composition analysis 138
4. 5. 3 Dielectric and piezoelectric properties........................... 144
4. 5. 4 A demonstration of applications: microbalance 147
4. 6 Conclusions 150

Chapter 5. Development and optimization of multilayered LTCC/PZT-SKN piezoelectric micropumps for LTCC-based microfluidic systems 152
5. 1 Introduction 152
5. 2 Design and fabrication of micropumps.. 153
5. 2. 1 LTCC and PZT-SKN tapes 153
5. 2. 2 Piezoelectric bimorph actuator 154
5. 2. 3 Multilayer design and fabrication of piezoelectric micropump 156
5. 2. 4 Micropump optimization 159
5. 3 Experimental setup 160
5. 4 Results and discussion 162
5. 4. 1 Modeling of piezoelectric bimorph actuator 162
5. 4. 2 Micropump performance 166
5. 4. 3 Effects of microchannel geometry 169
5. 5 Conclusions 174

Chapter 6. Summary and future work 177
6. 1 Summary 177
6. 1. 1 Low temperature sintering and properties of fluxed PZT-SKN ceramics 177
6. 1. 2 Sintering behaviors and properties of co-fired LTCC/PZT-SKN multilayer ceramics 179
6. 1. 3 Development and optimization of multilayered LTCC/PZT-SKN piezoelectric micropumps 182
6. 2 Future work 184

6. 2. 1 Investigation of stress development ... 185
6. 2. 2 Further optimization of micropump design ... 188
6. 2. 3 Integration of LTCC-based microfluidic systems ... 191
6. 3 Conclusions ... 196

Appendix ... 197

References ... 199

Vita ... 221

LIST OF TABLES

Table 2.1 Characteristics of hybrid thick-film processing, HTCC, and LTCC.. 10
Table 2.2 Applications of LTCC technology in different areas. 22
Table 2.3 Properties of commercial PZT piezoelectric ceramics. 38
Table 2.4 Comparison among the planar integration technologies for PZT-based piezoelectric MEMS. (modified after Z. Wang et al. [116]) 39
Table 2.5 Comparison of dielectric properties of PZT thick films made on Si substrates using different technical approaches. 41
Table 2.6 Characteristics of common used MEMS substrate materials......... 46
Table 2.7 Properties of PZT-*x*SKN ceramics sintered at 1250^{o}C and flux-sintered at 900^{o}C with 0.9 mol% Li_2CO_3 flux addition. (taken from N.J. Donnelly et al. [31,157]) 55
Table 2.8 Mechanisms of sintering in polycrystalline solids. (taken from W.D. Kingery et al. [160])... 60
Table 2.9 Plausible values of constants shown in the equations for initial stage of sintering. (taken from M.N. Rahaman [159]) 65
Table 2.10 Parameters in the sintering models represented by equation for intermediate stage of sintering. (taken from T.A. Ring [172])... 66
Table 2.11 Microstructure of two-phase ceramics produced by liquid-phase sintering for different ratios of $\gamma_{gb} / \gamma_{sl}$ and the corresponding ψ. (taken from M.N. Rahaman [159]) 69
Table 2.12 Characteristic features and performances of reciprocating displacement micropumps. 83
Table 2.13 Characteristic features and performances of continuous dynamic micropumps. 85
Table 3.1 Details of compounds/mixtures added as fluxes to the 0.98PZT-0.02SKN ceramics and the density obtained after sintering at 900^{o}C for 1 h... 99
Table 3.2 Main properties of 0.98PZT-0.02SKN ceramics with and without flux additions sintered at different temperatures.......................... 113
Table 3.3 Comparison of functional properties of 1 wt% $LiBiO_2$ + 1 wt% CuO fluxed 0.98PZT-0.02SKN and other low fire PZT-based ceramics. 115
Table 4.1 Compositions of PZT-SKN tape casting slurries. (wt%)............... 127
Table 4.2 MSC fitting parameters for fluxed PZT-SKN and LTCC tapes. 132
Table 4.3 EDS elemental analysis on the cross-section of LTCC/PZT-SKN multilayer ceramics. (wt%) 143
Table 4.4 Properties of co-fired HL2000/PZT-SKN multilayer ceramics under different sintering conditions. 145
Table 4.5 Dielectric and piezoelectric properties of fluxed PZT-SKN thick films co-fired with different LTCC materials.................................. 146
Table 5.1 Materials used in the fabrication of PZT-SKN/LTCC multilayer micropump. 154

Table 5.2 Effect of phase difference on flow rate for various actuation frequencies. (unit: µl/min) 166
Table 6.1 Properties of PZT-based thick-film ceramics fired on LTCC and alumina substrates…………………………………………….182

LIST OF FIGURES

Figure 2.1 LTCC manufacturing process. (modified after Heraeus – Design Guidelines for LTCC [43]) 12
Figure 2.2 Schematic view of a LTCC module illustrating multiple embedded components. (taken from M. Karppinen [46]) 16
Figure 2.3 Comparison of the same circuit implemented on PCB (20 mm × 20 mm, 0.8 g) and LTCC (7 mm × 7 mm, 0.2 g). (taken from M. Pudas et al. [50]) 17
Figure 2.4 A schematic of conceptual integrated microfluidic system using LTCC multilayer approach. (taken from M.R. Gongora-Rubio et al. [17]) 19
Figure 2.5 (a) Bottom view of the microanalyzer with electronics for data collection and processing; and (b) top view of the microanalyzer with fluidic components and detection systems. (taken from C.S. Martinez-Cisneros et al. [32]) 20
Figure 2.6 Simplified illustration of piezoelectric effect in quartz. (modified after Kistler – On-line Knowledge Base [86]) 25
Figure 2.7 (a) Lattice parameters of $BaTiO_3$ as a function of temperature (taken from H.F. Kay et al. [92]); and (b) dielectric constants of $BaTiO_3$ as a function of temperature. (taken from W.J. Merz [93]). 30
Figure 2.8 A typical hysteresis loop for ferroelectric materials. 31
Figure 2.9 Schematic illustration of the typical perovskite structure. 33
Figure 2.10 Composition-temperature phase diagram of $PbZrO_3$-$PbTiO_3$ solid solution. (taken from B. Jaffe et al. [81]) 34
Figure 2.11 Compositional dependence of the (a) dielectric constant and remnant polarization (taken from Yamamoto [101]); and (b) piezoelectric coefficients and coupling factor of PZT around MPB. (taken from B. Jaffe et al. [96]) 36
Figure 2.12 The structure of a PZT thick-film resonant sensor for microbalance application. (taken from M. Ferrari et al. [135]) 42
Figure 2.13 Schematic illustration of micropump made of screen printed PZT layer on micromachined Si structure. (taken from M. Koch et al. [136]) 43
Figure 2.14 Images of deformation and failure in co-fired LTCC multilayer structures. (a) camber, (b) delamination, (c) collapse, and (d) cracking. 48
Figure 2.15 (a) Dielectric constant and (b) piezoelectric coefficient d_{33} of PZT layer fired on Al_2O_3, LTCC, and LTCC substrate with diffusion barrier layer (LTCC+B). (taken from D. Belavic et al. [149]) 49
Figure 2.16 Sintering process for the self-constrained laminate consisting of two different layers with various sintering intervals. (taken from T. Rabe et al. [154]) 52

Figure 2.17 An illustration of self-constrained HL2000 tapes showing near-zero x-y shrinkage after firing. (taken from T. Rabe et al. [154]) 52
Figure 2.18 The high field d_{33} piezoelectric coefficient as a function of SKN addition and (inset) unipolar strain loop used for the d_{33}^{high} calculation. (taken from N.J. Donnelly et al. [31]) 54
Figure 2.19 Illustration of three main driving forces for sintering: surface free energy, external pressure, and chemical reaction. (taken from M.N. Rahaman [159]) 58
Figure 2.20 The difference between densification and coarsening processes. (taken from W.D. Kingery et al. [160]) 59
Figure 2.21 Six distinctive paths for matter transport during the sintering of a consolidated mass of crystalline particles. (taken from W.D. Kingery et al. [160]) 61
Figure 2.22 Illustration of idealized models for the three sintering stages. (a) initial stage of sintering model represented by spheres in tangential contact; (b) near the end of the initial stage: spheres have begun to coalesce; (c) intermediate stage: grains adopted shape of tetrakaidecahedron, enclosing pore channels at grain edges; and (d) final stage: pores are tetrahedral inclusion at corners where four tetrakaidecahedra meet. (taken from M.W. Barsoum [168]) 63
Figure 2.23 Schematic illustration of an idealized two-sphere model comparing the microstructural aspects of (a) solid-state sintering with (b) liquid-phase sintering. (taken from M.N. Rahaman [159]) 67
Figure 2.24 Schematic evolution of a powder compact during liquid-phase sintering. (taken from M.N. Rahaman [159]) 70
Figure 2.25 Schematic evolution of sintering stages in non-reactive liquid phase sintering (NLPS) model. (taken from K.G. Ewsuk et al. [160]) . 73
Figure 2.26 Schematic of the densification of ceramic-filled glass composites by NPLS through viscous flow. (taken from S. Kemethmuller et al. [158]) 75
Figure 2.27 Expectation of market growth for microfluidic devices and systems from 2006 to 2014. (taken from EMMA Report 2009 [195]) 80
Figure 2.28 Optical image of a microfluidic device containing 2056 micro-channels. Different colored dyes used to visualize the structure of the fluidic network. (taken from T. Thorsen et al. [198]) 81
Figure 2.29 Working principle of a peristaltic micropump with three chambers. (a) signal scheme and (b) pumping stages. (taken from N.T. Nguyen et al. [246]) 87
Figure 2.30 Design examples of peristaltic micropumps. (a) piezoelectric. Three piezoelectric discs glued on the pump chambers etched in silicon; (b) electrostatic. Polysilicon electrodes embedded in a silicon nitride pump body; and (c) thermopneumatic. Three heaters located inside the pressure chambers to achieve deflection. (taken from after N.T. Nguyen et al. [254]) 89

Figure 2.31 Schematic representations of (a) Si-glass based microfluidic system. (taken from C.G.J. Schabmueller et al. [237]); and (b) glass-PDMS based microfluidic chip. (taken from C. Lee et al. [260]) 92
Figure 3.1 Flowchart for solid-state synthesis of fluxed PZT-SKN. 97
Figure 3.2 X-ray diffraction patterns for unfluxed 0.98PZT-0.02SKN ceramics. (a) raw material mixture, (b) after 1st calcination, (c) after 2nd calcination, and (d) sintered at 1250°C for 2 h. 101
Figure 3.3 X-ray diffraction patterns for 0.98PZT-0.02SKN ceramics sintered at 900°C with (a) 6 wt% $LiBiO_2$, (b) 1 wt% $LiBiO_2$ + 1 wt% CuO addition, and (c) the unfluxed specimen sintered at 1250°C. . 102
Figure 3.4 Scanning electron microscopic micrographs of 0.98PZT-0.02SKN ceramics sintered at 900°C for 1 h with (a) 6 wt% $LiBiO_2$ and (b) 1 wt% $LiBiO_2$ + 1 wt% CuO addition, (c) 1 wt% $LiBiO_2$ + 1 wt% CuO-fluxed specimen sintered at 900°C for 2 h, and (d) unfluxed specimen sintered at 1250°C for 2 h. 103-104
Figure 3.5 Density of 0.98PZT-0.02SKN ceramics with flux additions as a function of sintering temperature. 106
Figure 3.6 The intergranular liquid phase observed in scanning electron microscopic micrographs of PZT-SKN ceramics sintered at 900°C for 1 h with 1 wt% $LiBiO_2$ + 1 wt% CuO addition. 107
Figure 3.7 Temperature dependence of (a) dielectric constant and (b) tangent loss of 0.98PZT-0.02SKN ceramics conventionally sintered at 1250°C and flux-sintered at 900°C. 109
Figure 3.8 (a) $P – E$ hysteresis loops and (b) unipolar loops of 0.98PZT-0.02SKN ceramics conventionally sintered at 1250°C and flux-sintered at 900°C. 110
Figure 3.9 High field d_{33} piezoelectric coefficient and planar-coupling factor k_p of 0.98PZT-0.02SKN ceramics with flux additions as a function of sintering temperature. 111
Figure 4.1 Schematic diagram of tape casting process. (taken from M.R. Gongora-Rubio [17]) 122
Figure 4.2 Viscosity of 75 wt% solid loading suspensions with different dispersant contents. 125
Figure 4.3 Schematic flow diagram for the tape casting process. 126
Figure 4.4 Example of determination of optimal apparent activation energy Q_a for fluxed PZT-SKN materials by minimizing the average residual square. 128
Figure 4.5 Schematic diagram of measurement setup for monitoring the resonant frequency response. 131
Figure 4.6 Densifications of (a) fluxed PZT-SKN, (b) HL2000, and (c) CT2000 tapes at different heating rates. 134
Figure 4.7 Master sintering curves of (a) fluxed PZT-SKN, (b) HL2000, and (c) CT2000 tapes based on the density data. 135
Figure 4.8 Prediction of sintering behaviors for (a) fluxed PZT-SKN, (b) HL2000, and (c) CT2000 tapes using derived MSC. 136

Figure 4.9 Optimized densification behaviors of fluxed PZT-SKN and LTCC tapes obtained from MSC fitting equations, using the inset firing profile. 137
Figure 4.10 Co-firing structure of LTCC/PZT-SKN multilayer ceramics. (a) schematic illustration and (b) optical microscopic images of the cross-section. 138
Figure 4.11 Co-fired CT2000/PZT-SKN and HL2000/PZT-SKN multilayer ceramics. 139
Figure 4.12 SEM micrographs of hybrid multilayer ceramics sintered at 870°C for 1 h. (a) HL2000/PZT-SKN interface and (b) center of PZT-SKN layer. 141
Figure 4.13 EDS mapping results of hybrid multilayer ceramics sintered at 870°C for 1 h. (a) HL2000/PZT-SKN interface and (b) center of PZT-SKN layer. 142
Figure 4.14 Backscattered electron image showing the Z-contrast of the interface in the hybrid HL2000/PZT-SKN multilayer ceramics sintered at 870°C for 1 h. 144
Figure 4.15 Schematic illustration of cross-section of co-fired multilayer ceramics for microbalance. 148
Figure 4.16 Resonant frequency shift as a function of the mass loading with linear fitting. 149
Figure 4.17 FEM simulation result of geometrical effect of piezoelectric layers on the mass sensitivity. 149
Figure 5.1 Bimorph actuator for the multilayer peristaltic micropump. (a) typical configuration, (b) multilayer structure, and (c) FEM model. 155
Figure 5.2 Multilayer design of the piezoelectric peristaltic micropump. 157
Figure 5.3 Picture of the fabricated micropump. (a) micropump body and (b) assembly for pumping test. 159
Figure 5.4 Geometry of planar diffuser element. 160
Figure 5.5 Schematic illustration of experimental setup for pumping test. 160
Figure 5.6 Picture of the working micropump. (a) control signal adjustment, (b) connected micropump, and (c) electronic control system. 162
Figure 5.7 FEM simulation results. (a) visualization of bimorph membrane deflection. (displacement scaled 10^3 times for clarity) and (b) maximum displacement ($d_{\max}$) as a function of membrane radius/thickness ratio (R/θ) for different diaphragm radii 164
Figure 5.8 Estimation of flow rate based on the FEM simulation results. (a) normalized flow rate as a function of R/θ ratio and (b) maximum flow rate as a function of membrane size R at a constant R/θ ratio of 240. 165
Figure 5.9 Measured variation in flow rate with actuation frequency at drive voltages of 50, 75, and 100 V_{pp}. 168
Figure 5.10 Measured flow rate versus backpressure under actuation frequency of 100 Hz with various driving voltages. 169

Figure 5.11 Effect of microchannel geometry on flow rate–backpressure characteristics of the micropump - planar diffuser elements. . 170
Figure 5.12 Effect of microchannel geometry on flow rate–backpressure characteristics of the micropump - straight microchannel in various aspect ratios. 172
Figure 5.13 Comparison of fabricated multilayer LTCC/PZT-SKN micropump with several reported micropumps based on the self-pump frequency f_{sp} and the package size S_p. 175
Figure 6.1 (a) Morphology of polished microstructure of low-temperature co-firable glass-ceramic system under constrained sintering (taken from S.Y. Tzeng [319]); and (b) observed microstructure of co-fired HL2000/PZT-SKN multilayer structure. 187
Figure 6.2 Effect of electrode pattern on bimorph membrane deflection 189
Figure 6.3 FEM simulation results of maximum membrane displacement of bimorph with modified electrode geometry at different electric fields. 190
Figure 6.4 (a) Illustration of synthesis conditions via co-laminar flow in a LTCC-based microfluidic reactor; and (b) experimental setup for chemical reactions in the microchannel by laminar diffusion. 192
Figure 6.5 (a) Schematic of LTCC-based cell culture chip; and (b) experimental setup for continuous perfusion and real-time monitoring. 194
Figure 6.6 A proposed LTCC-based integrated microfluidic system............ 195

Chapter 1. Introduction

1. 1 Motivation

Microfluidics is an interdisciplinary field of research for designing and manufacturing devices with capability of fluid handling and analysis of sample volumes on the order of microliter to picoliter. Additionally, it deals with investigating the novel characteristics of fluids in such devices which are associated with the scaling down of the size [1-3]. Miniaturization of fluidic processes to the micro-scale provides significant potential benefits including: minimized consumption of reagents and power, reduced manufacturing and operation cost, rapid analysis time, high throughput, and compact instrument size [4,5]. Integrated microfluidic systems incorporating necessary functional components onto a small chip (known as “lab-on-a-chip”) are expected to be applied in many application fields, such as chemical analysis and reaction [6], biological sample processing [7-9], drug delivery [10,11], and environmental monitoring [12]. Although individual microfluidic devices with specific functions have been developed using silicon (Si), glass, and polymer materials with associated fabrication approaches [13], the integration of discrete components or modules into one multifunctional system is still at the early stage of development [14].

Low temperature co-fired ceramic (LTCC) materials and processing, used commercially for more than twenty years, were originally developed as an electronic packaging technology providing high density electrical interconnects and hermetic packaging for integrated circuits [15]. Recently, the use of LTCC materials for integrated microfluidic device and system fabrication has been developed to take advantage of LTCC technology over other materials and associated processing methods [16]. The ability to construct multilayer modules with complex 3-D features and integrate various co-firable functional materials (*e.g.* insulators, dielectrics, resistors, ferrites, and conductors) is the most important merit of LTCC to be applied as a miniaturization technology for microfluidic device and system production, where LTCC plays multiple roles as a substrate, fluidic network, electrical interconnection, and package [17,18]. Since LTCC was initially designed for electronic packaging, LTCC modules are more durable than polymeric substrates and there is no need to use additional encapsulants as commonly required in Si-based micro-electromechanical system (MEMS) devices [19]. Furthermore, the manufacturing process in which all layers can be processed in parallel allows for inspection of each layer individually and rapid implementation of design modifications on individual layers prior to final stack up and the single co-firing heating treatment. This process is also highly scalable providing significant cost advantages for pilot level (100's to 1000's parts) production runs and rapid transition to full scale manufacturing. Growing numbers of LTCC-based microfluidic components have been developed by virtue of the versatile LTCC fabrication methodology [20]. The realization of highly integrated lab-on-a-chip systems with on-chip sample processing capabilities will decrease the reliance on external equipment [4]. The implementation of a high performance micropump incorporating piezoelectric actuators into the LTCC-based MEMS structure for providing on-chip fluidic control and delivery is one of the most interesting fields of current research.

Despite tremendous research and development on lead-free materials for piezoelectric applications, the solid solution of lead zirconate titanate (PZT) and its modified systems remain the most widely used piezoelectric materials because of their outstanding properties [21,22]. Si-based MEMS structures incorporating PZT thin films as piezoelectric elements have been extensively investigated taking advantage of the well-established Si micromachining techniques [23-25]. Using LTCC substrate materials for fabrication of thick-film PZT devices is a new attempt to extend the application fields for both LTCC technology and PZT-based MEMS devices. To date there have been only a few reports published on development of physical sensors using the combination of LTCC substrates and piezoelectric active PZT layers [26,27]. Integrating LTCC/PZT ceramics in a compatible multilayer assembly method with one co-firing process is still challenging work. The technological obstacles for fabrication of functional LTCC/PZT microdevices are formulating piezoelectric compositions which can be fired at temperature compatible with LTCC packaging materials, reducing the inter-diffusion between the LTCC package and the active piezoelectric layers, and developing a compatible co-firing profile to build LTCC/PZT multilayer structures with minimal defects [28-30]. Additionally, the resulting co-fired piezoelectric layers need to maintain desirable properties for use in specific applications.

A modified PZT ceramic with strontium (Sr), potassium (K), and niobium (Nb) addition with a stoichiometry of $Sr(K_{0.25}, Nb_{0.75})O_3$ (SKN) demonstrates excellent piezoelectric properties with high field d_{33} piezoelectric coefficient of over 600 pm/V and Curie temperature T_c greater than 350°C [31]. This material is considered to be a promising material for high strain multilayer piezoelectric actuator applications.

Integration of PZT-SKN ceramics into LTCC substrate materials in a single assembly and co-firing process would provide the possibility of manufacturing highly integrated LTCC/PZT-SKN multilayer devices (*e.g.* microbalance and micropump) for microfluidics and other applications. However, the densification of PZT-SKN ceramics requires high sintering temperature (~1250^{o}C) and long sintering time (>2 h) using conventional solid-state sintering process which is not compatible with typical LTCC processing (firing at 850^o-950^{o}C for <1 h). Therefore, it is highly desirable to develop a low fired PZT-SKN ceramic with favorable properties and a multilayer fabrication method compatible with LTCC materials and processing.

The current work presents the development of a low temperature sinterable high performance piezoelectric PZT-SKN ceramic and compatible processing methods which enable integration of piezoelectric elements with LTCC materials and subsequently the production of high performance integrated multilayer ceramic devices. It is believed that the materials and processing techniques implemented in this work would offer numerous unique advantages and improved capabilities in the design and fabrication of integrated multifunctional microfluidic devices and systems.

1. 2 Organization of the thesis

This thesis is organized into six chapters. The topic of each chapter follows.

Chapter 1 introduces the motivation of the present research work and the organization of the thesis.

Chapter 2 provides a literature review on LTCC materials and technology as well as PZT-based piezoelectric ceramics. Prior attempts to integrate LTCC with PZT thick films are also discussed. Next, the theoretical background of the various sintering processes for materials and multilayer structures in this study is discussed. Finally, a brief review on micropumps for microfluidic systems is presented to show a potential application of co-fired LTCC/PZT multilayer ceramics.

Chapters 3 through 5 present the research efforts on development of high performance piezoelectric materials and devices for multilayer LTCC-based microfluidic systems. In chapter 3 the low temperature sintering of fluxed PZT-SKN ceramics is introduced. The processing methods, microstructures, dielectric, and piezoelectric properties of flux-sintered ceramics are discussed. Chapter 4 follows with an investigation on the co-firing of LTCC/PZT-SKN multilayer ceramics and the resultant electric properties. Master sintering curve (MSC) approach is also introduced and applied to analyze the sintering behaviors of LTCC tapes, fluxed PZT-SKN materials, and LTCC/PZT-SKN multilayer ceramics. The resulting microstructures and elemental inter-diffusion of co-fired multilayers are also presented. Finally, a microbalance fabricated using the developed LTCC/PZT-SKN multilayer structure is presented. Chapter 5 describes the design, fabrication, and characterization of a LTCC/PZT-SKN multilayer piezoelectric micropump. In the included results the further optimization of pumping performance is reported.

Chapter 6 summarizes the research work presented in this thesis and provides suggestions for future studies on the development of highly integrated microfluidic systems using LTCC/PZT-SKN multilayer ceramics.

Chapter 2. Background

Materials, technologies, and theoretical background related to the present research work are introduced in the current chapter. First, low temperature co-fired ceramic (LTCC) materials and technologies are reviewed. LTCC has been applied in the fabrication of multilayer structured sensors, actuators, and microsystems with low cost and high productivity. Second, an overview of piezoelectric materials is presented. The solid solution of lead zirconate titanate $Pb(Zr_x, Ti_{1-x})O_3$ (PZT) and its modified systems are the most widely used piezoelectric ceramics because of their excellent properties. Recently, there is an increasing interest in the development of highly integrated micro-electromechanical systems (MEMS) incorporating active piezoelectric elements with LTCC materials. For integrating PZT piezoelectric ceramics with LTCC materials, the study on sintering behaviors for those materials is necessary for the development of a compatible co-firing process. Finally, current micropump technology is discussed.

2. 1 Low temperature co-fired ceramics (LTCC)

Low temperature co-fired ceramic (LTCC) technology is a multilayer ceramic fabrication technique that has many engineering and manufacturing advantages over both hybrid thick-film circuitry and high temperature co-fired ceramic (HTCC) technology [15]. LTCC materials, originally developed as a multilayer substrate for packaging integrated circuits, are widely used for the production of sensors, actuators, and integrated microsystems which have a wide range of applications in the automotive, aeronautic, and telecommunication areas [16-18]. Applications of LTCC-based devices in the microfluidics field have recently emerged. Integration of microfluidics and electronics into one monolithic LTCC system for micro total analysis system (μ-TAS) or lab-on-a-chip (LOC) applications is a most interesting and challenging field of current research [32,33].

2. 1. 1 Introduction to thick-film technology

Thick-film technology has been developed in the electronics industry as a method for producing high-density multilayer interconnect substrates at low cost and with fast turnaround time. Thick-film circuits are widely used for both low-volume high-performance applications (*e.g.* military, space, and medical products) and high-volume low-cost applications (*e.g.* telecommunication, automobile, and solar cell products) [15]. Conductor, resistor, and dielectric pastes are screen-printed, dried, and fired or cured onto ceramic, metal, or polymer substrates in a thick-film process. The thickness of deposited films is normally in the range from several microns to around one hundred microns. Ceramic thick-film processing can be separated into three major sub-groups: hybrid thick-film circuitry, high temperature co-fired ceramic (HTCC), and low temperature co-fired ceramic (LTCC) [34].

Hybrid thick-film processing is a bottom-up manufacturing technique capable of producing multilayer high-density thick-film circuits. Successive layers with various functions are printed, dried, and fired to build up a multilayer structure on a rigid ceramic or metal substrate. Multiple firing steps are required when the layer count increases, which lowers the fabrication yield of multilayer substrates because of the increasing non-planarity of the surfaces. Therefore, the development of co-fired ceramic tape processes has attracted remarkable attention [15]. HTCC has been used to fabricate hybrid ceramic multi-chip modules (MCM) – a package-level substrate combining multiple integrated circuits in one unit. In HTCC the multilayer ceramic substrate and refractory metal conductors (*e.g.* tungsten and molybdenum) can be co-fired in a single heating treatment which is significantly different from the multiple cycles of printing-firing used in hybrid thick-film processing. Individual unfired tapes are first machined and screen-printed separately, then stacked and laminated at certain sequence, and finally co-fired with conductor pastes in a typical HTCC process. Although HTCC process is applicable for high-volume production of multilayer interconnect substrates and packages at low cost, the high temperature (~1500^{o}C) sintering prevents the use of highly electrically conductive pastes (*e.g.* copper, silver, and gold) required in many applications [35]. The effort to increase the interconnect density, data transmission speed, and communication frequency for computers and microwave electronics accelerated in the middle 1980s. It is now necessary to use conductor materials with low electrical resistance for high-density packaging in applications requiring low loss and high frequency. In addition, the coefficient of thermal expansion (CTE) of the interconnect substrate is needed to be close to that of the silicon components for reliable connection. Furthermore, to achieve high speed signal transmission, it is desirable to have MCM substrates or packages with a low dielectric constant [35-37]. LTCC technology was invented to fulfill all these requirements and commercialized to produce high-performance, high-speed, and high-density MCM for realization of functional, reliable, and low-cost electronic devices. A summary of advantages of LTCC technology over other thick-film processes is listed in Table 2.1.

Table 2.1 Characteristics of hybrid thick-film processing, HTCC, and LTCC.

Characteristics	LTCC	HTCC	Hybrid thick-film
• Single printing per layer and one firing process	√	√	
• Firing at low temperature (<900°C)	√		√
• Using high conductive metals (*e.g.* copper, silver, and gold)	√		√
• Integration of passive components, such as resistors	√		√
• Adjustable CTE to match silicon and other substrate materials	√		
• Ability to form cavities and shaped substrates	√	√	
• Ability to integrate interconnect substrates in a hermetic package	√	√	
• Thickness control of dielectric	√	√	
• High layer count	√	√	
• Monolithic structure, no need for the base to support layers	√	√	
• Easy inspection and rapid modification	√	√	

2. 1. 2 LTCC materials and technology

As its name suggests LTCC is a ceramic substrate which can be co-fired with highly conductive metal conductors (*e.g.* gold, silver, and silver alloys) and other passive components at “low” temperature, typically in the range of 850°-950°C. LTCC materials are commercially produced in tape format by tape-casting a slurry on polymeric carrier substrates (*e.g.* Teflon®, Mylar®, or cellophane) at varying thickness (50-350 μm). The manufacturing of LTCC tapes can be easily conducted using standard ceramic processing techniques, such as powder preparation, colloidal processing, and tape casting technique [34].

Most LTCC tapes are glass-ceramic composite materials mainly composed of ceramic fillers, glass frits, and an organic binder vehicle. The selection of ceramic fillers is related to the application of interest. Alumina (Al_2O_3) is the most widely used dielectric ceramic filler but other ceramic systems are also available for offering various properties, for example, high thermal conductive beryllia (BeO) [38], ferroelectric barium strontium titanate ($Ba_{0.7}Sr_{0.3}TiO_3$) [39], and dielectric magnesium calcium titanate ($MgCaTiO_3$) [40]. It has also been demonstrated that the CTE of LTCC materials can be adjusted by choosing proper ceramic formulations to match the other interested materials for hybrid integration, such as Al_2O_3, gallium arsenide (GaAs), and silicon (Si) [18]. Glass frits are introduced into the ceramic as low-softening-point glass or fully devitrifying glass to lower the sintering temperature for the glass-ceramic composite [41]. The glass additives should have minimum effect on the desirable properties of the base ceramic without forming new phases after firing; unless the ceramic-glass reaction is required to obtain certain characteristics for the fired ceramic [42]. The final component of the composite is the organic vehicle. This organic medium, in which the ceramic particles and glass frits are dispersed, normally consists of polymeric binders, plasticizers, dispersants, and other optional constituents which are all dissolved in an organic or aqueous-based solvent. Defect-free LTCC "green" tapes with proper strength and flexibility are prepared for further processing. A flow diagram of the LTCC manufacturing process is illustrated in Figure 2.1.

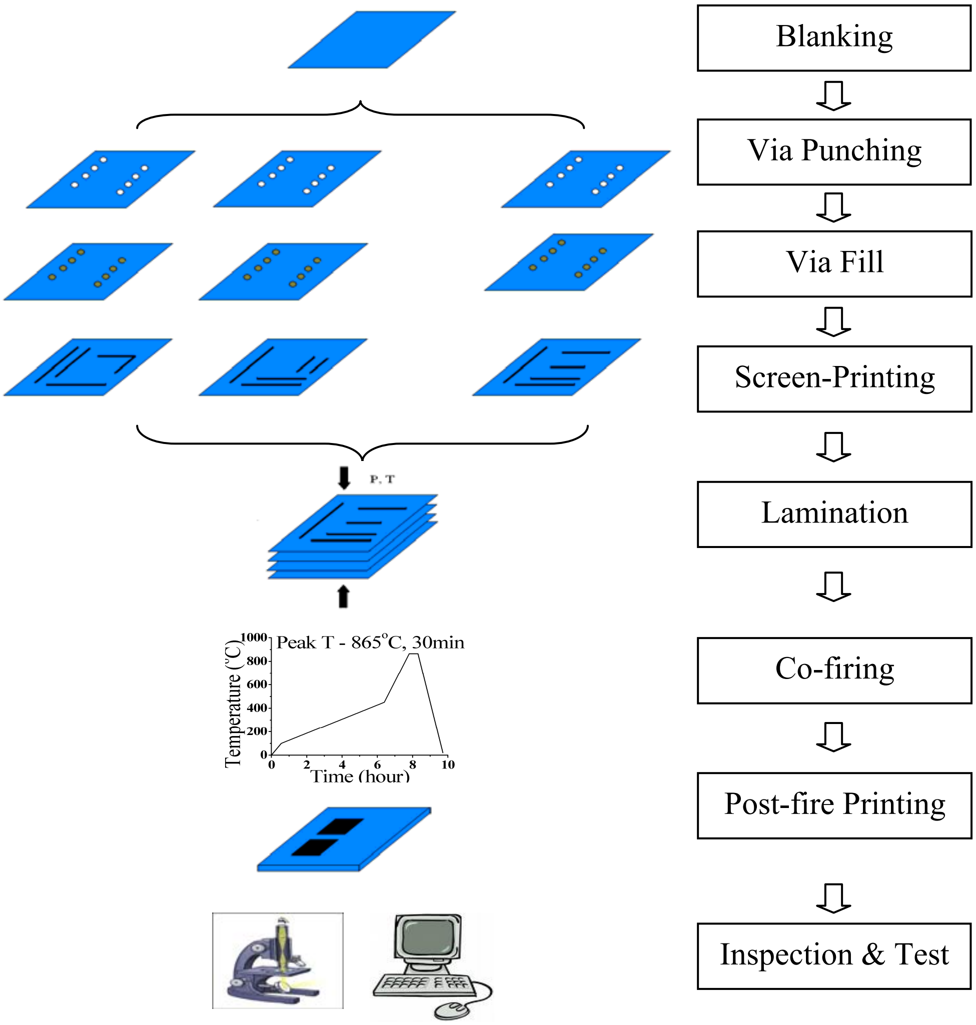

Figure 2.1 LTCC manufacturing process. (modified after Heraeus – Design Guidelines for LTCC [43])

LTCC "green" tapes are first blanked to a specific size and registration holes are made simultaneously. Traditionally, electrical circuitry and interconnects are produced by punching and filling electrical via holes, followed by screen-printing of conductor, resistor, and dielectric pastes on each layer of "green" tape. Cavities are made by drilling, punching, or laser ablation on the printed tapes if necessary. The individual layers are then aligned, stacked, and laminated using an either isostatic or uniaxial press under specified pressure and temperature. The laminated stack is finally co-fired to burnout organics and sinter the ceramic substrate and electronic components into a dense monolithic ceramic package. The shrinkage of tape (typically 10-15%) during co-firing must be accurately controlled and compensated for in the design process. Additional active and passive components can be printed, wire-bonded, or soldered on the fired surfaces according to the desired application. This processing route has been extensively applied for the production of integrated radio frequency (RF) and microwave modules.

LTCC materials and processing, as an alternative for Si materials and associated micromachining techniques, have also been considered and utilized to design and construct sensors, actuators, and micro-electromechanical systems (MEMS) in the last decade [7]. Si-based MEMS processing techniques (*e.g.* deep etching, bulk/surface micromachining, and anodic bonding) are well engineered and extensive work has been done to optimize this route of making MEMS devices. However, using Si technology for MEMS fabrication remains a complex, expensive, and time-consuming process. LTCC material, showing proper electrical and mechanical properties, good chemical and thermal stability, and high reliability, could expand the availability and flexibility in design and fabrication of MEMS devices. Application of LTCC processing has additional advantages compared to microfabrication techniques using Si materials [16-18]: (1) simple and inexpensive LTCC tape patterning methods (punching, machining, laser ablation) are available when feature sizes in the range from several microns to several hundred microns are required (increasing feature size in Si (*e.g.* >50 microns) can greatly increase production time and require significant surface area, increasing die size and cost); (2) the parallel layer-by-layer manufacturing process utilized for LTCC means that design changes and inspections can be performed on individual layers and rapidly incorporated into the final device, leading to improved yield, short development time and lower cost production; (3) since LTCC is a true packaging technology, there is no need for an additional protective envelope as when utilizing Si-based MEMS devices.

Microfluidic systems have been fabricated in a number of materials including Si, glass, metal, and polymers. The chemical inertness, temperature and pressure stability, solvent compatibility, and ease of fabrication suggest that LTCC materials and fabrication processes are appropriate for the microfluidics. Recently, use of LTCC materials for microfluidic systems has been emphasized to capitalize on the significant advantages offered by LTCC technology. LTCC utilizes a layered assembly process and is compatible with wide range of metallic and ceramic materials, making LTCC a logical choice for the fabrication of multilayer modules with complex 3-D features and various co-firable functional materials (*e.g.* dielectrics and conductors). LTCC may play multiple roles as a substrate, fluidic network, electrical interconnection, and package in an integrated LTCC-based microfluidic system [17].

Several modifications and improvements in standard LTCC processing are needed in order to fulfill the requirement of MEMS and microfluidics implementation. Computer numerically controlled (CNC) milling machines are used to pattern holes, cavities, and microchannels (feature size of the order of 100 μm) onto LTCC tapes. Alternatively, laser ablation can be utilized when the small feature sizes and tolerances are needed. Sacrificial volume or fugitive materials and adhesive or organic bonding agents have been developed to prevent the sagging and other undesirable deformations after lamination [44,45]. Constrained sintering of LTCC tapes is demonstrated as an effective method to minimize the shrinkage in *x-y* direction. Hybrid bonding techniques are investigated to integrate LTCC tapes with other materials in a co-fired or post-fired scheme [17].

2. 1. 3 LTCC applications

LTCC, originally developed as a multilayer interconnect substrate and packaging material, has been widely applied in the production of microelectronic modules and devices immediately after its commercialization by DuPont in the middle 1980s [15]. The multilayer approach and low firing temperature of LTCC technology enables the integration of dielectric ceramic tapes with electrodes made of high conductivity metals and other planar passive components (*e.g.* resistors, inductors, and capacitors) embedded or screen-printed on the surfaces, making a high-density, high-performance, and small-size MCM [19]. In addition, functional discrete electronic elements can be soldered or wire-bonded on the fired surfaces based on the application demands. Figure 2.2 shows an example of LTCC module integrated with various components.

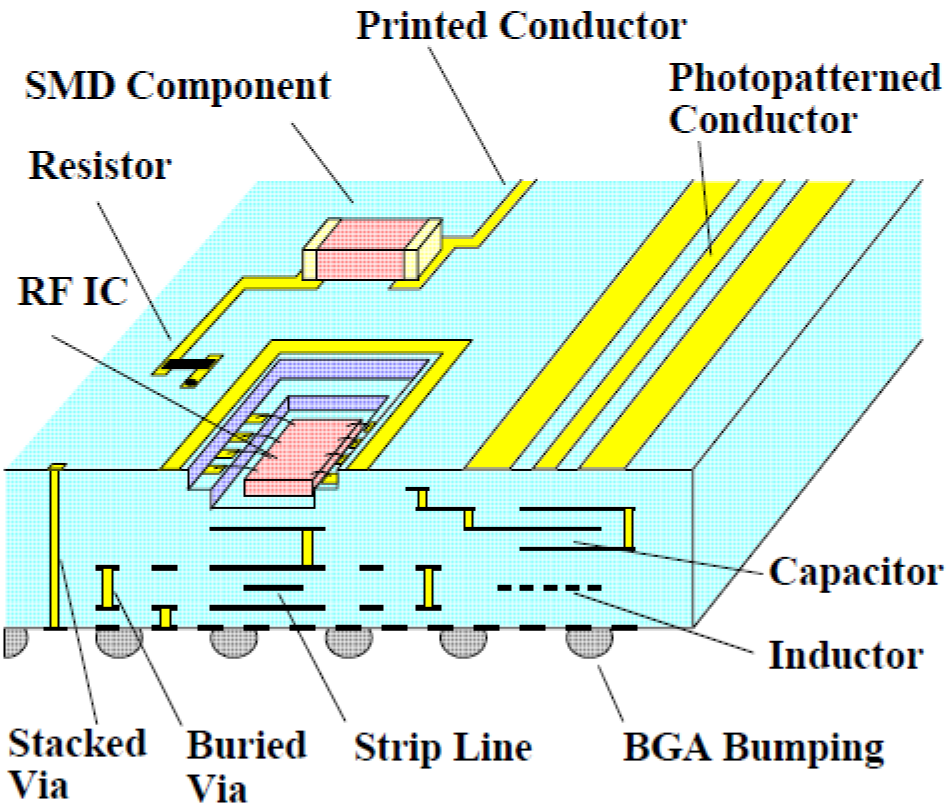

Figure 2.2 Schematic view of a LTCC module illustrating multiple embedded components. (taken from M. Karppinen [46])

RF and microwave devices for telecommunication applications are extensively developed using hybrid LTCC modules [47-49]. Although numbers of LTCC material systems including ceramic tapes and suitable functional pastes have been commercialized for this purpose, developing novel LTCC systems is still an attractive field for many researchers and manufacturers in order to meet specific electrical and thermomechanical requirements for the desired function. Several LTCC materials have been developed with desirable properties for the fabrication of RF multilayer resonators and band-pass filters [40,47]. Another example of a novel LTCC material system demonstrates ideal dielectric properties with high quality factor *Q* and low CTE for the fabrication of devices requiring high signal propagation speeds at microwave frequencies [49]. The resultant devices in hybrid LTCC modules are more compact in comparison with those fabricated using traditional printed circuit board (PCB) manufacturing technique. In addition, using LTCC technology for the production of RF and microwave devices is cost-effective, adaptable to changes of design, and allows rapid replacement and/or post-trimming of surface components. A comparison between PCB and LTCC technology for the construction of a microelectronic module is shown in Figure 2.3.

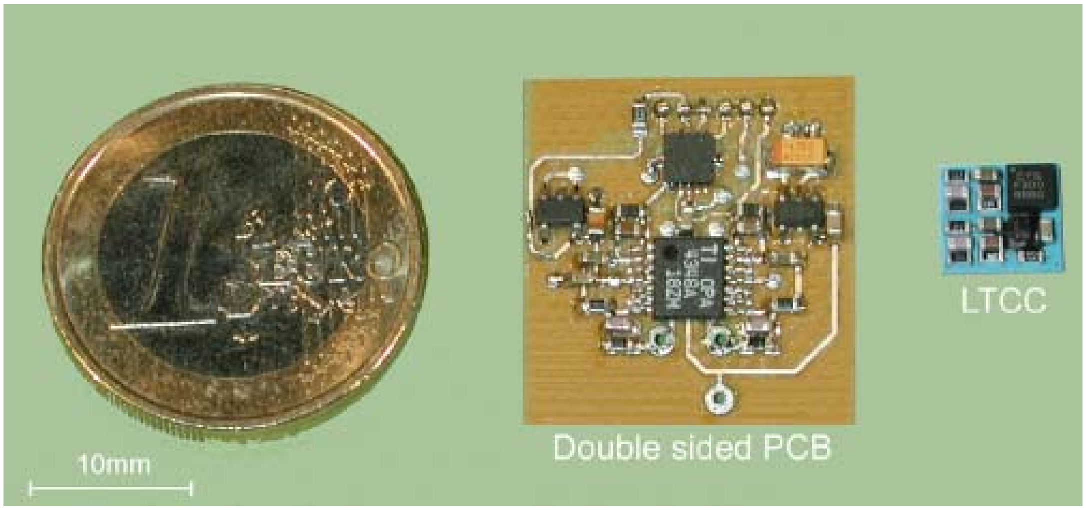

Figure 2.3 Comparison of the same circuit implemented on PCB (20 mm × 20 mm, 0.8 g) and LTCC (7 mm × 7 mm, 0.2 g). (taken from M. Pudas et al. [50])

Taking advantage of the versatility of LTCC materials and technology, numbers of microdevices [51-55], sensors [30,56-64], and actuators [65,66] have been developed since the first LTCC-based sensor was reported in 1996 [67]. Many microdevices and sensors are designed for use in a harsh circumstances involving high-temperature, high-voltage, and high-pressure or vacuum. LTCC material systems have excellent thermomechanical and chemical stability and are a suitable choice for such applications. For example, LTCC material systems were used to fabricate a micro-plasma generator [26]. The LTCC was robust enough to stand up to the high voltage and high temperature conditions caused by the plasma generation. A micro-scale methanol reformer and a partial oxidation reactor were also built using LTCC technology for the miniature fuel cell energy conversion system [53]. LTCC-based systems proved to be more resistant to a strong acid environment, more compact, and less costly compared to the fuel processor made of stain-less steel or Si. LTCC-based sensors with various functions are also extensively considered to be applied in the automotive field: Schmid [59] designed a mass flow sensor to control the fuel injection under high pressure; Fonseca et al. [60] reported a pressure sensor capable of working in high temperature turbine engines; LTCC-based eddy proximity sensors for automobile wheel positioning were fabricated by Gongora-Rubio et al. [63] and Wilde et al. [64]. Other LTCC-based sensors were also developed and reported recently, including gas detection and flow sensors [31-33], force and pressure sensors [30,61], and hot-layer electrochemical sensors [62]. In addition, leaf spring vertical actuators and spherical stepper motors were made by virtue of LTCC multilayer processing [65,66].

The fields of microfluidic systems and microfluidic chemical sensors in LTCC technology have also been increasingly studied in recent years, showing an exciting new application area for LTCC material systems. The ease of integrating fluidic components (*e.g.* microchannels and microchambers) with both passive and active electrical and mechanical components in one module is a significant advantage of LTCC technology over Si, glass and polymer technologies. Applications of LTCC based microfluidic devices and systems also earn interest due to its' low price and short development time. Individual LTCC-based devices have been implemented for different steps in a continuous-flow analytical procedure, including microvalves and micropumps for fluidic sample supply and control [17,68], micromixers and microchambers for sample pretreatment [69], microreactors for chemical synthesis [70,71], and sensors for chemical detection and analysis [72-78]. The integration of these discrete functional fluidic components into one miniaturized microfluidic system is also possible using LTCC multilayer fabrication methodology. A conceptual platform of this multi-functional integration is illustrated in Figure 2.4. Further development of LTCC microfluidic systems is expected to be utilized for cell handling and sorting, drug delivery, gas or liquid chromatographs, and biological parameter monitoring [17].

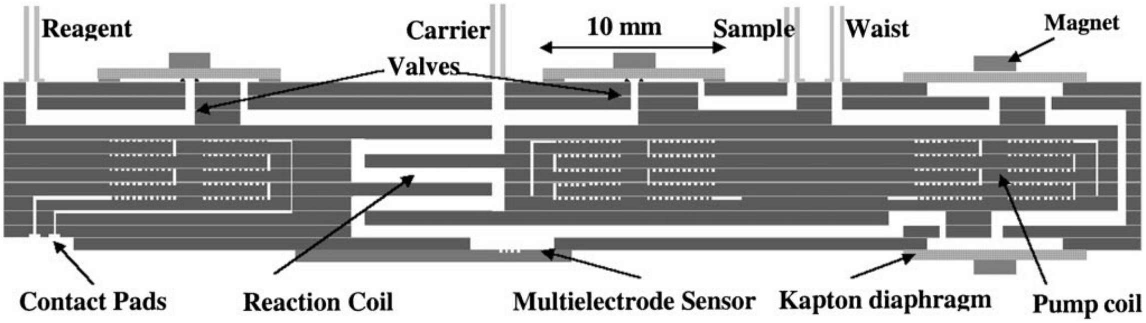

Figure 2.4 A schematic of conceptual integrated microfluidic system using LTCC multilayer approach. (taken from M.R. Gongora-Rubio et al. [17])

Most of the LTCC-based devices described above were developed as stand-alone products in two major groups: (1) sensing and microfluidic platforms for microanalytical systems, and (2) electronics for actuators and signal processing [19]. The intrinsic advantages of LTCC technology suggest the possibility for easy integration of both microfluidics and electronics functions to build a monolithic microanalytical system. Until now, few attempts have been reported which translated this conceptual approach into real functioning integrated microsystems. Molianen et al. [79] reported the implementation of a preamplifier and multiplexing circuit module integrated with lead sulphide (PdS) detector arrays in one LTCC module. Fournier et al. [80] presented a LTCC-based fluidic multisensor with integrated control circuits for signal conditioning and amplification in a monolithic package. Figure 2.5 presents an example of a monolithic microanalyzer fabricated using LTCC technology. Using both the modular approach and monolithic integration concept for the incorporation of electronics and microfluidics shows the versatility of LTCC fabrication methodology [32]. Table 2.2 presents a comprehensive summary of LTCC devices and microsystems utilized in different areas.

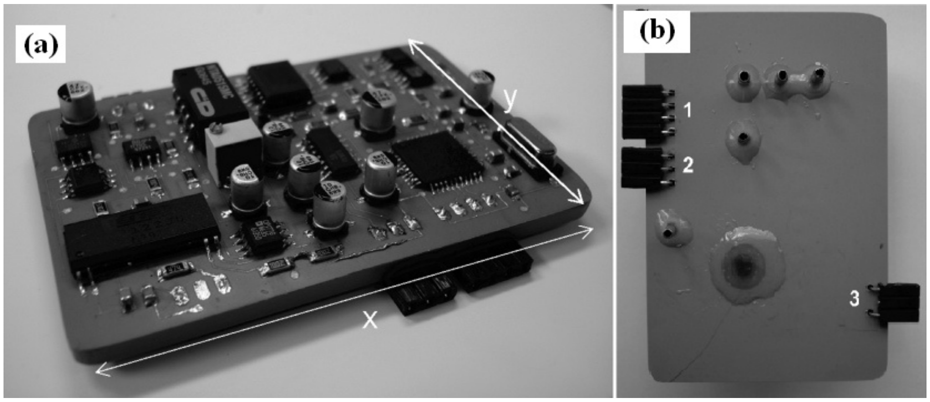

Figure 2.5 (a) Bottom view of the microanalyzer with electronics for data collection and processing; and (b) top view of the microanalyzer with fluidic components and detection systems. (taken from C.S. Martinez-Cisneros et al. [32])

LTCC technology, including attractive features and various potential applications, has been introduced in this review section. Growing numbers of LTCC-based MEMS devices have been developed to take advantage of the versatile LTCC fabrication methodology. However, there are still a number of challenging issues to be solved to fulfill the potential of LTCC technology for integrated microsystems. One demanding task is to develop high performance piezoelectric ceramics with proper composition and processing method compatible with LTCC materials and technology. The development of LTCC-based micropumps which can be integrated into microfluidic systems for on-chip fluidic control and delivery is another most interesting field of research.

Table 2.2 Applications of LTCC technology in different areas.

Type	Device	Application	Ref.
Sensors	Gas detection sensors	Monitoring of carbon monoxide and methane	[56]
		Detection of hydrogen and ethanol	[57]
	Flow sensors	Thermistor-based sensor for gas flow measurement	[58]
		Onboard detection of high pressure fuel injection	[59]
	Pressure and force sensors	Operation in high temperature turbine engine and compressor	[60]
		Capacitive pressure sensor suitable for stress analysis in solid media	[61]
		Piezoresistive force sensor responding to the forces below 100mN	[30]
	Chemical sensors	Hot layer electrochemical sensor for studies of protein denaturalization	[62]
		Amperometric detection of heavy metals (*e.g.* mercury and copper)	[72]
		Pesticide monitoring by enzymatic inhibition and amperometric detection	[73]
		Potentiometric detection of nitrate and ammonium ions	[74]
		Detection of chloride ion in drinking waters using ion selective electrode	[75]
		Separation and detection of phenolic compounds	[76]
		Optical detection using transmittance and fluorescence measurements	[77,78]
	Eddy current proximity sensors	Precise positioning metallic objects in automotive industry	[63,64]
Actuators	Micropumps	Magnetohydrodynamic pump for handling and control of fluidic samples	[68]
	Microvalves	Electromagnetic valve for fluid control	[17]
	Leaf spring vertical actuators	Generating displacement in micrometer scale by electrostatic actuation	[65]
	Spherical motors	Omni-directional wheel for vision cameras and robots	[66]

Table 2.2 (Continued)

Type	**Device**	**Application**	**Ref.**
Other devices	Microwave and RF devices	Chip-type low pass filter	[47]
		RF MEMS package with low-loss characteristics in a wide band range	[48]
		Integration of passive components for radar and antenna technologies	[49]
	Micro-generators	In-plane rotary electromagnetic micro-generator for MEMS	[52]
	Polymerase chain reaction (PCR) and DNA detection	DNA identification, genomic cloning, diagnostics	[70,71]
	Micro-plasma generators	Surface treatment, semiconductor etching, waste water treatment	[51]
	Micro-methanol reformers	Supplying hydrogen for the operation of fuel cells	[53]
	Ion mobility spectrometers	Identification of ground water pollutants, drugs, and explosives	[54,55]
	Micromixers	Modular devices for chemical reaction in high temperature and pressure	[69]
Integrated microsystems	Chloride ion detection system	Integration of a potentiometric detection system and the electronics for data acquisition and processing	[32]
	Lead sulphide detection system	Incorporating high performance preamplifier and multiplexing circuits into lead sulphide (PdS) detector array packages	[79]
	Industrial compressed air diagnostic system	Fluidic pressure-flow-temperature multi-sensors with integrated signal conditioning electronics	[80]

2. 2 Lead zirconate titanate Pb(Zr, Ti)O_3 (PZT) ceramics

Piezoelectric materials are widely used in modern industry for their capability to convert between electrical signals and mechanical energy [81]. Piezoelectric materials and solid solutions with the general ABO_3-type perovskite structure, particularly the lead zirconate titanate Pb(Zr, Ti)O_3 (PZT) based ceramics, have been extensively investigated due to their superior properties for a variety of applications. PZT ceramics show a strong piezoelectric effect for compositions near the rhombohedral-tetragonal morphotropic phase boundary (MPB). Properties of PZT can also be modified by the addition of various isovalent, subvalent (donor type), and supervalent (accepter type) impurities depending on application requirements [82-84]. There is also continued interest and progress in the integration of high performance piezoelectric PZT ceramics into Si-based MEMS devices for developing novel sensors and actuators [85].

2. 2. 1 Piezoelectric and ferroelectric ceramics

The piezoelectric effect, first discovered in 1880 by Pierre and Jacques Curie, exists in natural crystals (*e.g.* quartz and tourmaline), poled ceramics, and some polymers. The conversion between electrical energy and mechanical energy based on the piezoelectric effect has led to the development of novel devices for sensor and actuator applications. Depending on the application, technological piezoelectric materials may be fabricated in the form of bulk polycrystalline ceramics, single crystals, thick films, or thin films. Figure 2.6 demonstrates the piezoelectric effect in a simplified atomic structure of quartz. An unstrained quartz crystal has a network of electric dipoles which does not possess a net dipole moment. When a stress is applied, the center of positive charge does not coincide with the center of negative charge, resulting in a net dipole moment. The dipole moments appear in every unit cell in the crystal causing a finite net polarization.

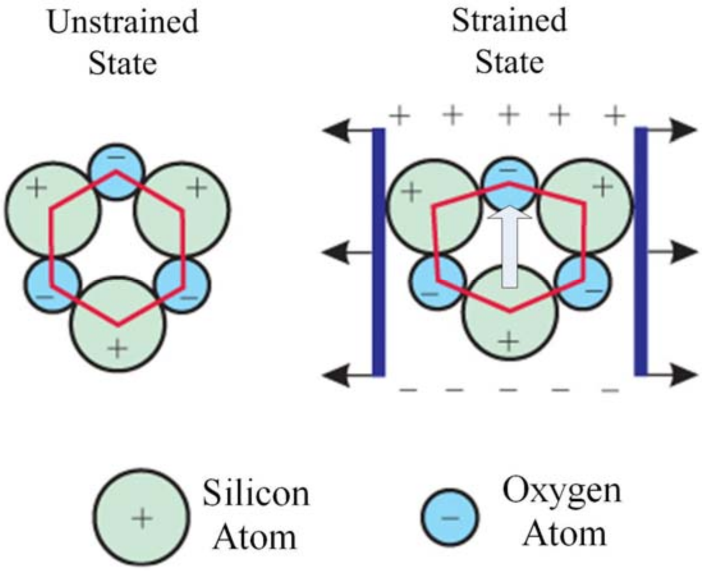

Figure 2.6 Simplified illustration of piezoelectric effect in quartz.
(modified after Kistler–Knowledge Base [86])

Crystalline materials can be classified into 32 crystal classes or point groups. 20 of the 21 classes which lack a center of symmetry can show piezoelectricity. Out of such 20 classes, 10 have a unique polar axis (an electric dipole moment) in the unstrained condition. Crystals from such classes are called polar crystals exhibit a net spontaneous polarization. Polar crystals can develop an electric charge when uniformly heated. The change of polarization caused by the uniform heating is called pyroelectricity. Ferroelectricity, by analogy to ferromagnetism, is defined as the "reversible or reorientable spontaneous electric polarization by application of an electric field over some range of temperature" [87]. Ferroelectricity is an experimental phenomenon that distinguishes one group of pyroelectric crystals from others. Ferroelectric behavior was first discovered in Rochelle salt by Joseph Valasek in 1920 [88]. Ceramic compounds of perovskite structure including Pb(Zr, Ti)O_3, $BaTiO_3$, and $KTaO_3$; ilmenite structure, $LiTaO_3$ and $LiCdO_3$; and tungsten-bronze structure, such as (Sr, Ba)Nb_2O_6 and $LiNb_2O_6$ are often ferroelectric [89]. Ferroelectric ceramics, with the development of ceramic processing and thin film technology, have been utilized for a variety of novel applications, such as ferroelectric thin films for high-density non-volatile memories and ferroelectric electrooptic ceramics for data storage and displays [90].

Piezoelectricity

A stress T [N/m^2] causes a proportional strain S [m/m] related by an elastic modulus Y [N/m^2] ($T = YS$) for most solids. Piezoelectricity is the additional creation of a dielectric displacement D [C/m^2] by the applied stress T (direct effect). The corresponding converse effect of piezoelectricity occurs such that an applied electric field E [V/m] produces a proportional strain S. These piezoelectric effects can be expressed as follows:

$$D = d \cdot T \text{ (direct effect)}$$

$$S = d \cdot E \text{ (converse effect)}$$

where d is the piezoelectric coefficient [C/N] or [m/V] which is numerically identical for both direct and converse effect. The general form of liner piezoelectric equations relating the electric and elastic variables can be written as follows:

$$\begin{cases} S = s^E T + dE \\ D = dT + \varepsilon^T E \end{cases} \qquad \begin{cases} T = c^E T - eE \\ D = dT + \varepsilon^T E \end{cases}$$

$$\begin{cases} S = s^D T + gD \\ D = -gT + D/\varepsilon^T \end{cases} \qquad \begin{cases} T = c^D S - hD \\ D = -hS + D/\varepsilon^S \end{cases}$$

where s^X, c^X and ε^X are elastic compliance [m^2/N], elastic stiffness [N/m^2], and dielectric permittivity [F/m] at constant X, respectively. The parameters of d, g, h, and e are piezoelectric constants which can be defined by:

$$d = \left(\frac{\partial S}{\partial E}\right)_T = \left(\frac{\partial D}{\partial T}\right)_E \qquad g = \left(-\frac{\partial E}{\partial T}\right)_D = \left(\frac{\partial S}{\partial D}\right)_T$$

$$h = \left(-\frac{\partial T}{\partial D}\right)_S = \left(-\frac{\partial E}{\partial S}\right)_D \qquad e = \left(-\frac{\partial T}{\partial E}\right)_S = \left(\frac{\partial D}{\partial S}\right)_E$$

The piezoelectric constant d, which relates dielectric displacement D to stress T in the direct effect and strain S to electric field E in the converse effect, is the most important parameter used to characterize piezoelectric properties. Since D, E are vectors and T, S are second rank tensors, d can be transformed as a third rank tensor for both direct and converse effects [91]:

$$D_j = d_{jkl}\, T_{kl} \quad \text{(direct effect)}$$

$$S_{ij} = d_{ijk}\, E_k \quad \text{(converse effect)}$$

The piezoelectric effect can be presented by a 6 × 3 or 3 × 6 matrix because only 18 of the total 27 tensor components are independent because of the symmetry of second rank tensors T and S ($T_{ij} = T_{ji}$, $S_{ij} = S_{ji}$). The matrix of piezoelectric coefficient for direct effect can be written out as:

$$\begin{pmatrix} D_1 \\ D_2 \\ D_3 \end{pmatrix} = \begin{pmatrix} d_{11}\, d_{12}\, d_{13}\, d_{14}\, d_{15}\, d_{16} \\ d_{21}\, d_{22}\, d_{23}\, d_{24}\, d_{25}\, d_{26} \\ d_{31}\, d_{32}\, d_{33}\, d_{34}\, d_{35}\, d_{36} \end{pmatrix} \begin{pmatrix} T_1 \\ T_2 \\ T_3 \\ T_4 \\ T_5 \\ T_6 \end{pmatrix}$$

where d uses only 2 subscripts $D_i = d_{ij}T_j$ (i = 1-3, j = 1-6). The relationship of different tensor forms can be determined by comparing coefficients expressed in both tensor and matrix forms for D_i. The converse coefficient matrix can be obtained by transposing the direct effect matrix. Written out it is:

$$\begin{pmatrix} S_1 \\ S_2 \\ S_3 \\ S_4 \\ S_5 \\ S_6 \end{pmatrix} = \begin{pmatrix} d_{11}\, d_{21}\, d_{31} \\ d_{12}\, d_{22}\, d_{32} \\ d_{13}\, d_{23}\, d_{33} \\ d_{14}\, d_{24}\, d_{34} \\ d_{15}\, d_{25}\, d_{35} \\ d_{16}\, d_{26}\, d_{36} \end{pmatrix} \begin{pmatrix} E_1 \\ E_2 \\ E_3 \end{pmatrix}$$

Ferroelectricity

A ferroelectric is a spontaneously polarized material possessing a noncentrosymmetric point group symmetry in with an experimentally reversible or reorientable polarization. Most ferroelectric crystals undergo a structural transformation which is accompanied by the disappearance of the spontaneous polarization at the phase transition from the noncentrosymmetric polar lattice to a centrosymmetric nonpolar lattice as the temperature increases above the Curie temperature T_c. A ferroelectric in the high-temperature nonpolar phase above T_c is called paraelectric and obeys a Curie-Weiss law [81]:

$$K - 1 = \frac{C}{T - T_c}$$

where K is the relative dielectric constant, C is Curie constant which is usually in the range of 10^3-10^5 Kelvin degrees. The crystallographic and corresponding dielectric changes observed in barium titanate ($BaTiO_3$) illustrate the structural changes resulting in the paraelectric-ferroelectric state transition in a crystal, as shown in Figure 2.7. At high temperature, $BaTiO_3$ has the ideal cubic perovskite crystal structure and there is no permanent electrical dipole. When the temperature decreases to below T_c, Ti ions move to an off-center position resulting in a structural change from cubic to tetragonal symmetry and a corresponding permanent dipole. Neighboring dipoles are ordered, giving a domain structure with a net spontaneous polarization within the domain.

A domain is a microscopic region in a crystal where the dipoles are oriented in the same direction. Neighboring domains along different polarization directions which are basically high temperature symmetry axes (*e.g.* <001>, <110>, or <111>) are separated by domain walls. Angles between the dipoles of neighboring domains are those between such symmetry axes. For example, there exist 90^o and 180^o domain walls in a crystal with tetragonal symmetrical structure. The movement of domain walls has a profound influence on the mechanical and electrical properties of ferroelectric materials [90]. Domain structures observed in a crystal can be considered as an evidence of ferroelectricity [81].

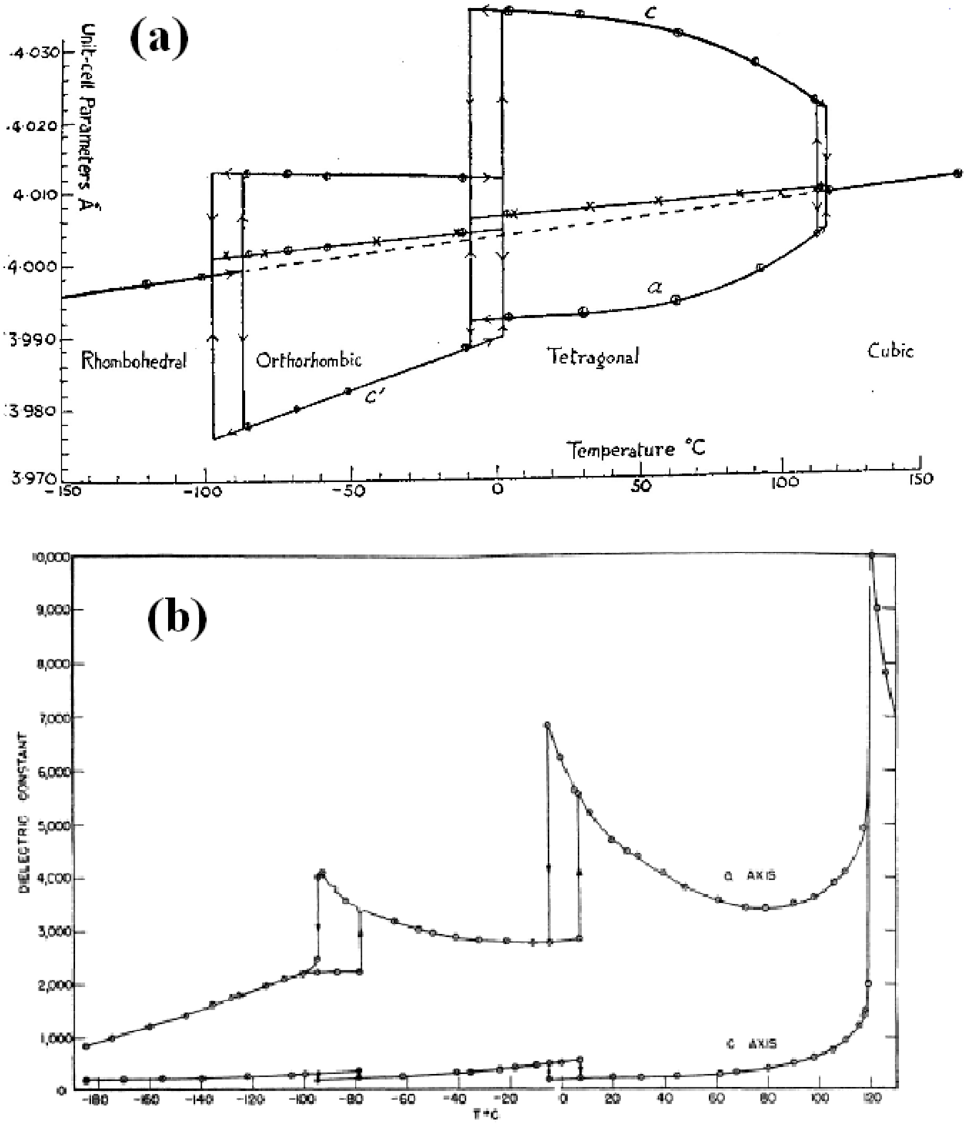

Figure 2.7 (a) Lattice parameters of $BaTiO_3$ as a function of temperature (taken from H.F. Kay et al. [92]); and (b) dielectric constants of $BaTiO_3$ as a function of temperature. (taken from W.J. Merz [93])

As another experimental characteristic of ferroelectricity, a hysteresis loop illustrating polarization-electric field *P-E* response is shown in Figure 2.8. The hysteresis arises from the electric field needed to reverse the dipoles during each excursion of the electric field.

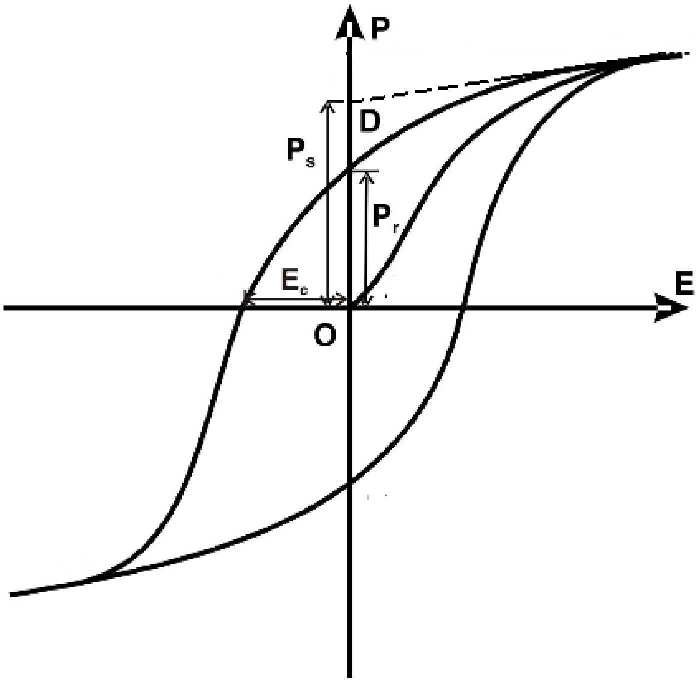

Figure 2.8 A typical hysteresis loop for ferroelectric materials.

Initially, polarization is reversible and nearly linear with the electric field. As higher fields are applied, the polarization increases more rapidly due to the switching of ferroelectric domains along the applied field. Ultimately, the highest polarization achieved is the saturation polarization P_s, which can be extrapolated from the slope of hysteresis loop at the highest field to $E = 0$. The P_s corresponds to the spontaneous polarization with all the dipoles aligned in parallel. When the external electric field is released, the polarization does not become zero, and there is a remnant polarization P_r, as most of the domain alignment remains. The domain alignment can again be reoriented by reversing the polarity of the field. The field required to induce switching is known as coercive field E_c. The domains again align with the field as applied field increases to the opposite polarity, resulting in the opposite polarization. The inner area of hysteresis loop in the *P-E* relationship indicates the energy stored or lost in moving domain boundaries [81]. Polycrystalline ferroelectric materials are agglomerates of single crystals (grains) with random orientations which results in zero net spontaneous polarization. The poling process of applying a high electric field to a polycrystalline ferroelectric is necessary to realize piezoelectric behavior by orienting the ferroelectric domain structure with the applied electric field resulting in a net remnant polarization in the bulk ceramic component.

2. 2. 2 Pb(Zr, Ti)O_3 solid solutions

Lead zirconate titanate Pb(Zr, Ti)O_3 (PZT) is a piezoelectric ceramic made by a solid solution of two ABO_3-perovskite type oxides, namely lead zirconate ($PbZrO_3$) and lead titanate ($PbTiO_3$). The ferroelectric material PZT was first developed in both Japan and US in the mid 1950s and has become the most widely used piezoelectric ceramic to date [94-96]. The structures and properties of PZT-based solid solutions and their manufacturing processes are thoroughly studied since discovered.

Perovskite structure

The majority of technologically important piezoelectric ceramics crystallize in the perovskite structure, named after the $CaTiO_3$ perovskite mineral. The perovskite-like crystal is a ternary compound with the formula ABO_3, which can be described by a simple cubic unit cell with large cations (A) on the corners, smaller cations (B) in the body center, and the oxygen atoms at the face centers. A network of corner–linked oxygen octahedral is also used to represent this structure with the smaller cations filling the octahedral holes and larger cations inside the dodecahedral holes. An example of the ideal perovskite cubic structure is shown in Figure 2.9.

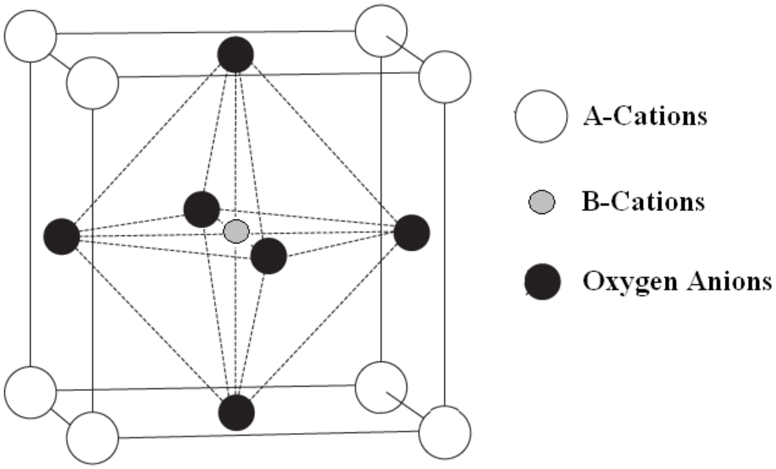

Figure 2.9 Schematic illustration of the typical perovskite structure.

In the ideal cubic structure, the coordination numbers for A and B cations are 12 and 6 respectively. Most perovskite materials are slightly distorted from the ideal cubic symmetry. Common distortions such as cation displacement within the octahedra and the tilting of the octahedra are caused by the substitution of A and B atoms with different characteristics, which can be used to adjust physical properties for the perovskite materials. Radius size and Jahn-teller effects have been used to explain the distortion in the ABO_3 perovskites. According to Golschmidt, the ideal cubic perovskite structure is characterized by a tolerance factor *t* [97]:

$$t = \frac{r_A + r_O}{\sqrt{2}\,(r_B + r_O)}$$

where $t = 1$ and r_A, r_B and r_O indicate the ionic radius of large cations, small cations, and anions respectively. Stable perovskite structures are expected to have t in the range from 0.88 to 1.09 where the ionic radii of the A-cations are corrected for the coordination number 12 [98].

Pb(Zr, Ti)O₃ phase diagram

The composition-temperature phase diagram of the $Pb(Zr_x, Ti_{1-x})O_3$ solid solution is shown in Figure 2.10.

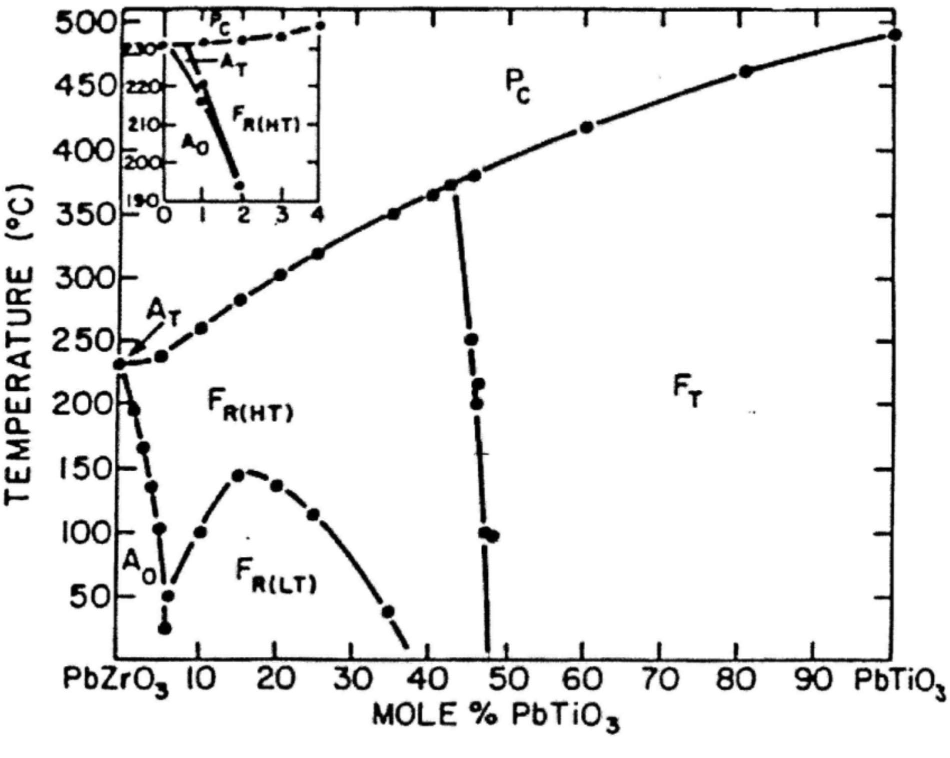

Figure 2.10 Composition-temperature phase diagram of $PbZrO_3$-$PbTiO_3$ solid solution. (taken from B. Jaffe et al. [81])

At high temperatures, $Pb(Zr_x, Ti_{1-x})O_3$ (PZT) system is in the cubic perovskite phase for all values of zirconium (Zr) incorporation x. Lead titanate ($PbTiO_3$) is ferroelectric at room temperature and ambient pressure. On heating $PbTiO_3$ goes through a first-order transition from the ferroelectric tetragonal symmetry to a paraelectric cubic phase at a T_c of 490°C. Lead zirconate ($PbZrO_3$) is antiferroelectric with orthorhombic symmetry, which is transformed from paraelectric cubic phase at T_c of 230°C. A small field of stability of a tetragonal antiferroelectric phase near the T_c appears as more Ti^{4+} substitute for Zr^{4+} at the $PbZrO_3$ end. The rhombohedral ferroelectric region is divided into two phases, as indicated by the measurement of dielectric and elastic properties, thermal expansion and neutron diffraction [99,100]. Substitution of Zr^{4+} for Ti^{4+} in $PbTiO_3$ reduces the tetragonal distortion and causes the appearance of another ferroelectric phase in rhombohedral form. The phase boundary between tetragonal and rhombohedral phases, observed at composition with $x = 0.48$, is often referred as a morphotropic phase boundary (MPB). The MPB is nearly independent of temperature up to around 370°C. The MPB, at which the two ferroelectric phases are presented in equal quantity, is the most prominent feature of the PZT materials. The dielectric constant, remnant polarization, piezoelectric coefficients, and coupling factor are maximized at compositions near the MPB, as shown in Figure 2.11.

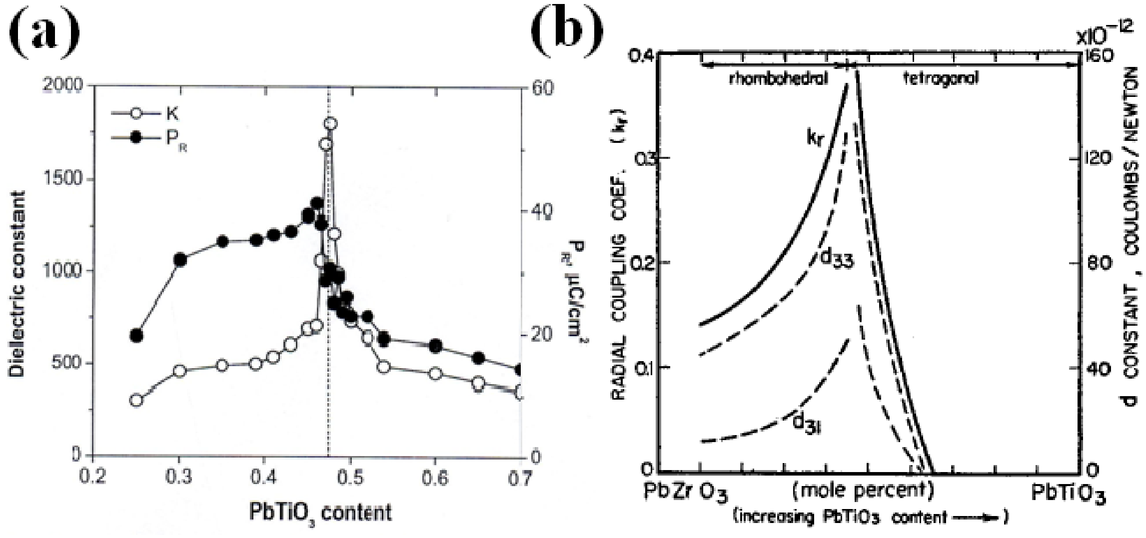

Figure 2.11 Compositional dependence of the (a) dielectric constant and remnant polarization (taken from Yamamoto et al. [101]); and (b) piezoelectric coefficients and coupling factor of PZT around MPB. (taken from B. Jaffe et al. [96])

Numerous experimental results and theoretical analyses show that the proximity to the MPB favors strong piezoelectric behavior in a ceramic partially due to the increased ability to orient the spontaneous dipoles during the poling process. There are 6 and 8 equivalent polar axes in the tetragonal and rhombohedral phases, respectively. The polarization of the PZT solid solution at the MPB composition may easily switch between ferroelectric tetragonal and rhombohedral phase, effectively resulting in 14 available equivalent polar directions [102,103]. Recent studies have also suggested the existence of a monoclinic phase near the MPB which may explain the exceptional dielectric and piezoelectric properties of PZT in that region [104-106].

Modifications of PZT ceramics

As described above, undoped PZT ceramics with compositions in proximity to MPB possess maximum dielectric and piezoelectric properties. Tailored properties for specific applications can be achieved through compositional modifications that can be summarized as donor doping, acceptor doping, and isovalent substitutions. Donor type additives of higher charges, like Nb^{5+} in the B sites replacing Zr^{4+} or La^{3+} in the A sites substituting for Pb^{2+}, are compensated by cation vacancies in the crystal structure which enhance domain wall mobility [107-109]. Such ceramics are called “soft” PZT, showing high dielectric constant and loss, high remnant polarization with low coercive field, and a relatively square hysteresis loop. The “hard” PZT ceramics are doped by acceptor type additives. Ions with lower charges, such as K^{+} for A sites or Fe^{3+} for B sites, are compensated by oxygen vacancies which pin the domains [83,84]. These compounds demonstrate the opposite characteristics compared to the “soft” PZT materials, such as low dielectric constant and loss and high coercive field [110]. Isovalent substitutions with ions of the same valence and similar size, such as Ba^{2+} or Sr^{2+} for A sites or Sn^{4+} for B sites, tend to inhibit domain reorientation process and reduce the T_c [81]. For compensating valence substitutions, stoichiometry is maintained if one substitutes combinations instead of individual ions in such manner as described below:

$$\sum X_A V_A + \sum X_B V_B = 6$$

where X is concentration and V is the valance of ions entering the A or B positions. If such a combination is proved to be ferroelectric and able to be poled, the properties should be similar to isovalent modifications of PZT. In practice, the stoichiometry of undoped PZT at MPB composition is not equivalent to the batch values because of the high volatility of PbO. The resulting lead-oxygen vacancy associates may become oriented along the local polarization vector and subsequently act as pinning sites to domain wall motion. This results in the stabilization of domain wall structure, leading to “hard” acceptor character in nominally “undoped” PZT ceramics. Intentional acceptor doping gives rise to a further “hardening” of undoped PZT ceramics by generating of additional oxygen vacancies. Donor dopants added to PZT materials compensate effects of acceptor cations that naturally existed [81]. Several examples of modified PZT ceramics with their electric properties are shown in Table 2.3.

Table 2.3 Properties of commercial PZT piezoelectric ceramics.

Type	**Piezo-ceramics**	**Dielectric constant ε**	**Piezoelectric coefficient d_{33} (pm/V)**	**Coupling factor k_p**	**Curie Temperature T_c (^{o}C)**	**Ref.**
Donor-doped	PZT-5H	3400	585	0.59	180	[111]
	PZT-5A	1700	374	0.60	365	[111]
Acceptor-doped	APC 841	1350	275	0.60	320	[112]
	PZT-4	1300	289	0.58	328	[111]
Undoped	PZT	730	220	0.52	386	[113]

2. 2. 3 PZT ceramics for piezoelectric devices

There has been increasing interest in incorporating high performance piezoelectric components into MEMS for both sensing and actuating applications. PZT ceramics integrated on the micromachined Si structures have been widely investigated taking advantage of the well-established Si micromachining techniques. Large numbers of piezoelectric MEMS devices have been developed using PZT ceramics in thin-film [114,115], thick-film [116,117], or bulk wafer forms [118] based on the various application requirements where the thickness of the PZT film is a critical parameter. Different technical approaches are applied for the integration of piezoelectric layers with the Si MEMS body. A comparison among the fabrication and integration of thin-film, thick-film, and bulk-wafer PZT ceramics on Si substrates is listed in Table 2.4.

Table 2.4 Comparison among the planar integration technologies for PZT-based piezoelectric MEMS. (modified after Z. Wang et al. [116])

	Thin Film	**Thick Film**	**Bulk Wafer**
Integration technologies	Sputtering, chemical vapor deposition (CVD), spin-coating, etc.	Screen-printing, aerosol deposition, sol-gel method, etc.	Fusion bonding, and other adhesive bonding techniques
Patterning process	Easy	Difficult	Very difficult
Etching process	Wet, dry, and lift-off	Wet and ion-milling	Wet, laser ablation, dicing, and sand blasting
Process temperature	500^o-700^oC	650^o-900^oC	20^o-550^oC
Piezoelectric properties	Good	Inferior to bulk wafer	Excellent
Main applications	Sensors	Actuators and transducers	Actuators and transducers

The preparation and characterization of high performance PZT thick films made on the Si substrates were first presented by Chen et al. [119,120], showing a broad variety of potential applications. Moreover, the deposition of PZT thick films directly onto the Si substrates allows for the integration of devices and control circuits onto a single chip using the compatible manufacturing technology. Implementation of PZT films with a thickness of 50-150 μm into meso-scale piezoelectric MEMS devices using thick-film technology has attracted considerable attention during the past few years [23]. Preparation of films in that thickness range is difficult using either thin-film technology (*e.g.* sputtering and chemical vapor deposition) or bulk machining techniques (*e.g.* dicing bulk PZT and chemical polishing). Therefore, developing suitable fabrication techniques is important for making piezoelectric PZT layers with reasonable piezoelectric properties and the further implementation in MEMS devices. A summary of properties of PZT-based thick film made on Si substrates using various approaches is listed in Table 2.5. The comparison of dielectric properties for thick-film PZT ceramics and their bulk counterparts is also included for different material systems.

It can be observed that most thick-film PZT ceramics exhibit lower values of dielectric constant compared to the bulk PZT. This is consistently related to differences in the microstructure, whereby the PZT thick films normally exhibit a high degree of porosity than the bulk PZT ceramics. However, recent development in material composition and device structure allows the patterned PZT thick films to deliver equivalent functions to bulk materials, for example, using PZT multilayer actuators for piezoelectric MEMS devices requiring large generative force [23]. Functional devices, such as microresonators for mass sensing applications and micropumps for microfluidic systems, have been implemented by virtue of the corresponding modified fabrication techniques. Reviewing the design and working principles of these devices would facilitate a quick transition to realize the same functions using LTCC/PZT structures.

Table 2.5 Comparison of dielectric properties of PZT thick films made on Si substrates using different technical approaches.

Thick film processing route and temperature	Material composition	Thickness (µm)	ε_r (& dielectric loss tanδ) at 1kHz		Ref.
			Thick film	Bulk	
Screen-printing, 1100°C	La doped PZT (60/40)	100	190 (0.014)	1129 (0.028)	[121]
Screen-printing, 1000°C	$Pb(Ti_{0.04}Zr_{0.68}Fe_{0.14}Nb_{0.14})O_3$	100	204 (0.019)	560 (0.085)	[122]
Screen-printing, 1050°C	Doped PZT (50/50) + 3 or 4 wt% sintering aids	80	840 (0.009)	2010-2050 (0.004)	[123]
Screen-printing, 900°C	PZT (BM500) + 3 wt% sintering aids	20-40	970	1750	[124]
Screen-printing, 1135°C	Doped PZT (52/48)	66	710 (0.024)	–	[125]
Screen-printing, 900°C	$0.1Pb(Zn_{1/2}W_{1/2})O_3$+0.9PZT (50/50)	25	703 (0.030)	1221 (0.032)	[126]
Aerosol deposition + annealing, 900°C	$0.2Pb(Zn_{1/3}Nb_{2/3})O_3$+0.8PZT (50/50) + 2 wt% excess PbO	50	1400 (0.50)	–	[127]
Sol-gel process, 950°C	PZT (53/47) coated with $Pb_5Ge_3O_{11}$	10-50	771 (0.052)	1200	[128]
Sol-gel process + wet etching, 720°C	Nb, Sb doped PZT (52/48)	40	690 (0.013)	–	[129]
Sol-gel process, 710°C	PZT (PZ26)	10	600	1200	[130]
Diol sol-gel process, 700°C	PZT (53/47)	10	1000 (0.040)	1200	[131]
Sol-gel process, 700°C	PZT (53/47)	10	1400 (0.036)	–	[132]
Sputtering, 600°C	PZT (52/48)	4.6	1300	–	[133]

Micromachined silicon beam resonators with thick-film PZT drive and detection layer have been demonstrated by Beeby et al. [134]. The device consists of a silicon membrane and the screen-printed film PZT of 40 μm thickness, which is sandwiched between an evaporated Pt bottom electrode and an Au printed top electrode. The presented PZT thick-film resonator has proved the feasibility to use this structure for mass sensing. Another microbalance based on the PZT thick-film structure has been fabricated and presented by Ferrari et al. [135], demonstrates a mass sensitivity of 500 Hz/μg with a thickness of PZT layer in 140-150 μm. A planar capacitor structure printed onto an Al_2O_3 substrate can be operated as a thickness mode resonant structure, as shown in Figure 2.12. This structure is sensitive to mass loads applied on the free surface. This developed thick-film structure, which can be used as a chemical sensor, is coated by a chemically sensitive material that adsorbs certain molecules. Fabricating an oscillator control circuit around the sensor will provide an integrated device.

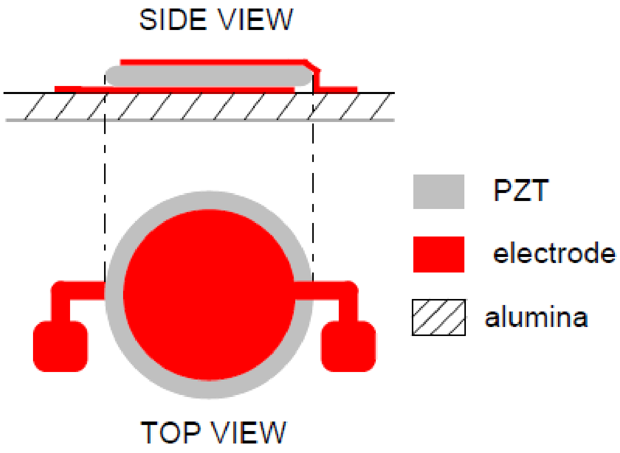

Figure 2.12 The structure of a PZT thick-film resonant sensor for microbalance application. (taken from M. Ferrari et al. [135])

Koch et al. [136] reported a micropump designed and fabricated combining screen printed thick-film PZT layers with a Si micromachined structure. Passive cantilever check-valves were incorporated into the Si structure by fusion bonding. The device is depicted in Fig. 2.13. The pump rate of up to 400 µl/min with a maximum backpressure of up to 35 kPa at 100 V driving voltage across the PZT layer is expected using finite element analysis results.

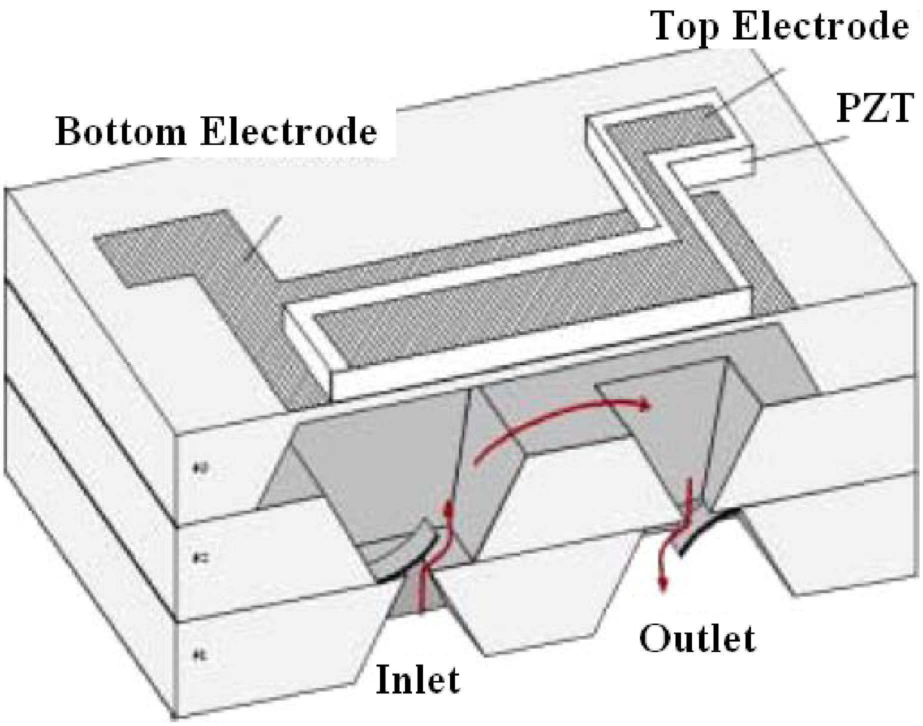

Figure 2.13 Schematic illustration of micropump made of screen printed PZT layer on micromachined Si structure. (taken from M. Koch et al. [136])

2. 3 Integration of LTCC with PZT ceramics

Thick-film technologies provide the possibility of directly integrating the functional films onto the certain substrates. Most thick-film applications incorporate the substrate into the whole device structure. Hence the substrate material becomes a critical component in any sensor or actuator design [137]. Al_2O_3, glass, and Si are common substrate materials for the design and fabrication of thick-film PZT devices. However, LTCC materials provide more advantages than Al_2O_3 and Si substrates especially for the fabrication of 3-D ceramic microfluidic devices and hybrid integration of microsystems. Using LTCC material as the substrate or package for thick-film PZT devices is a new attempt to extend the application field for both LTCC technology and PZT-based MEMS devices.

2. 3. 1 Ceramic micro-electromechanical systems (C-MEMS)

Ceramics are widely used in the fabrication of MEMS devices and systems because of their versatile structural, chemical, and functional properties, such as: (1) chemical inertness for applications in biological fields; (2) corrosion resistance at high temperatures for chemical engineering and sensor applications in severe environments; (3) suitable mechanical and electrical properties provided for making functional components. Design and fabrication of fully ceramic MEMS (C-MEMS) is an emerging research field in MEMS technology, which has attracted increasing interest in a variety of application areas [138]. Development of such C-MEMS devices and systems requires using ceramics for construction of both MEMS body structure and functional components. Incorporating piezoelectric PZT thick films into a ceramic substrate for the fabrication of high-performance and reliable C-MEMS is one of the most challenging tasks. Those devices are important in diverse fields such as industrial process control, environmental monitoring, communications, and medical instrumentation [139].

C-MEMS made with compatible thick-film technology on a ceramic substrate are widely used in harsh environments. In comparison with Si-based MEMS they are more robust and resistant to high operating temperature, showing better long-term stability. Al_2O_3 is one of widely used inert ceramic substrates for MEMS fabrication, which provides good adhesion for the printed functional thick films, compatible CTE with most thick-film pastes, high robustness, and limited capability for 3-D component integration [137]. The combination of Al_2O_3 substrates with integrated piezoelectric ceramic components has been studied for making novel C-MEMS devices in a miniaturized ceramic package [140-142], Development of such devices can offer advanced sensor, actuator, and transducer solutions for new fields of application.

However, LTCC provides advantages over Al_2O_3 in certain applications. For example, the lower Young's modulus for LTCC compared to the Al_2O_3 makes it more effective for the application of thick-film pressure sensors. However, pure Al_2O_3 substrate require sintering above 1500^oC which is not applicable for co-firing with PZT ceramics while the LTCC materials provide the possibility of co-firing with other functional elements (conductors, dielectrics, and piezoelectrics) to build multilayer structures in a more versatile approach. Several characteristics of typical MEMS substrate materials, LTCC, Al_2O_3, and Si are listed in Table 2.6. LTCC materials and processing are particularly suitable for the implementation of 3-D microfluidic C-MEMS devices and systems using the multilayer ceramic technology [143]. Developing C-MEMS based on piezoelectric PZT thick films integrated on a 3-D LTCC structure has recently arisen as a challenging research topic. Technological obstacles are needed to be overcome to make such hybrid systems. A thorough understanding of electrical and piezoelectric properties of PZT thick films integrated onto the LTCC substrate is necessary for the successful usage of developed C-MEMS in sensing and actuating applications.

Table 2.6 Characteristics of common used MEMS substrate materials.

	Fired LTCC (DuPont 943)	**Al_2O_3 ceramics (~99.5%)**	**Silicon**
Density (g/cm^3)	3.2	3.7 – 3.97	2.3
Young's modulus (GPa)	150	394	186.5
Dielectric constant	7.4 (at 40GHz)	~10 (at 1MHz)	~12 (at 1GHz)
Loss tangent (%)	0.2 (at 40GHz)	~0.2 (at 1MHz)	~0.5 (at 1GHz)
Resistivity (Ω cm)	$> 10^{12}$	$> 10^{14}$	$10^3 – 10^5$
Breakdown voltage ($V\ cm^{-1}$)	$> 4 \times 10^5$	1.5×10^5	3×10^5
Thermal conductivity ($W\ m^{-1}\ K^{-1}$)	4.4	35	148
TCE (10^{-6}K)	6.0	8.4	2.6

* LTCC data source: DuPont 943 green tape data sheet; Al_2O_3 data source: Ferro Ceramic Grinding Inc., 99.5% Al_2O_3 property table; Si data source: EL-CAT Inc., online information, properties of silicon.

2. 3. 2 Compatibility between LTCC and PZT

Piezoelectric PZT thick films made on LTCC provide more possibilities for their applications in integrated microsensors and actuators [16]. However, the majority of reported LTCC-based piezoelectric devices are made by post-firing or adhesive bonding PZT components on the fired LTCC structures. For maximum utility LTCC/PZT multilayer structures for C-MEMS fabrication should be obtained in a single co-firing process using the advanced thick-film technology and ceramic processing techniques. Three important issues for co-firing LTCC and thick-film PZT materials are needed to be considered in advance. Firstly, the conventional sintering temperature (1100^o-1300^oC) of PZT needs to be lowered to be comparable with LTCC firing temperature (850^o-900^oC). Many types of sintering aids have already been used to reduce the PZT sintering temperature to a range of 700^o-950^oC [144-146]. Secondly, elemental inter-diffusion between LTCC and PZT layers during sintering is a significant problem for obtaining PZT thick films with desired properties. Thirdly, the mismatch of sintering behaviors (heating process) and CTE (cooling process) between LTCC and PZT components generates shear stress at the interface, which can cause deformations after sintering, such as delamination and camber. Structural failures may occur in the laminated multilayers after co-firing, showing collapse and macroscopic cracking. Typical deformations and failures in co-fired LTCC-based multilayer structures are shown in Figure 2.14.

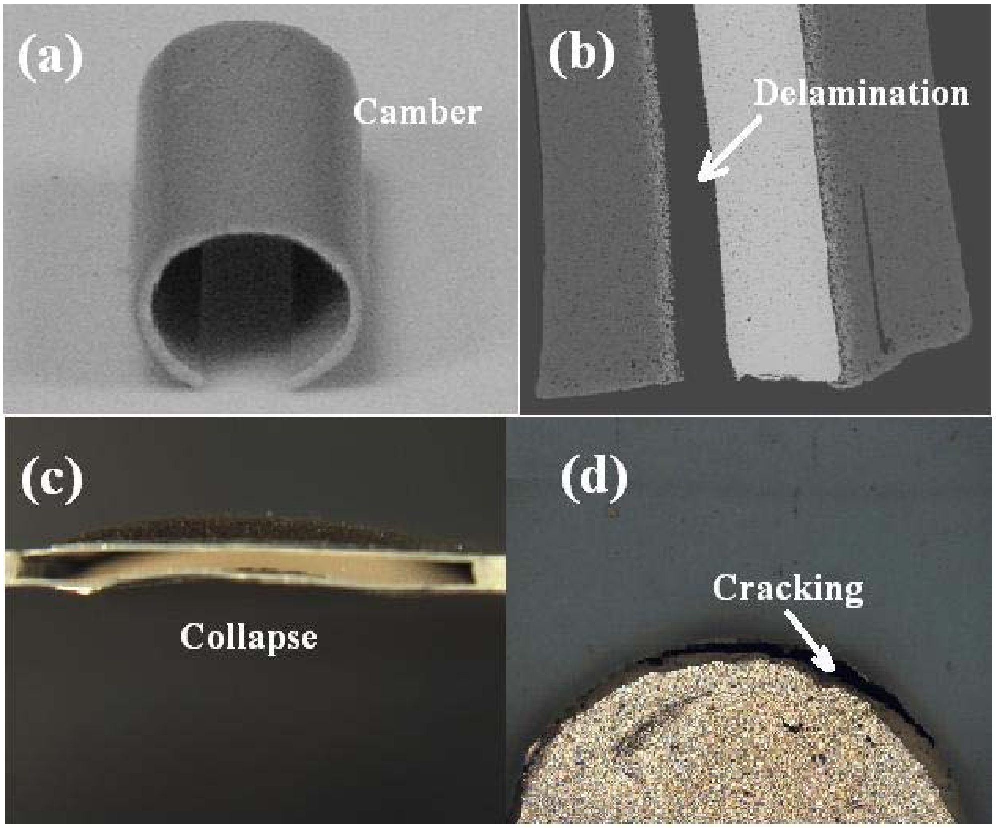

Figure 2.14 Images of deformation and failure in co-fired LTCC multilayer structures. (a) camber, (b) delamination, (c) collapse, and (d) cracking.

There were previously several attempts to investigate co-firing LTCC/PZT multilayer ceramics. However, a serious interfacial diffusion problem and deteriorated properties were revealed. A study on the compatibility between LTCC substrate and screen printed PZT-based thick film was reported by Hrovat et al. [147]. PZT (53/47) powders with an excess 6 mol% of PbO and 2 mol% of $Pb_5Ge_3O_{11}$ (PGO) as a sintering aid were prepared by solid state route. The calcined powders were mixed with an organic vehicle to make thick-film paste for screen printing. The DuPont 951 LTCC materials were used as the substrate and compared with Al_2O_3. Gold electrode layers were printed on both types of substrates and co-fired with PZT thick films. The relative dielectric constant of PZT layer on LTCC was only one tenth of that on Al_2O_3 and much lower than the value of bulk ceramics sintered at the same temperature. The deterioration of dielectric properties was considered to be induced by the inter-diffusion of PbO and SiO_2 upon co-firing. Golonka et al. [148] investigated the inter-diffusion of LTCC and PZT with various co-firing conditions and electrode materials. It was found that the shorter firing time and Pd/Ag electrode materials resulted in better dielectric and piezoelectric properties for the PZT layers. Belavic et al. [28,149] used a barrier layer to reduce the interfacial diffusion between LTCC and PZT during the co-firing process. The results showed a limited improvement on the electric properties, as illustrated in Figure 2.15. The additional barriers did not hinder the diffusion of Si from LTCC to PZT layer but it prevented the loss of PbO from the active PZT layer. The preliminary study using both LTCC and traditional thick-film technologies for developing C-MEMS was also reported in the same articles.

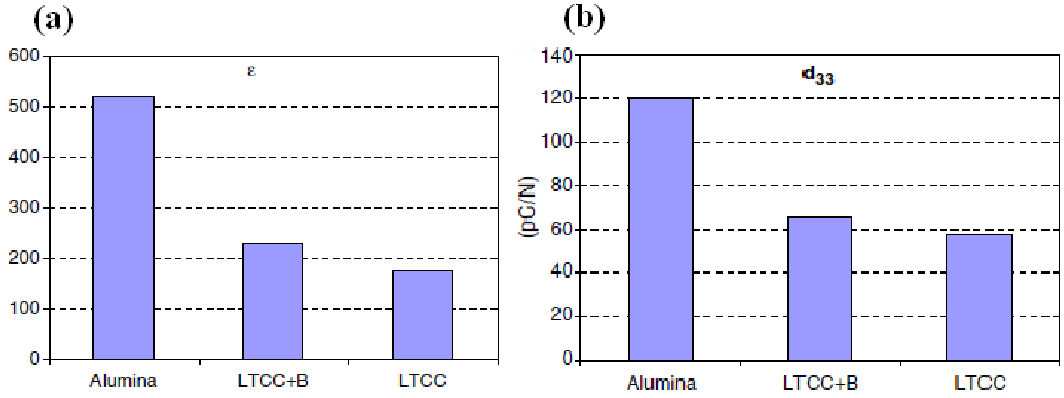

Figure 2.15 (a) Dielectric constant and (b) piezoelectric coefficient d_{33} of PZT layer fired on Al_2O_3, LTCC, and LTCC substrate with diffusion barrier layer (LTCC+B). (taken from D. Belavic et al. [149])

A further study, reported by Ursic et al. [150], on the piezoelectric properties of thick-film PZT made on the LTCC substrate has not exhibited any significant improvement. Other studies on the co-firing compatibility between LTCC and other functional materials have been conducted recently, for example, co-firing magnetic ceramic layers with commercial LTCC tapes [151] and integrating different conductive layers into the LTCC modules [152,153]. To date only a few physical sensors were constructed by the combination of LTCC substrates and piezoelectric active layers [26,27]. Co-firing LTCC/PZT multilayer ceramics to fabricate actuators for C-MEMS devices and integrated microsystems is still a challenging work.

2. 3. 3 Current development in LTCC and PZT materials

Prior experiments do not exhibit favorable results on the compatibility between LTCC and printed thick-film PZT ceramics, particularly the inferior electric properties of PZT in co-fired LTCC/PZT structures. Current development in LTCC and PZT material systems provides new opportunities for co-firing LTCC/PZT multilayer ceramics by integrating self-constrained LTCC tapes with high performance modified PZT materials. The PZT layer in the co-fired LTCC/PZT structure is expected to show reasonable dielectric and piezoelectric properties with minimum deformation for the whole multilayer ceramics.

Self-constrained LTCC tapes

One of the limitations in LTCC technology involves the *x-y* shrinkage of LTCC structures during firing the process and the dimensional tolerance of that shrinkage. This affects component design, materials utilization, and surface-circuit feature location in the

LTCC fabrication process. Moreover, the shrinkage behaviors of LTCC materials are not designed to match the densification conditions for most PZT-based ceramics, which cause additional issues in LTCC/PZT co-firing process. A newly self-constrained HeraLock^{TM} HL2000 tape developed by Heraeus [154,155] provides a sintering shrinkage in *x*, *y* directions of less than 0.2% and a shrinkage tolerance of ±0.02% without using sacrificial layers and external pressure during firing.

The HL2000 tapes are multilayer laminates prepared by special casting process. A symmetric laminate with two different types of layers is laminated in the green state, as shown in Figure 2.16, illustrating the different layers sintered at different temperature intervals. The inner layer starts to densify in the first sintering stage while the outer layers function as rigid substrates preventing the lateral shrinkage. In the second sintering stage, the outer tapes shrink while the fully densified inner layer prevents the shrinkage of the outer layers in *x*-*y* direction. The specific composition of each LTCC layer sintered at different temperature intervals is carefully controlled. The effective suppression of lateral shrinkage requires that the inner layer should completely stop densification before the outer layers start [154].

A demonstration of near-zero *x*-*y* shrinkage of HL2000 tapes is illustrated in Figure 2.17. A green laminate with metallization was cut in half along the diagonal. No visible mismatch between the two parts was observed after sintering only one half. HL2000 enables large-area metallization, integration of channels, cavities and passive electronic components without waviness and camber.

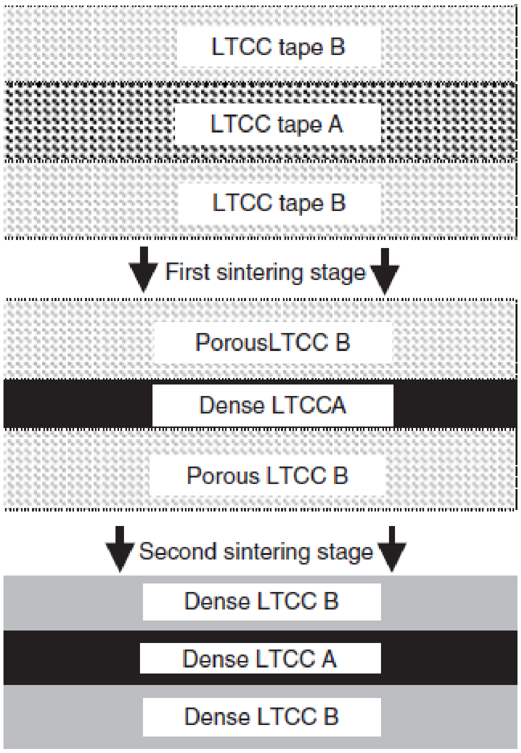

Figure 2.16 Sintering process for the self-constrained laminate consisting of two different layers with various sintering intervals. (taken from T. Rabe et al. [154])

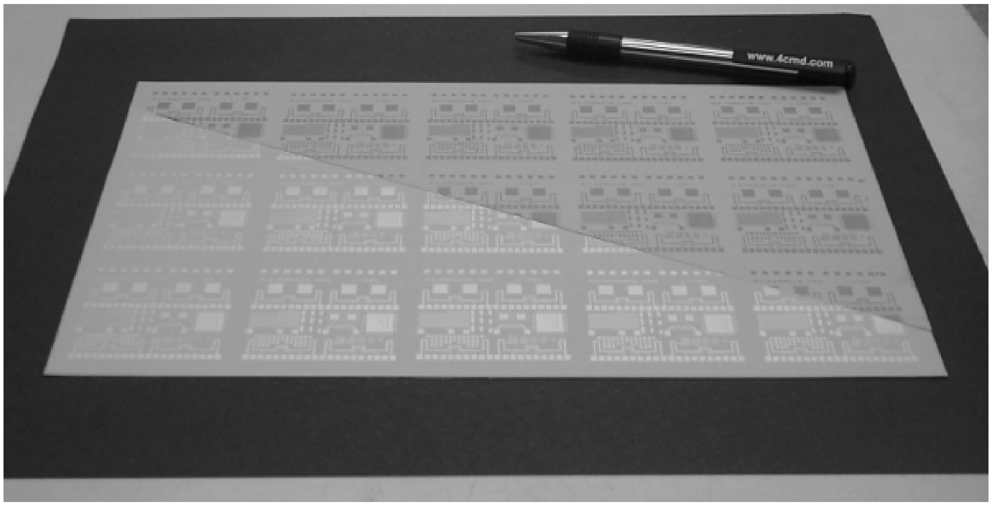

Figure 2.17 An illustration of self-constrained HL2000 tapes showing near-zero *x*-*y* shrinkage after firing. (taken from T. Rabe et al. [154])

Using HL2000 tapes as substrates for temperature and pressure sensors was evaluated by screen-printing and firing thick-film thermistors and piezoelectric PZT ceramics on the fired HL2000 tapes [156]. The uniform self-constrained HL2000 tape provides excellent compatibility with materials that have significantly different densification profiles, which reduces the need to tailor densification behaviors and greatly saves development time.

High performance doped-PZT ceramics

Recently, Donnelly et al. [31] reported a high-performance piezoelectric ceramic made by (1-x)PZT-xSKN (x = 0.2) that Zr/Ti ratio is fixed to undoped MPB composition ($Zr_{0.53/}Ti_{0.47}$) and the composition of Sr, K and Nb is in the formula of $Sr(K_{1/4}, Nb3_{/4})O_3$ (SKN) with specific ratio of 4:1:3. Showing high d_{33} value and high T_c, this PZT-based ceramic can be used for piezoelectric multilayer actuators which satisfy the requirements of fuel injectors for automotive application. Despite the chemical formula it is expected that both Sr^{2+} and K^+ will substitute for Pb^{2+} at the A sites in the perovskite structure, as isovalent and acceptor additives respectively. Nb^{5+}, as a donor dopant, occupies the B sites. However, the precise doping effect, site occupation, and defect chemistry associated with the SKN combination are complicated and remain unclear. The result is a high Curie temperature material with moderate strain-field hysteresis and an exceptionally large high field piezoelectric strain coefficient. The high field d_{33} value, which is taken as the ratio of strain to field at 20 kV/cm, is a function of SKN content. The maximum d_{33} value 779 pm/V was found at the 0.98PZT-0.02SKN composition, as shown in Figure 2.18. The variation of piezoelectric properties with the SKN addition can be explained by the competing effects from donor doping and grain size-related phenomena or the dopant-induced shift in the MPB composition of PZT solid solutions.

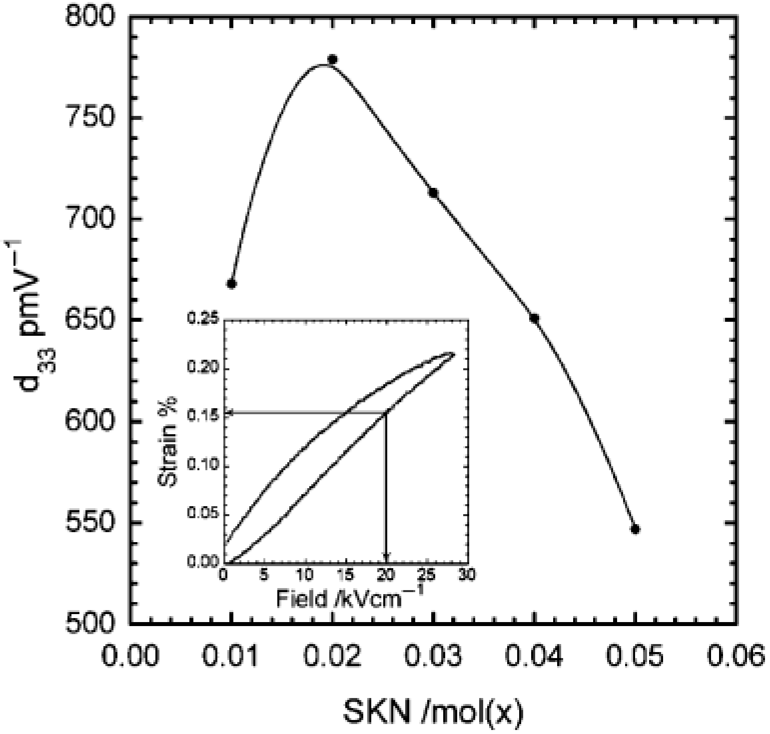

Figure 2.18 The high field d_{33} piezoelectric coefficient as a function of SKN addition and (inset) unipolar strain loop used for the d_{33}^{high} calculation. (taken from N.J. Donnelly et al. [31])

A further attempt to lower the sintering temperature of (1-x)PZT-xSKN by the addition of fluxes was reported [157]. The most successful flux was found to be the Li_2CO_3 with 0.9 mol% addition which promotes the densification at 900°C and the sintering was carried out for 3-6 h. The partial Li substitution in the low fired ceramics may lead to the reduced resistivity and permittivity compared to the conventionally sintered samples. The Li_2CO_3 fluxed (1-x)PZT-xSKN showed a shift in the optimum composition. The flux-sintered 0.97PZT-0.03SKN exhibited a maximum high field d_{33} of 640 pm/V and T_c of ~350°C. The functional properties of (1-x)PZT-xSKN ceramics conventionally sintered at 1250°C and flux-sintered at 900°C with 0.9 mol% Li_2CO_3 addition are compared in Table 2.7. A multilayer structure of fluxed PZT-SKN layers with printed silver electrodes was also successfully co-fired using the low temperature firing profile.

Table 2.7 Properties of PZT-xSKN ceramics sintered at 1250°C and flux-sintered at 900°C with 0.9 mol% Li_2CO_3 flux addition. (taken from N.J. Donnelly et al. [31,157])

SKN (mol%)		**Grain size (μm)**	**T_c (°C)**	**ε_r (1kHz)**	**d_{33}^{high}**	**k_p**
0.01	High fired	11.4±2.9	375	1300	668	0.53
	Low fired	2.4±1.0	380	1214	522	0.53
0.02	High fired	6.2±2.0	356	1400	779	0.59
	Low fired	3.4±1.0	364	1260	590	0.62
0.03	High fired	2.8±1.0	341	1430	713	0.58
	Low fired	2.7±0.8	347	1339	640	0.60
0.04	High fired	1.5±0.5	323	1500	651	0.55
	Low fired	1.7±0.5	331	1398	630	0.60
0.05	High fired	1.5±0.5	305	1500	547	0.47
	Low fired	1.5±0.5	314	1479	605	0.57

2. 4 Sintering of ceramics

Sintering is the most critical processing technique used to produce a ceramic with desired microstructures and properties by applying thermal energy into a powder compact. Depending on the complex nature of different starting materials, several basic types of sintering processes have been used to analyze the densification behavior and the evolution of microstructure. In this thesis work, high-density polycrystalline PZT-SKN ceramics are prepared by solid-state sintering route. The enhanced densification rate of PZT-SKN ceramics sintered at low temperature will be achieved using low-melting-point additives, which is referred to as liquid-phase sintering. The densification of glass-ceramic composite materials like LTCC is attributed to the viscous sintering, which is controlled by the viscosity of the glass during the heat treatment [158]. The constrained sintering process can be used to explain the sintering behavior of hybrid LTCC/PZT-SKN multilayer laminates. The resulting properties of sintered piezoelectric ceramics in the multilayer structures are directly related to the performance of the fabricated devices.

2. 4. 1 Driving force for sintering

The sources that cause the reduction of the total free energy of the system are considered as the driving forces for sintering. There are three possible driving forces [159]: (1) surface free energy, (2) externally applied pressure, and (3) chemical reaction.

Surface free energy provides the main driving force if no external pressure and chemical reaction are involved during sintering. The surface area of a powder system consisting of one mole spherical particles with a radius a is given by $3V_m/a$, where the V_m

is the molar volume. The change of surface free energy ΔG_s associated with the system of particles is described by:

$$\Delta G_s = 3\gamma_{sv} V_m \left(\frac{1}{a} - \frac{1}{a'}\right)$$

where γ_{sv} is the specific surface energy. The ΔG_s is related to the difference in the reciprocal of the radius of curvature of the particles before and after sintering.

An externally applied pressure is considered as the major source of driving forces in the absence of a chemical reaction. The contribution of surface curvature change is significant smaller than that of external pressure in the reduction of the free energy of the system. The work exerted on the one-mole particle system by the external pressure can be determined by [159]:

$$W = p_a\, V_m$$

where p_a is the applied pressure and W represents the driving force for the resulting densification of the powder system.

The change in free energy ΔG^{o} determined by a chemical reaction is given by [159]:

$$\Delta G^{o} = -RT\ln K_{eq}$$

where R is the gas constant, T is the absolute temperature, and K_{eq} is the equilibrium constant for the reaction. The driving force induced by chemical reaction is considerably greater than that caused by external pressure. However, the chemical reaction is rarely used to facilitate densification in the preparation of advanced ceramics because the complexity of reaction makes the microstructure control extremely difficult during sintering [159]. Figure 2.19 illustrates the three main driving forces for sintering.

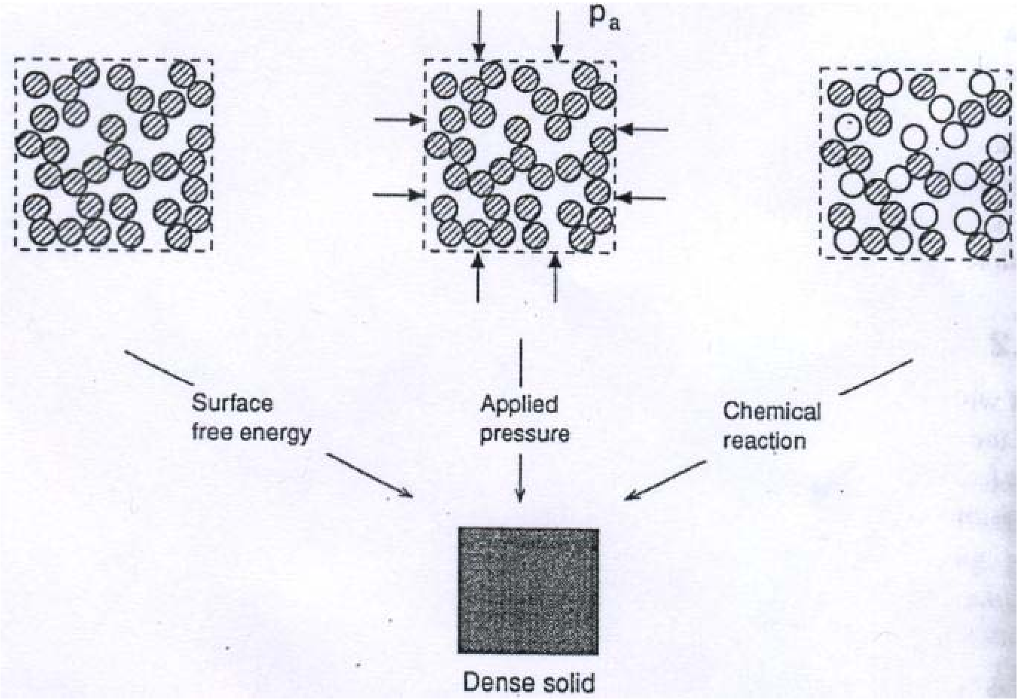

Figure 2.19 Illustration of three main driving forces for sintering: surface free energy, external pressure, and chemical reaction. (taken from M.N. Rahaman [159])

2. 4. 2 Solid-state sintering

Driving force

In the absence of applied external pressure and chemical reaction, the driving force for solid-state sintering is the reduction of surface free energy achieved by the atomic diffusion which results in two competing processes: densification and coarsening.

Densification is caused by the elimination of pore volume interfaces and the simultaneous formation of new but lower-energy grain boundaries. Coarsening is a result of the rearrangement of the pore surfaces without the decrease in the pore volume accompanied by grain growth. The dominant process will determine the final microstructure of the consolidated mass of particles after sintering, the production of a high-density body will be favored by densification while the production of a highly porous body by coarsening. The difference between densification and coarsening is schematically shown in Figure 2.20.

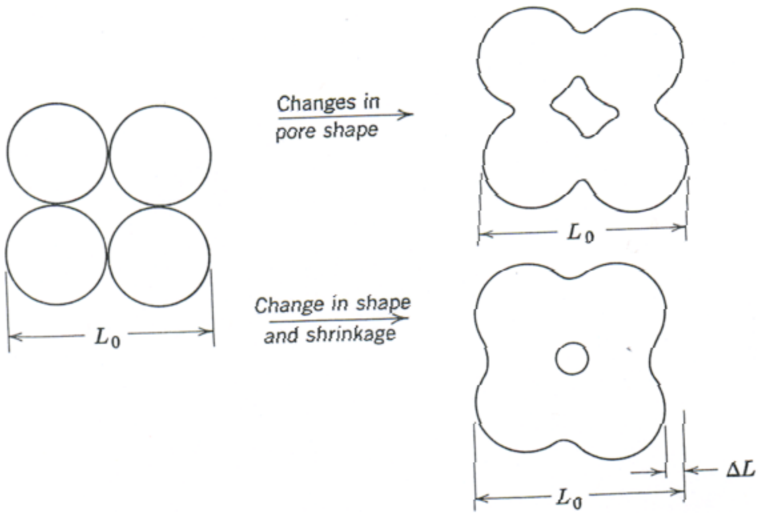

Figure 2.20 The difference between densification and coarsening processes. (taken from W.D. Kingery et al. [160])

The shape of pores defined by the grain boundaries in polycrystalline materials is important for the densification process. In equilibrium state the tension in grain boundary and the tension in the solid-vapor interface are balanced at the junction where the grain boundary intersects the pore. The balance of forces is given by:

$$\gamma_{gb} = 2\gamma_{sv}\cos\frac{\psi}{2}$$

where ψ is defined as dihedral angle, γ_{sv} and γ_{gb} are the interface tension and grain boundary tension, respectively. The dihedral angle ψ has to be less than 180^{o} for densification to occur. When the ψ is low, the pores will stabilize in the structure and the further removal of pores is limited.

Mechanisms of sintering

During the sintering process, matter transports from regions of higher chemical potential (source of matter) to regions of lower chemical potential (sink of matter). The diffusion path of mass transport in polycrystalline materials defines the mechanisms of sintering, as shown in Table 2.8 and Figure 2.21.

Table 2.8 Mechanisms of sintering in polycrystalline solids. (taken from W.D. Kingery et al. [160])

Mechanism number	Transport path	Source of matter	Sink of matter	Process
1	Surface diffusion	Surface	Neck	Coarsening
2	Lattice diffusion	Surface	Neck	Coarsening
3	Vapor transport	Surface	Neck	Coarsening
4	Boundary diffusion	Grain Boundary	Neck	Densification
5	Lattice diffusion	Grain Boundary	Neck	Densification
6	Plastic flow	Dislocations	Neck	Densification

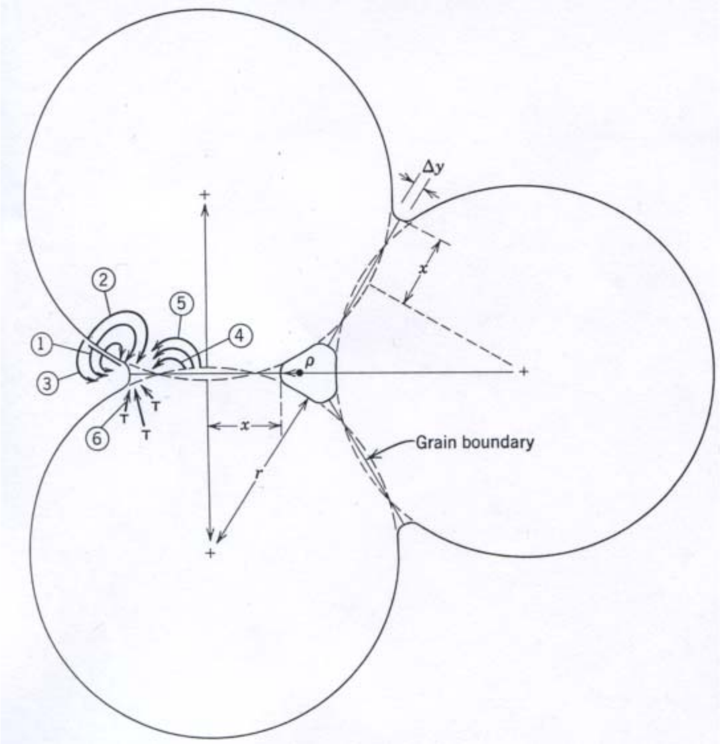

Figure 2.21 Six distinctive paths for matter transport during the sintering of a consolidated mass of crystalline particles. (taken from W.D. Kingery et al. [160])

All of the introduced sintering mechanisms lead to neck growth between particles, resulting in an increase in the compact strength. Certain mechanisms that do not cause the particle centers to move closer together, will not lead to densification but coarsening. The nondensifying mechanisms occur when matters transport from the particle surfaces to the neck region, including surface diffusion, lattice diffusion from the surface, and vapor transport (mechanisms 1, 2, and 3). Although not leading to densification, these mechanisms cause a decrease in the neck curvature; it hence reduces the driving force for sintering which in turn slows the densification rate. The neck growth and densification occur by grain boundary diffusion and lattice diffusion from the grain boundary to the pore (mechanism 4 and 5) in polycrystalline ceramics. Another densifying mechanism is plastic flow by dislocation motion (mechanism 6), a common path of mass transport for sintering metal powders. The sintering rates can be measured by the rates at which the width of the neck increases and compared for the corresponding mechanisms. In addition, the rate of shrinkage of the powder compact can be used to measure the rate of densification [159].

Stages of sintering

Many analytical models have been proposed to describe sintering process using an idealized geometry for the powder system [161-167]. In order to simplify the analysis of micro- structural evolution and the formation of mass transport equations, the sintering process is typically divided into three sequential stages based on the connectivity of microstructure: (1) initial stage, (2) intermediate stage, and (3) final stage. The Figure 2.22 shows the idealized geometrical structures that represent each stage defined by Coble [161].

The rapid inter-particle neck growth is involved in the initial stage, which is represented as the transition between Figure 2.22(a) and Figure 2.22(b). The density increases to about 65% of the theoretical density when the densifying mechanisms dominate in this stage. The intermediate stage is characterized by continuous cylindrical pore channels coincident with three-grain junctions as illustrated in Figure 2.22(c). The density increases from 65% to about 90% by pore shrinkage which is controlled by lattice and grain boundary diffusion in the intermediate stage. In the final stage the pore channels are eventually pinched off into separate pores located at the grain corners as shown in Figure 2.22(d).

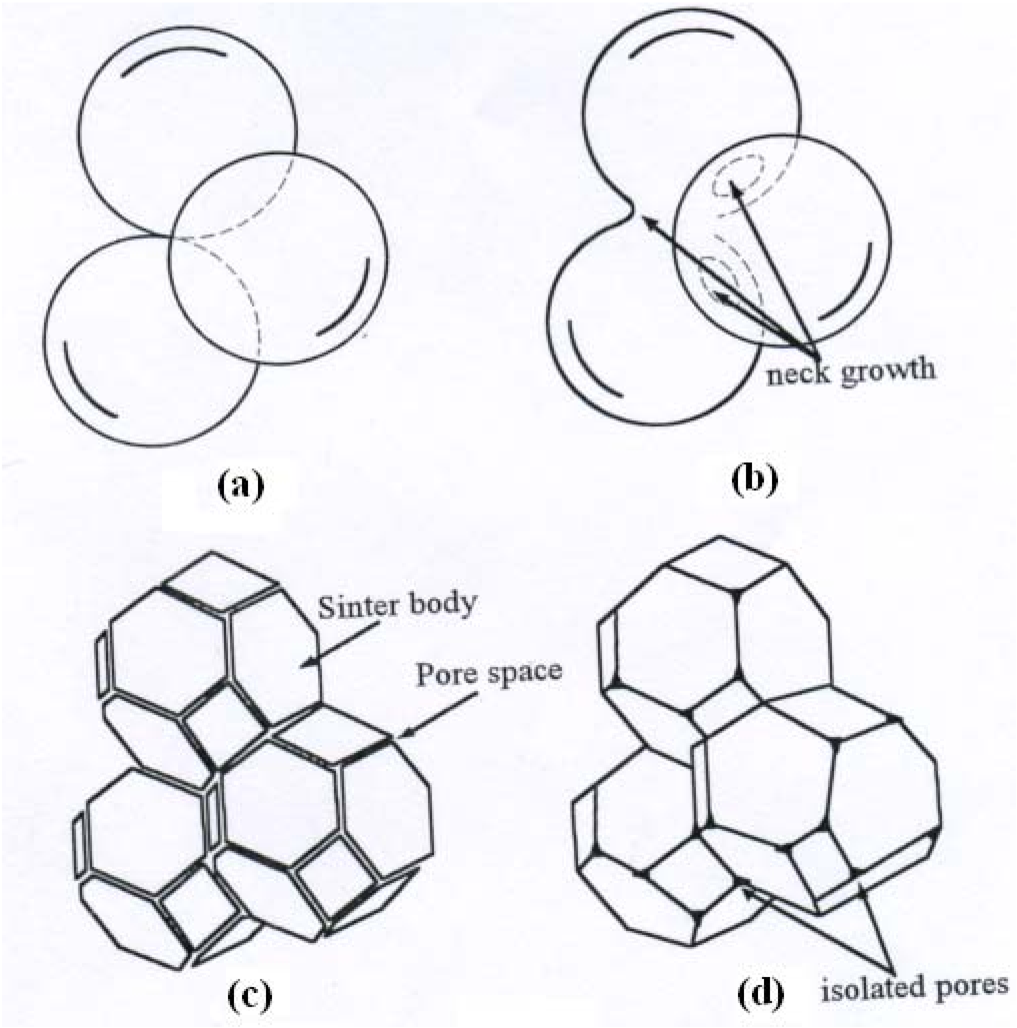

Figure 2.22 Illustration of idealized models for the three sintering stages. (a) initial stage of sintering model represented by spheres in tangential contact; (b) near the end of the initial stage: spheres have begun to coalesce; (c) intermediate stage: grains adopted shape of tetrakaidecahedron, enclosing pore channels at grain edges; and (d) final stage: pores are tetrahedral inclusion at corners where four tetrakaidecahedra meet. (taken from M.W. Barsoum [168])

The simple two-sphere model, consisting of two equal-sized spheres in contact, is used to analyze the initial sintering stage. The neck growth between particles is determined by both densifying and nondensifying mechanisms. Assuming that all the transport paths are independent and additive, the rate of neck growth during the initial stage can be expressed as [169]:

$$\frac{dx}{dt} = \frac{C_1 \gamma D_l R}{x^3} + \frac{C_2 \gamma D_{gb} R^2}{x^5} + \frac{C_3 \gamma D_s R^2}{x^5} + \frac{C_4 \gamma p_o R}{x}$$

where x is the radius of neck, R is the sphere radius, γ is the specific surface energy, C_i (i = 1-4) is a constant relating to the specific diffusion path and the geometry of the model, p_o is the vapor pressure, and the D_l, D_{gb}, D_s are the diffusion coefficients for lattice, grain boundary, and surface diffusion respectively. The general form of equations for neck growth (x/R) and shrinkage ($\Delta L/L_o$) in the initial stage are given by [159]:

$$\left(\frac{x}{R}\right)^m = \frac{H}{R^n}\, t$$

$$\left(\frac{\Delta L}{L_o}\right)^{m/2} = -\frac{H}{2^m R^n}\, t$$

where m and n are numerical exponents that determined by the specific mechanism of sintering and H is a function that depends on the geometrical and material parameters of the powder system. Table 2.9 summarizes the values of m and n as well as the expressions of H for each sintering mechanism [170].

Most of the densification of a powder system occurs during the intermediate stage. Coble [161] first proposed a geometrical model to explain this complex process. Nondensifying mechanisms cannot be applied in this model because the chemical potential is the same everywhere on the pore surface based on the assumption that all particles are equal-sized tetrakaidecahedra and all pores are cylindrical with the same size. Only lattice diffusion and grain boundary diffusion are considered to dominate the densification process. The porosity function, $f(\varphi)$, can be derived as [171]:

$$f(\varphi) = K\left(\frac{\gamma_{sv}\Omega D}{R_{go}^{m}kT}\right)(t_f - t)$$

where φ is the porosity, K and m are constants that determined by the sintering mechanism, γ_{sv} is the specific surface energy, Ω is the atomic volume, D is the diffusion coefficient, R_{go} is the initial grain size, k is the Boltzman constant, T is the absolute temperature, and t_f is the extrapolated time for the vanishing of the cylindrical pores. The values of $f(\varphi)$, K, and m for lattice diffusion and grain boundary diffusion mechanisms are listed in Table 2.10 according to the different suggested models.

Table 2.9 Plausible values of constants shown in the equations for initial stage of sintering. (taken from M.N. Rahaman [159])

Mechanism	***m***	***n***	***H***
Surface diffusion	7	4	$\frac{56D_s\delta_s\gamma_{sv}\Omega}{kT}$
Lattice diffusion from the surface	4	3	$\frac{20D_l\gamma_{sv}\Omega}{kT}$
Vapor transport	3	2	$\frac{3p_o\gamma_{sv}\Omega}{(2\pi mkT)^{1/2}kT}$
Grain boundary diffusion	6	4	$\frac{96D_{gb}\delta_{gb}\gamma_{sv}\Omega}{kT}$
Lattice diffusion from the grain boundary	5	3	$\frac{80\pi D_l\gamma_{sv}\Omega}{kT}$
Plastic flow	2	1	$\frac{3\gamma_{sv}}{2\eta}$

* D_l, D_{gb}, and D_s are the lattice, grain boundary, and surface diffusion coefficients respectively; δ_s and δ_{gb} are the thickness for surface and grain boundary diffusion; γ_{sv} is the specific surface energy; Ω is the atomic volume; m is mass of an atom; k is the Boltzman constant; T is the absolute temperature; and η is the viscosity.

Table 2.10 Parameters in the sintering models represented by equation for intermediate stage of sintering. (taken from T.A. Ring [172])

Model	$f(\varphi)$	***K***	***m***
Lattice diffusion			
Coble [142]	φ	720	3
Johnson [146]	$-\ln(1-\varphi)$	378	3
Grain boundary diffusion			
Coble [142]	$\frac{2}{3}\varphi^{3/2}$	$80\ \delta_{gb}$	4
Johnson [146]	$\int_{\varphi}^{0}\frac{\sqrt{x}}{1-x}\,dx$	$1000\ \delta_{gb}$	4

* δ_{gb} is the thickness for grain boundary diffusion.

The final density and the resulting properties of the sintered ceramics are largely decided by the final stage of sintering. The shrinkage of isolated pores takes place in the final stage of sintering. In an idealized powder system, the spherical pores of the same size are located at the intersections of particles. As in the intermediate stage, only densifying mechanisms (lattice and grain boundary diffusion) account for the shrinkage of the pores because the pore geometry is uniform. Coble [161] presented a model to describe the lattice diffusion in final stage of sintering:

$$Ps = \frac{6\pi}{\sqrt{2}}\left(\frac{D_l \gamma_{sv} \Omega}{l_p^3 kT}\right)(t_f - t)$$

where P_s is the porosity at a time t, D_l is the lattice diffusion coefficient, γ_{sv} is the specific surface energy, Ω is the atomic volume, l_p is the edge length of the tetrakaidecahedron, k is the Boltzman constant, T is the absolute constant, and t_f is the time when the pores disappear. This approximate equation is valid when the porosity is less than 2%.

2. 4. 3 Liquid-phase sintering

The method of using one or more additives that form a liquid phase between grains at sintering temperature is referred to as liquid-phase sintering. Compared to solid-state sintering, the formation of the liquid phase leads to the enhanced densification rates, accelerated grain growth, or specific grain boundary properties [159]. The amount of liquid phase formed is normally small but needs to be sufficient for providing a path for enhanced mass transport. The comparison of diffusion paths is shown in Figure 2.23 for solid-state sintering and liquid-phase sintering using idealized two-sphere model.

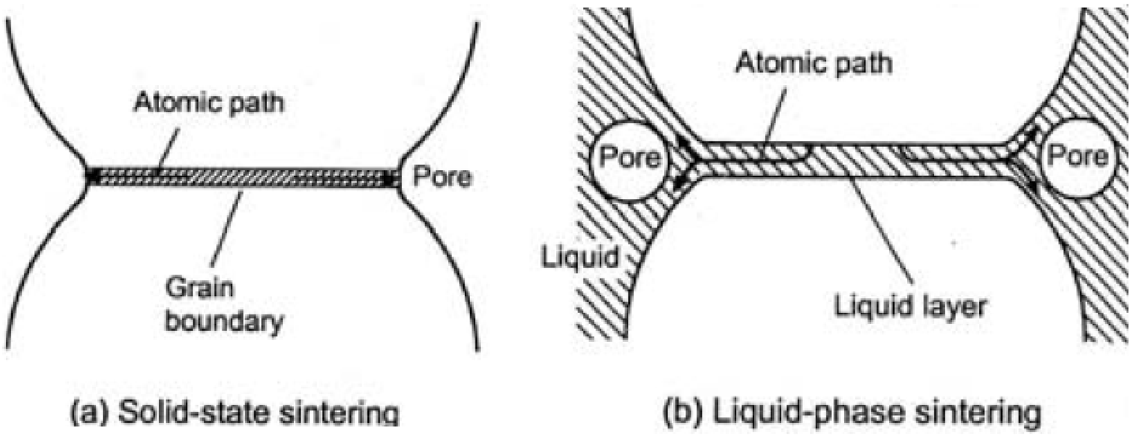

Figure 2.23 Schematic illustration of an idealized two-sphere model comparing the microstructural aspects of (a) solid-state sintering with (b) liquid-phase sintering. (taken from M.N. Rahaman [159])

Driving force

In an idealized model of liquid-phase sintering, the solid particles and pores are separated by the surrounding liquid phase. The reduction of the liquid-vapor interface energy is the source of driving force for the densification in this system if no external pressure and chemical reaction are involved. Considering a spherical pore of r in the liquid phase, the pressure difference Δp across the curved surface is given by:

$$\Delta p = -\frac{2\gamma_{lv}}{r}$$

where γ_{lv} is the specific surface energy of the liquid-vapor interface. The pressure deficit in the liquid generates a large compressive capillary stress on the particles, which provides the driving force for sintering.

Good wetting and appreciable solid solubility in liquid are fundamental requirements for liquid-phase sintering. The contact angle θ, defined by the angle between the solid surface and the tangent of to the liquid surface at the contact point, is used to characterize the degree of wetting. An equilibrium equation is derived for a solid-liquid-vapor system:

$$\gamma_{sv} = \gamma_{sl} + \gamma_{lv}\cos\theta$$

where the γ_{sv}, γ_{sl}, and γ_{lv} are specific energies for solid-vapor, solid-liquid, and liquid-vapor interfaces, respectively. Good wetting (low θ), which can be obtained with high values of γ_{sv} and low values of γ_{sl} and/or γ_{lv}, is a necessary condition for liquid-phase sintering. However, the solubility of solid in the liquid leads to the detailed wetting geometry in a powder system, which is another important factor for the occurrence of liquid-phase sintering.

In the same way that a dihedral angle ψ is defined in a solid-vapor system used in solid-state sintering, the dihedral angle ψ in a solid-liquid system is derived as:

$$\cos\frac{\psi}{2} = \frac{\gamma_{gb}}{2\gamma_{sl}}$$

where γ_{gb} and γ_{sl} are specific energy for grain boundary and the solid-liquid interface respectively. When the ratio γ_{gb}/γ_{sl} is small, solid-state sintering mechanisms dominate the sintering process because the liquid phase penetration of the grain boundary is limited. The liquid penetration of the grain boundary is complete when the ratio $\gamma_{gb}/\gamma_{sl} \geq 2$. The microstructures of ceramics determined by liquid-phase sintering for different ratios of γ_{gb}/γ_{sl} are described in Table 2.11.

Table 2.11 Microstructure of two-phase ceramics produced by liquid-phase sintering for different ratios of γ_{gb}/γ_{sl} and the corresponding ψ. (modified after M.N. Rahaman [159])

γ_{gb}/γ_{sl}	ψ	**Microstructure**
≥ 2	0^{o}	All grains separated by liquid phase
$\sqrt{3} - 2$	$0\text{-}60^{o}$	Continuous liquid phase penetrating all three-grain junction; partial penetration
$1 - \sqrt{3}$	$60\text{-}120^{o}$	Isolated liquid phase partially penetrating the three-grain junctions
≤ 3	$\geq 120^{o}$	Isolated liquid phase at four-grain junctions

Stages of liquid-phase sintering

During sintering in the presence of a liquid phase, three dominant stages of densification occur [173-175]. Firstly, rearrangement of solid particles under the influence of capillary stress gradient which gives rise to the increased density; Secondly, solution-precipitation process in which solid particles are dissolved at the solid-liquid interface, allowing the centers of particles to approach; Finally, a sintering stage controlled by the densification of the solid particulate network. The sequential stages of liquid-phase sintering are demonstrated in Figure 2.24. There is significant overlapping in connecting densification stages in an actual powder compact during sintering. Moreover, the densification process at each stage is dependent on the volume fraction of liquid. At approximately 35 vol% liquid, complete densification can be achieved with high uniformity by the rearrangement process alone [173]. For situations in which the liquid content is low, solution-precipitation and final stage sintering dominate the densification process in the powder systems.

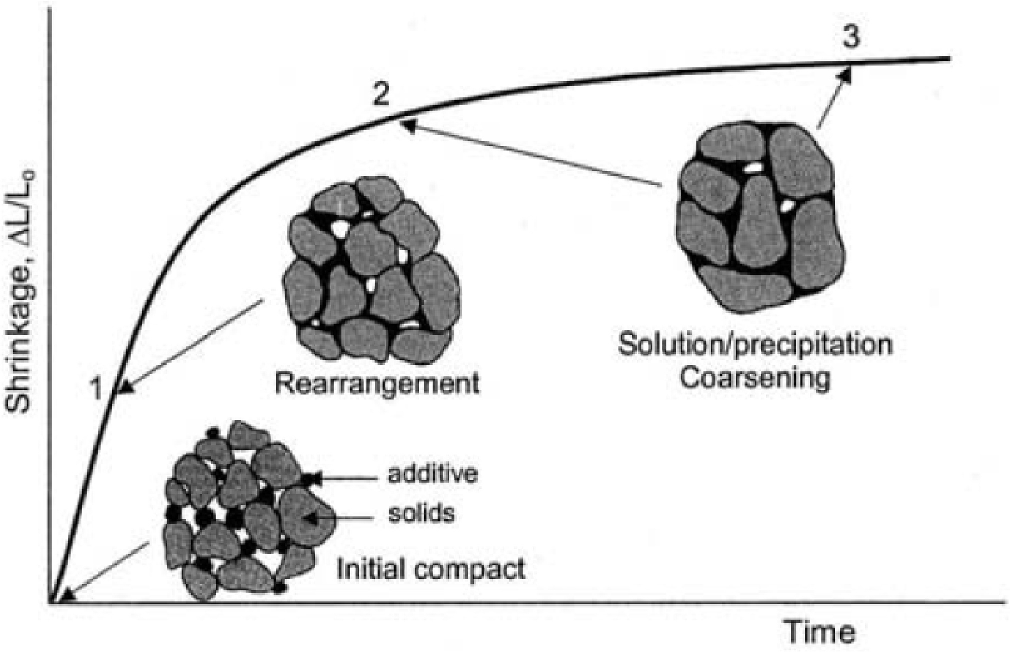

Figure 2.24 Schematic evolution of a powder compact during liquid-phase sintering. (taken from M.N. Rahaman [159])

Kingery [173,174] proposed a simple kinetic relationship to describe the shrinkage ($\Delta L/L_o$) in rearrangement process:

$$\frac{\Delta L}{L_o} = C_1 t^{1+y} \quad (0 < y < 1)$$

where C_1 is the constant at fixed composition and temperature for a given powder system and t is the sintering time. The exponent $(1 + y)$ is larger than unity because the increasing of driving force by the reduction in pore size is balanced by the increasing of resistance to rearrangement by viscous flow at the same time. Two mechanisms control the matter transport in the solution-precipitation process: (1) diffusion from the liquid and (2) interface reaction leading to either dissolution into the liquid or precipitation onto the particle surfaces. For a two-sphere particle model, the shrinkage in the solution-precipitation process which is diffusion rate controlled is given by [173]:

$$\frac{\Delta L}{L_o} = C_2^{\frac{1}{3}} r^{-\frac{4}{3}} t^{\frac{1}{3}}$$

or, for phase boundary reaction rate controlled:

$$\frac{\Delta L}{L_o} = C_3^{\frac{1}{2}} r^{-1} t^{\frac{1}{2}}$$

where C_2, and C_3 are the constants for any given composition and temperature, r is the radius of the particle, and t is the sintering time. The shrinkage controlled by the diffusion mechanism is proportional to the one-third power of time and inversely proportional to the four-thirds power of the initial particle size. In the case of interface reaction mechanism the shrinkage is proportional to the square root of time and the reciprocal of initial particle size.

2. 4. 4 Viscous sintering

Densification of amorphous materials occurs by viscous flow which reduces the free energy of the system. Frenkel [176] first analyzed the viscous sintering based on that statement. A simple model consisting two-sphere particles was constructed to study the shrinkage of the material during sintering, according to:

$$\frac{\Delta L}{L_o} = \frac{3\gamma t}{8\eta a}$$

where L_o is the initial distance between the centers of the spheres and the ΔL is the change (decrease) of that distance, γ is the surface tension, t is the sintering time, η is the viscosity, and a is the initial radius of the two identical spheres. It was found that the shrinkage rate (ration of $\Delta L/L_o$ to t) is linear if the viscosity does not change through sintering. Other models have been used to describe the densification process during viscous sintering. Mackenzie and Shuttleworth [177] presented a spherical shell model, which is suitable for representing the final stage of sintering when the pores become isolated. Scherer [178] proposed a cylinder model which is appropriate for explaining sintering of materials with low initial densities. A good agreement was observed between these models in spite of the different microstructural geometries used [179]. The grain size, viscosity, and surface tension of the material system corresponding to the time required for full densification can be controlled by composition and temperature.

Non-reactive liquid phase sintering (NLPS) model

Ewsuk et al. [180,181] presented a sintering model to explain the densification behavior of ceramic-filled glass composites. According to the proposed non-reactive liquid phase sintering (NLPS) model, the densification occurs by a combination of three sintering stages: (a) glass redistribution, (2) grain rearrangement, and (3) viscous flow, as shown in Figure 2.25.

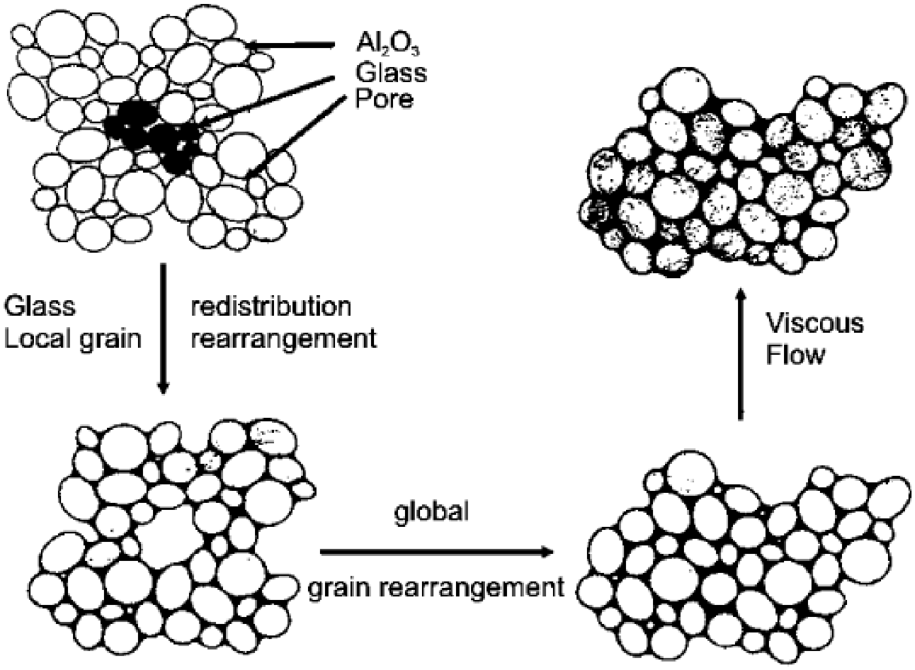

Figure 2.25 Schematic evolution of sintering stages in non-reactive liquid phase sintering (NLPS) model. (taken from K.G. Ewsuk et al. [181])

Glass melts and infiltrates the ceramic-rich regions in the initial stage where the densification occurs by glass redistribution and local grain rearrangement. The glass-filled cylindrical pore channels are formed through capillary force, which is considered as the driving force (*DF*) for this process:

$$DF_{redistribution} = \frac{\gamma_{lv}\cos\theta}{r}$$

where γ_{lv} is the glass surface tension, θ is the wetting angle, and r is the radius of the cylindrical pore channel. The intermediate stage of sintering is mainly characterized by the global grain rearrangement process that accounts for the densification of the powder system from ~65% to ~90% of the theoretical density. The driving force for this process is given by:

$$DF_{gr} = 2\pi\gamma_{lv}R\sin(\varphi + \theta) - 2\pi\gamma_{lv}\frac{R^2}{r}\sin\varphi$$

where R is the particle diameter and φ is a geometrical factor related to the solid-vapor-liquid intersect. The degree of wetting and glass viscosity are the most important parameters involved in this densification process. The final stage of densification occurs once all solid-vapor interfaces disappear. The ~10% residual porosity is closed by the viscous flow, not affected by the wetting condition. The driving force for the final stage viscous flow is defined by Laplace equation as follow:

$$DF_{final} = \frac{2\gamma_{lv}}{r}$$

The time required to eliminate a pore of a radius r during final sintering stage is directly related to the viscosity of the glass-ceramic composite:

$$t = \frac{2r\eta}{\gamma_{lv}}$$

Ewsuk et al [180,181] showed that the elimination of the closed pores in the glass-ceramic composite with a high filler concentration requires a glass of low viscosity while only low filler concentration can be accepted for using a glass with high viscosity. It is also found that the densification improved with decreasing filler content and increasing filler particle size.

The densification process for LTCC, a ceramic-filled glass composite material, is examined using NLPS model [158]. This implies the glass is expected to wet the ceramic fillers in the initial and intermediate stages of sintering and a low-viscosity glass is needed to eliminate the pores in the final sintering stage. However, it was demonstrated that the glass does not wet the filler in the entire temperature range but the densification occurs by viscous flow which is controlled by the viscosity of the glass.

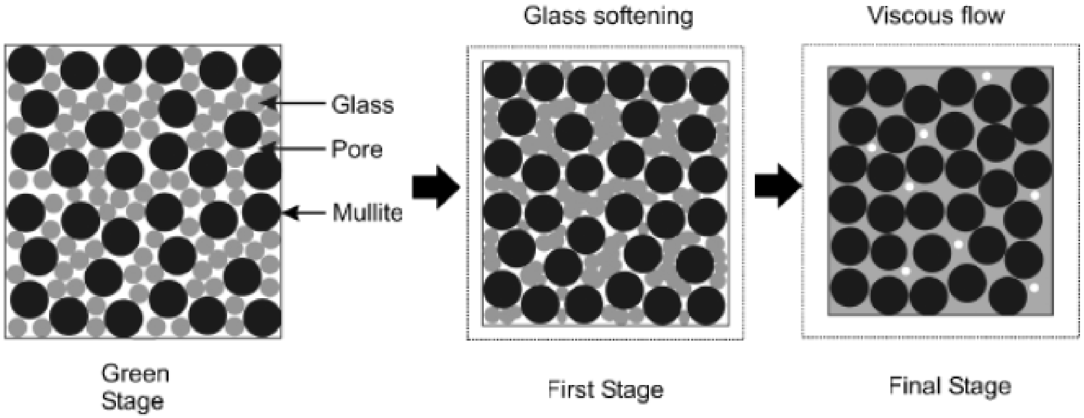

Figure 2.26 Schematic of the densification of ceramic-filled glass composites by NPLS through viscous flow. (taken from S. Kemethmuller et al. [158])

Figure 2.26 illustrates schematically the densification mechanism for the examined LTCC material. For ceramic-filled glass composites with glass contents above 60 vol%, like most commercial LTCC systems, it is important to control the viscosity of the glass for sufficient densification during firing. This knowledge is important for the future evaluation and selection of glasses for developing new LTCC systems.

2. 4. 5 Constrained sintering

Constrained sintering is a common phenomenon in practical sintering process in which the shrinkage behavior of a material is affected by external and/or internal constraints. The constraints may be the attached substrate or laminated heterogeneous layer that has a different sintering behavior (external) or the inclusion of non-sintering particles or fibers (internal). The influence of constraints on the densification process of a material can be either positive or negative, leading to a classification of constraint components as (1) retarding constraint which results in hindrance in densification and (2) enhancing constraint which leads to the enhancement of densification [182].

The mechanical properties of the involved materials, like Young's modulus, Poisson's ratio, and viscosity, are important for the determination of stresses developed in the constrained sintering process. A variety of models have been proposed to calculate such stresses [183-185]. Bordia and Scherer [183] suggested a linear viscous model describing the stress-strain relationship for a porous material under constrained sintering. Based on the proposed viscous model, the constitutive equations for the strain response of an ideal isotropic and porous material are given as (in Cartesian coordinates):

$$\dot{\varepsilon_x} = \frac{\sigma_x}{\eta} - \frac{\sigma_y}{\eta} - \frac{\sigma_z}{\eta} + \dot{\varepsilon_{fx}}$$

$$\dot{\varepsilon_y} = \frac{\sigma_y}{\eta} - \frac{\sigma_z}{\eta} - \frac{\sigma_x}{\eta} + \dot{\varepsilon_{fy}}$$

$$\dot{\varepsilon_z} = \frac{\sigma_z}{\eta} - \frac{\sigma_x}{\eta} - \frac{\sigma_y}{\eta} + \dot{\varepsilon_{fz}}$$

where $\dot{\varepsilon}$ and $\dot{\varepsilon_f}$ are the strain rates with and without stresses, σ is the stress, υ is the viscous Poisson's ratio, and η is the uniaxial viscosity. For the case of the material under uniaxial compress ($\dot{\varepsilon_x} = \dot{\varepsilon_y}$) and the isotropic transverse shrinkage ($\sigma_z \neq \sigma_x = \sigma_y = 0$), the strain rates are written out as:

$$\dot{\varepsilon_z} = \frac{\sigma_z}{\eta} + \dot{\varepsilon_{fz}}$$

$$\dot{\varepsilon_{x/y}} = -\frac{\sigma_z}{\eta} + \dot{\varepsilon_{fx/y}}$$

The compressive stress required for the zero transverse shrinkage rate is given by:

$$\sigma_z = \frac{\eta}{\upsilon}\dot{\varepsilon_{fx}}$$

Multilayer laminates, commonly used as interconnect substrates and packages, consist of different conductor, resistor, and dielectric layers produced by thick-film technology. The most important manufacturing step is the co-sintering (or co-firing) of the hybrid multilayered structure. Constrained sintering has significant effects on the densification behaviors of all constituents in the multilayer structure and the resulting microstructures and properties. It can lead to microstructural defects (*e.g.* cracking and delamination) and anisotropic shrinkage (*e.g.* warping). The cause of the defects is normally attributed to the transient stresses (*e.g.* in-plane tensile stresses) due to the mismatch in sintering rates of the constituent layers. Cheng and Raj [186] observed cracks and void in axial symmetrical multilayers of co-fired ceramic/metal and glass/metal systems. Jean et al. [187] analyzed stress development and curvature formation in a co-fired LTCC-silver system based on the theoretical models. The most effective solution to the problems of reduced sintering and structural defects is to minimize the difference in sintering behaviors for all component materials. However, it's extremely difficult to fully match the sintering rate of two completely dissimilar materials.

LTCC material has been widely used in microelectronics, requiring precise control of sintering shrinkage and dimensional tolerance. The concept of zero-shrinkage processing has gained increasing interest in LTCC technology in order to minimize or eliminate the defects and deformation caused by co-firing [188]. The constrained sintering approach enables control of dimensional shrinkage during sintering process. There are three common techniques used in LTCC industry to constrain the densifying materials: (1) pressure-assisted sintering which adds an external pressure exerted on the multilayer in z direction, (2) self-constrained sintering which applies unique non-shrinking layers, and (3) pressure-less constrained sintering which uses a release tape or forms a layer that constrains the green ceramic body due to interfacial stress. These techniques involve additional cost and materials and add further steps to the manufacturing process [189].

2. 5 Micropumps for lab-on-chip microfluidic systems

Recent development in microfluidic MEMS and the increased interest of biochemical companies for integrated microanalytical systems have led to the emergence of lab-on-a-chip (LOC) or micro total analysis system (μ-TAS). However, effective on-chip transport and control of small quantities of fluidic samples remains an important challenge for implementing the conceptual integrated microfluidic systems. Numbers of micropumps developed to date are Si- or polymer-based peristaltic pumps actuated piezoelectrically. However, manufacturing such pumps is complicated and expensive. In addition, it is difficult to integrate these developed micropumps with other fluidic components. Therefore, further incorporation of micropumps into the microfluidic system requires the development of other suitable substrate materials and microfabrication techniques.

2. 5. 1 Micropumps for microfluidics

Microfluidics is the science and technology of designing and manufacturing devices that manipulate small volumes of fluids on the order of nanoliter to attoliter. Scaling down fluidic processes to the micro-scale offers numerous benefits including reduced reagent and power consumption, rapid response for analysis, high selectivity and sensitivity in separations and detections, low cost, and small size for the devices [190-192]. The miniaturized devices enable the construction of a single integrated chip containing multiple components providing different functionalities. Such Integrated microfluidic devices or systems have attracted considerable interest for a wide range of applications from biological and chemical analysis to molecular and medical diagnostics

[193,194]. Still at its beginning, the development of microfluidic devices towards commercialization has been done mostly in America and Europe during the last few years. The prospective market for the microfluidic MEMS devices and systems will exceed \$3 billion in 2014, as shown in Figure 2.27.

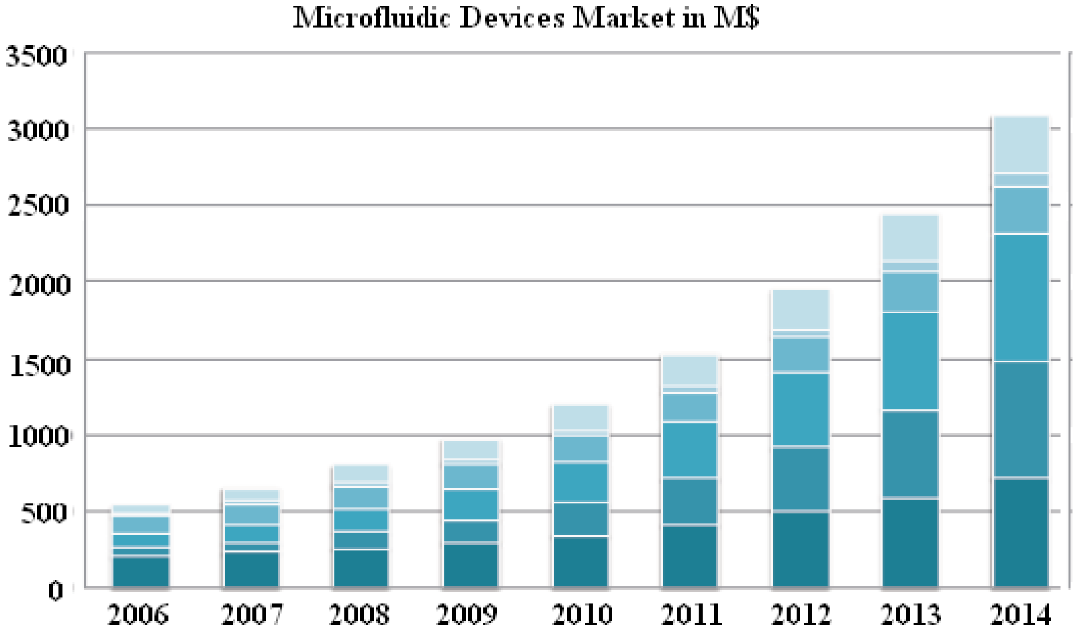

Figure 2.27 Expectation of market growth for microfluidic devices and systems from 2006 to 2014. (taken from EMMA Report 2009 [195])

Laminar flow is expected in the developed microfluidic devices because the Reynolds number R is significantly smaller than the laminar-turbulent transition number ($R_t \sim 2300$) in a wide variety of circumstances. For example, in a circular channel with diameter of 100 μm, a flow with water at a typical speed 10^{-2} m/sec has a Reynolds number of unity. Even increasing the flow velocity by a factor of 100 will not change the flow pattern in this simple fluidic geometry. Consequently, typical velocity profiles in such geometries are parabolic in pressure-driven flows and nearly uniform for electro-osmotic flows (EOF) [196]. The laminar nature of fluid flow in micro-scale fluidic conduits enables accurate control of diffusive mixing and precise metering of multiple streams of fluids and exploitation of the interfaces between them [197]. An extensively reported high-density microfluidic chip with a complex network of microchannels is illustrated in Figure 2.28, demonstrating the striking capability of fluid manipulation in the microfluidics.

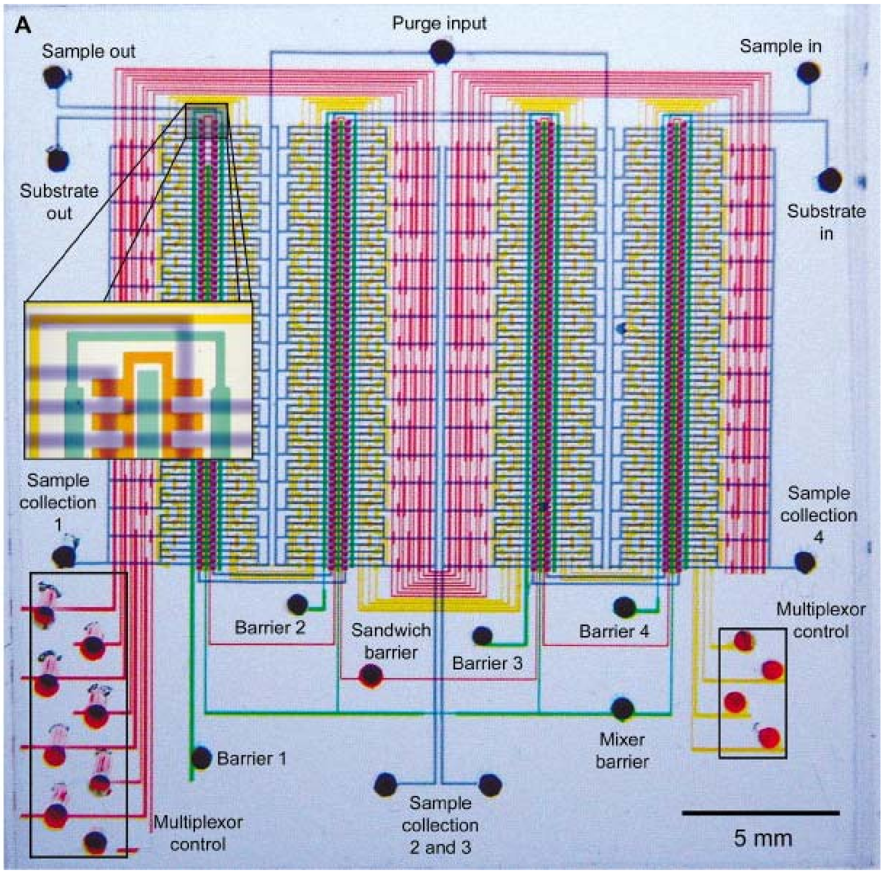

Figure 2.28 Optical image of a microfluidic device containing 2056 micro-channels. Different colored dyes used to visualize the structure of the fluidic network. (taken from T. Thorsen et al. [198])

Individual microfluidic devices have been developed using Si, glass, and other materials with associated methods of fabrication to meet the requirement of specialized applications. However, the integration of different functional components or modules into one complete system is still at an early stage of development. Micropumps are essential components for providing efficient fluid control and delivery in a LOC microfluidic system. The area of micropumping has become an active and interesting research area in microfluidics in both academia and industry. After the first micropump reported in the early 1990s [199] a large numbers of micropumps have been developed using different types of materials and the associated fabrication processing based on various actuation mechanisms [200-205]. However, the on-chip pumping remains a key challenge for the fluidic transportation in microsystems for clinical and environmental analysis which require prompt processing of samples. Therefore, the development of a chip- or package-level micropump with the capability of being easily integrated into suitable microfluidic systems is highly desirable.

Micropumps are generally divided into two categories: (1) reciprocating displacement pumps, which generate pressure by one or more moving surfaces of reciprocating membranes that compress and expand periodically on the working fluid; (2) continuous dynamic pumps, which continuously transform energy directly to the working fluid to increase its momentum or pressure [200,201]. The major structural features and characteristic performances of reported typical reciprocating displacement micropumps and continuous dynamic micropumps are summarized in Table 2.12 and Table 2.13 respectively.

Table 2.12 Characteristic features and performances of reciprocating displacement micropumps.

Actuation mechanism	**Valve**	**Construction materials**	**Size (cm^3)**	**Driving voltage (V)**	**Driving frequency (Hz)**	**Max. flow rate (ml/min)**	**Max. Back-pressure (kPa)**	**Year & Ref.**
Piezoelectric	valveless	PMMA-glass + PZT	~0.8	120	400	0.22	9.2	2009 [206]
Piezoelectric	valveless	Si-glass + PZT	~5	140	140	0.12	3.2	2007 [207]
Piezoelectric	valveless	Si-glass + PZT	~1	385	130	0.32	0.29	2007 [208]
Piezoelectric	valveless	PDMS-PMMA + Piezo-actuators	n/a	160	60	0.9	1.8	2007 [209]
Piezoelectric	valveless	Si-glass + PZT	n/a	120	10	0.012	~ 4	2004 [210]
Piezoelectric	nozzle-diffuser	Si + PZT	~0.12	190	2400	1.5	1.0	2002 [211]
Piezoelectric	check-valve	Si + PZT	n/a	160	220	1.2	n/a	1998 [212]
Piezoelectric	check-valve	Si + Thick-film PZT	n/a	600	200	0.12	1.8	1998 [213]
Piezoelectric	nozzle-diffuser	Si-glass + Piezo-actuators	~0.26	200	3500	1.1	74	1997 [214]
Piezoelectric	valveless	Si-Perspex + Piezo-bimorph	n/a	200	190	1.5	17	1996 [215]
Piezoelectric	nozzle-diffuser	Brass + Piezo-actuators	~1.6	130	540	16	16.6	1995 [216]
Piezoelectric	valveless	Si-glass + PZT	~1.5	100	15	0.1	5.9	1990 [199]

Table 2.12 (Continued)

Actuation mechanism	**Valve**	**Construction materials**	**Size (cm^3)**	**Driving voltage (V)**	**Driving frequency (Hz)**	**Max. flow rate (ml/min)**	**Max. Back-pressure (kPa)**	**Year & Ref.**
Electrostatic	valveless	Parylene + Cr/Au	n/a	110	20	1.7×10^{-6}	1.6	2004 [217]
Electrostatic	check-valve	Si	~0.01	200	300	0.16	29	1995 [218]
Thermo-pneumatic	valveless	PDMS-glass + Ti/Au	~0.5	9	1.2	0.02	0.49	2011 [219]
Thermo-pneumatic	valveless	PDMS-glass + Cr/Au	n/a	14	0.033	0.82×10^{-3}	n/a	2006 [220]
Thermo-pneumatic	Nozzle-diffuser	Si-glass	~0.78	n/a	2	0.53	12	2001 [221]
Thermo-pneumatic	check-valve	Polysulphone	n/a	15	5	0.044	3.8	1994 [222]
Electro-magnetic	valveless	PDMS-glass + magnet	n/a	$I = 0.6$ A	200	7.2	n/a	2008 [223]
Electro-magnetic	check-valve	Plastic + magnet	~1	5	50	2.1	10	1999 [224]
Pneumatic	check-valve	PDMS-glass	n/a	n/a	< 1	2.8×10^{-3}	30	2003 [225]
Pneumatic	valveless	PDMS-glass-Si	n/a	n/a	1	6.0×10^{-3}	0.17	2003 [226]
Electrowetting	check-valve	Si-glass-SU8	n/a	2.3	25	0.07	0.7	2002 [227]

Table 2.13 Characteristic features and performances of continuous dynamic micropumps.

Actuation mechanism	**Construction materials**	**Size (cm^3)**	**Working Fluid**	**Driving voltage (V)**	**Max. flow rate (ml/min)**	**Max. Back-pressure (kPa)**	**Year & Ref.**
Electro-hydrodynamic	Ceramic	~0.64	3M HFE-7100	250	n/a	0.78	2002 [228]
Electro-hydrodynamic	Si-glass	~0.09	Ethyl alcohol	100	0.04	0.25	1998 [229]
Electroosmotic	Glass + packed-bed channels	n/a	Aqueous buffer	500	0.22×10^{-3}	10^3	2010 [230]
Electroosmotic	Fused-silica based matrix	n/a	DI water	6000	2.9×10^{-3}	300	2006 [231]
Electroosmotic	Soda-lime glass	~9	Water	1000	0.015	33	2002 [232]
Electroosmotic	Glass + packed-bed channels	~0.085	Water	2000	3.6×10^{-3}	2000	2001 [233]
Electroosmotic	Glass	n/a	0.35mM NH_4OH	500	3.0	150	2000 [234]
Electroosmotic	Glass + packed-bed channels	~0.12	Aqueous-sodium solution	1500	0.04×10^{-3}	4000	1998 [235]
Electro-chemical	PDMS-glass + Pt/Teflon	n/a	Whole blood	2.5	0.09×10^{-3}	11	2009 [236]
Magneto-hydrodynamic	PDMS + Au	~0.04	PBS solution	3.6	12.9×10^{-3}	n/a	2011 [237]
Magneto-hydrodynamic	Si + magnet	n/a	Sea water	n/a	0.063	0.17	2000 [238]
Magneto-hydrodynamic	Si-glass + magnet	n/a	1M NaCl solution	n/a	0.018	0	2000 [239]

Nowadays, continuous dynamic pumps are the most desirable pumps to be fabricated directly on the microfluidic systems in a LOC format due to their small size, simple structure, and absence of moving mechanical parts. However, this type of micropumps has some intrinsic disadvantages, such as the need of high driving voltage in electroosmotic micropumps [230], specific requirements for the properties of fluid samples in electrohydrodynamic micropumps [240], and the interference of applied electric field on the pumping liquid in electrochemical micropumps [236]. Additionally, the typical flow rate for continuous dynamic pumps is in the range of pl/min to nl/min. In applications requiring rapid chemical analysis and synthesis, the high performance reciprocating pumps in small package size has attracted particular attention for pumping biological fluids on the order of several μl/min to several ml/min [202].

2. 5. 2 Peristaltic micropump

Peristaltic micropumps, as one of the earliest micropumps developed, have been studied for twenty years and still gain significant attention [241-245]. A variety of peristaltic micropumps using novel structures and advanced fabrication methods have been made to satisfy the pumping requirement in different applications. The pumping principle of most developed peristaltic micropumps is demonstrated schematically in Figure 2.29. Adapting directly from the macroscopic concept, a net flow across the micropump is generated by the peristaltic motion of multiple microchambers aligned in series. Most of the realized peristaltic micropumps have three microchambers with actuating membranes. Check valves are not required in peristaltic micropumps for flow rectification. Additionally, there is no need to construct specific fluid rectifiers (*e.g.*

nozzle/diffuser) used to manipulate fluids in other valveless micropumps, which greatly save the manufacturing cost and time.

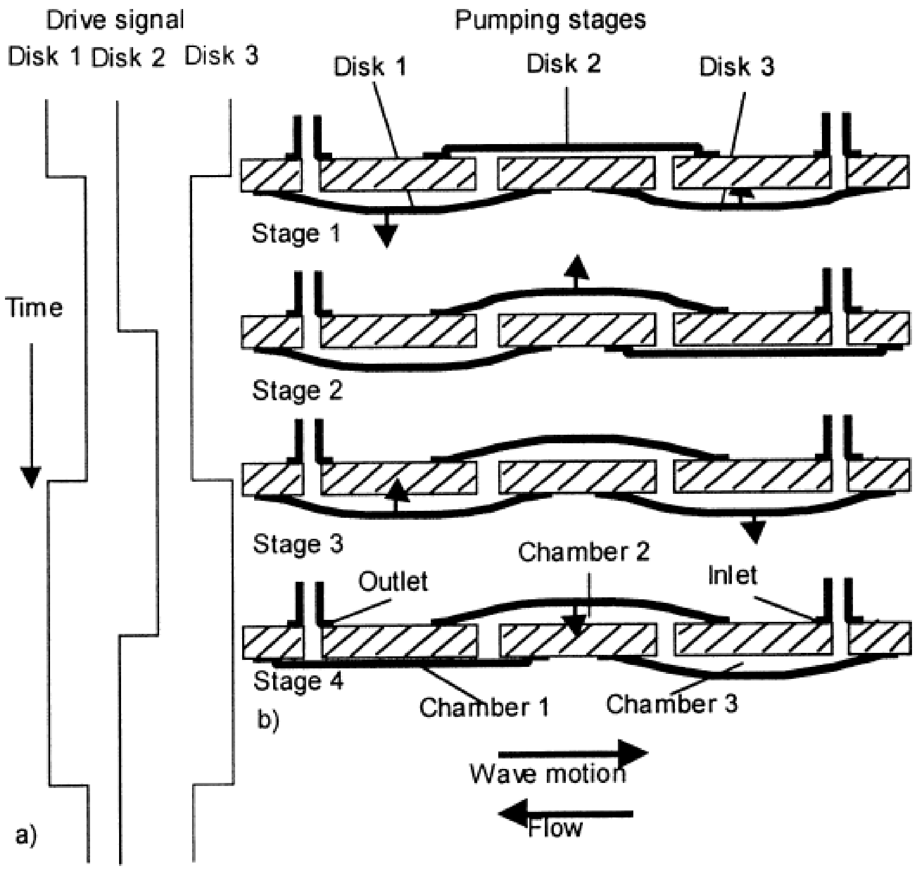

Figure 2.29 Working principle of a peristaltic micropump with three chambers. (a) signal scheme and (b) pumping stages. (taken from N.T. Nguyen et al. [246])

In contrast to check-valve micropumps, peristaltic pumps eliminate the risk of failure due to the fatigue of check valves and reduce the risk of channel clogging and damage of biological particles in the pumping fluids. Both the reliability and the expectant life-time have greatly improved because of the removal of the unnecessary mechanical parts. Moreover, the bidirectional flow in peristaltic pumps can be easily achieved by changing the actuation sequence of driving units. Compared with continuous dynamic micropumps, peristaltic pumps provide a wide range of flow rate without complex electrode arrangement or requirements for the conductivity of pumping fluid. Peristaltic micropumps have the potential to be used in a wide variety of microfluidic applications, such as bioengineering, pharmaceutical, and food industries. However, the leakage is a serious drawback for peristaltic micropumps. Even a small pressure difference between the outlet and the inlet will cause a back flow when the pump is not actuated. This valveless design also leads to a lower maximum backpressure compared to the check-valve pumps. A common optimization strategy for peristaltic micropumps is to increase the stroke volume ΔV (the volume change of pump chamber caused by membrane displacement) and the compression ratio ε (the ratio of stroke volume to chamber volume without actuation). Several novel designs were investigated to prohibit the back flow inside the peristaltic micropumps. Cao et al. [247] reported the design of a piezoelectric peristaltic micropump with normally-closed microchannels when no power is applied. Only the analytical and experimental results on the membrane deflection were introduced and no pumping performance was presented. Trenkle et al. [241] demonstrated a functional peristaltic micropump with the same normally-closed mechanism most recently. The pump actuated in a peristaltic manner shows a maximum flow rate of 0.12 ml/min with an extraordinary maximum backpressure expected to be 180 kPa. However, the overall size of this pump is large (~20 cm^3), which limits its applications in which the small size of the pump is a critical requirement. More importantly, the size of this micropump and the associated fabrication processing are definitely not compatible with on-chip integration.

2. 5. 3 Piezoelectric actuation

A wide range of materials (*e.g.* Si, glass, and PDMS) have been used for the design and fabrication of peristaltic micropumps based on various driving mechanisms including piezoelectric [199,206-210,248], thermopneumatic [220,249], electrostatic [217,250], and other actuation principles [251-253]. Figure 2.30 depicts several design examples of peristaltic micropumps based on various actuation mechanisms.

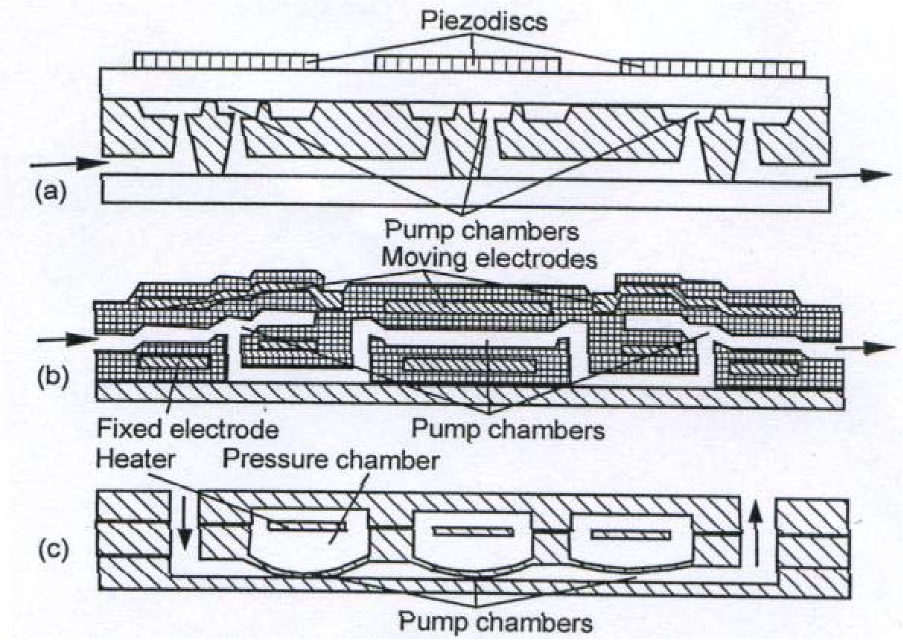

Figure 2.30 Design examples of peristaltic micropumps. (a) piezoelectric. Three piezoelectric discs glued on the pump chambers etched in silicon; (b) electrostatic. Polysilicon electrodes embedded in a silicon nitride pump body; and (c) thermopneumatic. Three heaters located inside the pressure chambers to achieve deflection. (taken from N.T. Nguyen et al. [254])

Compared with other actuation principles developed for the peristaltic micropump, piezoelectric actuation offers reliable pumping with high actuation strength and good energy efficiency. The flow rate of piezoelectrically actuated peristaltic micropumps is typically in the range from several μl/min to several hundred μl/min by virtue of the comparatively large stroke volume and a fast mechanical response which allows the pumps to be operated at high frequency. Moreover, micropumps with piezoelectric actuation have the potential to be integrated into LOC microfluidic devices at the package level [255].

Piezoelectric components are commonly deposited or mounted on pump membranes for generating necessary pressure difference inside the microchambers for the pumping [256-258]. PZT ceramics are the most widely applied piezoelectric materials for design and fabrication of micropumps due to their effective and reliable electro-mechanical response. Thin-film PZT can be deposited on different substrate materials for developing microsensors and other microdevices but it is rarely used in micropump applications since the total displacement generated by the thin-film drive is normally not large enough for the pumping purpose. Most of current developed piezoelectric micropumps, incorporating bulk PZT ceramics as the actuators, are fabricated using MEMS processing techniques often requiring additional hybrid bonding methods. The piezoelectric actuator is mounted on a Si or glass MEMS body using adhesive bonding which is critical for the reliability and yield of this type of actuator and not compatible with integrated fabrication [204]. Additionally, the fabrication of silicon/glass based reciprocating membrane micropumps is usually complex which makes it expensive and time consuming. Thick-film PZT, as the alternative to thin-film and bulk materials, has been screen printed on Si substrates for micropump fabrication [138]. However, there are two major issues associated with this fabrication process, inter-diffusion and/or reaction between Si substrates and PZT thick films as well as the defects induced by significant stresses generated in sintering. Other thick-film preparation methods (*e.g.* dip/spray coating and polymerization), PZT ceramics with various sintering aids, and substrate materials (*e.g.* glass and polymer) have been investigated to solve the processing difficulties for the micropump manufacturing [116]. Therefore, a practical optimization of piezoelectric micropumps needs not only the high performance piezoelectric actuators but also the compatible fabrication technique.

2. 5. 4 Integration of micropumps in microfluidic systems

Many discrete microfluidic devices are under development ranging from single components such as micropumps, microvalves, and flow sensors, to complex microfluidic systems for chemical analysis and biomedical engineering, consisting of all necessary functional elements integrated on a single substrate or as sandwiched modules. Schabmueller et al. [259] reported the design and fabrication of a microfluidic “circuitboard” consisting micropumps, flow sensors, and micromixers mounted on a single Si-glass substrate. Wet etching and anodic bonding techniques were used to fabricate the integrated system. However, the performance of this developed microfluidic system was not introduced. Another example of integrated microfluidic system developed by Lee et al. [260] incorporates an electroosmotic pump, a micromixer, a chemical reaction chamber, and an on-chip temperature control system. The various modules were integrated on glass substrates and poly(dimethylsiloxane) (PDMS) materials. The experimental results showed a more effective polymerase chemical reaction (PCR) using this microfluidic system compared to the results of using other conventional approaches. The schematic illustrations of these two integrated microfluidic systems are shown in Figure 2.31.

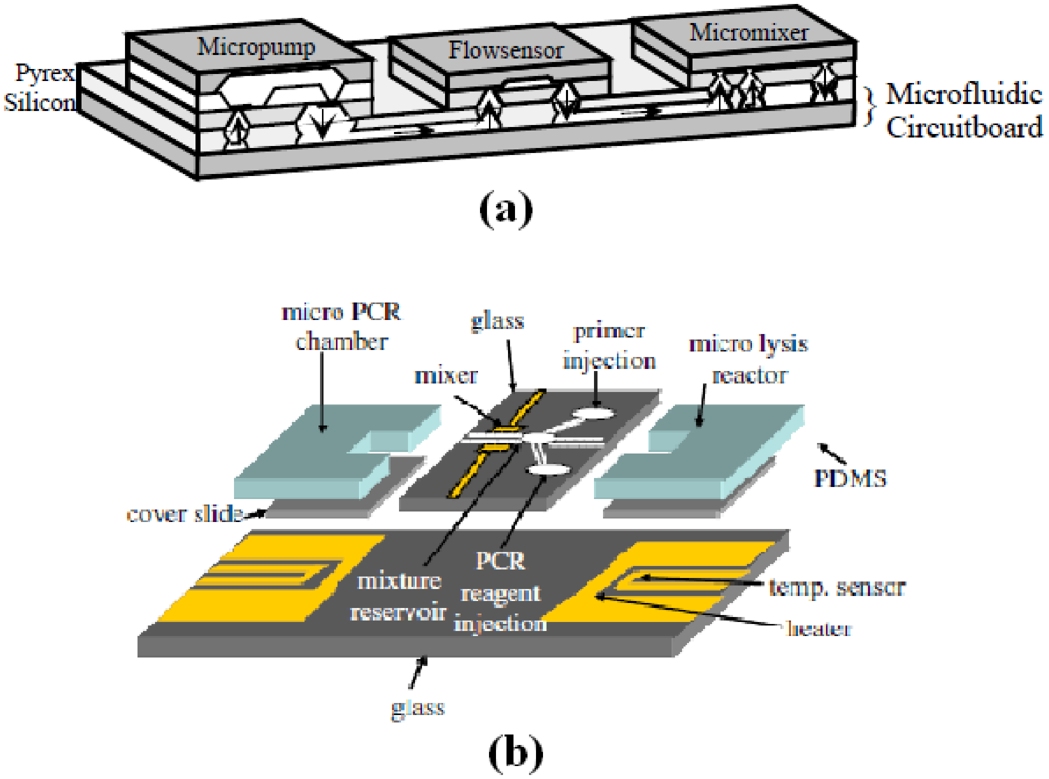

Figure 2.31 Schematic representations of (a) Si-glass based microfluidic system (taken from C.G.J. Schabmueller et al. [259]); and (b) glass-PDMS based microfluidic chip. (taken from C. Lee et al. [260])

Effective and precise supply and control of liquid are among most important unit operations for microfluidic systems, which need the integration of micropumps at package- or chip-level. Intensive research efforts are focused on this topic and a wide variety of novel micropumps have been developed in order to provide on-chip fluid supply and control. A power-free valveless micropump based on the capillary and/or evaporation effects was developed for providing a steady flow in μl/min range for the flow injection analysis system [261]. A cellular micropump without check valves powered by a cultured cardiomyocyte sheet was demonstrated to produce a flow in nl/min range [262]. Yokokawa et al. developed an on-chip syringe pump for picoliter-scale liquid manipulation using electrostatically controlled actuators [263].

LTCC technology can combine materials that have different characteristics; it is therefore possible to integrate and build different types of components into one ceramic-based system [264,265]. A wide range of LTCC microfluidic devices incorporated with functional passive and active elements have been successfully fabricated and reported, such as (1) incorporation of hydrogel nanocomposites as valves into LTCC microfluidic devices [266]; (2) integration of optic fibers in a LTCC chemical analysis microsystem [78]; and (3) a magnetohydrodynamic micropump fabricated with LTCC tapes [68]. Recently, there is an increasing interest in the development of highly integrated LTCC-based MEMS incorporating active piezoelectric elements in microfluidic applications, for example, a piezoelectric unimorph valve assembled on a multilayer LTCC fluidic chip [267] and a piezoelectric cantilever controlled throttle integrated into a LTCC substrate to provide the flow manipulation [268]. However, piezoelectric actuators are usually attached on the fired LTCC body during post-firing and assembly process. The realization of co-fired piezoelectric elements with required electronics and fluidic components into one LTCC module can offer additional capabilities in the fabrication of microfluidic devices.

The unique approach of the current research is co-firing LTCC substrates with PZT-based actuators according to a low temperature sinterable high performance piezoelectric composition [269]. Piezoelectric and dielectric properties are characterized on the 1 wt% $LiBiO_2$ and 1 wt% CuO added 0.98PZT-0.02SKN ceramics sintered at 900^oC for 1 h. Subsequently, an investigation on sintering behavior and properties of co-fired LTCC/PZT-SKN multilayer ceramics is performed to develop an optimized co-firing profile which can be used to construct hybrid multilayer microdevices [270]. The focus of following study is primarily on the fabrication and characterization of a LTCC/PZT-SKN multilayer piezoelectric peristaltic micropump. LTCC thick-film technology is applied to build multilayer micropumps, which allows a rapid and inexpensive fabrication. Further optimization of pumping performance has been studied based on the experimental and simulation results by using different microchannel geometries. The developed micropump demonstrates the possibility to be integrated into LTCC-based lab-on-a-chip microfluidic systems at the package-level, providing efficient on-chip fluid control and transport for the practical applications in chemical analysis and synthesis, biological sensing, and environmental monitoring.

Chapter 3. Low temperature sintering and properties of Pb($Zr_{0.53}$, $Ti_{0.47}$)O_3-Sr($K_{0.25}$, $Nb_{0.75}$)O_3 (PZT-SKN) ceramics with $LiBiO_2$ and CuO addition

3. 1 Introduction

The Pb($Zr_{0.53}$, $Ti_{0.47}$)O_3-Sr($K_{0.25}$, $Nb_{0.75}$)O_3 (PZT-SKN) system, first reported by Helke et al. [271], is considered to be a promising material for multilayer piezoelectric actuator applications. Reducing the conventional sintering temperature (~1250^{o}C) of PZT-SKN ceramics would not only offer the advantage of a reduction in energy consumption and decrease in lead volatility but also provide the possibility of co-firing with low-melting-point electrodes and low temperature co-fired ceramic (LTCC) materials to form novel multilayered devices. As introduced in chapter 2, liquid-phase sintering is a common technique for lowering the sintering temperature by incorporating suitable additives into the original solid solution systems [272-275].

The present chapter provides a detailed description of the experimental procedures and results for preparation and characterization of low fire PZT-SKN ceramics. In order to tailor the sintering profile of PZT-SKN ceramics compatible with LTCC materials, liquid-phase sintering additives $LiBiO_2$ and CuO, both extensively reported as effective fluxes to lower sintering temperature for PZT-based ceramics [276-285], were used for the purpose of accelerating densification by the liquid phase generated at low temperature. Specifically, the low temperature sintering of 6 wt%

$LiBiO_2$ and 1 wt% $LiBiO_2$ + 1 wt% CuO added 0.98PZT-0.02SKN piezoelectric ceramics was studied. The microstructure, dielectric, and piezoelectric properties of flux-sintered ceramics were examined and compared with materials conventionally sintered at 1250°C to understand the structure-property relations in this flux-ceramic system.

3. 2 Experimental methods and materials preparation

The 0.98PZT-0.02SKN powder was prepared by the conventional solid-state route according to the formula $Pb_{1-3x/2}Sr_xK_{x/4}[(Zr_{0.53}, Ti_{0.47})_{1-3x/4}Nb_{3x/4}]O_3$ [31]. The processing flowchart is illustrated in Figure 3.1. High-purity metal oxides and carbonates $PbCO_3$ (Halstab, Hammond, ID), ZrO_2 (Alfa Aesar, Ward Hill, MA), TiO_2 (Ishihara, Tokyo, Japan), $SrCO_3$ (Sigma Aldrich, St. Louis, MO), K_2CO_3 (Sigma Aldrich, St. Louis, MO), and Nb_2O_5 (H.C. Starck, Berlin, Germany) were stoichiometrically mixed in an aqueous solution with organic dispersant (Darvan 821®, R.T. Vanderbilt Company Inc., Norwalk, CT). Suspensions were then ball milled with 5 mm spherical highly wear-resistant Y-stabilized zirconia (YTZ) media (TOSOH, Grove City, PA) on a vibratory mill (ML16-5, Sweco, Florence, KY) for 24 h. After drying, the powder was sieved and calcined at 850°C for 4 h. A second calcination step with intermediate milling cycle was performed to achieve better homogeneity and purity of the final powders.

The fluxes were prepared as either single phase compounds or mixtures. These powders were added to the calcined PZT-SKN and vibratory milled for a further 12 h, then dried and sieved. The resulting powders were mixed with 2-3 wt% organic binder (Acrylic copolymer, R.E. Mistler Inc., Yardley, PA) in acetone, and uniaxially pressed into circular pellets with ~13 mm diameter under 200 MPa using a rigid steel die.

Following the binder burnout at 450°C for 2 h, green pellets were sintered in air atmosphere at different temperatures between 750°C and 1000°C for 1-2 h without source powder. For comparison, the unfluxed PZT-SKN samples were conventionally sintered at 1250°C for 2 h with lead source powder.

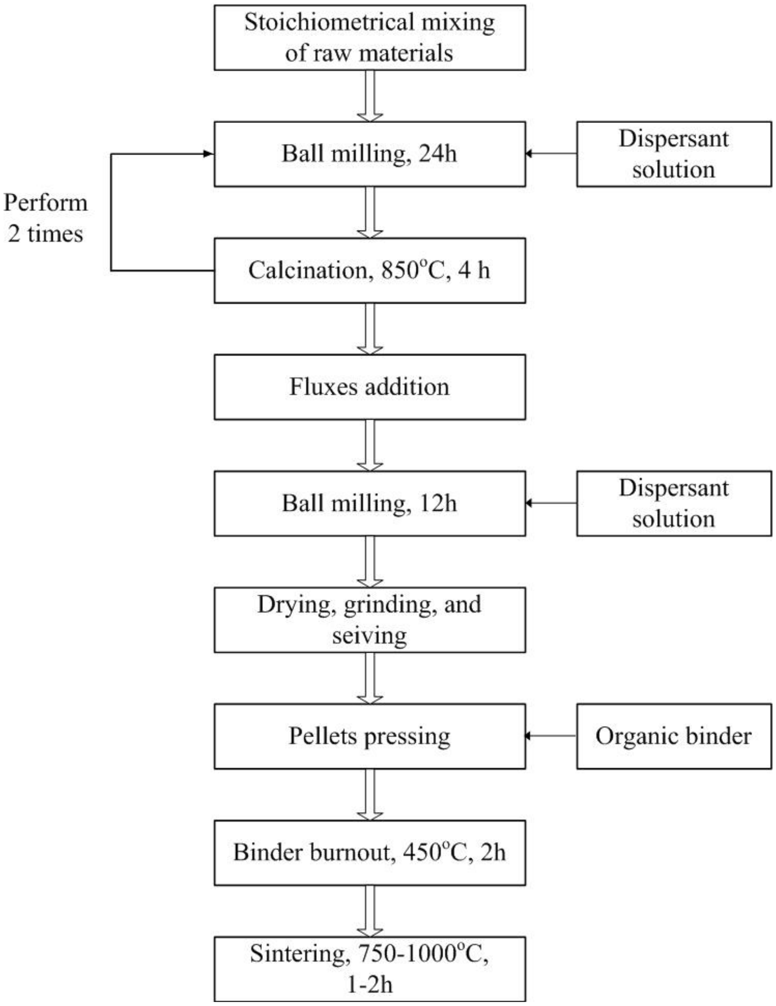

Figure 3.1 Flowchart for solid-state synthesis of fluxed PZT-SKN.

The microstructure and phase purity of sintered ceramics was determined by scanning electron microscope (SEM: S-3200, Hitachi, Tokyo, Japan) and X-ray diffraction (XRD: Model-D500, Siemens, Munich, Germany. The bulk density of sintered samples was measured using the Archimedes method.

Sintered pellets were polished parallel to a thickness of approximately 0.5 mm and electroded on both surfaces with a conductive Ag electrode paste (DuPont 6160, Research Triangle Park, NC) fired at 850°C for 10 min, for measuring electrical characteristics. Samples were poled in silicon oil at 100°C under a DC field of 30 kV/cm for 15 min. Dielectric properties were obtained by the measurement of the capacitance and loss at several frequencies as a function of temperature performed in the range of 20°-500°C using a precision LCR meter (Agilent E4980A, Agilent, Santa Clara, CA) in combination with a temperature-controlled tube furnace (Model-F21130, Barnstead, Waltham, MA) and automated data recording by using LabVIEW™ software. The planar coupling coefficient k_p was calculated from electromechanical resonance, by measuring resonance and antiresonance frequencies using an impedance analyzer (Model-HP4194A, Agilent, Santa Clara, CA) on the basis of the IEEE standard [286]. Low field d_{33} piezoelectric coefficients were measured using a Berlincourt-style d_{33} meter (YE2730A, APC International Ltd., Mackeyville, PA). Polarization and strain hysteresis loops were measured using a custom Sawyer-Tower circuit with a linear variable differential transducer coupled to a high-voltage amplifier (Model-610B, TReK, Medina, NY). The high field d_{33} piezoelectric coefficients were calculated as the ratio of strain to electric field at 30 kV/cm on the unipolar loop.

3. 3 Results and discussion

3. 3. 1 Effectiveness of fluxes

LTCC materials are typically sintered at temperatures in the range of 850°-900°C for less than 1 h. For the purpose of co-firing PZT-SKN ceramics with LTCC, the fluxes need to have a melting point lower than the desired sintering temperature 900°C and the ability to facilitate the densification of fluxed ceramics in a short soaking time. The densities obtained for PZT-SKN ceramics with different flux additions sintered at 900°C for 1 h are indicated in Table 3.1. Only 6 wt% $LiBiO_2$ and 1 wt% $LiBiO_2$ + 1 wt% CuO fluxed ceramics were shown to sinter to high density (> 95% theoretical density) under the given sintering condition.

Table 3.1 Details of compounds/mixtures added as fluxes to the 0.98PZT-0.02SKN ceramics and the density obtained after sintering at 900°C for 1 h.

Flux	**Melting point (°C)**	**Addition (wt%)**	**Density achieved at 900°C (relative to theoretical density)**
$LiBiO_2$	~ 700	0.5	66.2%
		1	74.8%
		3	89.0%
		6	95.1%
$LiBiO_2$ + CuO	~ 600*	1 + 1	97.6%

* Melting occurs at ~600°C when $LiBiO_2$ and CuO both exist [287].

Based on the given results in Table 3.1, 6 wt% $LiBiO_2$ and 1 wt% $LiBiO_2$ + 1 wt% CuO were chosen as the low-melting-point fluxes to investigate the low temperature sintering and properties of 0.98PZT-0.02SKN ceramics. Detailed information about the determination of the amount and the type of fluxes used in this study is introduced in Appendix.

3. 3. 2 Phase and microstructure

Phase development of unfluxed 0.98PZT-0.02SKN powders after calcinations and sintering was determined using X-ray diffraction scans. Figure 3.2 shows the XRD patterns for the raw mixture, PZT-SKN powders after first and second calcinations, and powder from crushed pellets after sintering at 1250°C for 2 h. An intermediate secondary phase was observed in the diffraction pattern of powders after the first calcination. Single phase high-purity perovskite structure was confirmed after the second calcination step with further reaction between the initial chemicals. The splitting of peaks for (100), (200), (201), and (211) planes was clearly observed in the XRD pattern of sintered ceramics. It was found that the conventionally sintered PZT-SKN ceramics with highly pure perovskite structure.

XRD patterns of 6 wt% $LiBiO_2$ and 1 wt% $LiBiO_2$ + 1 wt% CuO added 0.98PZT-0.02SKN ceramics sintered at 900°C and the unfluxed specimens sintered at 1250°C are shown in Figure 3.3. A small diffraction peak near 28° (2θ), indicating a small quantity of secondary phase, existed in ceramics with 6 wt% $LiBiO_2$ added. The intensity of the secondary phase peak was lower in samples containing the 1 wt% $LiBiO_2$ + 1 wt% CuO flux. Unfluxed specimens fired at 1250°C exhibited phase-pure perovskite structure with no evidence of secondary phase formation. The appearance of secondary phase in the flux-sintered ceramics could be explained by the formation of a $Bi_2Pb_2O_7$ pyrochlore phase during the low temperature sintering [288].

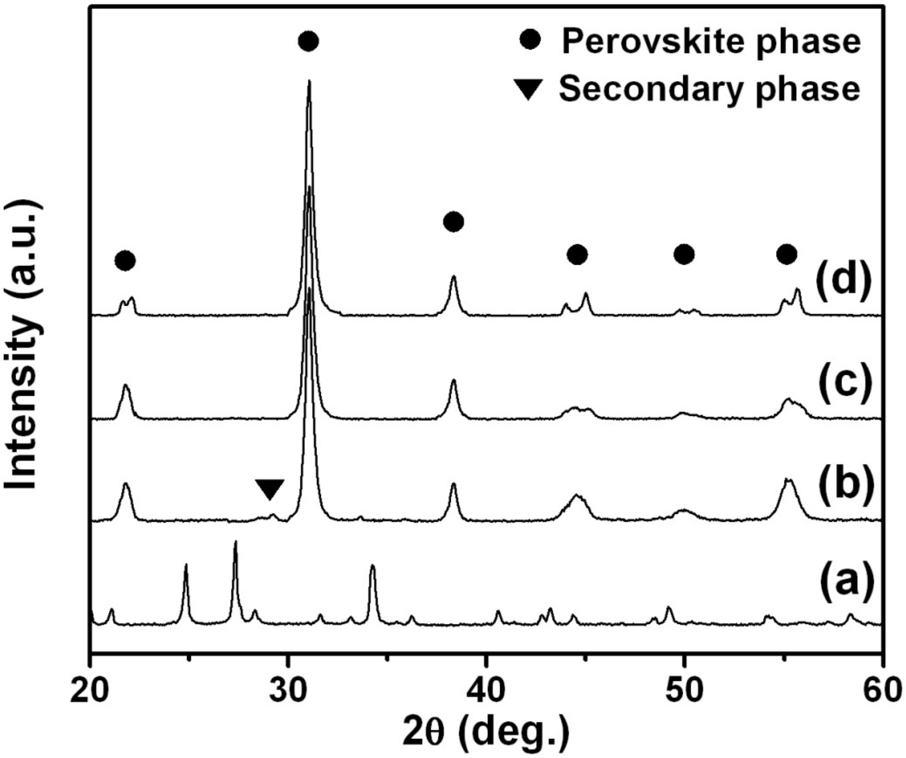

Figure 3.2 X-ray diffraction patterns for unfluxed 0.98PZT-0.02SKN ceramics (a) raw material mixture, (b) after 1st calcination, (c) after 2nd calcination, and (d) sintered at 1250°C for 2 h.

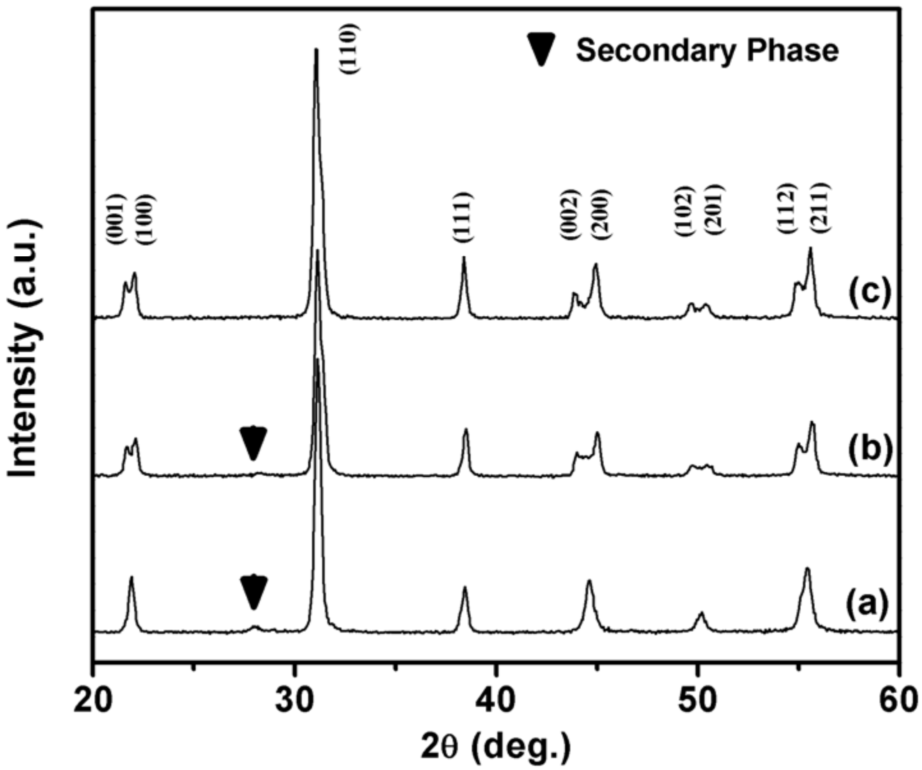

Figure 3.3 X-ray diffraction patterns for 0.98PZT-0.02SKN ceramics sintered at 900°C with (a) 6 wt% $LiBiO_2$, (b) 1 wt% $LiBiO_2$ + 1 wt% CuO addition, and (c) the unfluxed specimen sintered at 1250°C.

Fracture surface SEM microstructure of PZT-SKN ceramics sintered with (a) 6 wt% $LiBiO_2$ addition at 900°C for 1 h, (b) and (c) 1 wt% $LiBiO_2$ + 1 wt% CuO addition at 900°C for 1 or 2 h, and (d) the unfluxed specimens sintered at 1250°C for 2 h are shown in Figure 3.4. The grain size of samples with 6 wt% $LiBiO_2$ addition sintered at 900°C for 1 h was estimated to be around 1.2 μm, increasing to 1.8 μm with 1 wt% $LiBiO_2$ + 1 wt% CuO addition sintered for the same time. The grain size was unchanged for 1 wt% $LiBiO_2$ + 1 wt% CuO added samples sintered at 900°C when sintering time increased from 1 to 2 h. As a comparison the grain size of the unfluxed PZT-SKN ceramics sintered at 1250°C was found to be around 5.6 μm.

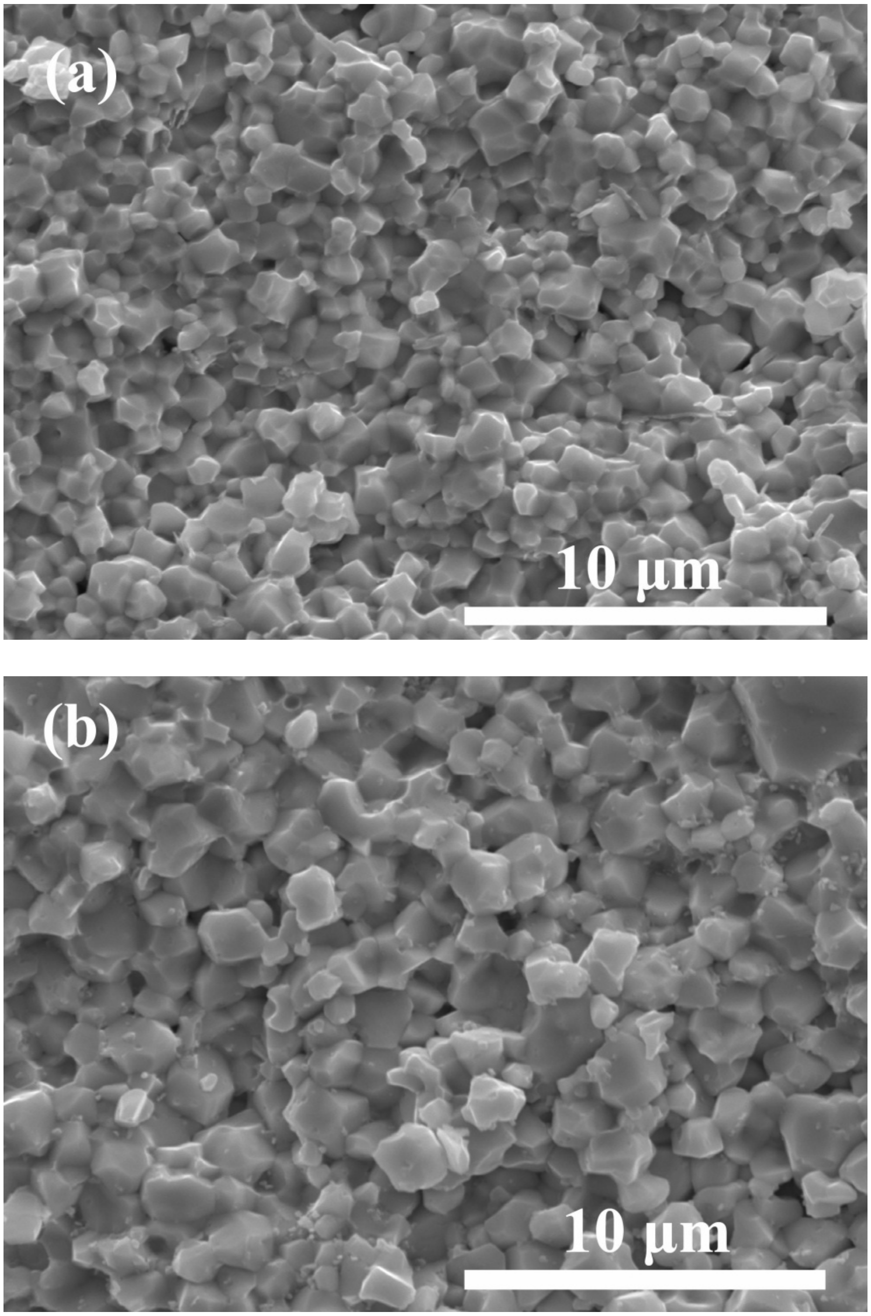

Figure 3.4 Scanning electron microscopic micrographs of 0.98PZT-0.02SKN ceramics sintered at 900°C for 1 h with (a) 6 wt% $LiBiO_2$ and (b) 1 wt% $LiBiO_2$ + 1 wt% CuO addition, (c) 1 wt% $LiBiO_2$ + 1 wt% CuO-fluxed specimen sintered at 900°C for 2 h, and (d) unfluxed specimen sintered at 1250°C for 2 h.

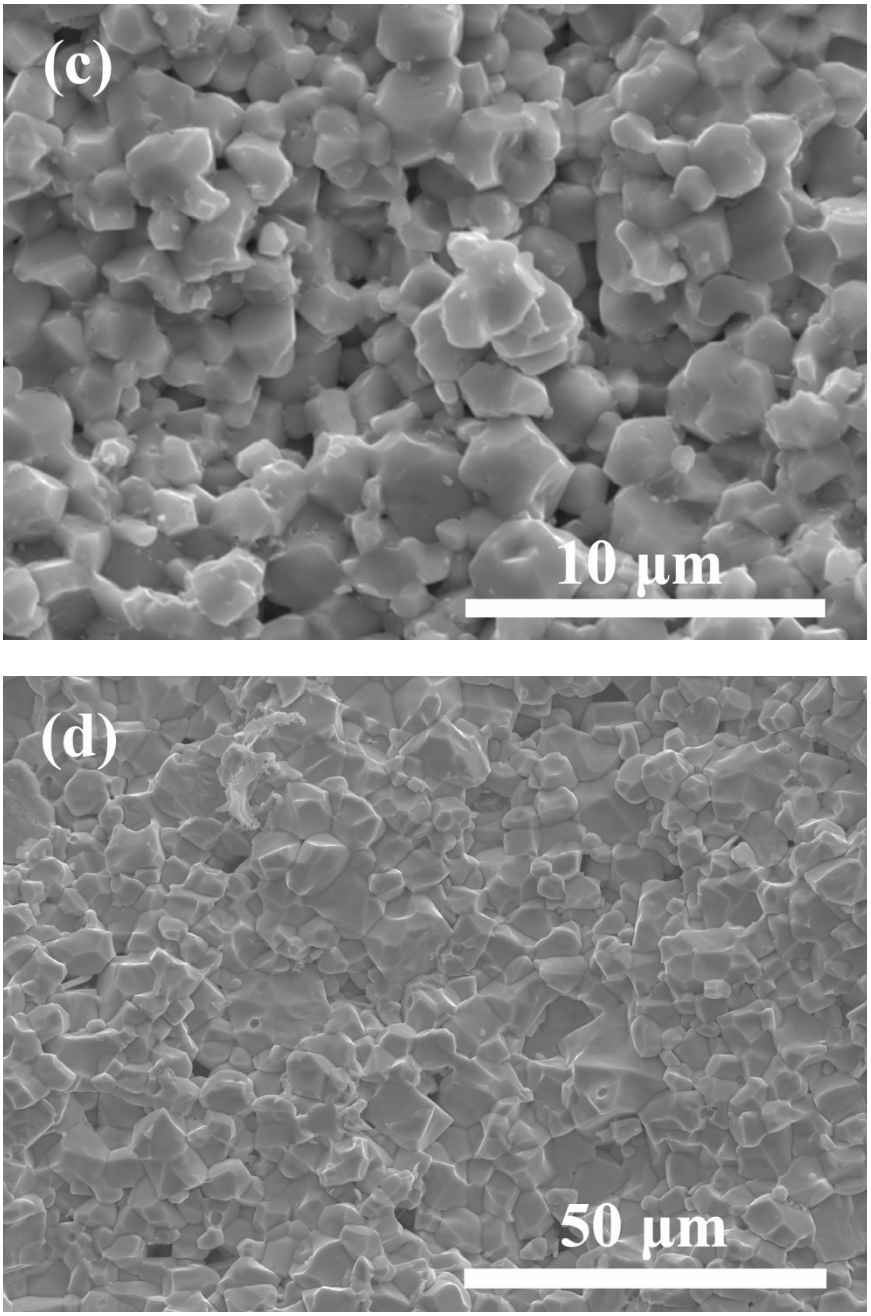

Figure 3.4 (continued) Scanning electron microscopic micrographs of 0.98PZT-0.02SKN ceramics sintered at 900°C for 1 h with (a) 6 wt% $LiBiO_2$ and (b) 1 wt% $LiBiO_2$ + 1 wt% CuO addition, (c) 1 wt% $LiBiO_2$ + 1 wt% CuO-fluxed specimen sintered at 900°C for 2 h, and (d) unfluxed specimen sintered at 1250°C for 2 h.

The bulk density of the 0.98PZT-0.02SKN ceramics sintered at different temperatures with various fluxes is given in Figure 3.5. The density was found to be low (<7.0 g/cm^3) for both the fluxed composition sintered at 750^{o}C. Density gradually increased to a maximum value of 7.75 g/cm^3 (~97.6% of theoretical density) for 1 wt% $LiBiO_2$ + 1 wt% CuO added ceramics sintered at 900^{o}C, and 7.65 g/cm^3 (~96.3% of theoretical density) for 6 wt% $LiBiO_2$ added ceramics sintered at 950^{o}C. However, the density of sintered materials tended to decrease slightly after maximum value indicating over firing.

It was found that 0.98PZT-0.02SKN ceramics without fluxes could not be fully densified at sintering temperatures below 1250^{o}C. The inset in Figure 3.5 shows the variation of measured density for unfluxed specimens with the maximum density of 7.80 g/cm^3 (~98.2% of theoretical density) when sintered at 1250^{o}C for 2 h with lead source powder. These results confirm that the high-density 0.98PZT-0.02SKN ceramics can be obtained with either 6 wt% $LiBiO_2$ or 1 wt% $LiBiO_2$ + 1 wt% CuO addition, yielding improved the sinterability and lowering the sintering temperature by more than 300^{o}C.

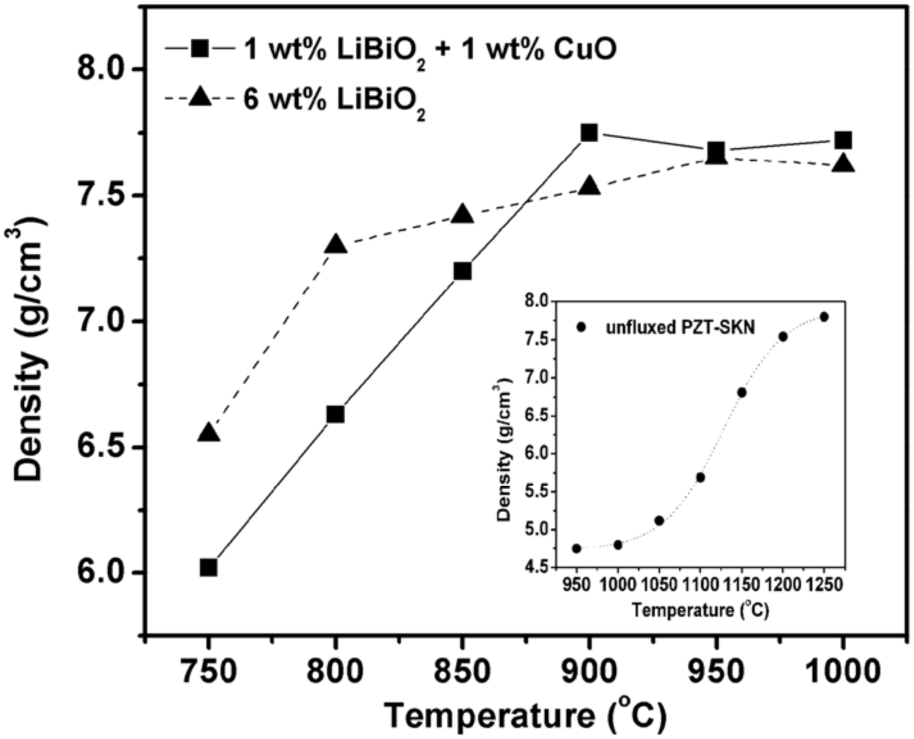

Figure 3.5 Density of 0.98PZT-0.02SKN ceramics with flux additions as a function of sintering temperature.

The addition of $LiBiO_2$ and CuO is believed to lower the sintering temperature of PZT-SKN ceramics due to the formation of a liquid phase. The additive $LiBiO_2$ promotes the sinterability of PZT-SKN ceramics by melting at about 700°C [279]. The additive CuO can react with PbO to form the liquid phase of Cu_2O-PbO at 680°C [289]. The temperature of liquid formation can be further lowered to around 600°C by adding both CuO and $LiBiO_2$ into PZT-SKN ceramics. SEM images also show evidence of liquid phase formation at grain boundaries and triple junctions, as demonstrated in Figure 3.6. However, neither SEM/EDS nor electron probe for microanalysis (EPMA) was able to quantify the localization/distribution of flux in the grain boundary regions.

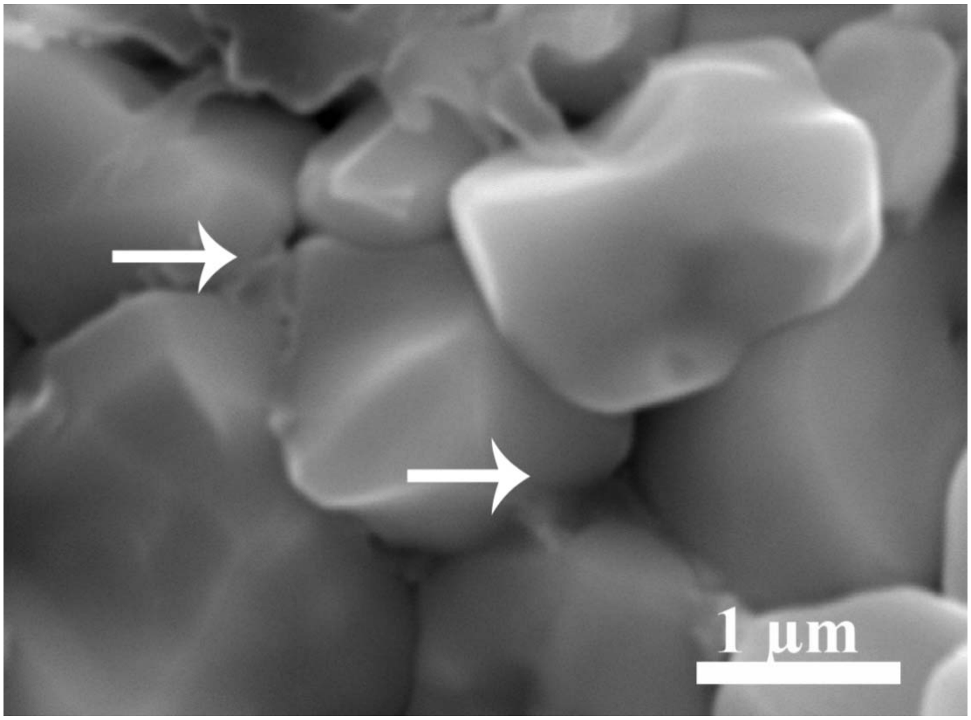

Figure 3.6 The intergranular liquid phase observed in scanning electron microscopic micrographs of PZT-SKN ceramics sintered at 900^{o}C for 1 h with 1 wt% $LiBiO_2$ + 1 wt% CuO addition.

3. 3. 3 Dielectric and piezoelectric properties

The variation in the dielectric constant ε_r and loss tangent tanδ of the 0.98PZT-0.02SKN ceramics conventionally sintered at 1250^{o}C and flux sintered at 900^{o}C as a function of temperature are presented in Figures 3.7(a) and (b), respectively. A lower maximum permittivity and broader permittivity and loss peaks were observed for the fluxed ceramics, compared with the conventionally sintered materials. Additionally, the 1 wt% $LiBiO_2$ + 1 wt% CuO added ceramics exhibited a larger and sharper dielectric peak than the 6 wt% $LiBiO_2$ fluxed ceramics. The Curie temperature T_c for ceramics with 1 wt% $LiBiO_2$ + 1 wt% CuO addition was observed at around 351^{o}C, only a few degrees lower than that for the unfluxed specimens (~357^{o}C), while the T_c shifted to the low temperature side (~302°C) for the ceramics with 6 wt% $LiBiO_2$ addition. The T_c is particularly sensitive to small compositional fluctuations in ferroelectric materials, with reduced T_c previously observed in PZT with CuO addition [290]. The small shift of the T_c for the specimens sintered with 1 wt% $LiBiO_2$ + 1 wt% CuO addition suggests minimal reaction between the additives and the PZT-SKN matrix. For 6 wt% $LiBiO_2$ added ceramics, the substantial decrease in T_c suggests significant diffusion and incorporation of lithium and bismuth into the PZT-SKN matrix.

Figures 3.8(a) and (b) compares the polarization-electric field (*P*-*E*) hysteresis loops and unipolar strain-field loops of 0.98PZT-0.02SKN ceramics conventionally sintered at 1250°C to those of flux sintered ceramics at 900°C. The *P*-*E* hysteresis loops indicate that the remnant polarization P_r decreased from 0.34 C/m^2 in unfluxed samples to 0.29 and 0.27 C/m^2 for 6 wt% $LiBiO_2$ and 1 wt% $LiBiO_2$ + 1 wt% CuO added ceramics, respectively. Also, the coercive field E_c decreased slightly from 15.6 to 14.5 kV/cm for both flux-sintered ceramics. Unipolar strain loops taken on poled samples confirm a high strain for unfluxed PZT-SKN ceramics sintered at 1250°C yielding a high field d_{33} piezoelectric coefficient of 680 pm/V. In fluxed samples sintered at 900°C, the lower unipolar strain loops indicate a reduction of high field d_{33} piezoelectric coefficient (415 pm/V for 1 wt% $LiBiO_2$ + 1 wt% CuO addition and 324 pm/V for 6 wt% $LiBiO_2$ addition) compared to the conventionally sintered samples.

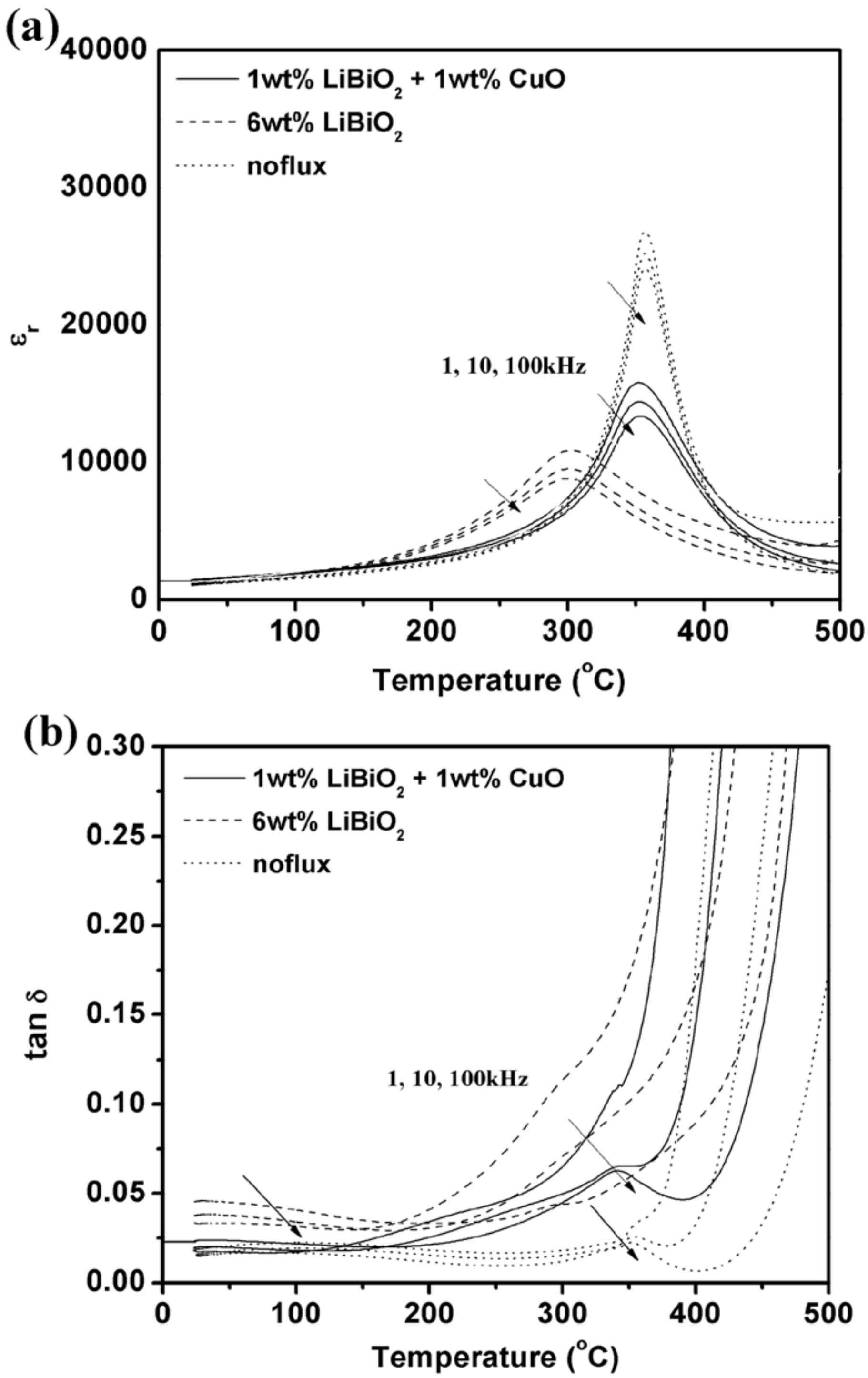

Figure 3.7 Temperature dependence of (a) dielectric constant and (b) tangent loss of 0.98PZT-0.02SKN ceramics conventionally sintered at 1250°C and flux-sintered at 900°C.

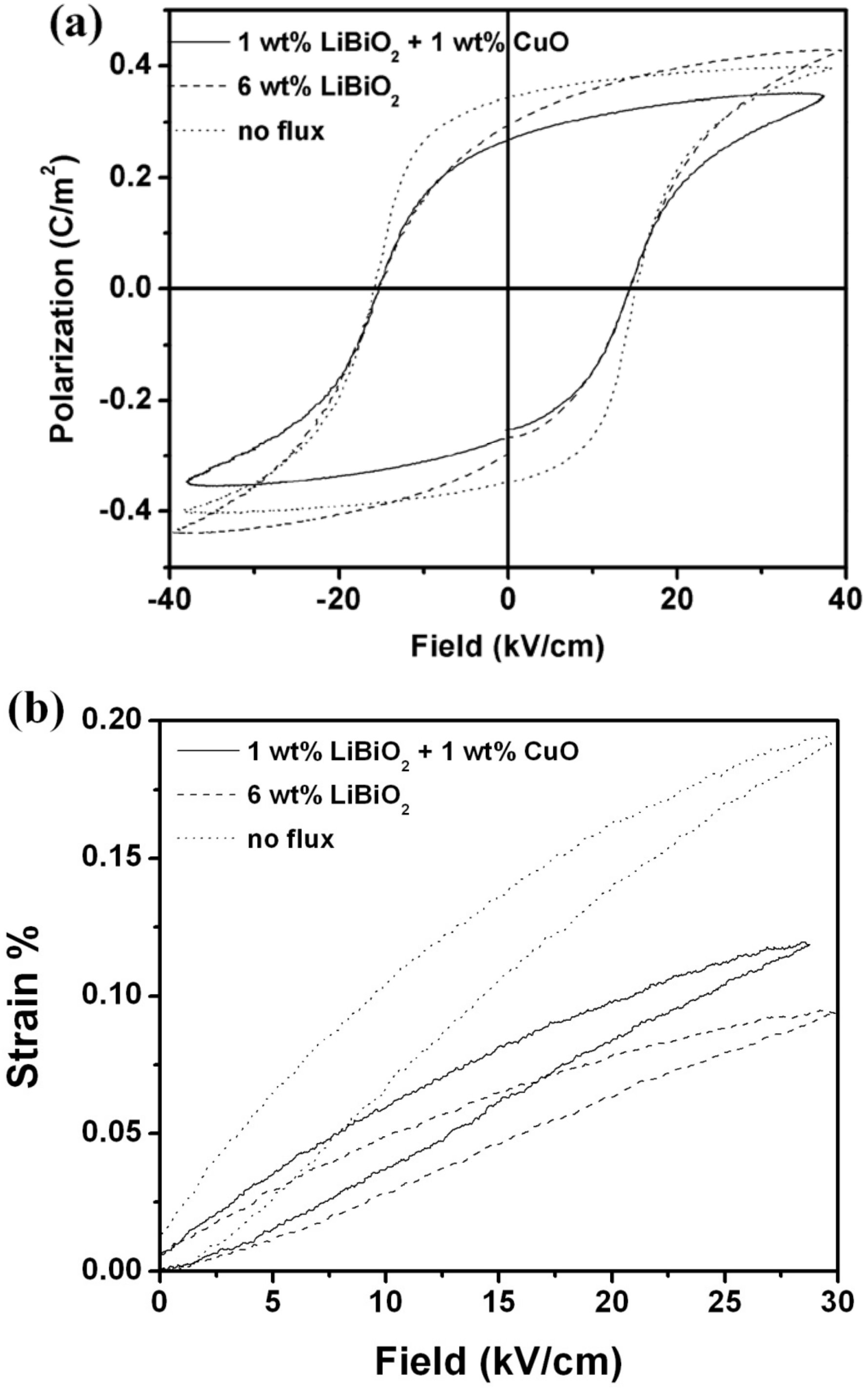

Figure 3.8 (a) $P - E$ hysteresis loops and (b) unipolar loops of 0.98PZT-0.02SKN ceramics conventionally sintered at 1250^{o}C and flux-sintered at 900^{o}C.

The high field d_{33} piezoelectric coefficient and planar coupling factor k_p of 0.98PZT-0.02SKN ceramics with flux additions as a function of sintering temperature are shown in Figure 3.9.

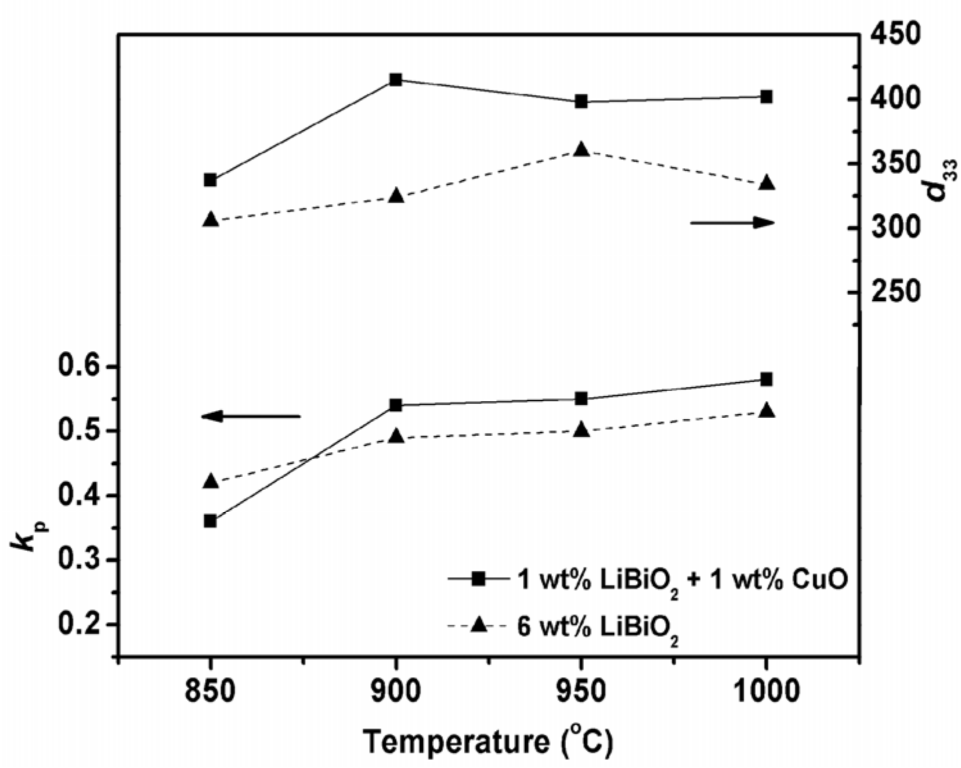

Figure 3.9 High field d_{33} piezoelectric coefficient and planar-coupling factor k_p of 0.98PZT-0.02SKN ceramics with flux additions as a function of sintering temperature.

The values of the planar coupling factor k_p for both fluxed ceramics increase with increasing sintering temperature. The k_p value for ceramics with 1 wt% $LiBiO_2$ + 1 wt% CuO addition is slightly higher than for 6 wt% $LiBiO_2$ added ceramics at temperature above 900°C. The high field d_{33} piezoelectric coefficient reaches the highest value of 415 and 360 pm/V when the sintering temperature increases to 900°C for 1 wt% $LiBiO_2$ + 1 wt% CuO and 950^{o}C for 6 wt% $LiBiO_2$ added ceramics, respectively. The d_{33} value for 1 wt% $LiBiO_2$ + 1 wt% CuO added ceramics is consistently higher than that for 6 wt% $LiBiO_2$ added ceramics for all the examined sintering temperatures. The significant reduction in the d_{33} piezoelectric coefficient in the fluxed PZT-SKN samples compared to high-sintered conventional PZT-SKN is largely attributed to suppressed extrinsic contributions, associated with the significantly reduced grain size in the low temperature sintered ceramics [113]. The strong interaction between the grain boundaries and the domain walls decreases the domain wall mobility which results in the reduction of dielectric and piezoelectric properties, such as dielectric constant ε_r and piezoelectric coefficients d_{33}. The detailed functional properties of flux-sintered ceramics fired at different temperatures and conventionally sintered specimen are listed in Table 3.2. The 1 wt% $LiBiO_2$ + 1 wt% CuO added ceramics sintered at 900^{o}C for 1 h exhibit favorable overall properties with high field d_{33} piezoelectric coefficient of 415 pm/V, Curie temperature T_c of around 351^{o}C, dielectric constant ε_r of 1235, and planar coupling factor k_p of 0.54, which show the possibility to co-fire with LTCC materials.

Table 3.2 Main properties of 0.98PZT-0.02SKN ceramics with and without flux additions sintered at different temperatures.

Flux	**Sintering temperature (^{o}C)**	**Density (g/cm^3)**	ε_r	**tanδ**	P_r **(C/m^2)**	E_c **(kV/cm)**	k_p	d_{33}^{high} **(pm/V)**
6wt% LiBiO$_2$	850	7.42	1130	0.035	0.20	14.5	0.42	306
	900	7.53	1116	0.033	0.29	14.5	0.49	324
	950	7.66	1222	0.030	0.31	14.5	0.50	360
	1000	7.62	1155	0.040	0.32	15.2	0.53	334
1 wt% LiBiO$_2$ + 1 wt% CuO	850	7.20	1104	0.030	0.23	14.5	0.36	337
	900	7.75	1235	0.018	0.27	14.5	0.54	415
	950	7.68	1220	0.020	0.29	14.8	0.55	398
	1000	7.72	1239	0.020	0.30	13.2	0.58	402
unfluxed	1250	7.80	1395	0.015	0.34	15.6	0.58	680

3. 3. 4 Compatibility for integration with LTCC

The sintering temperature profile for LTCC materials must be taken into consideration in order to incorporate LTCC processing with the developed PZT-SKN based piezoelectric ceramics. LTCC tapes are glass-ceramic composite materials allowing sintering at the low temperature, typically in the range of 850^o-900^{o}C for less than 1 h. The densification is achieved by the viscous flow of the low-melting-point glass phase. However, significant deformations can occur under the elevated sintering temperatures and prolonged sintering time [36]. The processing conditions and properties of other reported low temperature sintered PZT-based ceramics are summarized in Table 3.3 and compared with those of 1 wt% LiBiO$_2$ + 1 wt% CuO added 0.98PZT-0.02SKN ceramics developed in the current work. When sintered at temperature of no more than 900^{o}C, only the present fluxed PZT-SKN ceramics can be densified at a relatively short soaking time, even though the piezoelectric coefficient d_{33} is not as high as those of other PZT-based ceramics sintered for more than 4 h. As shown in Table 3.2, there are several other PZT-based systems which can be sintered at temperature in the range of 900^{o}-950^{o}C for less than 1 h, however, either the low d_{33} values (~200 pm/V) [146,282] or the high sintering temperature (950^{o}C) [144] limits their utilization in the fabrication of multilayer piezoelectric actuators with LTCC materials. Moreover, the T_c of developed low fired PZT-SKN is above 350^{o}C, higher than most of the reported fluxed PZT-based ceramics. This high T_c is required for applications covering a broad temperature range. Based on the properties mentioned above and comparison with other low fire piezoelectric ceramics, 0.98PZT-0.02SKN ceramics with 1 wt% $LiBiO_2$ + 1 wt% CuO addition represent an attractive high performance piezoelectric material for applications requiring low temperature and short hold processing conditions.

Table 3.3 Comparison of functional properties of 1 wt% $LiBiO_2$ + 1 wt% CuO fluxed 0.98PZT-0.02SKN and other low fire PZT-based ceramics.

PZT ceramics	**Additives**	**Sintering Temp. (^oC)**	**Sintering Time (h)**	**d_{33} (pm/V)**	**T_c (^oC)**	**Ref.**
PZT-PMN	$LiBiO_2$	800	12	504	225	[280]
PZT-SKN	$LiBiO_2$ + CuO	900	1	415	351	----
PZT-PNN-PMN	Fe_2O_3	900	2	377	330	[291]
PZT-PNN-PMW	Li_2CO_3 + $CaCO_3$	900	2	517	317	[292]
PZT-PMS-PZN	CuO	900	4	306	290	[281]
PZT-SKN	Li_2CO_3	900	6	640	347	[157]
PZT-PZN-PMN	$Ba(W_{0.5}Cu_{0.5})O_3$	920	4	351	320	[293]
PZ-PT-PNN	----	925	4	600	189	[294]
PZT-PMN-PFW	$LiSbO_3$	930	4	363	286	[295]
PZT-BF-BCW	CuO	935	0.5	236	290	[282]
PZT-BF-BCW	MnO_2	935	0.8	201	290	[146]
PZT-PNN-PMN	Li_2CO_3 + Na_2CO_3	950	1	419	332	[144]
PSNT	$LiBiO_2$	950	2	340	263	[276]
PZT-PMN	ZnO + CuO	950	2	351	280	[112]
PZT-PMN-PFW	ZnO	950	4	313	295	[296]
PZT-PMN	Li_2CO_3	950	4	517	225	[272]
PZT-PMN	CuO	1020	2	238	348	[285]
PZT-PMN-PFW	$YMnO_3$	1020	4	341	304	[297]
PZT-PMN-PFW	$BiFeO_3$	1020	4	309	308	[275]
PZT-PMS-PZN	ZnO	1120	4	300	270	[298]
PZT-PZN	La_2CO_3	1130	5	560	204	[273]
PZT-PMN	$CaCO_3$	1150	4	345	352	[274]

3. 4 Conclusions

Piezoelectric ceramics based Pb($Zr_{0.53}$, $Ti_{0.47}$)O_3-Sr($K_{0.25}$, $Nb_{0.75}$)O_3 (PZT-SKN) with $LiBiO_2$ and CuO addition have been synthesized by the conventional solid-state route. The addition of 6 wt% $LiBiO_2$ or 1 wt% $LiBiO_2$ + 1 wt% CuO reduces the sintering temperature by 300^o-350^oC through the formation of a liquid phase. It was found that the formation of the secondary phase and the smaller grain size for flux-sintered ceramics as indicated in XRD patterns and SEM micrographs, respectively, are considered to deteriorate the piezoelectric properties when compared with materials conventionally sintered at 1250^oC. However, the ceramics sintered at 900^oC for 1 hour with 1 wt% $LiBiO_2$ + 1 wt% CuO content exhibit desirable piezoelectric and dielectric properties with high field d_{33} piezoelectric coefficient of 415 pm/V, Curie temperature T_c of around 351^oC, dielectric constant ε_r of 1235, and planar coupling factor k_p of 0.54. The reduced sintering temperature and short soaking time, together with the favorable dielectric and piezoelectric properties of the fluxed 0.98PZT-0.02SKN ceramics, demonstrate the potential opportunity of co-firing with LTCC materials and compatible low-melting-point electrodes (*e.g.* Ag) to fabricate multilayer piezoelectric devices.

Chapter 4. Sintering behavior, properties, and applications of co-fired LTCC/PZT-SKN multilayer ceramics

4. 1 Introduction

The incorporation of co-firable piezoelectric ceramics into commercial low temperature co-fired ceramic (LTCC) materials would offer the possibility of manufacturing highly integrated microdevices or microsystems using thick-film technology. Materials and processing conditions have been developed allowing co-firing of fluxed $Pb(Zr_{0.53}, Ti_{0.47})O_3$-$Sr(K_{0.25}, Nb_{0.75})O_3$ (PZT-SKN) materials with LTCC tapes [269,270]. As presented in chapter 3, PZT-SKN ceramics with 1 wt% $LiBiO_2$ + 1 wt% CuO addition are shown to sinter to high density at 900^{o}C for 1 h with large high field d_{33} piezoelectric coefficient of 415 pm/V and other favorable electric properties [269]. This reduction in sintering temperature and time enables the possibility of integration with LTCC and low fire electrode materials for the application in multilayer device fabrication. The investigation of co-firing processes and the resultant properties of piezoelectric layers in the co-fired LTCC/PZT-SKN multilayer ceramics are introduced in the current chapter.

The master sintering curve (MSC) approach has been used to study the densification behavior of fluxed PZT-SKN and LTCC tapes. Different sintering mechanisms for fluxed PZT-SKN ceramics and LTCC materials were confirmed by analyzing the apparent activation energy Q_a. Using knowledge gained from MSC results, an optimized sintering profile was developed. The fluxed PZT-SKN thick films were prepared by the tape-casting method using a slurry consisting of ceramic powders and an organic binder vehicle. LTCC/PZT-SKN multilayer ceramics were first laminated and then co-fired using the derived optimal sintering profile. The microstructures, dielectric and piezoelectric properties of fluxed PZT-SKN layers co-fired with LTCC materials were investigated and compared with those of free sintered PZT-SKN samples in same composition to understand the influence of changing densification behaviors on the properties. HL2000/PZT-SKN multilayer stacks co-fired at 900°C for 0.5 h exhibited large d_{33} piezoelectric coefficient (high field d_{33}>340 pm/V). The elemental inter-diffusion conditions were examined at the heterogeneous interface and the center of piezoelectric layer in co-fired LTCC/PZT-SKN multilayer ceramics using EDS analysis. Finally, a piezoelectric microbalance was fabricated using co-fired LTCC/PZT-SKN multilayer ceramics, demonstrating the possibility of integrating useful thick-film piezoelectric structures into LTCC-based microsystems.

4. 2 Master sintering curve (MSC) model

As described in chapter 2, sintering is a complex process involving microstructure evolution related to different mass transport mechanisms. The sintering behavior of any specific powder compact depends on characteristics of the green body, including composition, particle size and shape, particle size distribution, degree of agglomeration, and other factors such as heating rate and sintering temperature, time, and atmosphere. The master sintering curve (MSC) approach proposed by Su and Johnson [299] has been widely used to predict and optimize the densification behavior for a given powder compact. The capability of sintering control based on MSC analysis could lead to the process optimization for multi-materials integration, co-firing, microstructure, density and quality control [300]. In the case of fabrication of LTCC/PZT-SKN multilayer ceramics MSC study can be used for the optimization of co-firing process for heterogeneous laminates with different sintering behaviors. Development of compatible co-firing profile is required for multilayer ceramic production and will impact both the microstructure and properties of the sintered body.

MSC theory assumes that the microstructural evolution of a powder compact depends only on density and that a single sintering mechanism controls the sintering process [299-302]. The activation energy Q for densification of a given material is a characteristic quantity that distinguishes different diffusion mechanisms during sintering process. In practice more than one sintering mechanism can be effective simultaneously over a certain temperature interval; if the proportional contribution of each sintering mechanism does not change with the variation of sintering temperature, then the MSC concept can still be applied [303]. The resultant temperature-independent activation energy, a weighted average of the various values corresponding to the multiple sintering mechanisms, is normally called the apparent activation energy Q_a. The MSC and Q_a for a given material can be obtained empirically from densification data collected over a wide range of constant heating rate or isothermal heating experiments. The densification rates at any sintering stage derived from MSC are related to the linear shrinkage rates.

Theoretically, the construction of MSC model is derived from the combined-stage sintering model which predicts the densification behavior (for isotropic shrinkage) as [299]:

$$-\frac{dL}{Ldt} = \frac{d\rho}{3\rho dt} = \frac{\gamma\Omega[\Gamma(\rho)]D_o}{kT[G(\rho)]^n}\exp(-\frac{Q_a}{RT})$$

where L is the compact size or length, ρ is the relative density, γ is the solid–vapor surface energy, Ω is the atomic volume, Γ is the scaling factor containing density-dependent geometric terms, D_o is the diffusivity pre-exponent, k is Boltzmann's constant, T is the absolute temperature, G is the grain size with $n = 3$ for lattice diffusion and $n = 4$ for grain boundary diffusion, Q_a is the apparent activation energy, and R is the ideal gas constant. It is assumed that the microstructural functions Γ and G depend only on density.

The above equation can be rearranged and integrated to build the relationship between the work of sintering Θ and the density ρ at any time point t during the sintering cycle, as shown in the following equation [299]:

$$\phi(\rho) = \Theta(t, T(t))$$

The left part of this equation is related to the evolving microstructure which is a function of density while the right part is determined by the time-temperature profile and Q_a. This relationship is defined as the MSC and both Φ (ρ) and Θ (t, $T(t)$) are defined in the following equations [299]:

$$\phi(\rho) \equiv \frac{k}{\gamma\Omega D_o}\int_{\rho_o}^{\rho}\frac{[G(\rho)]^n}{3\rho[\Gamma(\rho)]}d\rho$$

$$\Theta\big(t,T(t)\big) \equiv \int_0^t \frac{1}{T(t)}\exp(-\frac{Q_a}{RT(t)})dt$$

The densification of material is thus linked to the integral thermal work through an arbitrary time-temperature profile and a given Q_a. The optimal Q_a is determined on a trial-and-error basis when all the data converge to a single fitting curve. Further, the MSC can be formulated using the measured density data and the determined optimal Q_a. The obtained MSC can only be applied to compacts made from the same material and by the same green-body formation processing [299].

Recently, the MSC concept has been expanded to describe other common phenomena occurred during sintering. Firstly, if the Q_a is considered not a constant as the sintering temperature varies, the sintering process can be divided into several consecutive stages, each one with its own constant Q_a [304]. Secondly, the MSC has also been used to simulate the grain growth behavior [305]. Finally, the MSC concept is further developed by analyzing the grain size effect on densification during both solid-state and liquid-phase sintering [306].

4. 3 Tape casting technique

For incorporating piezoelectric elements into MEMS, screen printing [307,308] and sol-gel processing [309,310] have been widely investigated in order to deposit PZT-based thick films on silicon, alumina, LTCC, and other rigid substrates, particularly for the thickness of films ranging from several microns to tens of microns. However, both processes have technical problems to obtain the dense and crack-free films with uniform microstructure in building multilayer structures. For using screen printing or sol-gel processing multiple repeating steps of coating and drying or pre-firing are required to fabricate films with certain thickness which is limited due to the accumulation of internal stress, resulting in cracking and other defects during deposition process.

Tape casting is a low-cost, well-established efficient technique to produce dense, uniform, and self-supporting ceramics sheets with a wide range of thickness (from several microns up to several hundred microns), which offers great possibilities for fabricating functional multilayer ceramics [311-313]. Cast tapes with high strength and sufficient flexibility before firing can be easily micromachined to form the laminated structures using thick-film technologies [314,315]. Cast PZT-based piezoelectric tapes with proper compositions and sintering behaviors could also be patterned, laminated, and co-fired with LTCC materials to build hybrid multilayer ceramics which have the potential to be used in sensor and actuator applications. The composition, lamination process, and firing profile of cast PZT-based tapes have significant influence on the sintering behaviors of laminated LTCC/PZT multilayer structures.

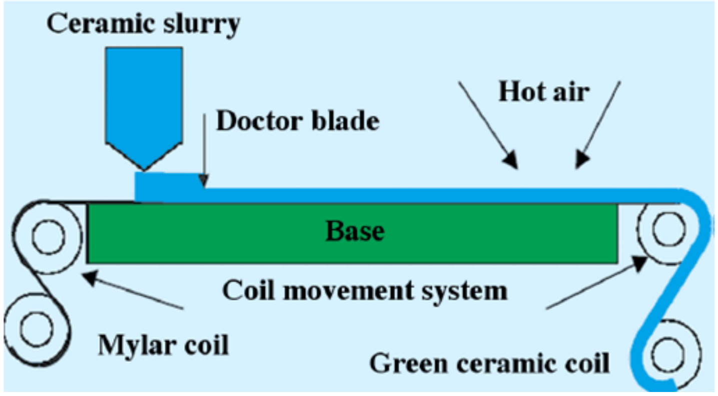

Figure 4.1 Schematic diagram of tape casting process. (taken from M.R. Gongora-Rubio [17])

Figure 4.1 illustrates the tape casting process. The prepared ceramic slurry is continuously dispensed onto a moving tape carrier under a doctor blade. The carrier is normally an organic film coated with additional elements (*e.g.* silicone coated Mylar) for easy separation of dried tapes from substrates. Cast slurries are dried in two steps: firstly, drying occurs by evaporation of solvent transported to the slurry surface by capillary force, and then further drying is controlled by solvent diffusion through the solidified part of the cast slurry. After drying the formed flexible green tapes with sufficient strength can be stored on take-up reels or stripped from the substrate and cut into the desired geometries for subsequent processing [159].

Considering the pressure flow under a doctor blade and the planar laminar flow generated by the moving tape carrier, the thickness of the dry tape h_d is given by [316]:

$$h_d = ADh_o(1 + \frac{h_o^2 \Delta p}{6\eta v L})$$

where A is a correction factor, D is the density ratio of the slurry and the dry tape, h_o is the height between the doctor blade and the carrier, Δp is the pressure difference (determined by the height of slurry in the reservoir), η is the viscosity of the slurry, v is the velocity of the doctor blade relative to the casting surface, and L is the thickness of the doctor blade. The equation indicates a polynomial relationship between h_d and h_o. The h_d also changes linearly as the Δp or v various in the tape casting process. For small values of $h_o<200$ µm, the h_d would simply be proportional to the h_o if the values of η, v, and Δp are carefully controlled in a certain range, resulting a uniform thickness for the cast tape [159]. The flat-bottom doctor blade with certain L (typically 1~2 cm) is more suitable than the knife-edged blade (small L) for tape casting based on the analysis of above equation.

4. 4 Experimental procedures

The piezoelectric ceramic thick films used in the present work were prepared from low temperature sinterable ceramic powder according to the formula of $0.98Pb(Zr_{0.53}, Ti_{0.47})O_3$-$0.02Sr(K_{0.25}, Nb_{0.75})O_3$ (PZT-SKN) + 1 wt% $LiBiO_2$ + 1 wt% CuO. The fluxed PZT-SKN ceramic powders were fabricated using conventional solid-state ceramic processing methods as described in the experimental section of chapter 3.

4. 4. 1 Tape casting

PZT-SKN tapes were prepared using an optimized organic-solvent based binder system. The preparation of the castable slurry is the most important step in the tape casting process. An ideal organic vehicle for tape casting requires certain properties, such as appropriate viscosity and rheological behavior, desirable wettability on the substrates and solid particles, suitable drying rate, and good dried film flexibility and strength to withstand rough handling [317]. For achieving high-density tapes, a high solid loading with a desirable mixture of solvent and additives is needed. The mixture of xylene and ethyl alcohol as solvent is selected for the current study, which has shown great adaptability and solubility for various organic additives to make a castable slurry [312]. The stability of powder suspension is largely determined by the dispersant. In order to lower the viscosity of the slurry for high particle concentration, the dispersant content needs to be optimized first for tape casting. Suspensions with 75 wt% solid loading of PZT-SKN powder were mixed with dispersant (Menhaden fish oil) at different dispersant/powder weight ratio varying from 0.25% to 2.5%. Figure 4.2 shows the viscosity data measured at shear rate of 45 s^{-1} (similar to the shear rate under tape casting) for different suspensions. It was found that the viscosity decreased to 10.5 mPa · s when the concentration of dispersant increases to about 0.8 wt% and the viscosity changed slightly when further adds the dispersant content to 3.5 wt%. The concentration of dispersant in about 0.8 wt% (dispersant/powder loading) is considered effective for colloidal property control.

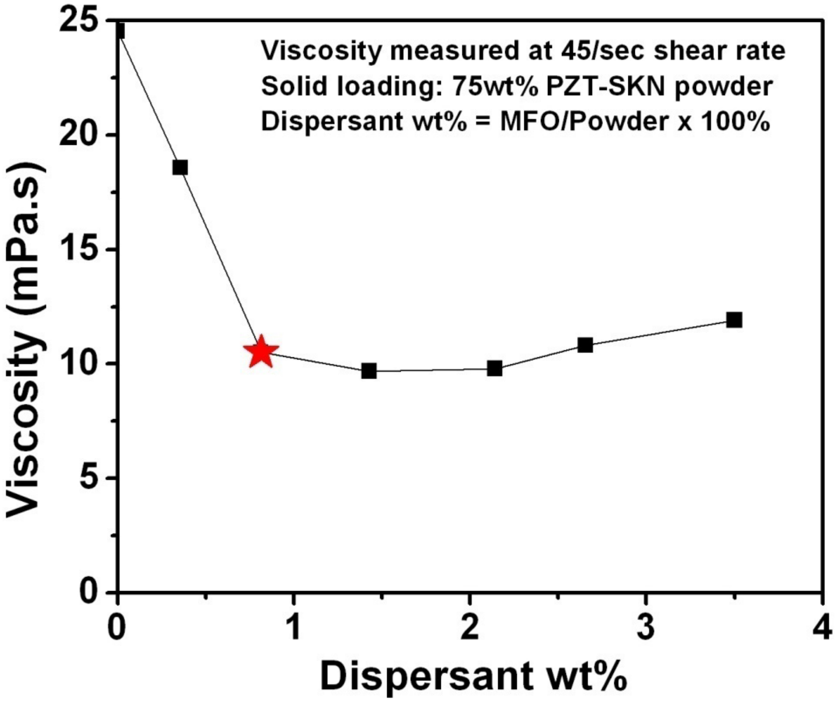

Figure 4.2 Viscosity of 75 wt% solid loading suspensions with different dispersant contents.

The steps in the tape casting process are summarized in Figure 4.3. The ceramic powders with solvent and dispersant were first mixed using 5 mm spherical highly wear resistant zirconia media (TOSOH, Grove City, PA) by rotary ball milling (US Stoneware, Mahwah, NJ) for 12 h. Then a binder (polyvinyl butyral) and plasticizers (polyalkylene glycol and butyl benzyl phthalate) in weight ratio of 1.2 dissolved in the solvent were added for another 12 h mixing to obtain a uniform castable slurry. This sequence of introducing the additives into the mixing process diminishes the competition for adsorption on the particles between the dispersant and binder/plasticizer and reduces the mechanical damage of the binder molecules [317], providing the required strength and flexibility of green tape. Before casting, a de-airing process is necessary in order to prevent the formation of bubbles in the cast tape. The exact slurry formulation utilized for tape casting is provided in Table 4.1.

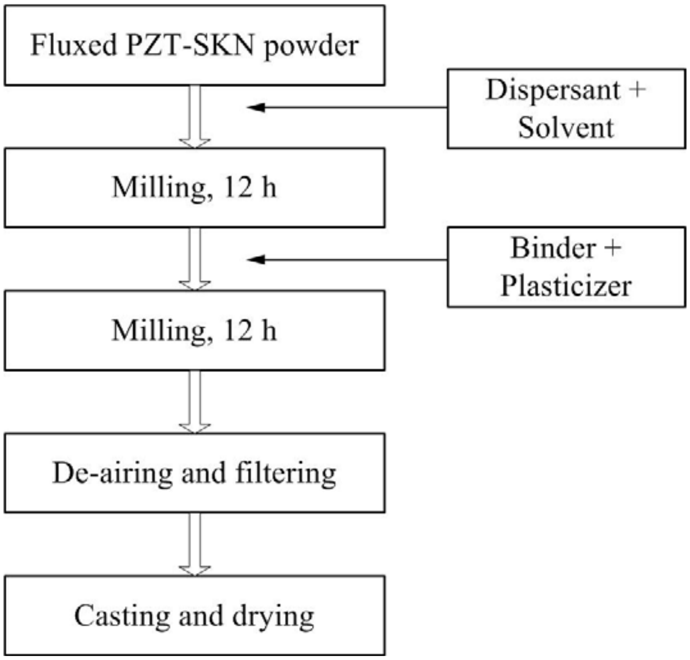

Figure 4.3 Schematic flow diagram for the tape casting process.

A bench-top caster (TTC-1200, R.E. Mistler Inc., Yardley, PA) with a single doctor blade was used to cast the tape on silicone coated Mylar substrates (R.E. Mistler

Inc., Yardley, PA) at the speed of ~10 cm/min. The fluxed PZT-SKN tapes were dried at room temperature for 6 h. The thickness of as cast tapes was typically in the range from 80 to 120 μm.

Table 4.1 Compositions of PZT-SKN tape casting slurries. (wt%)

Function	Composition	Amount
Ceramic powder	Fluxed PZT-SKN	76.5
Solvent	Xylene	10.0
	Ethyl alcohol	9.6
Dispersant	Menhaden Fish Oil	0.6
Binder	Polyvinyl Butyral (PVB)	1.8
Plasticizer	Polyalkylene Glycol (PAG)	0.6
	Butyl Benzyl Phthalate (BBP)	0.9

* Organic additives were supplied by Richard E. Mistler Inc., Yardley, PA.

4. 4. 2 Construction of MSC

The MSC was constructed from the measured density ρ data as a function of work of sintering Θ for a given sintering profile. Using constant heating rate experiments is the most efficient method to combine the data for ρ and Θ. The experimental sintering data were collected in the following steps for building the MSC: three layers of the LTCC and fluxed PZT-SKN tapes were stacked and laminated to obtain suitable thickness for easy handling and density measurements. The laminates were heated from room temperature to 450°C at a ramp rate of 1°C/min and then kept at peak temperature for 2 h to completely remove the organic binders. The samples then were fired at 4 different heating rates (1°C/min, 5°C/min, 8°C/min, and 12°C/min) to either 700°-950°C or 650°-

1050°C for the LTCC and fluxed PZT-SKN tapes, respectively. The green density of the pressed laminates was measured geometrically and the bulk densities of the sintered bodies were measured using Archimedes (immersion) method. With these sets of data the work of sintering Θ was initially calculated for each corresponding time-temperature data using an assumed value of the apparent activation energy Q_a. Then, the average residual square (sum of the residual squares divided by the total number of data points) is plotted as a function of assumed values of Q_a and the minimum of the average residual square corresponds to the optimum Q_a which is subsequently selected for the construction of MSC, as shown in Figure 4.4. Finally, data points from all heating rates were plotted simultaneously as density ρ versus log(Θ) and fitted with a sigmoidal curve using optimum Q_a value. The sintering behaviors of the LTCC and fluxed PZT-SKN tapes could then be predicted for an arbitrary schedule using the developed MSC models.

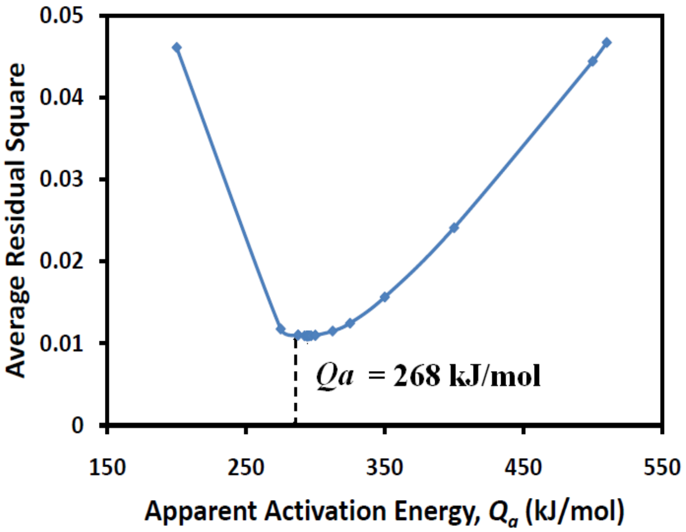

Figure 4.4 Example of determination of optimal apparent activation energy Q_a for fluxed PZT-SKN materials by minimizing the average residual square.

4. 4. 3 Fabrication of LTCC/PZT-SKN multilayer ceramics

Multilayer stacks of the PZT-SKN tape as well as several commercial LTCC systems Heralock® HL2000, Heratape® CT2000, and CT800 (Heraeus Inc.-Thick Film Division, West Conshohocken, PA) were fabricated by dicing and lamination. Square PZT-SKN and LTCC tapes of several sizes (length a = 10, 15, and 20 mm) with and without round cavities in the center were patterned using a CO_2-laser milling system (VLS 3.50, Universal Laser Systems Inc., Scottsdale, AZ). Multilayer samples were fabricated by stacking patterned LTCC green tapes on the top and bottom of PZT-SKN layers with different thickness and then laminating aligned stacks under 10 MPa at 75^oC for 10 min using a uniaxial press (3851,Carver, Wabash, IN). Different multilayer structures were studied to investigate the sintering behaviors and the properties of co-fired LTCC/PZT-SKN ceramics.

4. 4. 4 Characterization of microstructures and properties

The microstructures of co-fired PZT-SKN/LTCC multilayer ceramics were observed using an optical microscope (SZX12, Olympus, Tokyo, Japan) and scanning electron microscope (SEM: S-3200, Hitachi, Tokyo, Japan). SEM with an energy-dispersive X-ray detector (EDS: Evex detector, Evex Inc., Princeton, NJ) enabled elemental compositional determination near the interface between PZT-SKN and LTCC layers. An ARL-SEMQ electron microprobe analyzer was also used to quantify the extent of elemental inter-diffusion near the heterogeneous interface in co-fired multilayer ceramics. A conductive gold electrode paste (TC8101, Heraeus Inc.-Thick Film Division, West Conshohocken, PA) was printed on the green body of square shaped PZT-SKN tapes and the exposed PZT-SKN surfaces in laminated multilayer structures for measuring the electrical characteristics. Next, the fluxed PZT-SKN tapes and LTCC/PZT-SKN multilayer ceramics were co-fired with gold electrodes using different sintering profiles. Sintered samples were poled by applying a DC electric field of 30 kV/cm at the temperature of 100^{o}C for 15 min in a silicon oil bath. Characterization of dielectric and piezoelectric properties on sintered samples was conducted using the same procedures introduced in the experimental method section in chapter 3.

4. 4. 5 Microbalance fabrication and testing

Finally, a 1 cm × 1 cm piezoelectric microbalance was fabricated in a compact LTCC/PZT-SKN multilayer ceramic module using optimized processing techniques. The dependence of resonant frequency on mass loading for the developed multilayer PZT-SKN/LTCC ceramics was investigated using an impedance analyzer (4194A, Hewlett-Packard, Palo Alto, CA) with automated data acquisition program. The testing structure was securely mounted in a fixture and electrically connected to the impedance analyzer. A micropipette was used to generate uniform droplets of perfluoropolyether fluids (Galden HT-200, Solvay Solexis Inc., Thorofare, NJ) of known density and low volatility onto the top electrode surface. The experimental setup for monitoring the shift of resonant frequency is shown in Figure 4.5.

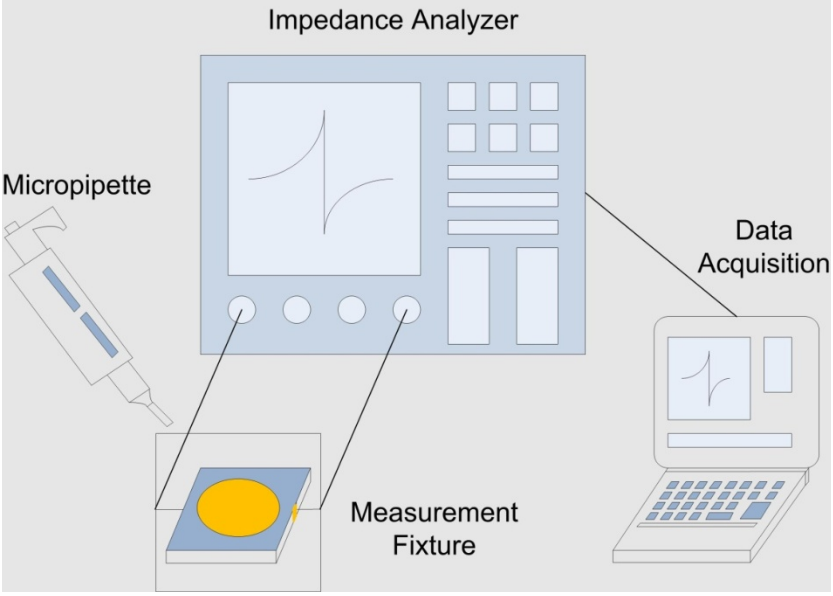

Figure 4.5 Schematic diagram of measurement setup for monitoring the resonant frequency response.

4. 5 Results and discussion

4. 5. 1 Master sintering curve analysis

The MSC approach was used to understand the sintering mechanisms and optimize the fabrication of co-fired LTCC/PZT-SKN multilayer ceramics. The densification data obtained for fluxed PZT-SKN, HL2000, and CT2000 tapes heated at 1°C, 5°C, 8°C, and 12°C/min are shown in Figure 4.6(a), (b), and (c), respectively. A single value of theoretical density for each material (7.90 g/cm^3 for fluxed PZT-SKN, 3.05 g/cm^3 for HL2000, and 3.12 g/cm^3 for CT2000) is defined to calculate the relative densities for samples sintered at all heating rates. In general, slower heating rates generated higher relative densities for samples sintered at equivalent temperature below the peak sintering temperature. The MSC describing the relationship between density ρ

and log(Θ) were determined using the density data and a MSC generating program (Master_Curve_V.1) using a sigmoid curve with five adjustable parameters proposed by Teng *et al*. [301]:

$$\rho = \rho_o + \frac{a}{[1 + \exp(-\frac{\log(\Theta) - \log(\Theta_o)}{b})]^c}$$

where a, b, c are fitting constants, ρ_o is green density, and the log(Θ_o) is calculated at the initial time t of sintering cycle. The three sets of fitting parameters were calculated to obtain the MSC for fluxed PZT-SKN and LTCC tapes, listed in Table 4.2.

Table 4.2 MSC fitting parameters for fluxed PZT-SKN and LTCC tapes.

Composition	ρ_o **(%TD)**	a	b	c	**log(**Θ_o**)**
PZT-SKN	48.88	50.182	0.091	0.057	-11.690
HL2000	73.08	25.954	0.320	0.898	-20.391
CT2000	65.41	33.833	0.165	0.178	-25.324

All MSC results demonstrate acceptable fit with the experimental data points, as shown in Figure 4.7(a)-(c). The insets of Figure 4.7(a)-(c) illustrate the determination of the best fit apparent activation energies Q_a, 268, 415, and 540 kJ/mol for fluxed PZT-SKN, HL2000, and CT2000 tapes, respectively. The obtained Q_a of 540 kJ/mol for CT2000 tapes is similar to the value of 530 kJ/mol reported by other researchers using density data calculated from precise dilatometry tests [318]. It is demonstrated that the density measurement method used in this study has high accuracy for the determination of Q_a and the generation of MSC. The resulting Q_a for fluxed PZT-SKN tapes is smaller than those for LTCC materials. This finding corresponds to differing sintering mechanisms in LTCC and PZT-SKN ceramics. The LTCC materials are crystallizable glass-ceramics in which sintering is controlled by the viscous flow. The densification of the low temperature sintered PZT-SKN ceramics is related to the atomic diffusion through the liquid phase formed by the CuO and $LiBiO_2$ fluxes additions, as described in chapter 3. Comparison of the MSC suggests that dissimilar densification behaviors of the different compositional layers will have significant effects on the deformation and stress development in the co-firing process.

The densification behaviors of fluxed PZT-SKN, HL2000, and CT2000 tapes under isothermal heating at different temperatures and holding time are predicted and illustrated in Figures 4.8(a), (b), and (c), respectively. It was found that the density increases from 67% to 77% of theoretical density for fluxed PZT-SKN tapes as the sintering time increases from 0.5 h to 2 h at 700^{o}C while the HL2000 starts to densify at the same temperature. There is no obvious densification observed for CT2000 tapes until the sintering temperature increases to 750^{o}C. For fluxed PZT-SKN tapes, the density increases gradually from 700^{o}C to 900^{o}C. The relatively fast densification process of the LTCC tapes is completed within a smaller temperature window compared to that of fluxed PZT-SKN tapes. It is extremely difficult to discover a firing profile provide exactly the same sintering behaviors for heterogeneous materials with different sintering mechanisms. However, the determination of a most compatible firing profile using MSC results for every compositional layers has been shown to enable reduction of the sintering stresses during co-firing of hybrid multilayer ceramics, providing a better yield for the multilayer integration [186].

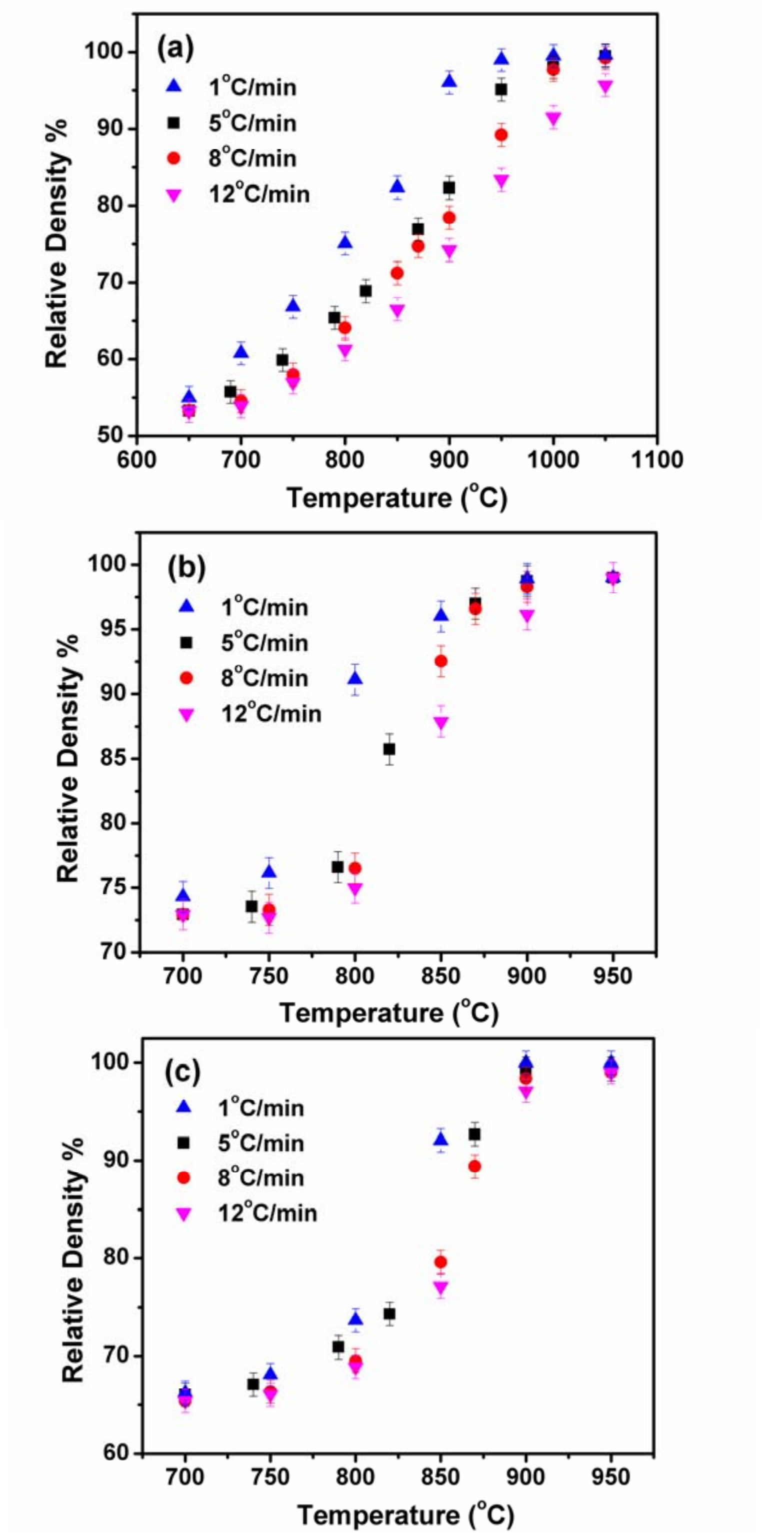

Figure 4.6 Densifications of (a) fluxed PZT-SKN, (b) HL2000, and (c) CT2000 tapes at different heating rates.

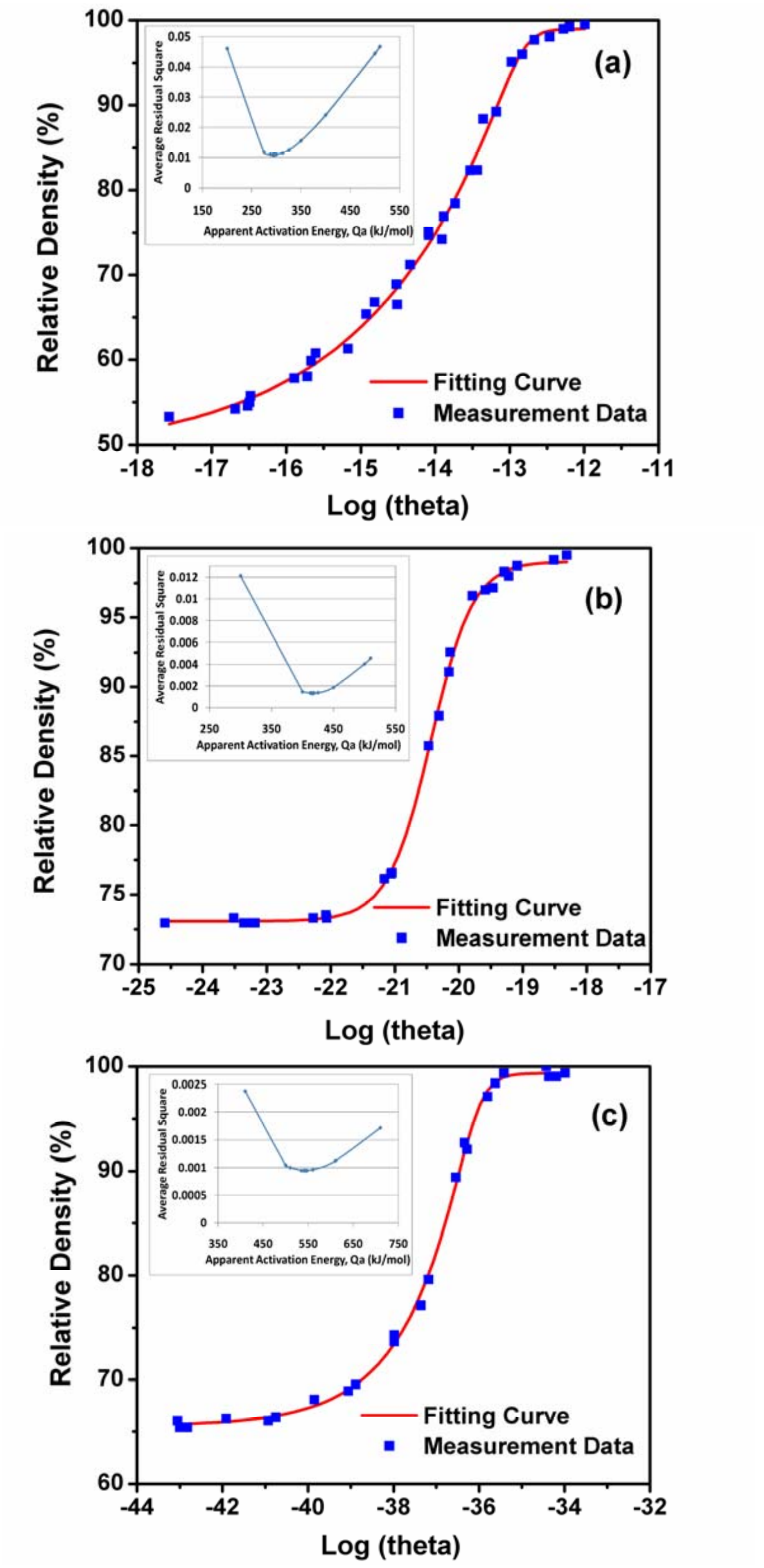

Figure 4.7 Master sintering curves of (a) fluxed PZT-SKN, (b) HL2000, and (c) CT2000 tapes based on the density data.

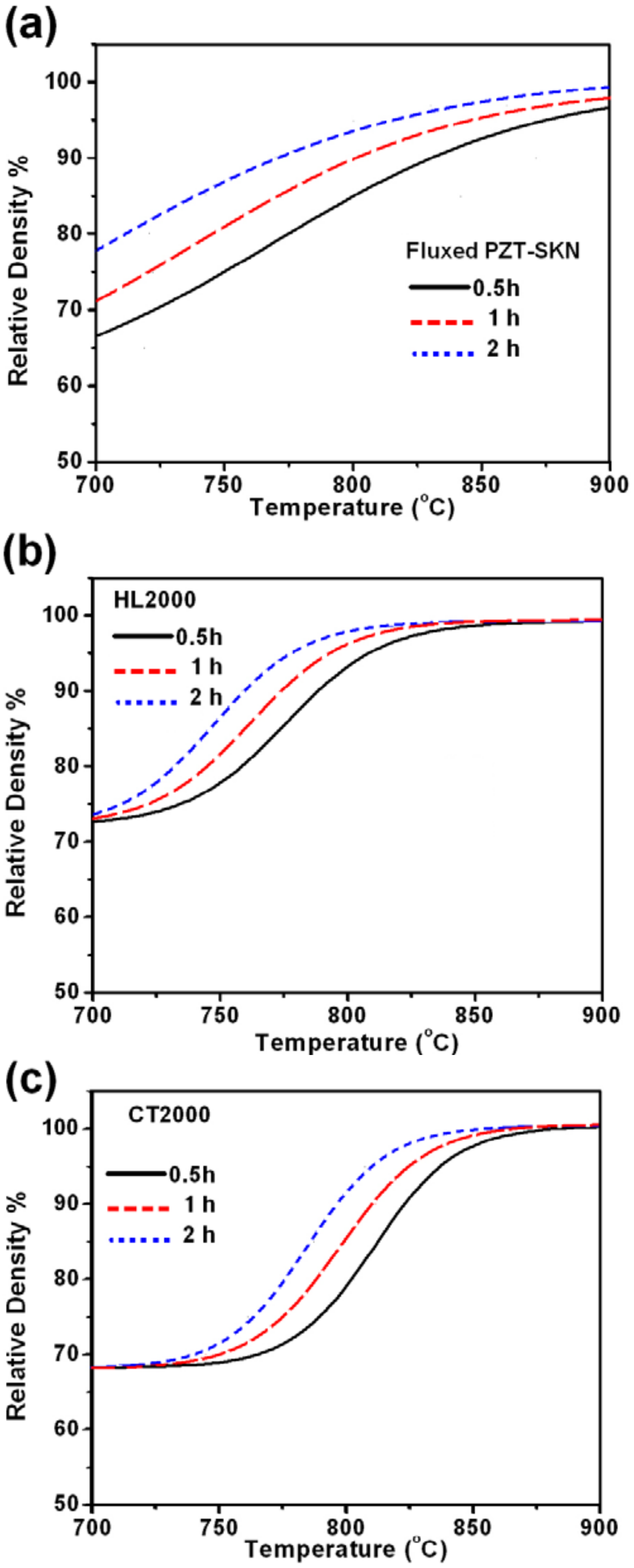

Figure 4.8 Prediction of sintering behaviors for (a) fluxed PZT-SKN, (b) HL2000, and (c) CT2000 tapes using derived MSC.

By comparison of sintering behaviors for various heating profiles based on the MSC predictions, similar densification behaviors of fluxed PZT-SKN and HL2000 tapes were founded in the temperature range of 780°-820°C using an optimized firing profile, as shown in Figure 4.9. The resulting optimized co-firing profile is divided into four steps in a continuous heating process: first, the multilayer structure was heated from room temperature to 450°C at a slow ramp rate of 1°C/min; next, the temperature was held at 450°C for 1 h to allow for complete organic binder burnout; and finally, the second ramping process at the rate of ~ 3°C/min to the peak temperature (870°-900°C) was conducted followed by soaking for 0.5-1 h.

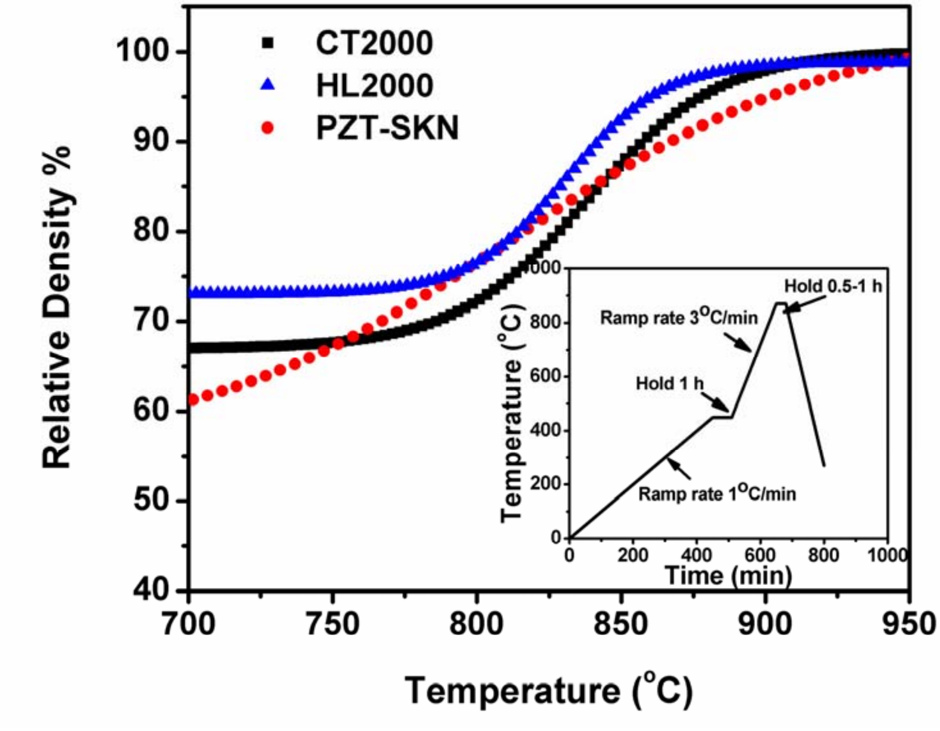

Figure 4.9 Optimized densification behaviors of fluxed PZT-SKN and LTCC tapes obtained from MSC fitting equations, using the inset firing profile.

4. 5. 2 Microstructure and chemical composition analysis

The test structure used to fabricate hybrid LTCC/PZT-SKN multilayer samples is shown in Figure 4.10(a). The middle piezoelectric PZT-SKN layer with two additional patterned buffer layers was laminated between two stacks of LTCC green tapes having round cavities. LTCC/PZT-SKN laminates with different dimensions were prepared in the following tape length/cavity diameter (mm) combinations: 10/6.5, 15/10, and 20/15. All multilayer stacks were sintered at 870°C for 1 h using the optimized co-firing profile. The resulting HL2000/PZT-SKN co-fired ceramics did not exhibit any visible camber, delamination, or cracking following sintering. However, significant camber and minor delamination were observed after co-firing CT2000/PZT-SKN multilayer ceramics when the round cavities fabricated were larger than 10 mm.

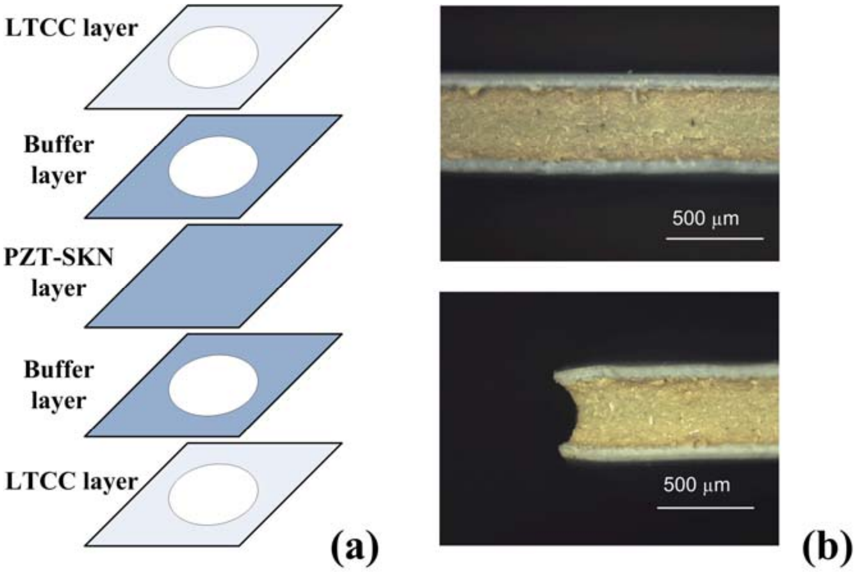

Figure 4.10   Co-firing structure of LTCC/PZT-SKN multilayer ceramics. (a) schematic illustration and (b) optical microscopic images of the cross-section.

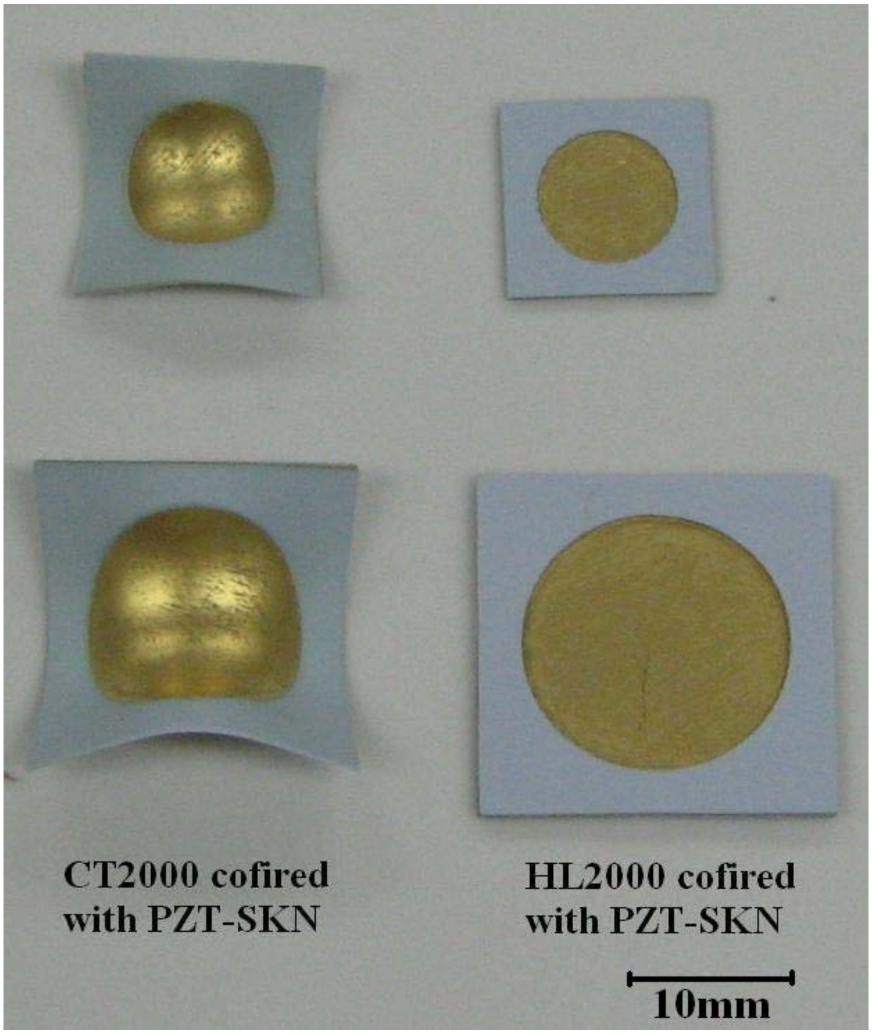

Figure 4.11 Co-fired CT2000/PZT-SKN and HL2000/PZT-SKN multilayer ceramics.

Optical microscopy images shown in Figure 4.10(b) illustrate the cross-section of co-fired HL2000/PZT-SKN multilayer ceramics. A slight concave morphology is observed at the edge of the piezoelectric layer indicating non-uniform shrinkage in the *x*-*y* direction caused by co-firing with self-constrained HL2000 tapes which only shrink in the *z* direction [154]. In free sintered laminates of CT2000/PZT-SKN or CT800/PZT-SKN the stresses generated due to the mismatch of shrinkage rate along *x*-*y* direction at heating process cause significant camber and delamination, as shown in Figure 4.11. The shear and in-plane tensile stresses developed during co-firing are relaxed from the heterogeneous interface to the middle of the PZT-SKN layer in HL2000/PZT-SKN laminates [319]. Therefore, the self-constrained HL2000 tapes minimize shrinkage variations in *x-y* direction and eliminate camber development for HL2000/PZT-SKN multilayer structures.

SEM micrographs on polished cross-sections of HL2000/PZT-SKN multilayer ceramics sintered at 870^{o}C for 1 h are shown in Figure 4.12. Figure 4.12(a) illustrates a typical interface in the co-fired HL2000/PZT-SKN structures. Porosity is observed in HL2000 layer near the interface which decreases moving towards the HL2000 surface. This observation suggests significant stress development during sintering near the HL2000/PZT-SKN heterogeneous interface. The exposed PZT-SKN area in the center of co-fired HL2000/PZT-SKN structures is shown in Figure 4.12(b). A dense and uniform piezoelectric PZT-SKN layer is obtained after co-firing with HL2000 tapes. The images of elemental mapping made on those areas are illustrated in Figure 4.13, demonstrating the elemental inter-diffusion qualitatively in the co-fired HL2000/PZT-SKN multilayer ceramics. The diffusion of Pb into LTCC layer in a limited distance (~20 μm) near the LTCC/PZT-SKN interface is clearly shown in Figure 4.13(a). The diffusion of Al, Ca, and Si from LTCC to PZT-SKN layer are also observed. The elemental mapping result shown in Figure 4.13(b) demonstrates that the diffusion of Al, Ca, and Si near the center of piezoelectric layer is less than that around heterogeneous interface.

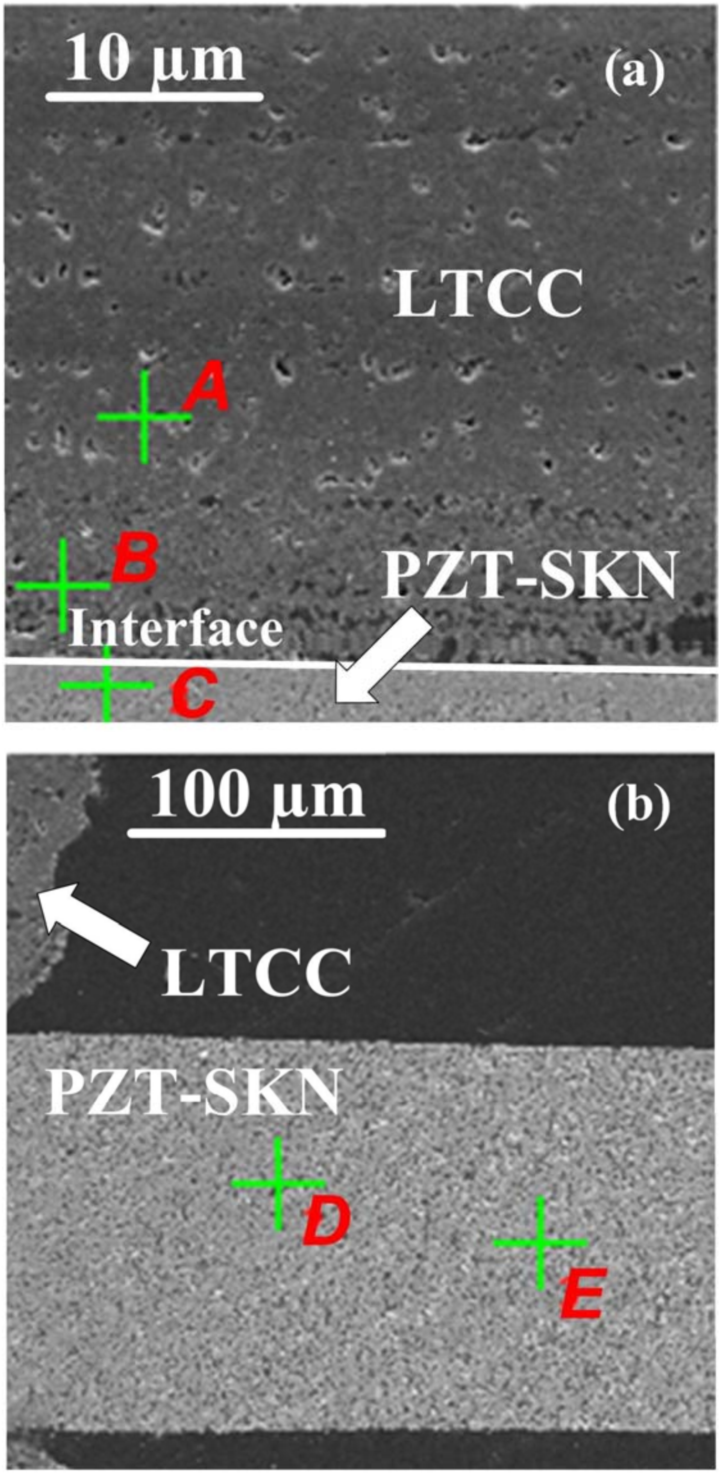

Figure 4.12 SEM micrographs of hybrid multilayer ceramics sintered at 870^{o}C for 1 h. (a) HL2000/PZT-SKN interface and (b) center of PZT-SKN layer.

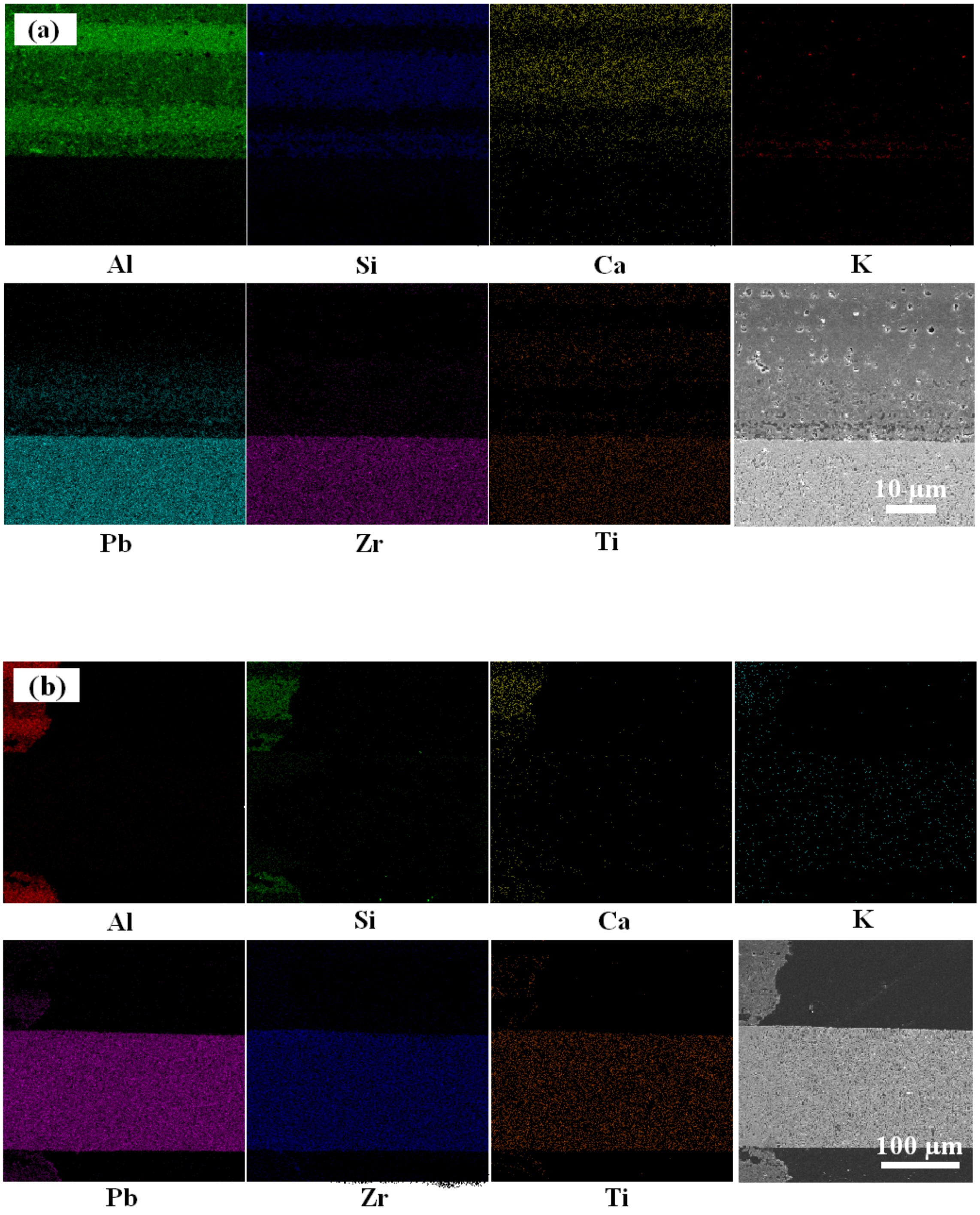

Figure 4.13 EDS mapping results of hybrid multilayer ceramics sintered at 870°C for 1 h. (a) HL2000/PZT-SKN interface and (b) center of PZT-SKN layer.

Table 4.3 EDS elemental analysis on the cross-section of LTCC/PZT-SKN multilayer ceramics. (wt%)

Composition	***A***	***B***	***C***	***D***	***E***
PbO	--	26.22	58.68	61.71	64.85
ZrO_2	--	--	20.14	18.72	19.80
TiO_2	4.72	2.03	9.55	10.93	11.70
Al_2O_3	45.60	37.47	2.76	1.66	--
SiO_2	39.30	29.55	3.48	2.75	--
CaO	10.36	4.40	1.21	--	--
Other Oxides	< 1%	< 1%	< 5%	< 5%	< 5%

The elemental compositions of different regions across the PZT-SKN/HL2000 interface are compared in Table 4.3. The elemental analysis at *A* was consistent with the pure LTCC composition mainly composed of Al_2O_3 and SiO_2 without showing any elemental diffusion from co-fired PZT-SKN layers. The pure PZT-SKN composition was detected at *E* in the piezoelectric layer near the center of multilayer structure. Inter-diffusion from across the interface between HL2000 and PZT-SKN layers was confirmed by analyzing the elemental compositions at *B* and *C*. The elemental analysis result at *B* indicates the diffusion of Pb during the co-firing process and the diffusion of Al, Si, and Ca was also determined from data collected in the PZT-SKN layer close to the interface at *C*. A small amount of Al_2O_3 and SiO_2 was observed at *D* in the piezoelectric layer near the edge of multilayer structure. However, the diffusion was minimal processing along the radial direction. The diffusion of Pb from PZT-SKN to HL2000 layer was visible by the Z-contrast image obtained using the backscattered electron detector, as shown in Figure 4.14. A lighter-colored layer was observed at the HL2000 side next to the interface, which demonstrated the occurrence of Pb diffusion because the backscattered electrons induced from heavy element (*e.g.* Pb) are stronger than those from light elements (*e.g.* Al, Si, and Ca).

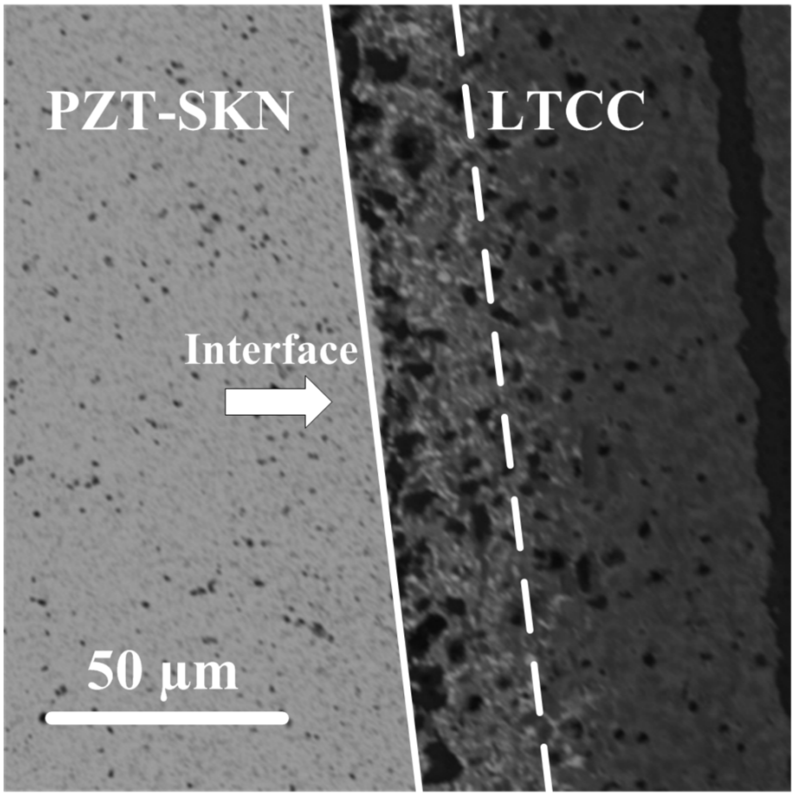

Figure 4.14 Backscattered electron image showing the Z-contrast of the interface in the hybrid HL2000/PZT-SKN multilayer ceramics sintered at 870°C for 1 h.

4. 5. 3 Dielectric and piezoelectric properties

The experimental results presented in chapter 3 indicated that the 1 wt% $LiBiO_2$ + 1 wt% CuO fluxed PZT-SKN ceramics sintered at 900°C for 1 h exhibit the optimum dielectric and piezoelectric properties; while the recommended firing condition for

HL2000 tapes is at 870°C and holding for 0.5 h to maintain the flat and complete structure after firing. In order to obtain the desirable piezoelectric properties and better multilayer structural integrity, a further investigation on sintering conditions for HL2000/PZT-SKN multilayer ceramics is desired to conciliate the discrepancies of peak sintering temperature and soaking time between LTCC and PZT-SKN materials using the co-firing profile suggested by the MSC analysis result. The typical dielectric and piezoelectric properties of PZT-SKN/HL2000 laminates sintered under different conditions are summarized in Table 4.4.

Table 4.4 Properties of co-fired HL2000/PZT-SKN multilayer ceramics under different sintering conditions.

Sintering conditions	ε_r	**tan**δ	d_{33}^{low} **(pm/V)**	d_{33}^{high} **(pm/V)**	E_c **(kV/cm)**	P_r **(C/m^2)**
870°C, 0.5 h	1030	0.015	216	298	11.7	0.12
890°C, 0.5 h	1100	0.020	237	316	12.3	0.15
900°C, 0.5 h	1200	0.017	255	356	12.5	0.18
870°C, 1 h	1205	0.022	240	345	12.0	0.15
890°C, 1 h	1145	0.020	235	325	12.1	0.16

The dielectric constant ε_r and piezoelectric coefficient d_{33} increase as the sintering temperature increases from 870° to 900°C when sintering time is controlled in 0.5 h at peak temperature. The contrary result was observed when test multilayer ceramics were sintered at peak temperature for 1 h. The remnant polarization P_r and coercive field E_c increase as the sintering temperature increases for both soaking periods. However, delamination and cracking were observed in some of the PZT-SKN/HL2000 laminates sintered at 900°C for 1 h. These defects may be attributed to the elevated sintering temperature with a longer soaking time which causes the additional stress in the multilayer structures. The fluxed PZT-SKN tapes laminated with HL2000 were sintered under pressure which also affects the densification of PZT-SKN layers. The HL2000/PZT-SKN multilayer ceramics sintered at 900°C for 0.5 h exhibit favorable properties with high field d_{33} piezoelectric coefficient of 356 pm/V and dielectric constant ε_r of 1200.

Table 4.5 Dielectric and piezoelectric properties of fluxed PZT-SKN thick films co-fired with different LTCC materials.

LTCC materials	$\boldsymbol{\varepsilon_r}$	**tan$\boldsymbol{\delta}$**	$\boldsymbol{d_{33}^{\text{low}}}$ **(pm/V)**	$\boldsymbol{d_{33}^{\text{high}}}$ **(pm/V)**	$\boldsymbol{E_c}$ **(kV/cm)**	$\boldsymbol{P_r}$ **(C/m^2)**
HL2000	1205	0.022	240	345	12.0	0.15
CT2000	1150	0.022	228	326	11.7	0.15
CT800	1132	0.020	235	335	11.8	0.14
PZT-SKN*	1270	0.018	313	450	12.5	0.28

* Fluxed PZT-SKN tapes were sintered at 900°C for 1 h.

The PZT-SKN layers co-fired with other LTCC materials may exhibit different properties compared with those co-fired with HL2000 tapes because the different sintering behaviors of LTCC layers have distinctive influence on the densification and the resulting properties of piezoelectric layers. The measured dielectric and piezoelectric properties of fluxed PZT-SKN thick films co-fired with different LTCC tapes at 870°C for 1 h are summarized in Table 4.5. The test structures were 10 mm on each side with a 6.5 mm diameter cavity defining the active region. The PZT-SKN/HL2000 samples co-fired with gold electrodes exhibited the dielectric constant ε_r of 1205 and low field d_{33} piezoelectric coefficient of 240 pm/V which demonstrated the highest values among all the multilayer structures examined. Compared with the stand-alone fluxed PZT-SKN tapes (low field d_{33} of 313 pm/V) fired using optimal sintering conditions (900°C for 1 h), the d_{33} piezoelectric coefficient of PZT-SKN layer co-fired with LTCC tapes is only moderately reduced. Based on similar dielectric properties and Curie temperature T_c between co-fired and stand alone materials this observed reduction can be largely attributed to the mechanical clamping effect by the inactive LTCC substrates. Further, compared with the other reported dielectric and piezoelectric properties of PZT-based thick films fired on LTCC substrates [147,149-151], the properties of currently developed PZT-SKN thick films co-fired with LTCC structures are significantly improved, indicating the possibility to be used for the device fabrication.

4. 5. 4 A demonstration of applications: microbalance

In order to demonstrate the utility of the developed co-fired LTCC/PZT-SKN system a resonant radial mode piezoelectric microbalance has been fabricated and characterized. Figure 4.15 depicts the cross-section of the co-fired multilayer microbalance structure. The resonant frequency shift with different mass loadings is used to characterize the performance of this resonant mass sensor. As shown in Figure 4.16, the resonant frequencies decrease linearly due to the additional mass loadings as the droplets are deposited on the top electrode surface.

The mass sensitivity can be defined as the ratio of the resonant frequency shift $\delta\omega_o$ to the accreted mass δM, where δM is proportional to the effective mass M_{eff} of the resonator [320]:

$$\delta M \approx -2\frac{M_{\mathrm{eff}}}{\omega_0}\delta\omega_0$$

The measured mass sensitivity of 15 kHz/mg was calculated as the inverse of the slope of the linear fit to the experimental data. A common approach to improve the mass sensitivity for the resonator is to reduce M_{eff} by making the device less massive [321].

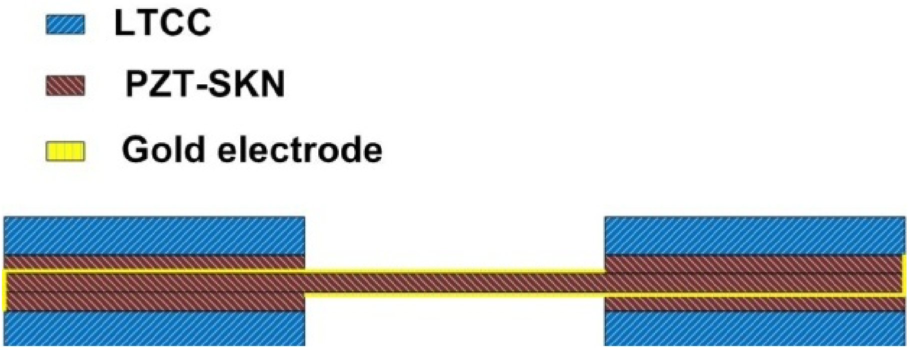

Figure 4.15 Schematic illustration of cross-section of co-fired multilayer ceramics for microbalance.

A preliminary simulation was conducted in order to study the effects of the geometry of piezoelectric PZT-SKN layers on the mass sensitivity using finite element modeling (FEM). The simulation results plotted in Figure 4.17 indicate that the thinner piezoelectric layer with a smaller diameter for the fixed diameter/thickness aspect ratio offers the higher sensitivity of mass detection, which is in agreement with the theoretical analysis. Also, operating this multilayer ceramic device at the higher order resonant modes would provide better mass sensitivities. The proposed method for improving mass sensitivity will require further miniaturization of this multilayer structure through additional fabrication process optimization. However, these results demonstrate the capability to integrate PZT-SKN ceramics into LTCC-based MEMS structures using commercially available materials and fabrication methods.

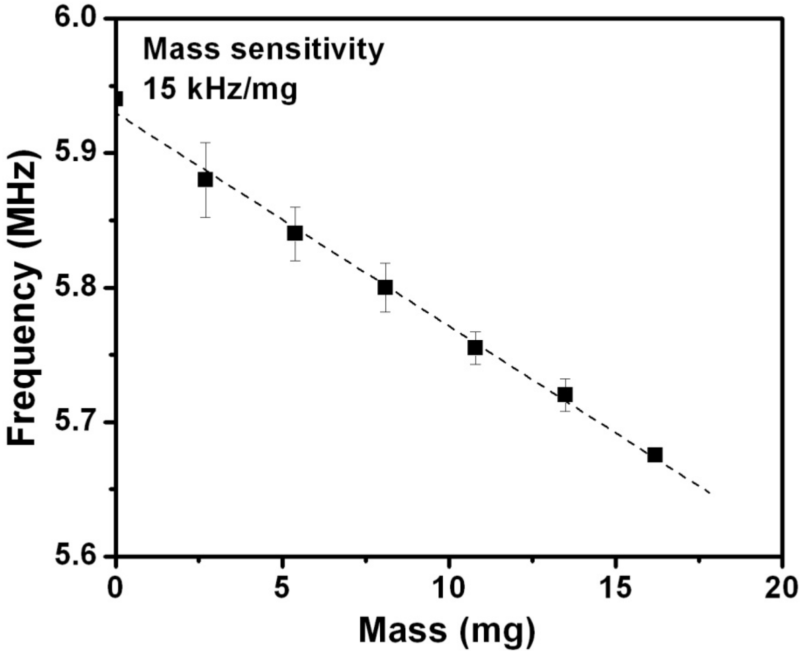

Figure 4.16 Resonant frequency shift as a function of the mass loading with linear fitting.

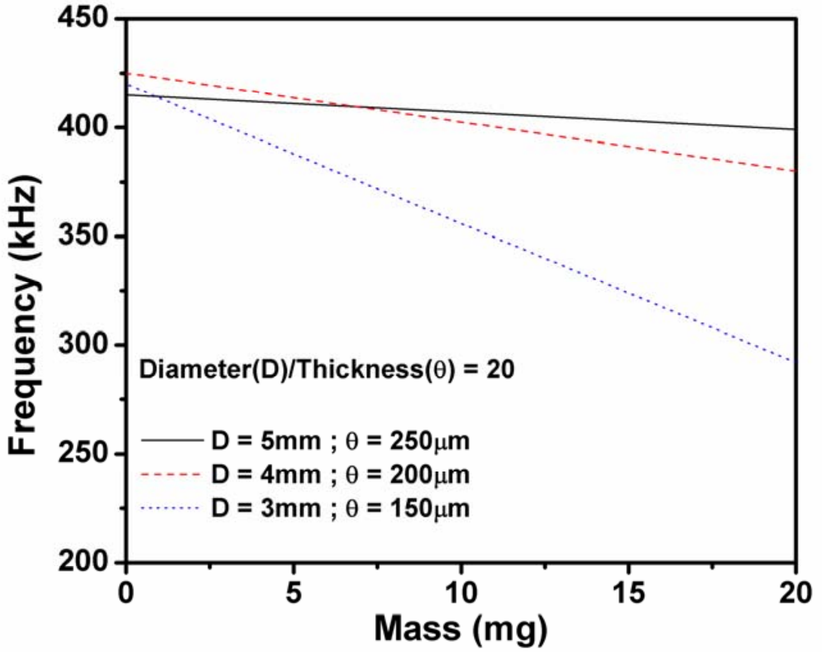

Figure 4.17 FEM simulation result of geometrical effect of piezoelectric layers on the mass sensitivity.

4. 6 Conclusions

In summary, a co-fired LTCC/PZT-SKN multilayer ceramic system for the fabrication of thick-film MEMS structures has been successfully developed and demonstrated. Master sintering curves (MSC) were constructed to understand the sintering mechanisms and investigate the sintering behaviors for the low fire PZT and LTCC materials. Dissimilar apparent activation energies obtained from the MSC models indicated different sintering mechanisms dominate the sintering behaviors in the various materials. Viscous flow controlled sintering is the dominant mechanism for LTCC materials while liquid phase sintering controls the fluxed PZT-SKN ceramics. The accurate prediction of densification behaviors using MSC analysis can significantly improve the development of hybrid LTCC/PZT-SKN multilayer ceramics and enable the co-firing process optimization. Using the optimized co-firing profile predicted by MSC, it was found that fluxed PZT-SKN ceramics co-fired with HL2000 tapes demonstrate the best sinterability without showing any defects, such as deformation, delamination, or cracking. The optimum electromechanical properties with high field d_{33} piezoelectric coefficient of 356 pm/V and dielectric constant ε_r of 1200 were obtained when the HL2000/PZT-SKN laminates were sintered at 900°C for 0.5 h. EDS and electron microprobe analysis revealed the inter-diffusion of Pb from PZT-SKN layers into LTCC layer in a limited length and the appearance of Al, Ca, and Si in the PZT-SKN layer near the LTCC/PZT-SKN interface. Further, elemental inter-diffusion was not detected at the center of piezoelectric layer in co-fired LTCC/PZT-SKN multilayer ceramics and no subsequent reduction in d_{33} piezoelectric coefficient was observed. Finally, a piezoelectric microbalance with a mass sensitivity of 15 kHz/mg was fabricated, demonstrating the feasibility of the current materials and processing methods for multilayer ceramic based micro-electromechanical device fabrication.

Chapter 5. Development and optimization of multilayered LTCC/PZT-SKN piezoelectric micropumps for LTCC-based microfluidic systems

5. 1 Introduction

Micropumps providing efficient fluid control and delivery are essential components in lab-on-chip (LOC) microfluidic systems. Compact integrated pumping solutions remain a key challenge in microsystems developed for clinical and environmental analysis which require prompt processing of samples [322]. The development of a chip- or package-level micropump with the capability of being easily integrated into a microfluidic LOC platform would be highly desirable. Low temperature co-fired ceramic (LTCC) materials offer a promising alternative to silicon, glass, and polymeric substrates for the fabrication of highly integrated microfluidic devices and microsystems in a multilayer ceramic module [32]. A number of LTCC microfluidic devices incorporating diverse functional elements have been successfully fabricated and reported [68,78,266-267]. As discussed in chapters 3 and 4, the realization of co-firable piezoelectric ceramics and the compatible processing methods for incorporating LTCC with low firing temperature PZT-SKN materials allows direct integration of high density electromechanical elements including actuators, fluidic networks, and electronic interconnects [269,270].

The current chapter describes the design, fabrication, and characterization of a LTCC/PZT-SKN multilayer piezoelectric peristaltic micropump implemented using the previously developed methods. Standard LTCC thick film processing methods were applied to design and fabricate the multilayer micropumps, allowing rapid development times and highly scalable production capabilities. Peristaltic pumping was achieved using 3 pairs of piezoelectric bimorph diaphragm actuators. Phase-shifted electrical signals generate a peristaltic pumping motion and enable completely reversible fluid flow. Finite element modeling (FEM) was conducting to simulate and optimize the deflection of piezoelectric bimorph actuators. Further optimization of pumping performance has been studied using modified microchannel geometries. As LTCC materials and technology have already been utilized to fabricate other microdevices (*e.g.* microvalves, flow sensors, and chemical detectors), the current demonstration of an LTCC-process compatible micropump promises the ability to commercialize highly multifunctional integrated LTCC-based microfluidic systems.

5. 2 Design and fabrication of micropumps

5. 2. 1 LTCC and PZT-SKN tapes

Heralock® HL2000 green tapes, which provide a sintering shrinkage in the *x*-*y* direction of less than 0.2%, were used as LTCC layers in the multilayer ceramic micropumps. Low-temperature sinterable piezoelectric ceramics with the composition of $0.98Pb(Zr_{0.53}, Ti_{0.47})O_3$-$0.02Sr(K_{0.25}, Nb_{0.75})O_3$ + 1 wt% $LiBiO_2$ + 1 wt% CuO were prepared using a solid state route, as introduced in chapter 3. PZT-SKN tapes were fabricated by tape casting from a slip consisting of fluxed PZT-SKN powders and a PVB-based binder vehicle, as described in chapter 4. Cast tapes of 120-130 μm thickness were used as piezoelectric layers. The raw materials used for PZT-SKN tape preparation, commercially available LTCC tapes, and conductor inks used in the fabrication of LTCC/PZT-SKN multilayer micropumps are summarized in Table 5.1.

Table 5.1 Materials used in the fabrication of PZT-SKN/LTCC multilayer micropump.

Functional materials	**Composition/Brand**	**Suppliers**
PZT-SKN powder	$PbCO_3$	Halstab
	TiO_2	Ishihara
	$SrCO_3$, K_2CO_3, Li_2CO_3	Sigma Aldrich
	Nb_2O_5	H.C. Stark
	CuO, ZrO_2	Alfa Aesar
Organic binder vehicle	Xylene, Ethyl alcohol	Fisher Chemical
	Polyvinyl butyral (PVB), Menhaden fish oil, Polyalkylene glycol (PEG), Butyl benzyl phalate (BBP)	Richard E. Mistler
LTCC tape	HeraLock^{TM} Tape HL2000	Heraeus
Conductor paste	TC8101 co-firing gold ink	Heraeus

5. 2. 2 Piezoelectric bimorph actuator

A bimorph piezoelectric actuator geometry was selected for use in the peristaltic micropump. The bimorph design, made possible by the multilayer LTCC/PZT-SKN co-firing process developed, utilizes two active piezoelectric layers driven in opposition to each other. This results in amplified actuator deflection and increase pump displacement relative to typical unimorph actuated pump designs. Figure 5.1(a) shows the configuration of the piezoelectric bimorph utilized in the current work. In this design, one piezoelectric layer's positive electrode is connected with the other layer's negative electrode (where the negative and positive orientations refer to the directions in which the piezoelectric layers were poled). When an alternating voltage is applied, one piezoelectric layer will contract while the other will expand, resulting in a vibrating motion normally many times greater than the length or thickness change of a single layer [323,324].

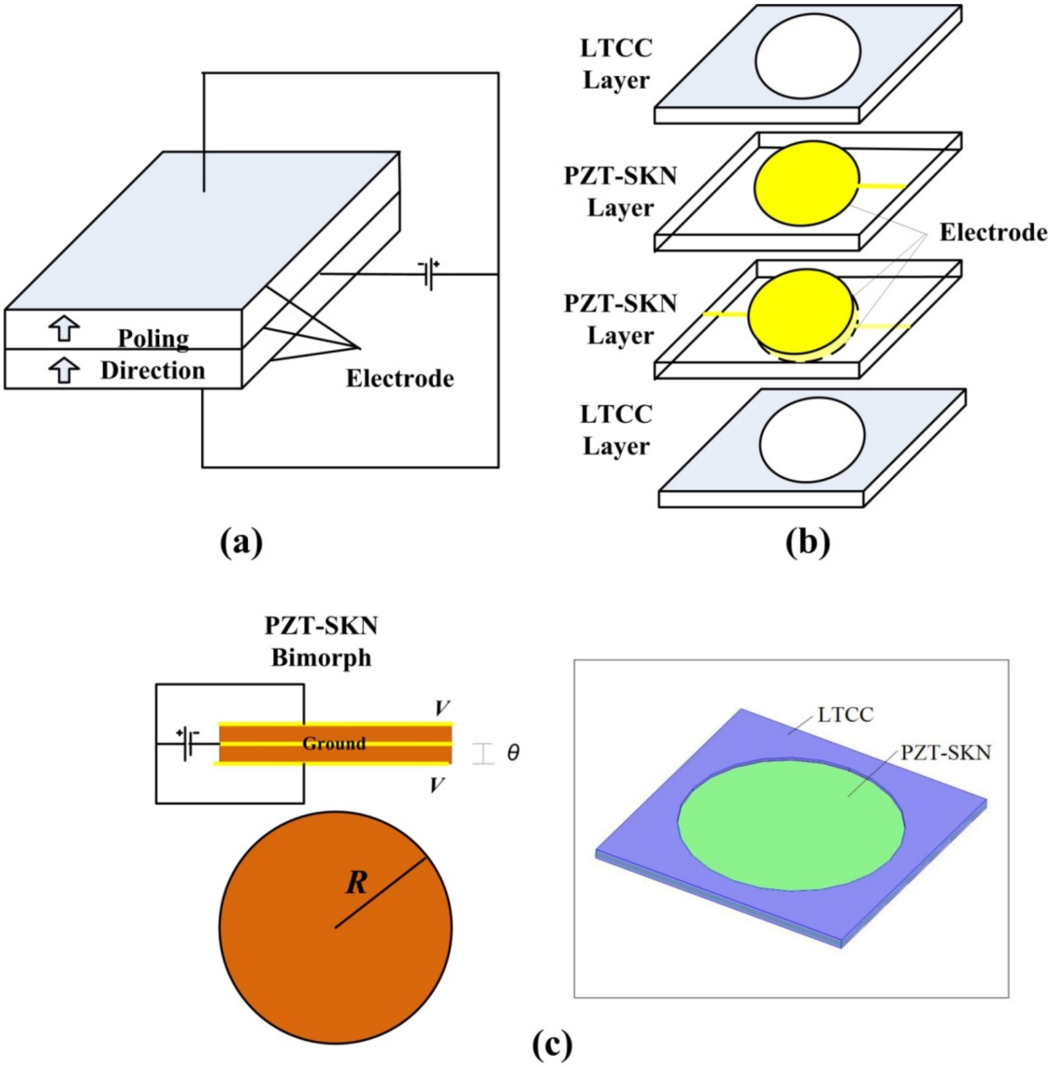

Figure 5.1 Bimorph actuator for the multilayer peristaltic micropump. (a) typical configuration, (b) multilayer structure, and (c) FEM model.

For the initial prototype designs, the bimorph elements were made of two PZT-SKN tapes laminated together with the HL2000 tapes as structural support elements, as shown in Figure 5.1(b). The total device size was 15 mm × 15 mm square by 1.2 mm thick (~0.3 cm^3). The round cavity (10mm diameter) in the HL2000 layers defines the actuator size. Corresponding 10 mm gold electrodes were printed on the center of PZT-SKN tapes. Additional conductor lines were printed to extend the electrical connections to the edge of the multilayer device. The laminated HL2000/PZT-SKN multilayers were co-fired using the previously optimized sintering profile. A finite element modeling (FEM) simulation constructed using COMSOL Multiphysics® 3.5 package was used to predict and optimize actuator performance. Figure 5.1(c) illustrates the schematic design and adjustable parameters utilized in the FEM model, where R is the diaphragm radius and θ is the thickness of single-layer of the PZT-SKN tape. Clamped boundary conditions were applied at the circumference of the bimorph layers, corresponding to complete clamping of the active layers by the inactive LTCC substrate.

5. 2. 3 Multilayer design and fabrication of piezoelectric micropump

The multilayer structure of designed piezoelectric micropump consists of five distinct layers, as illustrated in Figure 5.2. The top and bottom support layers and the intermediate layer defining the fluidic network (including inlet/outlet ports, microchannels, interconnects, flow rectification elements, and pump chambers) were patterned from HL2000 tapes. Each of the two active piezoelectric bimorph layers consist of two layers of low firing temperature PZT-SKN tapes, screen printed gold electrodes, defining the active pumping regions, and additional required electrical interconnects. The resulting pumping actuators are sandwiched between the structural LTCC layers, as illustrated. The assembled pump has three pumping chambers connected in series, with each chamber driven by two of the bimorph actuators located on the top and one on the bottom. This design doubles the stroke volume without increasing supply voltage requirement nor adding significant complexity to the design, fabrication, and assembly process. This ability to readily create stacked integrated structures exhibits one of the unique capabilities of the LTCC multilayer processing methodology.

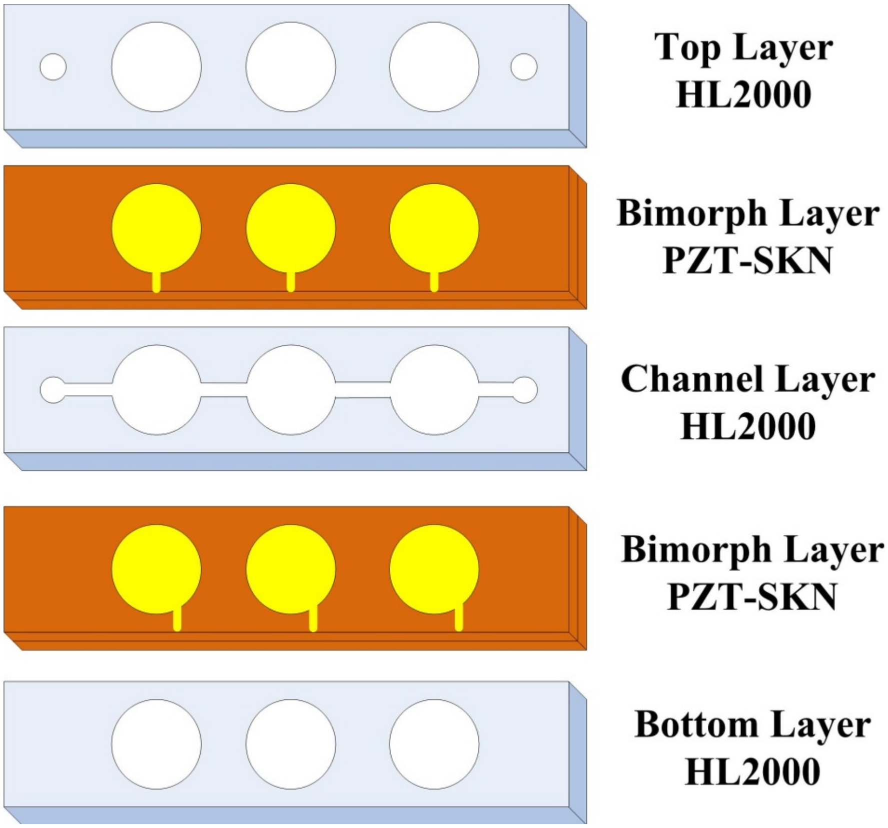

Figure 5.2 Multilayer design of the piezoelectric peristaltic micropump.

The individual pump layers were patterned using a combination of laser ablation and screen printing. The top, intermediate, and bottom structural layers were made from three-layer HL2000 green tape stacks. A CO_2-laser system (VLS 3.50, Universal Laser

Systems Inc., Scottsdale, AZ) was used to ablate the design features in the green tapes. Three round pump chambers (diameter: 10 mm) connected by microchannels (width: 0.6 mm) were cut on the intermediate layer while the three corresponding cavities within the same geometry as the pump chamber were patterned on both top and bottom layers. The small inlet/outlet holes were made on the top layer. The piezoelectric bimorph layers were prepared by pre-laminating two PZT-SKN tapes with round electrodes (diameter: 10 mm) and electrical interconnects (width: 0.5 mm). Electrode patterns were screen printed on PZT-SKN layer using co-firable gold ink (TC8101, Heraeus Thick Film Materials Division, West Conshohocken, PA). All individual patterned layers were aligned, stacked, and laminated at ~5 MPa and room temperature. A final high temperature co-firing treatment (870^{o}C for 1 h) was conducted to yield a monolithic sintered ceramic device. The overall size of the micropump package is about 60 mm × 15 mm × 1.2 mm (~1 cm^3).

The co-fired micropump was assembled for pumping tests by the following steps. First, the piezoelectric bimorph actuators were poled in a silicon oil bath. Plastic fluidic connectors and electric leads attached to the micropump body using fast-dry epoxy (E1009, Elmer’s Product Inc., Columbus, OH) and conductive silver epoxy (CW2400, ITW Chemtronics, Kennesaw, GA), respectively. The capacitance and dielectric loss each of the three sets of bimorph actuators were measured using a precision LCR meter (E4980A, Agilent, Santa Clara, CA) to ensure the proper connection and function. Pictures of the co-fired multilayer ceramic micropump body as assembled for pumping test are shown in Figure 5.3.

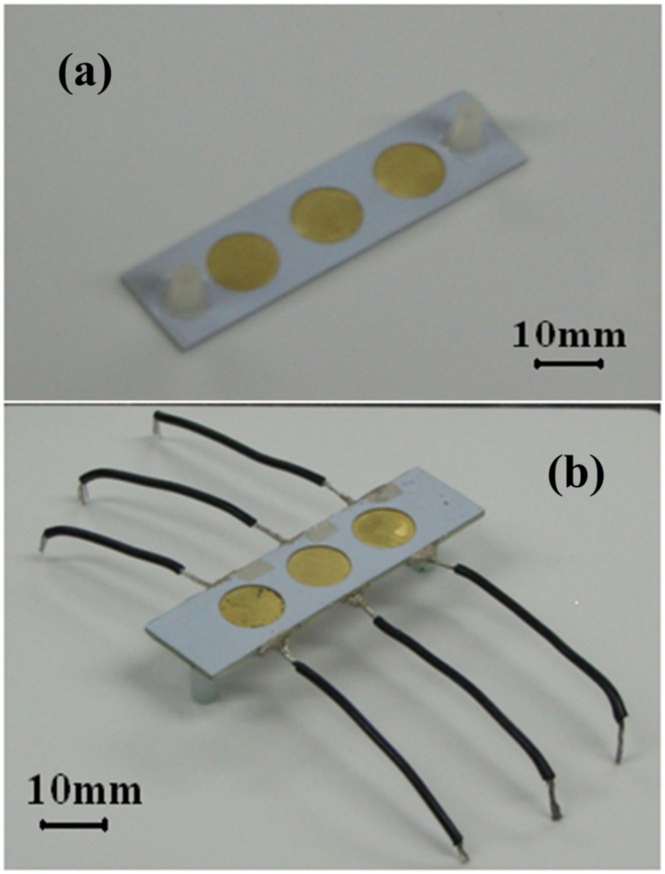

Figure 5.3 Picture of the fabricated micropump. (a) micropump body and (b) assembly for pumping test.

5. 2. 4 Micropump optimization

The velocity field of pressure driven flow through a microchannel is directly related to the geometry of the channel. Diffuser/nozzle fluidic rectifiers were added into the fluid interconnects, in an attempt to enhance the pumping performance at the expense of bidirectional fluid flow. Diffuser elements replaced straight microchannels connected to pump chambers, as shown in Figure 5.4. The entrance (W_1) and exit (W_2) width of diffuser were 200 µm and 750 µm, respectively. The opening angle θ was 8^o and the diffuser length L was 5 mm. In a subsequent investigation four distinct micropumps were fabricated with different microchannel aspect ratios by varying channel widths (*W*) at fixed channel height (*H*). The microchannel of initial micropump had a rectangular cross-section of 600 µm (*W*) × 300 µm (*H*). Three other pumps with a channel width of 300, 750, and 900 µm were fabricated to investigate the effect of changing microchannel aspect ratio (*W*/*H*) on the pumping performance.

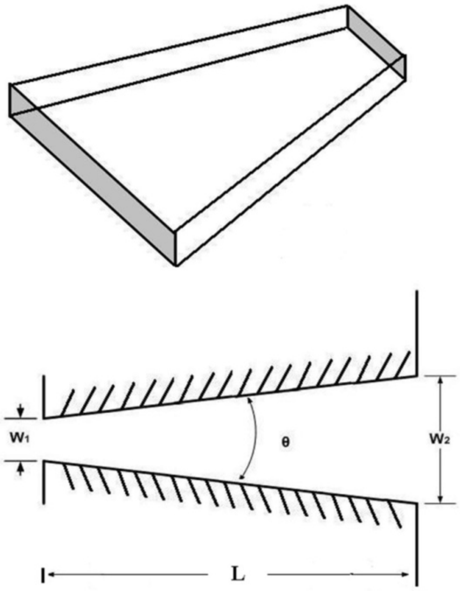

Figure 5.4 Geometry of planar diffuser element.

5. 3 Experimental setup

A schematic drawing of the experimental setup for the characterization of pumping performance is shown in Figure 5.5. The three phase shifted frequency matched drive signals were generated by a computerized DAQ board (USB-6259, National Instruments, Austin, TX) using LabVIEW^{TM} software. The sinusoidal output signals were routed through high speed amplifiers (4005 Type, NF Electronic Instruments, Yokohama, Japan) to achieve the required drive voltage. An initial phase shift of 120^o between each successive pair of actuators was used to create a traveling pressure wave to drive fluid flow. Changing the sign of the phase shift between the individual pumps cavities allows bidirectional pumping to be achieved (phase difference of 90^o and 60^o were also studied). Flow rates were measured as a function of operating frequency (50-200 Hz), backpressure (0-1.5 kPa), and driving voltage (50-100 V_{pp}). Colored DI water was used as the working fluid. The volumetric flow rate was calculated from linear velocity of the water column in the outlet tubing. The backpressure was adjusted by changing the height of inlet reservoir. Pictures of the working micropump, fluidic components, and electronic control system are provided in Figure 5.6

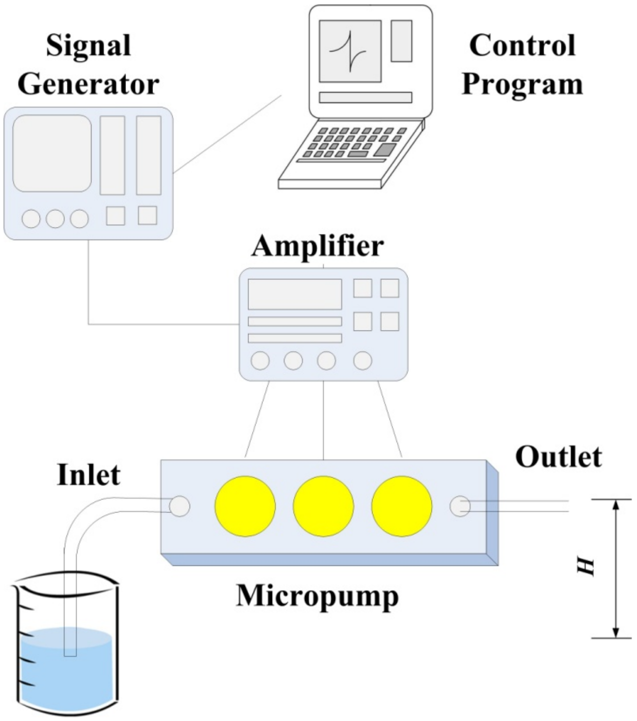

Figure 5.5 Schematic illustration of experimental setup for pumping test.

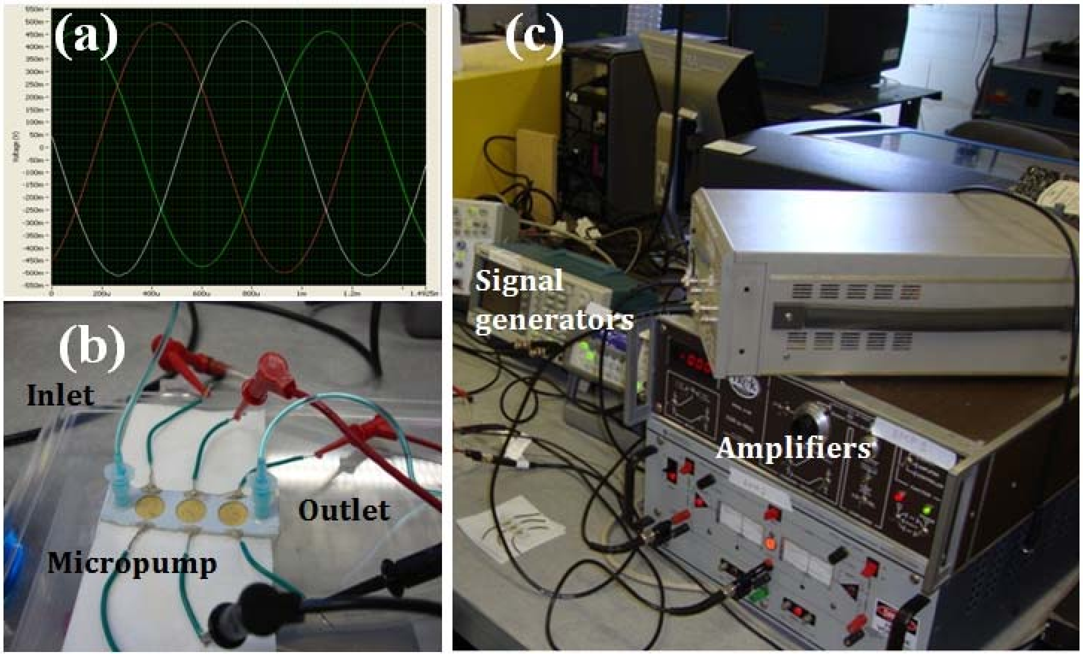

Figure 5.6 Picture of the working micropump. (a) control signal adjustment, (b) connected micropump, and (c) electronic control system.

5. 4 Results and discussion

5. 4. 1 Modeling of piezoelectric bimorph actuator

The FEM simulation of the pump membrane deflection is shown in Figure 5.7(a). The deflection profile shows the membrane displacement increases from the perimeter to the center with a roughly Gaussian profile, to a maximum displacement $d_{\max}$. The relationship between the R/θ ratio and the $d_{\max}$ for the PZT-SKN bimorph at different membrane thickness is illustrated in Figure 5.7(b). FEM results suggest an optimum R/θ ratio of about 240 for the largest membrane displacement when the bimorph is actuated at the same frequency and electric field. For estimating the volumetric flow rate based on the simulation results, it was assumed that the membrane deflection follows the deflection function of a thin circular plate [254]:

$$d\,(r) \;=\; d_{max}\,[1 - (\frac{r}{R})^2]^2$$

where r is the distance from the origin of the circular membrane. The maximum change of microchamber volume can be calculated as:

$$\Delta V \;=\; 2 \times \int_0^{2\pi}\int_0^{R} d_{max}\;[1 - (\frac{r}{R})^2]^2\; r dr d\varphi = \frac{2\pi}{3}\, d_{max}\, R^2$$

Considering a linear relationship between flow rate and pump frequency at low operating frequency range (~100 Hz) and doubling volume change to account for the two bimorph actuators for each microchamber, the estimated volumetric flow rate is:

$$Q \;=\; 2\,\Delta V f$$

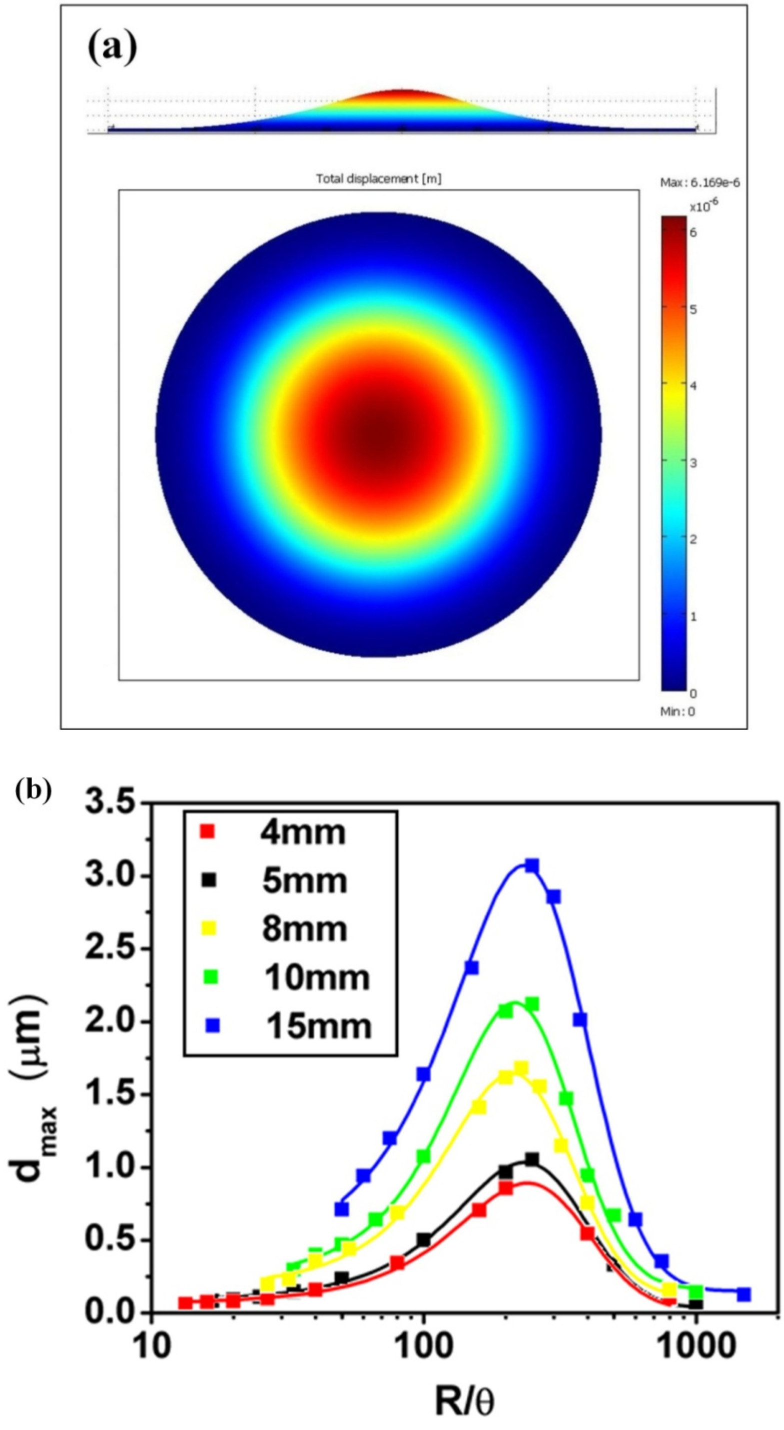

Figure 5.7 FEM simulation results. (a) visualization of bimorph membrane deflection. (displacement scaled 10^3 times for clarity) and (b) maximum displacement ($d_{\max}$) as a function of membrane radius/thickness ratio (R/θ) for different diaphragm radii.

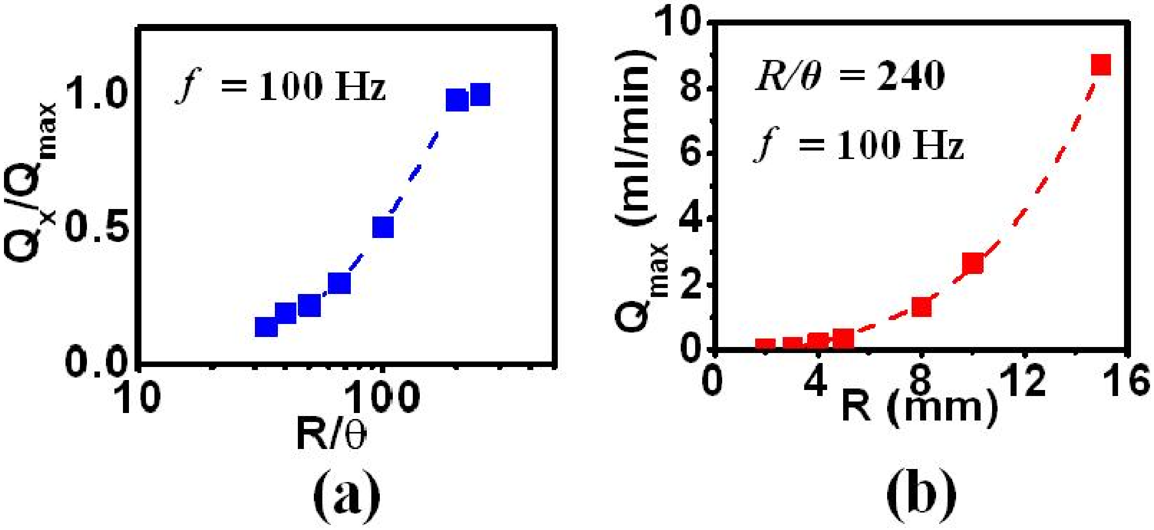

Figure 5.8 Estimation of flow rate based on the FEM simulation results. (a) normalized flow rate as a function of R/θ ratio and (b) maximum flow rate as a function of membrane size R at a constant R/θ ratio of 240.

The resulting relationship between the normalized flow rate and R/θ ratio for the LTCC/PZT-SKN micropump when driven at frequency of 100 Hz is illustrated in Figure 5.8(a). Similar to the membrane deflection simulation results, the micropump with membrane in the optimum R/θ ratio of 240 is expected to yield the maximum flow rate Q_{max}. Figure 5.8(b) plots the calculation results of the relationship between the Q_{max} and the diaphragm radius R at the optimum R/θ ratio. The Q_{max} is lower than 1 ml/min when R is smaller than 5 mm. The parabolic relationship between Q_{max} and R leads to a rapid increase in Q_{max} with increasing R. In practice, however, the aspect ratio (R/θ) of the bimorph actuator is expected to be limited by fabrication capabilities and durability concerns. Initially, a radius R of 5 mm and layer thickness θ of 100 µm (thickness after co-firing) corresponding to an R/θ of only 50 for the PZT-SKN bimorph actuators was used for micropump fabrication. This moderate aspect ratio leads to acceptable device yields for research scale testing and fabrication.

5. 4. 2 Micropump performance

Initial pumping trials are presented for a pump with a microchannel of constant rectangular cross-section (600 µm wide × 300 µm high). Table 5.2 reports the effect of varying the phase shift of the drive signals on flow rates at actuation frequencies of 50, 100, and 200 Hz. The three sets of bimorph actuators were driven at 100 V_{pp} with phase differences of 120^o, 90^o, and 60^o. The experimental results show that the pump excited by signals 120^o out of phase with one another produced higher flow rates for all examined actuation frequencies. One explanation for the flow rate trend is that the backflow from outlet to inlet increases as the phase difference decreases from 120^o to 90^o, 60^o during the actuation cycle [325]. In addition, the flow resistance working on the vibrating membranes is considered to be less when the actuators are operated at phase difference of 120^o rather than 90^o or 60^o for the peristaltic micropumps [326].

Table 5.2 Effect of phase difference on flow rate for various actuation frequencies. (unit: µl/min)

Phase Variation	50Hz	100Hz	200Hz
120^o	230	440	760
90^o	185	350	610
60^o	140	265	460

Figure 5.9 illustrates the volumetric flow rate as a function of actuation frequency when the micropump is operated at driving voltages of 50, 75, and 100 V_{pp}. At each

actuation frequency the higher driving voltage results in the higher flow rate due to the larger displacement of bimorph membranes. Pumping rate is also effectively controlled by varying the drive frequency. The flow rate increases linearly up to a frequency of 200 Hz. Pumping became unstable and air bubbles were observed inside the tubing when the actuation frequency was increased above 200 Hz. due to cavitation. The resulting air bubbles tended to accumulate at inlet/outlet connectors forming an air gap which interfered with the normal pump operation. Mechanical failure is another critical concern for the developed all ceramic micropumps. Piezoelectric bimorph membranes actuated at high-frequency AC electric field have increased occurrences of defects in the ceramic layers, including micro-scale cracks and pores [327]. Therefore, the actuation frequency is confined at 100 Hz in the following experiment in order to avoid the cavitation phenomenon and prolong the working lifetime for the developed micropump.

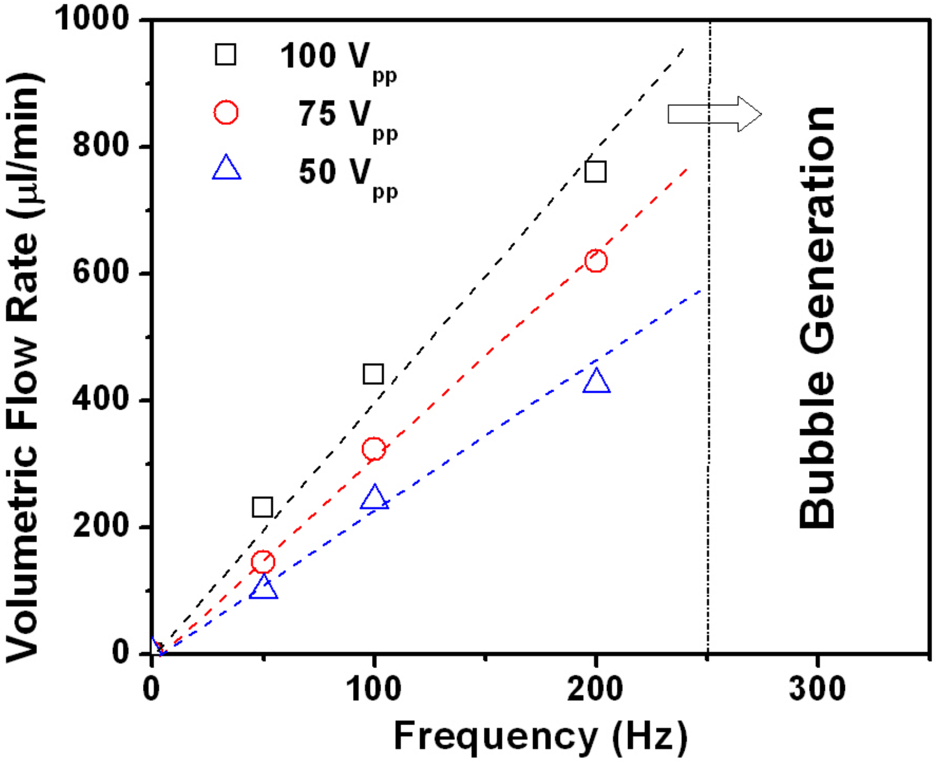

Figure 5.9 Measured variation in flow rate with actuation frequency at drive voltages of 50, 75, and 100 V_{pp}.

The maximum blocking pressure is one of the most important pumping performance parameters in terms of limiting potential application areas for a given micropump. Experimental results show that the volumetric flow rate decreases linearly with increasing backpressure, as illustrated in Figure 5.10. The flow rate-backpressure characteristics measured at different driving voltages demonstrate that the higher driving voltage results in both higher maximum flow rate (at zero backpressure) and increased blocking pressure (*i.e.* extrapolated backpressure at zero flow rate). The results indicate that the developed peristaltic micropump offers a maximum flow rate of 450 μl/min and a blocking pressure of 1.4 kPa when operated at voltage of 100 V_{pp} and frequency of 100

Hz. Subsequent studies exploring modified design parameters were conducted in order to enhance the pumping performance.

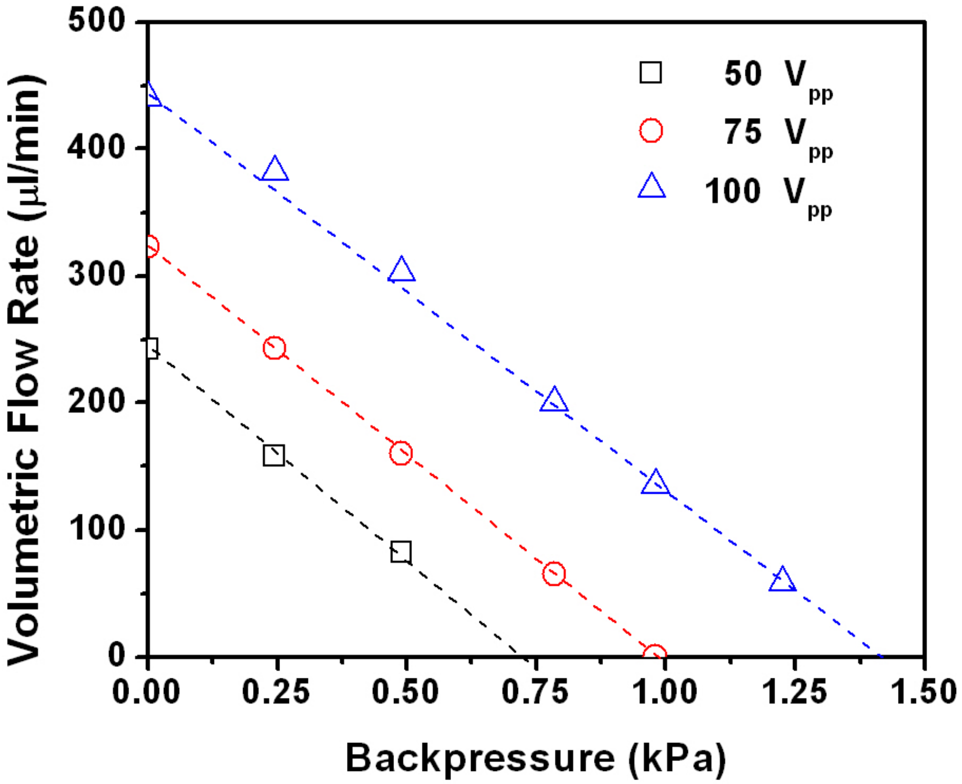

Figure 5.10 Measured flow rate versus backpressure under actuation frequency of 100 Hz with various driving voltages.

5. 4. 3 Effects of microchannel geometry

Diffuser elements

A planar diffuser element, a channel with an expanding cross-section area in the flow direction, was integrated into the micropump to replace the constant aspect ratio (W/H) rectangular-shaped microchannels. Figure 5.11 compares the measured flow rate/backpressure characteristics of a micropump with constant width microchannels and one incorporating diffuser elements. Both pumps were driven at voltage of 100 V_{pp} and frequency of 100 Hz. The straight channels in the first micropump are formed with a uniform width of 750 μm and diffuser elements in the other micropump are tapered from a width of 200 μm at the entrance to a width of 750 μm at the exit (Figure 5.5).

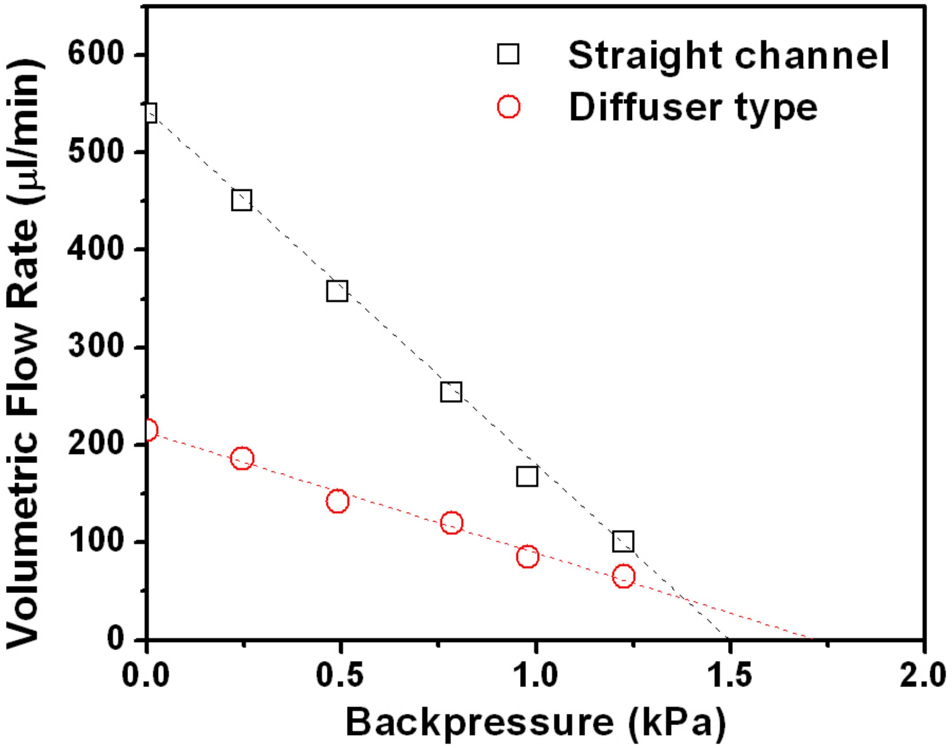

Figure 5.5 Effect of microchannel geometry on flow rate–backpressure characteristics of the micropump - planar diffuser elements.

The experimental results demonstrate that the pump with straight channels yielded a higher maximum flow rate than the pump using diffuser elements. However, flow rates of the diffuser pump showed reduced dependence on the backpressure. Consequently, the extrapolated maximum back pressure of the diffuser-type micropump is about 1.75 kPa which is significantly higher than that of straight-channel micropump. The lower maximum flow rates and higher maximum backpressure of the micropump with diffuser elements can be explained by considering the pressure drop across the diffuser element. The pressure drop ΔP in the positive diffuser direction is determined by the fluid density, flow velocity, and the pressure loss coefficient. The net maximum volumetric flow rate $Q_{\max}$ at zero backpressure can be written as [216]:

$$Q_{max} = 2\,f\,V_o \left(\frac{\eta^{\frac{1}{2}} - 1}{\eta^{\frac{1}{2}} + 1} \right)$$

where f is the actuation frequency, V_o is the stroke volume, and the diffuser element efficiency ratio η, defined as the ratio of pressure loss coefficient in the diffuser direction ξ_d to the one in the nozzle direction ξ_n, which is only determined by the diffuser geometry [328]. η ranges from 1 to 5 in common diffuser structures, making the last term $(\eta^{1/2} - 1)/(\eta^{1/2} + 1)$ of the above equation less than 1. Therefore, the maximum flow rate of diffuser type micropump is expected to be less than the pump using straight channels (where $Q_{\max}$ is estimated to be $2\,f\,V_o$). However, when integrating diffuser elements into the peristaltic micropump, an additional valving effect is added to the system which makes the flow rate is less sensitive to the backpressure. The diffuser element has the ability to increase the static pressure in the nozzle direction, which is considered to be the reason for the increase of the blocking pressure [329]. The resulting effect of adding diffuser elements into the developed peristaltic micropump is the increase of the maximum backpressure at the expense of the reduction of flow rate and the characteristic of the bidirectional flow.

Channel aspect ratio (W/H)

The microchannel geometry has a direct impact on the pressure driven liquid flow in MEMS involving fluid transport [330]. In this study, the relationship between flow rate and backpressure of the micropumps with different microchannel aspect ratios (*W*/*H*) was characterized at a driving voltage of 100 V_{pp}, as shown in Figure 5.11.

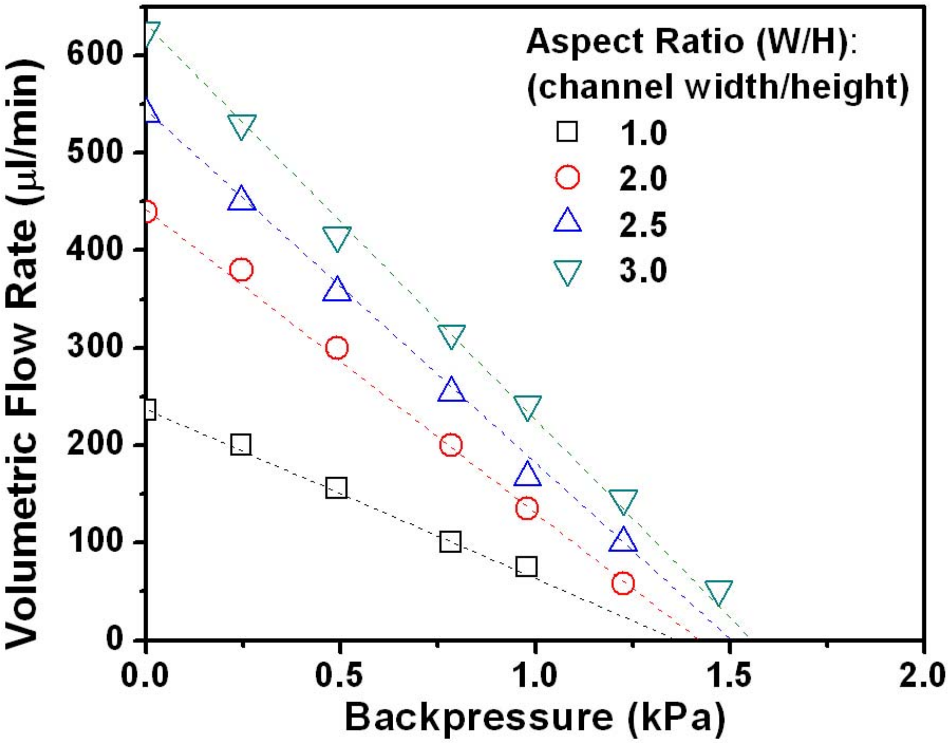

Figure 5.6 Effect of microchannel geometry on flow rate–backpressure characteristics of the micropump - straight microchannel in various aspect ratios.

It was observed that the maximum flow rate increases significantly as the microchannel aspect ratio increases while the blocking pressure is also slightly improved. Performance of the pump with aspect ratio of 3 exceeds other pumps showing a maximum flow rate of 630 μl/min with a maximum backpressure of 1.55 kPa. The experimental results can be explained by the analysis of liquid flow conditions in microchannels. The flow inside the peristaltic pump is directly related to the pressure differential generated by the vibrating motion of pump chambers. Meanwhile, the surface forces working on the boundary between channel walls and fluids are important in microchannel flow due to the large surface-to-volume ratio [331]. The relationship between pressure difference ΔP and volumetric flow rate Q can be expressed in the following formula [190]:

$$\frac{\Delta P}{Q} = \frac{C_{fr}\, L\mu}{2AD_h^2}$$

where C_{fr} is the friction coefficient which only depends on the channel shape, L is the length of the channel, μ is the viscosity of the fluid, A is the cross-sectional area of the channel, and D_h is the hydraulic diameter. In our experiment the pressure difference is considered to be constant when the bimorph actuators are actuated on the same conditions because the same stroke volume is generated in each pump chamber. Therefore, the difference of volumetric flow rate is dependent on the cross-sectional area of the channel and hydraulic diameter. The channel with higher aspect ratios shows larger cross-section area and hydraulic diameter, yielding a higher flow rate in the micropump. However, this analysis only considers the static pressure difference across the micropump. Further investigation on the dynamic differential pressure and the interaction between reciprocating membranes and the working fluid would provide a more insightful understanding for the effects of using different microchannel aspect ratios (*W*/*H*) on the pumping performance.

5. 5 Conclusions

A package-level peristaltic piezoelectric micropump was designed and fabricated in utilizing multilayer ceramic (MLC) technology. The device was fabricated using commercially available LTCC materials and a custom designed low-fire PZT-SKN piezoelectric ceramic composition. A single co-fire LTCC process was used to prepare the micropump structure including piezoelectric bimorph actuators on the both sides of the pump chambers. FEM simulation results suggested an optimum radius to thickness (R/θ) ratio of about 240 for the largest membrane displacement of bimorph actuator. However, the R and the θ of the sintered bimorph membranes were ~5 mm and 100 µm respectively, which were limited by the fabrication capabilities and durability concerns. Using control signals at frequency of 100 Hz with phase difference of 120^{o} was experimentally determined for optimum pumping performance. The Initial micropump when operated at the voltage of 100 V_{pp} and frequency of 100 Hz, generated a maximum flow rate of up to 450 µl/min with a maximum backpressure of 1.4 kPa. It was shown that using diffuser elements instead of straight channels to connect pump chambers could increase the maximum backpressure at the expense of flow rate and the bidirectional flow capability. Micropumps with different microchannel aspect ratios (W/H) were also compared with respect to flow rate and backpressure. It was determined that the micropump at the aspect ratio of 3 exceeded other pumps in maximum flow rate (630 µl/min) with a limited enhancement of maximum backpressure (1.55 kPa).

One of the most attractive characteristics of the developed multilayer LTCC/PZT-SKN micropump is the capability of providing efficient flow in a compact ceramic package compared to other valveless reciprocating pumps and continuous flow pumps fabricated using silicon, glass, or polymer. The self-pump frequency f_{sp}, defined as the ratio of maximum flow rate Q_{max} and the package size S_p [202], is used to characterize the effectiveness of the pumping. Figure 5.13 compares the LTCC/PZT-SKN micropump realized in this work with some other reported pumps in terms of f_{sp} and S_p (For S_p not provided explicitly, an estimated value is calculated from the image with known dimensions).

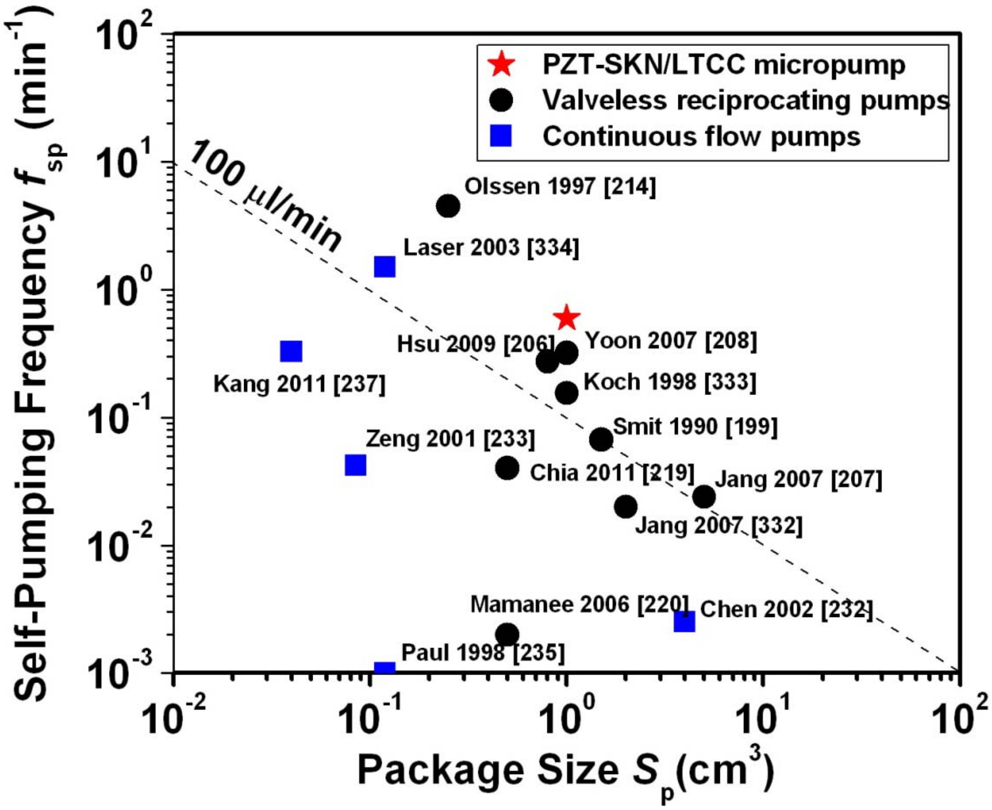

Figure 5.7 Comparison of fabricated multilayer LTCC/PZT-SKN micropump with several reported micropumps based on the self-pump frequency f_{sp} and the package size S_p.

As illustrated in Figure 5.13, our proposed multilayer ceramic micropump demonstrates a higher f_{sp} than the most of other valveless reciprocating pumps, with a competitive S_{p} in that category of micropump. Although most of examined continuous flow pumps are more compact, the lower self-pumping frequency is not comparable to the developed LTCC/PZT-SKN micropump. The two pumps, showing higher f_{sp} in a smaller S_{p} than the present micropump, are both fabricated using Si materials and associated processing techniques. However, LTCC material systems provide excellent thermomechanical and chemical stability compared to the MEMS devices and systems built in Si materials, making those more suitable for applications in a corrosive circumstance involving high-temperature and high-voltage.

Another appealing part of present micropump over other pumps developed is the use of LTCC-process compatible fabrication techniques which enable the direct patterning and integration of piezoelectrically actuated membranes into LTCC microfluidic substrate materials in a single assembly and high temperature firing process. Furthermore, many functional microfluidic devices have already been fabricated using LTCC materials and technology by taking advantage of its versatility; therefore, the resulting micropump can be easily integrated into LTCC-based lab-on-chip microfluidic systems at the package-level, providing efficient on-chip fluid control and transport for the potential applications in chemical analysis and synthesis, biological sensing, and environmental monitoring.

Chapter 6. Summary and future work

6. 1 Summary

The current chapter reviews the main research methodologies and results presented in this thesis. Specifically, the development of a low temperature sinterable PZT-SKN piezoelectric ceramic, detailed investigation of co-firing behavior of the developed PZT-SKN material with commercial LTCC materials, and the production of an LTCC-based piezoelectric micropump corresponding to the contents of chapters 3, 4, and 5 respectively. The discussion of the major contributions and potential impacts of this study on development of high performance LTCC-based piezoelectric devices for microfluidics is also included at the end of each section.

6. 1. 1 Low temperature sintering and properties of fluxed PZT-SKN ceramics

Low temperature sinterable $Pb(Zr_{0.53}, Ti_{0.47})O_3$-$Sr(K_{0.25}, Nb_{0.75})O_3$ (PZT-SKN) ceramics have been synthesized and optimized with respect to microstructures, dielectric, and piezoelectric properties. 0.98PZT-0.02SKN ceramics were prepared through conventional solid-state route using high purity metal oxides and carbonates as starting materials. Various amounts and types of sintering aids were added to the PZT-SKN system in order to lower the sintering temperature (~1250^oC) and accelerate densification process. It was found that the addition of 6 wt% $LiBiO_2$ or 1 wt% $LiBiO_2$ + 1 wt% CuO can reduce the sintering temperature by 300^o-350^oC through the liquid-phase sintering process.

The maximum density achieved for 1 wt% $LiBiO_2$ + 1 wt% CuO added ceramics was 7.75 g/cm^3 (~97.6% of theoretical density) when sintered at 900^{o}C. While the maximum density for 6 wt% $LiBiO_2$ added ceramics when sintered at 950^{o}C was 7.65 g/cm^3 (~96.3% of theoretical density). The dielectric and piezoelectric properties of flux-sintered 0.98PZT-0.02SKN ceramics are also influenced by the addition of fluxes compared to the conventionally sintered samples. The high temperature dielectric measurement revealed that the Curie temperature T_c decreased from 357^{o}C for unfluxed ceramics to 302^{o}C for 6 wt% $LiBiO_2$ fluxed samples and to 351^{o}C for 1 wt% $LiBiO_2$ + 1 wt% CuO fluxed samples. Additionally, a lower and broader permittivity peak was observed for flux-sintered 0.98PZT-0.02SKN ceramics. The *P-E* hysteresis loops demonstrated that both remnant polarization P_r and coercive field E_c decreased for flux-sintered samples.

Reduced grain size relative to the high-temperature sintered 0.98PZT-0.02SKN ceramics has been associated with observed decrease in piezoelectric properties. However, the desirable overall properties with high field d_{33} piezoelectric coefficient of 415 pm/V, Curie temperature T_c of around 351^{o}C, dielectric constant ε_r of 1235, and planar coupling factor k_p of 0.54 were obtained for the PZT-SKN system with addition of 1 wt% $LiBiO_2$ + 1 wt% CuO content sintered at 900^{o}C for 1 h.

The first significant impact of work presented in this thesis is the development of a low fire PZT-SKN ceramic with desirable properties and compatibility with LTCC material systems. The processing conditions and piezoelectric properties of other reported low fire PZT-based ceramics have not shown the promising results for co-firing with LTCC materials. Several other PZT-based systems have been shown the capability to be sintered to high density at temperatures of <1000°C for short time <1 h. However, utilizing these low fire ceramics in the fabrication of multilayer piezoelectric actuators with LTCC materials is limited by either the low d_{33} values (~200 pm/V) or the relatively high sintering temperature (950°C). The developed 0.98PZT-0.02SKN ceramics with 1 wt% $LiBiO_2$ + 1 wt% CuO addition can be densified at 900°C for 1 h, showing a favorable dielectric and piezoelectric properties. The low sintering temperature and short soaking time for $LiBiO_2$ and CuO fluxed 0.98PZT-0.02SKN ceramics make it possible to co-fire with LTCC materials for the multilayer actuator applications. Additionally, the high Curie temperature T_c (>350°C) of developed low fire PZT-SKN ceramic compared with other reported fluxed PZT-based ceramics is suitable for applications over a broad temperature range.

6. 1. 2 Sintering behaviors and properties of co-fired LTCC/PZT-SKN multilayer ceramics

Based on the above low-temperature sintering study, PZT-SKN ceramics fluxed with 1 wt% $LiBiO_2$ + 1 wt% CuO were selected to investigate co-firing with commercial LTCC materials. Fluxed PZT-SKN tapes were prepared using tape casting technique. A castable slurry consisting of ceramic powders and organic binder vehicle was mixed, degassed, and cast on the moving Mylar substrate using a bench-top tape caster. The composition of slurry (ceramic powder, solvent, and various organic additives) was carefully optimized to balance the viscosity of mixture as well as the strength and flexibility of cast PZT-SKN tape.

The master sintering curve (MSC) approach has been applied to understand and predict the sintering behaviors of LTCC tapes and fluxed PZT-SKN ceramics. It was assumed that the microstructural evolution of a powder compact is only a function of density and that only one sintering mechanism controls the sintering process in MSC theory. The MSC curves were constructed using measured density data obtained under constant heating rate experiment and the best determined apparent activation energy Q_a. The Q_a of 268, 415, and 540 kJ/mol were obtained for fluxed PZT-SKN, HL2000, and CT2000 tapes, respectively. The different range of Q_a values demonstrates the different sintering mechanisms for fluxed PZT-SKN ceramics (liquid-phase sintering) and LTCC materials (viscous-flow controlled sintering). However, using MSC the analysis of the sintering behaviors for LTCC and fluxed PZT-SKN ceramics an optimized sintering profile was obtained.

The fluxed PZT-SKN tapes were laminated with several commercially available LTCC tapes in a sandwich structure and co-fired using the optimized sintering profile. After co-firing the HL2000/PZT-SKN laminates exhibited a flat multilayer ceramic structure when compared to other the LTCC/PZT-SKN combinations explored. The self-constrained densification characteristic of the HL2000 tapes was considered to have a significant beneficial effect on reducing the camber development. The microstructure and elemental composition near the co-fired HL2000/PZT-SKN interfaces were analyzed using EDS. The results indicated limited inter-diffusion of Pb (from PZT-SKN to LTCC layer) and Al, Ca, Si (on the opposite direction) near the heterogeneous interface. Further, nearly pure PZT-SKN composition was observed at the center of piezoelectric layer.

Additionally, measurement of dielectric and piezoelectric properties of fluxed PZT-SKN ceramics co-fired with different LTCC materials at 870°C for 1 h indicated that the HL2000/PZT-SKN samples exhibited the best overall properties among all samples examined. The dielectric constant ε_r of 1205 and low field d_{33} piezoelectric coefficient of 240 pm/V showed only a moderate reduction compared with free standing flux-sintered PZT-SKN tapes. To demonstrate the device performance and potential applications of co-fired LTCC/PZT-SKN structures, a compact piezoelectric microbalance was fabricated. The mass sensitivity of the balance was experimentally determined to be 15 kHz/mg. FEM simulation results suggest that a thinner piezoelectric layer with a smaller diameter at fixed diameter/thickness ratio would provide higher mass sensitivity.

In the above section, compatible materials and processing methods for co-firing LTCC/PZT-SKN multilayer ceramics have been developed and reported for the very first time. Prior studies had focused on screen printing PZT-based thick films on the pre-sintered LTCC or alumina substrates and using additional firing steps to sinter the PZT layers. An optimized sintering profile has been constructed for co-firing LTCC materials and the developed low fire PZT-SKN ceramics by application of the master sintering curve (MSC) approach. The dielectric properties and T_c were the same for both co-fired LTCC/PZT-SKN and free standing low fire PZT-SKN materials. The resultant piezoelectric properties are among the highest reported for thick-film piezoelectric multilayers integrated with or onto an inactive substrate by any fabrication method, as listed in Table 6.1. The large observed piezoelectric properties of the current co-fired LTCC/PZT-SKN laminates and relative simplicity of the co-firing scheme suggest significant benefits and improved commercial relevance over previously reported attempts.

Table 6.1 Properties of PZT-based thick-film ceramics fired on LTCC and alumina substrates.

Materials	Sintering aids	Sintering condition	ε	d_{33}^{low} (pm/V)	Ref.
PZT-SKN on LTCC	1wt% $LiBiO_2$ + 1wt% CuO	co-fired, 900°C, 1 h	1200	255	—
PZT (53/47) on LTCC	2 wt% $Pb_5Ge_3O_{11}$	post-fired 850°C, 1 h	190	—	[148]
PZT (53/47) on LTCC	2 wt% $Pb_5Ge_3O_{11}$	post-fired 875°C, 15 min	225	55	[149]
PZT (53/47) on alumina	2 wt% $Pb_5Ge_3O_{11}$	post-fired 850°C, 15 min	445	120	[150]

6. 1. 3 Development and optimization of multilayered LTCC/PZT-SKN piezoelectric micropumps

A multilayered LTCC/PZT-SKN piezoelectric micropump has been designed and fabricated using the materials and processing methods presented above. The micropump was fabricated using standard LTCC thick-film technology. LTCC structural layers defining the fluidic network components were integrated with PZT-SKN tapes providing the electromechanical actuation. A single co-firing process was applied to the LTCC/PZT-SKN micropump body and screen printed conductive patterns. The overall package size of this developed micropump is about 1 cm^3. The peristaltic pumping action was generated using 3 pairs of bimorph actuators located on both the top and bottom of each of 3 microchambers arranged in series. The pumping performance was optimized using FEM tools and the expected maximum flow rate was calculated using simulation results and an analytical equation.

The characterization of pumping performance on the initially designed micropump indicated that using control signals at frequency of 100 Hz with phase difference of 120^{o} between successive pump chambers resulted in efficient and reliable pumping. Experimental results demonstrated that the volumetric flow rate decreased linearly as backpressure increased. A maximum flow rate (at zero backpressure) up to 450 μl/min and a blocking pressure (at zero flow rate) of 1.4 kPa were observed on the micropump when operated at the voltage of 100 V_{pp} and frequency of 100 Hz. The operating frequency was confined at 100 Hz to avoid the cavitation and prolong the lifetime of micropump.

An approach for enhancing the pumping performance integrated planar diffuser elements to replace the straight microchannels connecting the pump chambers. The diffuser-type micropump exhibited a higher maximum backpressure due to the additional valving effect resulting in a flow rate which was less sensitive to backpressure. However, this increase of maximum backpressure was realized at the expense of flow rate and bidirectional flow characteristics.

In order to optimize the pumping performance micropumps with channel of different aspect ratio (W/H) were fabricated, the maximum flow rates and backpressures compared. The microchannel with higher aspect ratio led to a lower flow resistance at the constant backpressure, yielding a higher flow rate. The performance of micropump with the largest aspect ratio showed the highest no load flow rate of 630 μl/min and the largest blocking pressure of 1.55 kPa.

In this section a compact "package-level" peristaltic piezoelectric micropump has been realized using co-firable piezoelectric ceramics and commercially accepted processing methods. The realized multilayer ceramic micropump has unique characteristics. The use of LTCC compatible fabrication methods allows the direct patterning and integration of piezoelectric drivers into LTCC-based microfluidic structures. Further, the developed micropump shows the possibility to be integrated into LTCC-based LOC microfluidic systems at the package-level, providing efficient on-chip fluid transport and control for a wide range of potential applications. The incorporation of LTCC with fluxed PZT-SKN materials provides direct integration of piezoelectric actuators, fluidic networks, and electronic interconnects into one single ceramic module using LTCC thick-film fabrication processing.

6. 2 Future work

Incorporating functional elements (*e.g.* piezoelectrics, dielectrics, ferrites, and conductors) into LTCC-based MEMS structures for the fabrication of highly integrated microfluidic devices and systems has attracted much attention from both ceramists and chemists [16-18]. The work described in this thesis primarily investigates the integration of a developed low fire piezoelectric PZT-SKN ceramic with commercial LTCC substrate materials and the implementation of a piezoelectric micropump using the co-fired LTCC/PZT-SKN multilayer structure. In addition to the research efforts covered in the current work it is suggested that further studies can be conducted on the following areas. First, improved understanding of the stress development during co-firing of the LTCC/PZT-SKN multilayer ceramics would help to analyze the densification behavior of the piezoelectric layer and reduce the potential processing defects. Second, there is a need to further optimize micropump performance including increasing maximum flow rate and backpressure for broadening the application areas of the demonstrated micropump structure. Finally, future attempts to integrate the developed LTCC-based piezoelectric micropump with other compatible fluidic components and electronic control circuits are expected to fully take advantage of the multifunctional capabilities and miniaturization possible using LTCC technology.

6. 2. 1 Investigation of stress development

As discussed in chapter 4, LTCC tapes were laminated and co-fired with low fire PZT-SKN layers to build the multilayer ceramics for microdevice development. The different sintering behaviors between LTCC and PZT-SKN layers induced both shear and in-plane tensile stresses in the ceramics. These contribute to the occurrence of delamination, camber, cracking, and other defects. However, using self-constrained LTCC tapes (HL2000) and a compatible co-firing profile for LTCC/PZT-SKN multilayer ceramics have been demonstrated. This approach resulted in a flat uniform multilayer module in a comparatively large size (compared to other tested commercial LTCC materials). However, the densification behavior of PZT-SKN ceramic is affected by the constrained HL2000 layers. The further research work to understand the sintering behavior and stress development of PZT-SKN layer under constrained sintering would help optimize the multilayer design (e.g. thickness of each component layer) and control the potential processing defects.

In other reported work [188,319,335] both linear regression analysis and the analytical modeling are used to calculate strain and stress distribution in the co-fired multilayer ceramics particularly in the densifying layer between the constraining LTCC layers. The relationship between linear shrinkage $\Delta L/L_o$ in the x-y dimensions and temperature T can be described as follows:

$$\frac{\partial(\Delta L/L_o)}{\partial T} = \sum_{0}^{i} a_i T^i$$

Application of this method would require numbers of measurements in order to determine the parameters a_i of fitting equation for each sintering profile. Therefore, tremendous experiment work is needed, leading to a significant consumption of time and energy. An example analysis based on this method is shown in Figure 6.1(a). Both a typical morphology of the densifying layer after constrained sintering and the calculated stress distribution are presented. Similar experimental results were observed in the co-fired LTCC/PZT-SKN multilayer ceramics, as shown in Figure 6.1(b).

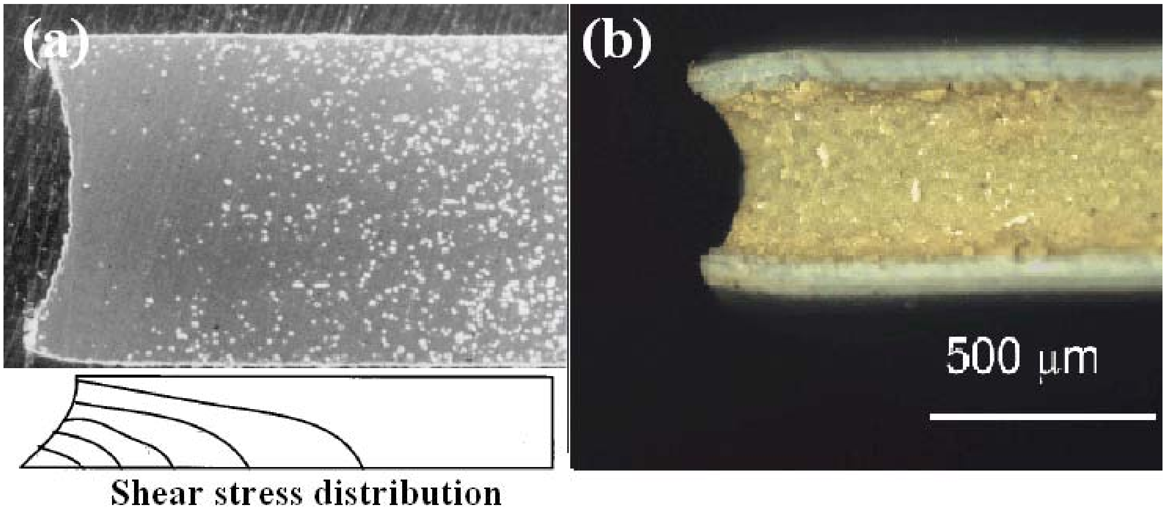

Figure 6.1 (a) Morphology of polished microstructure of low-temperature co-firable glass-ceramic system under constrained sintering (taken from S.Y. Tzeng et al. [319]); and (b) observed microstructure of co-fired HL2000/PZT-SKN multilayer structure.

Using the results of master sintering curve (MSC) studies on LTCC and PZT-SKN materials introduced in chapter 4 the relationship between $\Delta L/L_o$ and T can be determined for arbitrary sintering profiles based on the constructed MSC fitting equation:

$$\rho = \rho_o + \frac{\mathrm{a}}{[1 + \exp(-\frac{\log(\Theta) - \log(\Theta_o)}{\mathrm{b}})]^{\mathrm{c}}}$$

For isotropic shrinkage the densification rate can be converted to the linear shrinkage rate by the following:

$$-\frac{dL}{L_o dt} = \frac{d\rho}{3\rho_o dt}$$

Once the sintering profile $T(t)$ is determined the $\log(\Theta)$ can be calculated and subsequently a function for ($\Delta L/L_o$) and T will be constructed. Incorporating this function into a FEM modeling program (*e.g.* COMSOL® Multiphysics) would provide a more practical and effective means to analyze the strain and stress distribution in the co-fired PZT-SKN layer without the need of tedious experiment and calculation.

6. 2. 2 Further optimization of micropump design

Micropumps designed and used for different applications should have suitable features. For example, the high blocking pressure capabilities and pressure-independent flow rates could be important characteristics for micropumps required in drug delivery systems. In such an application high precision liquid drug dosing is required. In the case of IV delivery pumping must be achieved against the high backpressure encountered *in vivo* (~16 kPa) [336,337]. Tolerance to gas bubbles would also be desired when pumping a gas-liquid mixture [200]. The overall package size, pumping reliability, power consumption, manufacturing cost, and material biocompatibility are also critical issues [202]. To achieve better pumping performance (*e.g.* high backpressure, self-priming, and bubble-tolerance) and broaden the application area further optimization of currently developed LTCC/PZT-SKN micropump is required. Preliminary FEM simulation results suggest that modifying the electrode geometry of the bimorph actuators would increase the deflection of the pump membrane at comparable electric drive conditions and could subsequently enhance the pumping.

In the initial micropump design the conductor ink is screen printed on the entire exposed area of the bimorph actuator. Figure 6.2 illustrates the two modified electrode structures. In the first the electrode is only applied in the central region of the PZT-SKN membrane as shown in structure (a). Alternatively, a doughnut shaped electrode could be applied as shown in structure (b).

The ratio of the electrode radius over the entire pump radius (*r*/*R*) has been optimized using FEM simulations. The deflection of a bimorph actuator with radius *R* of 5 mm and thickness θ of 20 μm with various electrode geometries was studied. Figure 6.2 demonstrates the variation of maximum displacement $d_{\max}$ as a function of electrode areas (*r*/*R*) for the two types of electrode structures. An optimum *r*/*R* ratio of 0.5 is determined where the peak $d_{\max}$ is obtained for both electrode geometries. The electrode in structure (a) yields larger $d_{\max}$ than the electrode in structure (b) at *r*/*R* ratio of 0.5. The $d_{\max}$ of membrane with both types of modified electrode patterns is more than 40 times higher than that of membrane with full electrode as originally fabricated.

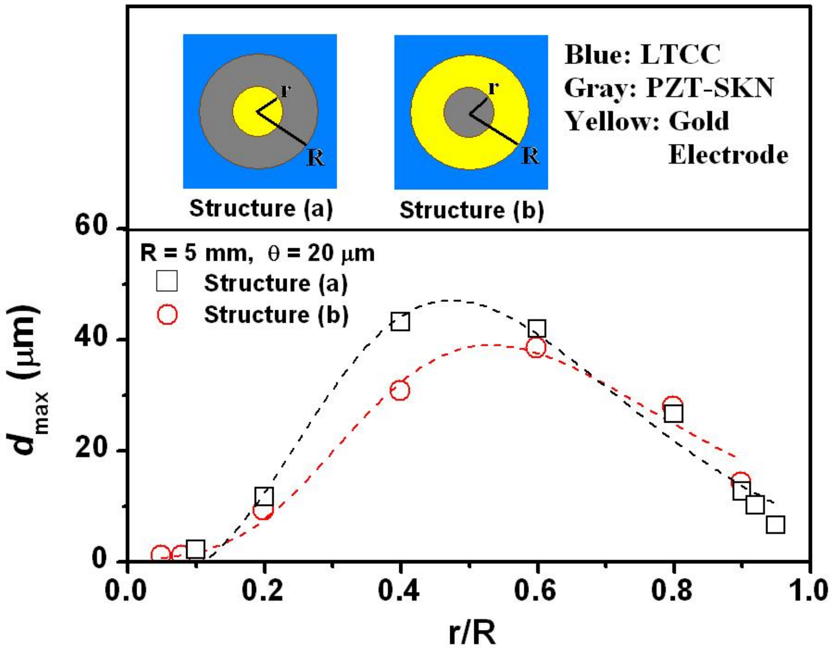

Figure 6.2 Effect of electrode pattern on bimorph membrane deflection

Two bimorph structures with same radius of 5 mm and different thickness of 100 μm and 150 μm are designed and used in the FEM simulation, which are similar to the fabricated bimorph geometries. The modified electrode structure (a) with $r/R = 0.5$ is used. The dependency of $d_{\max}$ on the driving electric field (voltage) at the actuation frequency of 100 Hz for these two bimorphs is shown in Figure 6.3. The deflection response of the bimorph membrane to the driving electric field is linear. The 100 μm thick bimorph generates a larger $d_{\max}$ than the 150 μm thick one because the R/θ ratio for the thinner bimorph is near to the optimum value (~240) predicted by the FEM simulation results (as discussed in chapter 5).

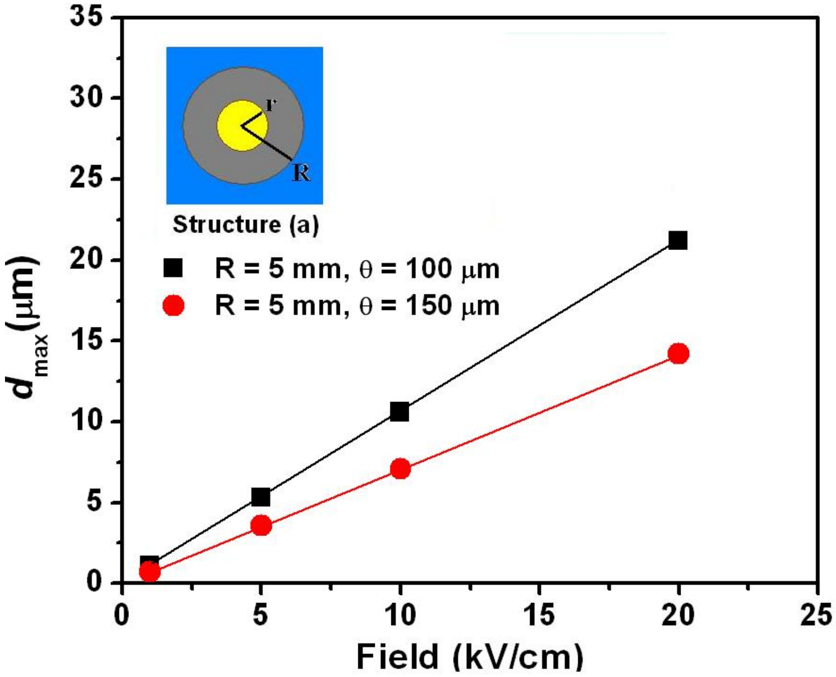

Figure 6.3 FEM simulation results of maximum membrane displacement of bimorph with modified electrode geometry at different electric fields.

The volumetric deflection and the resulting flow rate of the micropump are directly related to the applied voltage at low frequency range which is much less than the resonant frequency of the bimorph actuator. Applying high voltage at the constant actuation frequency can increase the flow rate. However, the voltage must be set up in a proper range because of the limitation of electric field strength for piezoelectric materials. The simulation results indicate that the larger membrane displacement is achieved by using the optimized electrode pattern, which can potentially enable the higher volumetric flow rate and backpressure with less power consumption for the micropump. Future experiment should be conducted to validate simulation results.

There are several other effective approaches for micropump optimization which would provide additional functions to enhance the pumping performance or improve the characterization method. Increasing compression ratio of the micropump by increasing the stroke volume and reducing the dead volume of the fluid chamber is one of the applicable methods. In addition, changing the direction of microfluidic connection between tubing and the micropump body from perpendicular to horizontal can also reduce the pressure loss. Moreover, flow and pressure sensors are expected to be integrated in the fluidic conduit for precisely measuring the flow rate and backpressure in the pumping characterization experiment.

6. 2. 3 Integration of LTCC-based microfluidic systems

There is an increasing drive toward to multiple fluidic, electronic, and mechanical components into one single miniaturized chip [19,20]. The LTCC/PZT-SKN piezoelectric micropump presented in this work is implemented using the LTCC thick-film technology. The capability of on-chip fluid delivery and control provided by the developed micropump is highly desirable for many microfluidic applications such as chemical sensing and synthesis as well as fast manipulation of biological samples. The realization of functional LTCC-based microfluidic systems with multiple components requires further investigation and experimental studies. There are two examples of microfluidic devices fabricated using LTCC materials and associated processing methods which demonstrate the possibility and necessity of being integrated with the developed LTCC-based micropump.

A LTCC-based microfluidic reactor is designed and fabricated to provide improved control of polymerization process [338]. The designed reactor utilizes three streams of co-laminar flow to allow for the controlled introduction of reactant solutions into the reaction channel. The schematic diagram of desired reaction in microchannels is shown in Figure 6.4(a).

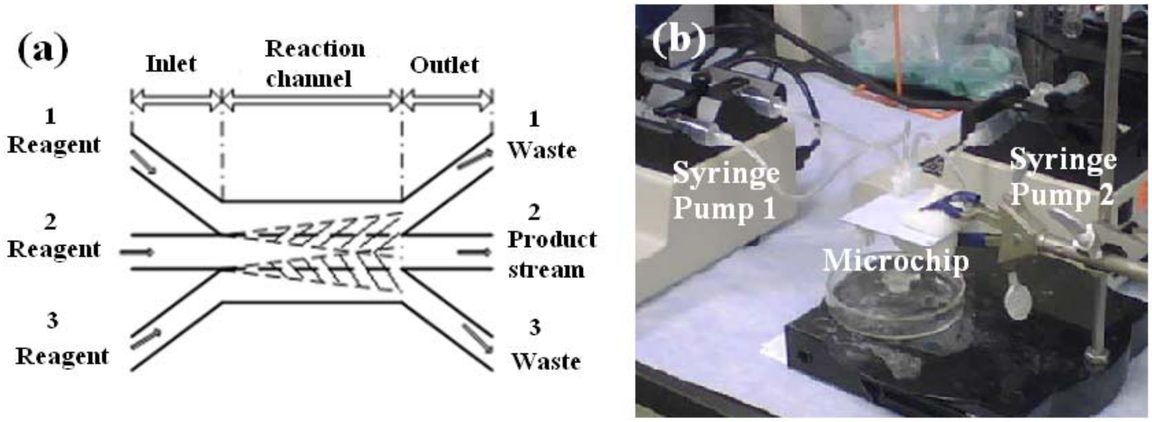

Figure 6.4 (a) Illustration of synthesis conditions via co-laminar flow in a LTCC-based microfluidic reactor; and (b) experimental setup for chemical reactions in the microchannel by laminar diffusion.

Previous experimental attempts used syringes and multiple external syringe pumps for infusing the reagents, as shown in Figure 6.4(b). Extreme care was required in order to avoid air bubble generation when loading the reagent into the syringes and connecting the syringes to the microreactor. In addition, the compatibility between the solvent and the materials used for connector/tubing/syringe/adhesive was also a critical issue. Using the LTCC/PZT-SKN micropump would help provide more efficient and accurate control of reagent pumping for the desired chemical synthesis if integrated with this LTCC-based micromixer, which exclude the need of external pumps and additional syringes not only saving the sample preparation time but also increasing the reliability of experimental results.

The other example is a cell culture platform built using an LTCC substrate [339]. Multiple cell culture wells with silver or gold electrodes are fabricated in one single LTCC-based microfluidic chip. The microchip design and electrical measurement methods are illustrated in Figure 6.5(a). The experimental setup is shown in Figure 6.5(b). On-chip transportation of cell samples achieved by valveless reciprocating micropumps is demonstrated as a practical and appropriate method for cellomics [340]. The pumping action has a minimal effect on the cell viability and proliferation. Incorporating the developed LTCC/PZT-SKN micropump into the microfluidic chip made by the same LTCC materials and fabrication techniques would provide a safe and reliable pumping of living cells with a suitable flow rate range.

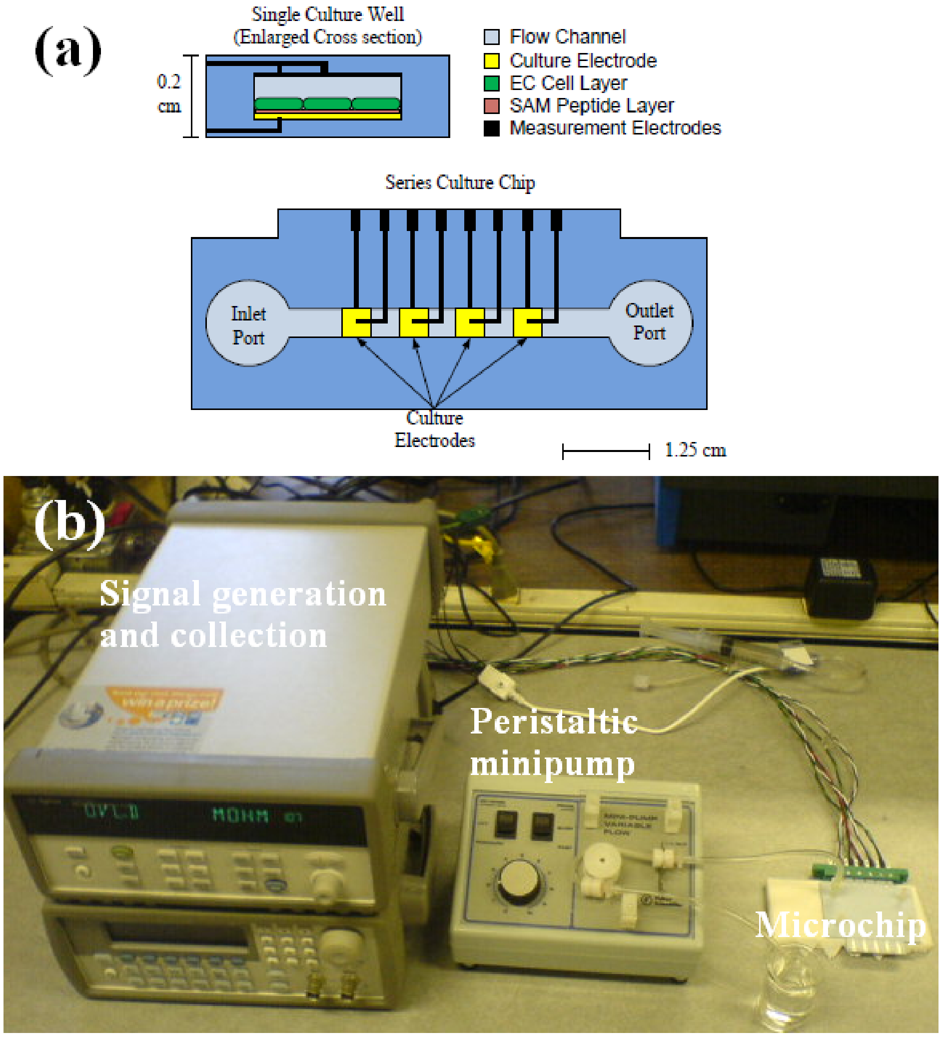

Figure 6.5 (a) Schematic of LTCC-based cell culture chip; and (b) experimental setup for continuous perfusion and real-time monitoring.

As discussed in chapter 2, LTCC technology is a promising alternative to Si materials and micromachining techniques for combining microfluidic and electronic elements in one single substrate using the same fabrication methodology. The realization of a complete microanalysis system using developed individual components based on LTCC technology is the ultimate goal. A further development of highly integrated microfluidic systems requires the incorporation of an electronic control circuit into microfluidic devices made on the same LTCC substrate. A conceptual illustration for the LTCC-based lab-on-a-chip system is shown in Figure 6.6. By completing this task, most of the sample processing steps (*e.g.* supply, pretreatment, and analysis) can be directly conducted in the on-chip level which results in not only the enhancement of portability but also the improvement of functionality.

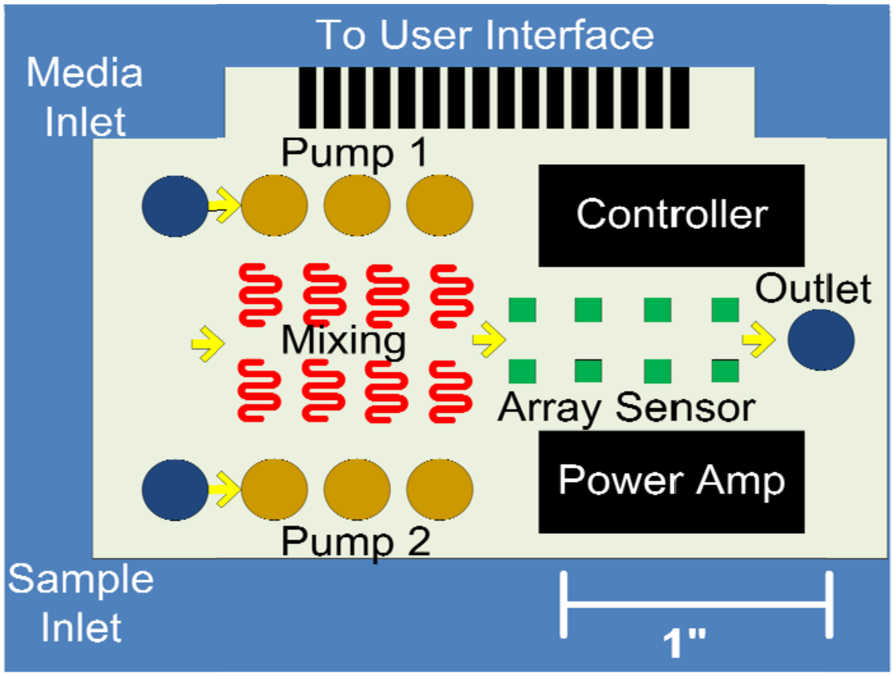

Figure 6.6 A proposed LTCC-based integrated microfluidic system

6. 3 Conclusions

The aim of this research is the development a high performance low fire piezoelectric ceramic, fabrication methods which are compatible with LTCC materials and processing techniques, and demonstration of an integrated piezoelectric micropump. It is suggested that further investigation on the stress development in the co-fired multilayer structure would help provide a better understanding on densification of PZT-SKN layer and more efforts on optimization of electrode design for micropump would be considered as an effective way to increase the micropump performance. Successful attempts on integrating the LTCC/PZT-SKN multilayer micropump with other fluidic devices and electronic components will lead to a significant progress on the development of a highly integrated LTCC-based microfluidic system.

Appendix

Properties of low-temperature sintered PZT-SKN ceramics with various sintering aid additions

Composition	Sintering Temperature	Density (g/cm^3)	ε_r (1kHz)	tanδ (1kHz)	d_{33}^{high} (pm/V)	E_c (kV/cm)	P_r (C/m^2)	T_c (^{o}C)
PZT-SKN + 6wt% LiBiO$_2$	850^{o}C	7.42	1130	0.035	306	14.5	0.20	301
	900^{o}C	7.53	1116	0.033	324	14.5	0.29	300
	950^{o}C	7.66	1222	0.030	360	14.5	0.31	302
	1000^{o}C	7.62	1155	0.040	334	15.2	0.32	300
PZT-SKN + 3wt% LiBiO$_2$	950^{o}C	7.26	820	0.029	91	14.4	0.20	325
	1000^{o}C	7.62	939	0.031	163	15.7	0.31	326
	1050^{o}C	7.72	975	0.030	248	15.6	0.32	325
	1100^{o}C	7.77	1007	0.028	329	16.7	0.35	324
PZT-SKN + 1wt% LiBiO$_2$	950^{o}C	6.63	760	0.050	78	13.5	0.28	--
	1000^{o}C	7.39	910	0.030	142	14.5	0.30	344
	1050^{o}C	7.58	1032	0.031	305	14.6	0.32	344
	1100^{o}C	7.65	1062	0.036	428	15.6	0.32	341
	1150^{o}C	7.65	1060	0.038	440	15.9	0.38	342

(continued) Properties of low-temperature sintered PZT-SKN ceramics with various sintering aid additions

Composition	Sintering Temperature	Density (g/cm^3)	ε_r (1kHz)	tanδ (1kHz)	d_{33}^{high} (pm/V)	E_c (kV/cm)	P_r (C/m^2)	T_c (^{o}C)
PZT-SKN + 0.5wt% $LiBiO_2$	950^{o}C	5.68	--	--	--	--	--	--
	1000^{o}C	6.85	820	0.060	72	17.5	0.24	352
	1050^{o}C	7.28	934	0.040	205	17.6	0.28	353
	1100^{o}C	7.35	962	0.035	362	15.6	0.29	351
	1150^{o}C	7.55	1142	0.025	420	15.5	0.34	351
PZT-SKN + 1wt% $LiBiO_2$ + 1wt% CuO	850	7.20	1104	0.030	337	14.5	0.23	351
	900	7.75	1235	0.018	415	14.5	0.27	351
	950	7.68	1220	0.020	398	14.8	0.29	352
	1000	7.72	1239	0.020	402	13.2	0.30	352
PZT-SKN	1250^{o}C	7.80	1395	0.015	680	15.6	0.34	357

References

[1] A. Manz, N. Graber, and H.M. Widmer, "Miniaturized Total Chemical Analysis Systems: A Novel Concept for Chemical Sensing," *Sensor. Actuat. B-Chem.*, **1**, 244-248 (1990).

[2] D.R. Reyes, D. Iossifidis, P.A. Auroux, and A. Manz, "Micro Total Analysis Systems. Part 1. Introduction, Theory, and Technology," *Anal. Chem.*, **74**, 2623-2636 (2002).

[3] P.A. Auroux, D. Iossifidis, D.R. Reyes, and A. Manz, "Micro Total Analysis Systems. Part 2. Analytical Standard Operations and Applications," *Anal. Chem.*, **74**, 2637-2652 (2002).

[4] D. Erickson and D. Li, "Integrated Microfluidic Devices," *Anal. Chim. Acta*, **507**, 11-26 (2004).

[5] N.T. Nguyen and Z. Wu, "Micromixer-A Review," *J. Micromech. Microeng.*, **15**, R1-R16 (2005).

[6] A.J. deMello, "Control and Detection of Chemical Reactions in Microfluidic Systems," *Nature*, **442**, 394-402 (2006).

[7] J. El-Ali, P.K. Sorger, and K.F. Jensen, "Cells on Chips," *Nature*, **442**, 403-411 (2006).

[8] H. Andersson and A. van den Berg, "Microfluidic Devices for Cellomics: A Review," *Sensor. Actuat. B-Chem.*, **92**, 315-325 (2003).

[9] J. Khandurina and A. Guttman, "Bioanalysis in Microfluidic Devices," *J. Chromatogr. A*, **943**, 159-183 (2002).

[10] S.Z. Razzacki, P.K. Thwar, M. Yang, V.M. Ugaz, and M.A. Burns, "Integrated Microsystems for Controlled Drug Delivery," *Adv. Drug Deliv. Rev.*, **56**, 185-198 (2004).

[11] P. Dario, M.C. Carrozza, A. Benvenuto, and A. Menciassi, "Micro-Systems in Biomedical Applications," *J. Micromech. Microeng.*, **10**, 235-244 (2000).

[12] M.R. Gongora-Rubio, M.B.A. Fontes, Z.M. Rocha, E.M. Richter, and L. Angnes, "LTCC Manifold for Heavy Metal Detection System in Biomedical and Environmental Fluids," *Sensor. Actuat. B-Chem.*, **103**, 468-473 (2004).

[13] A.D. Stroock and M. Cabodi, "Microfluidic Biomaterials," *Mater. Res. Soc. Bull.*, **31**, 114-119 (2006).

[14] G.M. Whitesides, "The Origins and the Future of Microfluidics," *Nature*, **442**, 368-373 (2006).

[15] J.J. Licari, "Thin and Thick Films," Electronic Materials and Processes Handbook, Second Edition, eds., C.A. Harper and R.M. Sampson. McGraw-Hill Inc., New York, NY, 8.59-8.97, 1994.

[16] T. Thelemann, H. Thust, and M. Hintz, "Using LTCC for Microsystems," *Microelectron. Int.*, **19**, 19-23 (2002).

[17] M.R. Gongora-Rubio, P. Espinoza-Vallejos, L.M. Sola-Laguna, and J.J. Santiago-Aviles, "Overview of Low Temperature Co-Fired Ceramics Tape Technology for Meso-System Technology (MsST*)," Sensor. Actuat. A-Phys.*, **89**, 222-224 (2001).

[18] L.J. Golonka, "Technology and Applications of Low Temperature Cofired Ceramic (LTCC) Based Sensors and Microsystems," *Bull. Pol. Acad. Sci. Tech.*, **54**, 221-231 (2006).

[19] N. Ibanez-Garcia, C.S. Martinez-Cisneros, F. Valdes, and J. Alonso, "Green-Tape Ceramics. New Technological Approach for Integrating Electronics and Fluidics in Microsystems," *Trends Anal. Chem.*, **27**, 24-33 (2008).

[20] K.A. Peterson, K.D. Patel, C.K. Ho, S.B. Rohde, C.D. Nordquist, C.A. Walker, B.D. Wroblewski, and M. Okandan, "Novel Microsystem Applications with New Techniques in LTCC," *Int. J. Appl. Ceram. Technol.*, **2**, 345-363 (2005).

[21] Y. Saito, H. Takao, T. Tani, T. Nonoyama, K. Takatori, T. Homma, T. Nagaya, and M. Nakamura, "Lead-Free Piezoceramics," *Nature*, **432**, 84-87 (2004).

[22] S. Zhang, R. Xia, and T.R. Shrout, "Lead-Free Piezoelectric Ceramics vs. PZT," *J. Electroceram.*, **19**, 251-257 (2007).

[23] N.R. Harris, M. Hill, R. Torah, R. Townsend, S. Beeby, N.W. White, and J. Ding, "A Multilayer Thick-Film PZT Actuator for MEMS Applications," *Sensors Actuat. A-Phys.*, **132**, 311-316 (2006).

[24] R. Lou-Moeller, C.C. Hindrichsen, L.H. Thamdrup, T. Bove, E. Ringgaard, A.F. Pedersen, and E.V. Thomsen, "Screen-Printed Piezoceramic Thick Films for Miniaturised Devices," *J. Electroceram.*, **19**, 333-338 (2007).

[25] N.M. White, P. Glynne-Jones, and B.P. Beeby, "A Novel Thick-Film Piezoelectric Micro-Generator," *Smart Mater. Struct.*, **10**, 850-852 (2001).

[26] M.S. Zarnik, D. Belavic, S. Macek, and J. Holc, "Feasibility Study of a Thick-Film PZT Resonant Pressure Sensor Made on a PreFired 3D LTCC Structure," *Int. J. Appl. Ceram. Technol.*, **6**, 9-17 (2009).

[27] V.T. Zaspalis, M. Kolenbrander, and J. Boerekamp, "Materials for Inductive and Microwave Function Integration in LTCC-Technology Multichip Modules," *J. Phys. Conf. Ser.*, **10**, 357-360 (2005).

[28] D. Belavic, M. Hrovat, J. Holc, M.S. Zarnik, M. Kosec, and M. Pavlin, "The Application of Thick-Film Technology in C-MEMS," *J. Electroceram.*, **19**, 363-368 (2007).

[29] M.S. Zarnik and D. Belavic, "Design Study for a Thick-Film Piezoelectric Actuator in an LTCC Structure," Proceedings of the 6th International Conference on Thermal, Mechanical and Multi-Physics Simulation and Experiments in Micro-Electronics and Micro-Systems, Berlin, Germany, April 18-20, 2005.

[30] H. Birol, T. Maeder, I. Nadzeyka, M. Boers, and P. Ryse, "Fabrication of a Millinewton Force Sensor Using Low Temperature Co-Fired Ceramic (LTCC) Technology," *Sensors Actuat. A-Phys.*, **134**, 334-338 (2007).

[31] N.J. Donnelly, T.R. Shrout and C.A. Randall, "Addition of a Sr, K, Nb (SKN) Combination to PZT (53/47) for High Strain Applications," *J. Am. Ceram. Soc.*, **90**, 490-495 (2007).

[32] C.S. Martinez-Cisneros, N. Ibanez-Garcia, F. Valdes, and J. Alonso, "Miniaturized Total Systems: Integration of Electronics and Fluidics Using Low-Temperature Co-Fired Ceramics," *Anal. Chem.*, **79**, 8376-8380 (2007).

[33] C.S. Martinez-Cisneros, N. Ibanez-Garcia, F. Valdes, and J. Alonso, "LTCC Microflow Analyzers with Monolithic Integration of Thermal Control," *Sensor. Actuat. A-Phys.*, **138**, 63-70 (2007).

[34] H. Birol, Fabrication of Low Temperature Co-fired Ceramic (LTCC) – Based Sensor and Micro-fluidic Structures, Ph.D. Dissertation, Éole Polytechnique Federale De Lausanne (EPFL), 2007.

[35] J.E. Sergent, "Hybrid Microelectronics and Multichip Module Technologies," Electric Assembly Fabrication-Chips, Circuit Boards, Packages, and Components First Edition, ed., C.A. Harper. McGraw-Hill Inc., New York, NY, 625-629, 2002.

[36] Y. Imanaka, *Multilayered Low Temperature Cofired Ceramics (LTCC) Technology*, 1-17, Springer Science+Business Media Inc., New York, NY, 2005.

[37] C. Rusu, K. Persson, B. Ottosson, and D. Billger, "LTCC Interconnects in Microsystems," *J. Micromech. Microeng.* **16**, S13-S18 (2006).

[38] DuPont Microcircuit Materials, *DuPont Green Tape^{TM} Material System Design and Layout Guidelines*, E.I. du Pont de Nemours and Company, Wilmington, DE, 2003.

[39] T. Hu, BST-Based Low Temperature Co-Fired Ceramic (LTCC) Modules for Microwave Tunable Components, Ph.D. Dissertation, University of Oulu, 2002.

[40] H. Jantunen, A Novel Low Temperature Co-Firing Ceramic (LTCC) Material for Telecommunication Devices, Ph.D. Dissertation, University of Oulu, 2001.

[41] H. Jantunen, R. Rautioaho, A. Uusimäki, and S. Leppävuori, "Compositions of $MgTiO_3$-$CaTiO_3$ Ceramic with Two Borosilicate Glasses for LTCC Technology," *J. Am. Ceram. Soc.*, **83**, 2855-2857 (2000).

[42] C.L. Lo, J.G. Duh, B.S. Chiou, and W.H. Lee, "Low-Temperature Sintering and Microwave Dielectric Properties of Anorthite-Based Glass-Ceramics," *J. Am. Ceram. Soc.*, **85**, 2230-2235 (2002).

[43] Heraeus Circuit Materials Division, *Design Guidelines for LTCC - HeraLock® HL2000 Materials Systems*, Heraeus Inc., West Conshohocken, PA, 2004.

[44] J. Dominik and G. Leszek, "Cold Chemical Lamination-New Bonding Technique of LTCC Green Tapes," *Int. J. Appl. Ceram. Technol.*, **7**, 814-820 (2010).

[45] H. Birol, T. Maeder, and P. Ryser, "Application of Graphite-based Sacrificial Layers for Fabrication of LTCC (Low Temperature Co-fired Ceramic) Membranes and Micro-channels," *J. Micromech. Microeng.*, **17**, 50-60 (2007).

[46] K. Karppinen, High Bit-Rate Optical Interconnects on Printed Wiring Board-Micro-Optics and Hybrid Integration, Ph.D. Dissertation, VTT Technical Research Centre of Finland, 2008.

[47] S.H. Sim, C.Y. Kang, J.W. Choi, H.W.W. Choi, Y.J. Yoon, S.Y. Yoon, and H.J.J. Kim, "A Compact Lumped-Element Low Pass Filter Using Low Temperature Cofired Ceramic Technology," *J. Eur. Ceram. Soc.*, **23**, 2717-2720 (2003).

[48] K.I. Kim, J.M. Kim, J.M. Kim, G.G. Hwang, C.W. Baek, and Y.K. Kim, "Packaging for RF MEMS Devices Using LTCC Substrate and BCB Adhesive Layer," *J. Micromech. Microeng.*, **16**, 150-156 (2006).

[49] O. Dernovsek, A. Naeini, G. Preu, W. Wersing, M. Eberstein, and W.A. Schiller, "LTCC Glass-Ceramic Composites for Microwave Application," *J. Eur. Ceram. Soc.*, **21**, 1693-1697 (2001).

[50] M. Pudas, S. Viollet, F. Ruffier, A. Kruusing, S. Amic, S. Leppävuori and N. Franceschini, "A Miniature Bio-Inspired Optic Flow Sensor Based on Low Temperature Co-Fired Ceramics (LTCC) Technology," *Sensor. Actuat. A-Phys.*, **133**, 88-95 (2006).

[51] A. Baker, C. Randall, R. Stewart, R. Fantazier, and F. Wise, "Fabrication of a Multilayered Low-Temperature Cofired Ceramic Micro-Plasma-Generating Device," *Int. J. Appl. Ceram. Technol.*, **3**, 413-418 (2006).

[52] C.T. Pan and Y.J. Chen, "Application of Low Temperature Co-Fired Ceramics on In-Plane Micro-Generator," *Sensor. Actuat. A-Phys.*, **144**, 144-153 (2008).

[53] Y. Shin, O. Kim, J.C. Hong, J.H. Oh, W.J. Kim, S. Haam, and C.H. Chung, "The Development of Micro-Fuel Processor Using Low Temperature Co-Fired Ceramic (LTCC)," *Int. J. Hydrogen Energ.*, **31**, 1925-1933 (2006).

[54] B. Jaques, H. Weston, D.G. Plumlee, A.J. Moll, "Advanced Fabrication Techniques for an Ion Mobility Spectrometer for Low Temperature Co-Fired Ceramics," Proceedings of the IMAPS/ACerS 2nd International Conference and Exhibition on Ceramic Interconnect and Ceramic Microsystems Technologies (CICMT), Denver, CO, April 25-27, 2006.

[55] K.B. Pfeifer and A.N. Rumpf, "Measurement of Ion Swarm Distribution Functions in Miniature Low-Temperature Co-Fired Ceramic Ion Mobility Spectrometer Drift Tubes," *Anal. Chem.*, **77**, 5215-5220 (2005).

[56] H. Teterycz, J. Kita, R. Bauer, L.J. Golonka, B.W. Licznerski, K. Nitsch, and K. Wisniewski, "New Design of an SnO2 Gas Sensor on Low Temperature Cofiring Ceramics," *Sensor. Actuat. B-Chem.*, **47**, 100-103 (1998).

[57] T. Pisarkiewicz, A. Sutor, P. Potempa, W. Maziarz, H. Thust, and T. Thelemann, "Microsensor Based on Low Temperature Cofired Ceramics and Gas-Sensitive Thin Film," *Thin Solid Films*, **436**, 84-89 (2003).

[58] M.R. Gongora-Rubio, L.M. Sola-Laguna, P.J. Moffett, and J.J. Santiago-Aviles, "The Utilization of Low Temperature Co-Fired Ceramics LTCC-ML Technology for Meso-Scale EMS, a Simple Thermistor Based Flow Sensor," *Sensor. Actuat. A-Phys.*, **73**, 215–221 (1999).

[59] U. Schmid, "A Robust Flow Sensor for High Pressure Automotive Applications," *Sensor. Actuat. A-Phys.*, **97-98**, 253–263 (2002).

[60] M.A. Fonseca, J.M. English, M. Arx, and M.G. Allen, "Wireless Micromachined Ceramic Pressure Sensor for High-Temperature Applications," *J. Microelectromech. S.*, **11**, 337-343 (2002).

[61] M.G.H. Meijerink, E. Nieuwkoop, E.P. Veninga, M.H.H. Meuwissen, and M.W.W.J. Tijdink, "Capacitive Pressure Sensor in Post-Processing on LTCC Substrates," *Sensor. Actuat. A-Phys.*, **123-124**, 234–239 (2005).

[62] T. Voß, P. Grundler, A. Kirbs, and G.U. Flechsig, "Temperature Pulse Voltammetry: Hot Layer Electrodes Made by LTCC Technology," *Electrochem. Commun.*, **1**, 383-388 (1999).

[63] M.R. Gongora-Rubio, L.M. Sola-Laguna, M. Smith, J.J. Santiago-Aviles, "LTCC Technology Multilayer Eddy Current Proximity Sensor for Harsh Environments," Proceedings of the 32nd International Symposium on Microelectronics, IMAPS'99, Chicago, IL, October 26-28, 1999.

[64] J. Wilde and Y.Q. Lai, “Design Optimization of an Eddy Current Sensor Using the Finite-Elements Method,” *Microelectron. Reliab.*, **43**, 345-349 (2003).

[65] C.H. Newborn, J.M. English, and D.J. Coe, “LTCC Fabrication for a Leaf Spring Vertical Actuator,” *Int. J. Appl. Ceram. Technol.*, **3**, 61-67 (2006).

[66] J. Li and G.K. Ananthasuresh, “Three-Dimensional Low-Temperature Co-Fired Ceramic Shells for Miniature Systems Applications,” *J. Micromech. Microeng.*, **12**, 198-203 (2002).

[67] T. Kirchner, H. Riecke, H. Thust, L.J. Golonka, and B.W. Licznerski, “Thermal Vias in LTCC”, Proceeding of the 19th ISHM Poland Chapter Conference, Jurata, Poland, September 15-18, 1996.

[68] J. Zhong, M. Yi, and H.H. Bau, “Magneto Hydrodynamic (MHD) Pump Fabricated with Ceramic Tapes,” *Sensor. Actuat. A-Phys.*, **96**, 59-66 (2002).

[69] G.A. Groß, T. Thelemann, S. Schneider, D. Boskovic, and J.M. Kohler, “Fabrication and Fluidic Characterization of Static Micromixers Made of Low Temperature Cofired Ceramic (LTCC),” *Chem. Eng. Sci.*, **63**, 2773-2784 (2008).

[70] C.F. Chou, R. Changrani, P. Roberts, D. Sadler, J. Burdon, F. Zenhausern, S. Lin, A. Mulholland, N. Swami, and R. Terbrueggen, “A Miniaturized Cyclic PCR Device-Modeling and Experiments,” *Microelectron. Eng.*, **61-62**, 921-925 (2002).

[71] D.J. Sadler, R. Changrani, P. Roberts, C.F. Chou, and F. Zenhausern, “Thermal Management of BioMEMS Temperature Control for Ceramic-Based PCR and DNA Detection Devices,” *IEEE Trans. Compon. Packag. Technol.*, **26**, 309-317 (2003).

[72] M.R. Gongora-Rubio, M.B.A. Fontes, Z.M. Rocha, E.M. Richter, and L. Angnes, “LTCC Manifold for Heavy Metal Detection System in Biomedical and Environmental Fluids,” *Sensor. Actuat. B-Chem.*, **103**, 468-473 (2004).

[73] X. Llopis, N. Ibanez-Garcia, S. Alegret, and J. Alonson, “Pesticide Determination by Enzymatic Inhibition and Amperometric Detection in a Low-Temperature Cofired Ceramics Microsystem,” *Anal. Chem.*, **79**, 3662-3666 (2007).

[74] N. Ibanez-Garcia, M.B. Mercader, Z.M. Rocha, M.R. Gongora-Rubio, C.A. Z. J.A. Chamarro, “Continuous Flow Analytical Microsystems Based on Low-Temperature Co-Fired Ceramic Technology. Integrated Potentiometric Detection Based on Solvent Polymeric Ion-Selective Electrodes,” *Anal. Chem.*, **78**, 2985-2992 (2006).

[75] N. Ibanez-Garcia, R.D.M. Goncalves, Z.M. Rocha, M.R. Gongora-Rubio, A.C. Seabra, and J.A. Chamarro, “LTCC Meso-Analytical System for Chloride Ion Determination in Drinking Waters,” *Sensor. Actuat. B-Chem.*, **118**, 67–72 (2006).

[76] M. Goldbach, H. Axthelm, and M. Keusgen, “LTCC Based Microchips for the Electrochemical Detection of Phenolic Compounds,” *Sensor. Actuat. B-Chem.*, **120**, 346-351 (2006).

[77] L.J. Golonka, T. Zawada, J. Radojewski, H. Roguszczak, and M. Stefanow, ‘‘LTCC Microfluidic System,’’ *Int. J. Appl. Ceram. Technol.*, **3**, 150–156 (2006).

[78] L.J. Golonka, H. Roguszczak, T. Zawada, J. Radojewski, I. Grabowska, M. Chudy, A. Dybko, Z. Brzozka, and D. Stadnik, “LTCC Based Microfluidic System with Optical Detection,” *Sensor. Actuat. B-Chem.*, **111-112**, 396-402 (2005).

[79] V. Moilanen, A. Kemppainen, J. Malinen, M. Kansakoski, and R. Marbach, “Multiplexed Read-Out Electronics Implemented on LTCC Substrate for PbS Array,” *Meas. Sci. Technol.*, **15**, 2188-2192 (2004).

[80] Y. Fournier, T. Maeder, G. Boutinard-Rouelle, A. Barras, N. Craquelin, and P. Ryser, “Integrated LTCC Pressure/Flow/Temperature Multisensor for Compressed Air Diagnostics,” *Sensors*, **10**, 11156-11173 (2010).

[81] B. Jaffe, W.R. Cook Jr., and H. Jaffe, *Piezoelectric Ceramics*, 7-21, Academic Press Inc., New York, NY, 1971.

[82] G.A. Rossetti, “Structure and Bonding in $PbZrO_3$-$PbTiO_3$ (PZT) Alloys,” *Brit. Ceram. T.*, **103**, 83-87 (2004).

[83] C.L. Huang, B.H. Chen, and L. Wu, “Variability of Impurity Doping in the Modified Pb(Zr, Ti)O_3 Ceramics of Type ABO_3,” *Solid State Commun.*, **130**, 19-23 (2004).

[84] B.W. Lee and E.J. Lee, “Effects of Complex Doping on Microstructural and Electrical Properties of PZT Ceramics,” *J. Electroceram.*, **17**, 597-602 (2006).

[85] Z.H. Wang, J.M. Miao, C.W. Tan, T. Xu, “Fabrication of Piezoelectric MEMS Devices-from Thin Film to Bulk PZT Wafer,” *J. Electroceram.*, **24**, 25-32 (2010).

[86] Kistler Knowledge Base, *The Piezoelectric Effect – Longitudinal Effect*, Kistler, Amherst, NY.

[87] American National Standards Institute/The Institute of Electrical and Electronics Engineers, *IEEE Standard Definition of Primary Ferroelectric Terms*, The Institute of Electrical and Electronics Engineers, Inc., New York, NY, 1985.

[88] L.E. Cross and R.E. Newnham, “History of Ferroelectrics,” Ceramics and Civilization, Volume III. High-Technology Ceramics-Past, Present, and Future, ed. W.D. Kingery. The American Ceramic Society, Inc., Westerville, OH, 1987.

[89] W.D. Kingery, H.K. Bowen, and D.R. Uhlmann, *Introduction to Ceramics*, Second Edition, 964-972, John Wiley & Sons, Inc., New York, NY, 1976.

[90] D. Damjanovic, “Ferroelectric, Dielectric and Piezoelectric Properties of Ferroelectric Thin Films and Ceramic,” *Rep. Prog. Phys.*, **61**, 1267-1324 (1998).

[91] R.E. Newnham, *Properties of Materials*, 87-102, Oxford University Press Inc., New York, NY, 2005.

[92] H.F. Kay and P. Vousdan, “*Symmetry Changes* in *Barium Titanate* at *Low Temperatures* and Their Relation to its Ferroelectric Properties,” *Phil. Mag.*, **7**, 1019-1040 (1949).

[93] W.J. Merz, “The Electric and Optical Behavior of $BaTiO_3$ Single-Domain Crystals,” *Phys. Rev.*, **76**, 1221-1230 (1949).

[94] G. Shirane, K. Suzuki, and A. Takeda, “Ferroelectricity versus Antiferroelectricity in the Solid Solutions of $PbZrO_3$ and $PbTiO_3$,” *J. Phys. Soc. Jpn.*, **8**, 615-629 (1953).

[95] D.A. Berlincourt, C. Cmolik, and H. Jaffe, “Piezoelectric Properties of Polycrystalline Lead Titanate Zirconate Compositions,” *Proc. IRE*, **48**, 220-229 (1960).

[96] B. Jaffe, R.S. Roth, S. Marzullo, “Piezoelectric Properties of Lead Zirconate-Lead Titanate Solid-Solution Ceramics,” *J. Appl. Phys.*, **25**, 809-810 (1954).

[97] C. Li, K.C.K. Soh, and P. Wu, “Formability of ABO_3 Perovskite,” *J. Alloy. Compd.*, **372**, 40-48 (2004).

[98] R.E. Eitel, C.A. Randall, T.R. Shrout, P.W. Rehrig, W. Hackenberger, and S.E. Park, "New High Temperature Morphotropic Phase Boundary Piezoelectrics Based on Bi(Me)O_3-$PbTiO_3$ Ceramics," *Jpn. J. Appl. Phys.*, **40**, 5999-6002 (2001).

[99] C. Michel, J.M. Moreau, G.D. Achenbach, R. Gerson, and W.J. James, "Atomic Structures of Two Rhombohedral Ferroelectric Phases in the Pb(Zr, Ti)O_3 Solid Solution Series," *Solid State Commun.*, **7**, 865-868 (1969).

[100] H.M. Barnet, "Evidence for a New Phase Boundary in the Ferroelectric Lead Zirconate-Lead Titanate System," *J. Appl. Phys.*, **33**, 1606-1607 (1962).

[101] T. Yamamoto, "Ferroelectric Properties of the $PdZrO_3$-$PdTiO_3$ System," *Jpn. J. Appl. Phys.*, **35**, 5104-5108 (1996).

[102] F. Kulcsar, "Electromechanical Properties of Lead Titanate Zirconate Ceramics with Lead Partially Replaced by Calcium or Strontium," *J. Am. Ceram. Soc.*, **42**, 49-51 (1959).

[103] R. Roy, "Multiple Ion Substitution in the Perovskite Lattice," *J. Am. Ceram. Soc.*, **37**, 581-588 (1954).

[104] B. Noheda, D.E. Cox, G. Shirane, J.A. Gonzalo, L.E. Cross, and S.E. Park, "A Monoclinic Ferroelectric Phase in the $Pb(Zr_{1-x}, Ti_x)O_3$ Solid Solution," *Appl. Phys. Lett.*, **74**, 2059-2061 (1999).

[105] B. Noheda, J.A. Gonzalo, L.E. Cross, R. Guo, S.E. Park, D.E. Cox, and G. Shirane, "Tetragonal-to-Monoclinic Phase Transition in a Ferroelectric Perovskite: The Structure of $PbZr_{0.52}Ti_{0.48}O_3$," *Phys. Rev. B*, **61**, 8687-8695 (2000).

[106] B. Noheda, D.E. Cox, G. Shirane, R. Guo, B. Jones, and L.E. Cross, "Stability of the Monoclinic Phase in the Ferroelectric Perovskite $PbZr_{1-x}Ti_xO_3$," *Phys. Rev. B*, **63**, 014103 (2001).

[107] R.B. Atkins, R.L. Holman, R.M. Fulrath, "Substitution of Bi and Nb Ions in Lead Zirconate-Titanate," *J. Am. Ceram. Soc.*, **54**, 113-115 (1971).

[108] A. Suárez-Gómez, F. Calderón-Piñar, M.D. Durruthy, A. Peláiz-Barranco, J. Saniger-Blesa, and J. de Frutos, "Characterization of PZT (54/46) Ferroelectric Ceramics under the Influence of a 'Soft' Double Modification with La and Nb," *Phys. Stat. Sol.*, **242**, 1892-1896 (2005).

[109] K.L. Yadav and R.N.P. Choudhary, "Piezoelectric Properties of Modified PZT Ceramics," *Ferroelectrics*, **325**, 87-94 (2005).

[110] J.F. Chang and S.B. Desu, "Effects of Dopants in PZT Films," *J. Mater. Rev.*, **9**, 955-969 (1994).

[111] H. Jaffe and D.A. Berlincourt, "Piezoelectric Transducer Materials," *Proceedings of the IEEE*, **53**, 1372-1386 (1965).

[112] C. Ahn, H. Song, S. Nahm, S. Priya, S. Park, K. Uchino, H. Lee, and H. Lee, "Effect of ZnO and CuO on the Sintering Temperature and Piezoelectric Properties of a Hard Piezoelectric Ceramic," *J. Am. Ceram. Soc.*, **89**, 921-925 (2006).

[113] C.A. Randall, N. Kim, J.P Kucera, W.W. Cao, and T.R. Shrout, "Intrinsic and Extrinsic Size Effects in Fine-Grained Morphotropic-Phase-Boundary Lead Zirconate Titanate Ceramics," *J. Am. Ceram. Soc.*, **81**, 677-688 (1998).

[114] I.Y. Shen, G.Z. Cao, C.C. Wu, and C.C. Lee, "PZT Thin-Film Meso- and Micro Devices," *Ferroelectrics*, **342**, 15-34 (2006).

[115] T.B. Myers, S. Bose, A. Bandyopadhyay, and J.D. Fraser, "Micromachining of PZT-Based MEMS," *Am. Ceram. Soc. Bull.*, **82**, 30-34 (2003).

[116] R.A. Dorey and R.W. Whatmore, "Electroceramic Thick Film Fabrication for MEMS," *J. Electroceram.*, **12**, 19-32 (2004).

[117] Z. Wang, W. Zhu, C. Chao, C. Zhao, and X. Chen, "Characterization of Composite Piezoelectric Thick Film for MEMS Application," *Surf. Coat. Tech.*, **198**, 384-388 (2005).

[118] K. Tanaka, T. Konishi, M. Ide, Z. Meng, and S. Sugiyama, "Fabrication of Microdevices Using Bulk Ceramics of Lead Zirconate Titanate," *Jpn. J. Appl. Phys.*, **44**, 7068-7071 (2005).

[119] H.D. Chen, K.R. Udayakumar, C.J. Gaskey, L.E. Cross, J.J. Bemstein, and L.C. Niles, "Fabrication and Electrical Properties of Lead Zirconate Titanate Thick Films," *J. Am. Ceram. Soc.*, **79**, 2189-2192 (1996).

[120] H.D. Chen, K.R. Udayakumar, L.E. Cross, J.J. Bemstein, and L.C. Niles, "Dielectric, Ferroelectric, and Piezoelectric Properties of Lead Zirconate Titanate Thick Films on Silicon Substrates," *J. Appl. Phys.*, **77**, 3349-3353 (1995).

[121] A. Lozinski, F. Wang, A. Uusimaki, and S. Leppavuori, "PLZT Thick Films for Pyroelectric Sensors," *Meas. Sci. Technol.*, **8**, 33-37 (1997).

[122] C. Lucat, F. Menil, and R. Von Der Muhll, "Thick-film densification for pyroelectric sensors," *Meas. Sci. Technol.*, **8**, 38-41 (1997).

[123] S. Le Dren, L. Simon, P. Gonnard, M. Troccaz, and A. Nicolas, "Investigation of Factors Affecting the Preparation of PZT Thick Films," *Mat. Res. Bull.*, **35**, 2037-2045 (2000).

[124] E.S. Thiele, D. Damjanovic, and N. Setter, "Processing and Properties of Screen-Printed Lead Zirconate Titanate Piezoelectric Thick Films on Electroded Silicon," *J. Am. Ceram. Soc.*, **84**, 2863-2868 (2001).

[125] K. Yao and W. Zhu, "Improved Preparation Procedure and Properties for a Multilayer Piezoelectric Thick-Film Actuator," *Sensor. Actuat. A-Phys.*, **71**, 139-143 (1998).

[126] J.J. Choi, J.H. Jang, B.D. Hahn, D.S. Park, W.H. Yoon, J. Ryu, and C. Park, "Preparation of Highly Dense PZN-PZT Thick Films by the Aerosol Deposition Method Using Excess-PbO Powder," *J. Am. Ceram. Soc.*, **90**, 3389-3394 (2007).

[127] T.Y. Kwon, J.H. Park, Y.B. Kim, D.S. Yoon, C.I. Cheon, H.L. Lee, T.S. Kim, "Preparation of Piezoelectric $0.1Pb(Zn_{0.5}W_{0.5})O_3$–$0.9Pb(Zr_{0.5}Ti_{0.5})O_3$ Solid Solution and Thick Films for Low Temperature Firing on a Si-Substrate," *J. Cryst. Growth*, **295**, 172-178 (2006).

[128] T. Tsurumi, S. Ozawa, G. Abe, N. Ohashi, S. Wada, and M. Yamane, "Preparation of $Pb(Zr_{0.53,}\ Ti_{0.47})O_3$ Thick Films by an Interfacial Polymerization Method on Silicon Substrates and Their Electric and Piezoelectric Properties," *Jpn. J. Appl. Phy.*, **39**, 5604-5608 (2000).

[129] F. Dauchy and R.A. Dorey, "Patterned Crack Free PZT Thick Films for Micro Electromechanical System Applications," *Int. J. Adv. Manuf. Technol.*, **33**, 86-94 (2007).

[130] R.A. Dorey, R.W. Whatmore, S.P. Beeby, R.N. Torah, and N.M. White, "Screen Printed PZT Thick Films Using Composite Film Technology," *Integr. Ferroelectr.*, **54**, 651-658 (2003).

[131] R.A. Dorey, S.B. Stringfellow and R.W. Whatmore, "Effect of Sintering Aid and Repeated Sol Infiltrations on the Dielectric and Piezoelectric Properties of a PZT Composite Thick Film," *J. Eur. Ceram. Soc.*, **22**, 2912-2916 (2002).

[132] R. Kurchania and S.J. Milne, "Characterization of Sol-Gel $Pb(Zr_{0.53}Ti_{0.47})O_3$ Films in the Thickness Range 0.25-10 μm," *J. Mater. Res.*, **14**, 1852-1858 (1999).

[133] A. Teeramongkonrasmee, T. Tanaka, H. Miyoshi, S. Aoyagi, K. Yamashita, Y. Suzuki, and M. Okuyama, "(111) Preferred Oriented $Pb(Zr, Ti)O_3$ Thick Film Prepared by Multilayer Process and Its Application to Ultrasonic Sensors," *Jpn. J. Appl. Phys.*, **43**, 7207-7212 (2004).

[134] S.P. Beeby and N.M. White, "Thick-Film PTZ-Silicon Micromechanical Resonator," *Electron. Lett.*, **36**, 1661-1662 (2000).

[135] M. Ferrari, V. Ferrari, D. Marioli, A. Taroni, M. Suman, and E. Dalcanale, "Cavitand-Coated PZT Resonant Piezo-Layer Sensors: Properties, Structure, and Comparison with QCM Sensors at Different Temperatures under Exposure to Organic Vapors," *Sensor. Actuat. B-Chem.*, **103**, 240-246 (2004).

[136] M. Koch, N.R. Harris, R. Maas, A.G.R. Evans, N.M. White, and A. Brunnschweiler, "A Novel Micropump Design with Thick-Film Piezoelectric Actuation," *Meas. Sci. Technol.*, **8**, 49-57 (1997).

[137] R.N. Torah, S.P. Beeby, M.J. Tudor, and N.M. White, "Thick-Film Piezoceramics and Devices," *J. Electroceram.*, **19**, 95-110 (2007).

[138] L.A. Liew, W. Zhang, L. An, S. Shah, R. Luo, Y. Liu, T. Cross, M.L. Dunn, V. Bright, J.W. Daily, R. Raj, and K. Anseth, "Ceramic MEMS-New Materials, Innovative Processing and Future Applications," *Am. Ceram. Soc. Bull.*, **80**, 25-30 (2001).

[139] M.S. Zarnik, D. Belavic, H. Ursic, and S. Macek, "Numerical Modelling of Ceramic MEMS Structures with Piezoceramic Thick Films," *J. Electroceram.*, **20**, 3-9 (2008).

[140] J. Juuti, A. Lozinski, and S. Leppavuori, "LTCC Compatible PLZT Thick Films for Piezoelectric Devices," *Sensor. Actuat. A-Phys.*, **110**, 361-364 (2004).

[141] K. Sivanandan, A.T. Achuthan, V. Kumar, and I. Kanno, "Fabrication and Transverse Piezoelectric Characteristics of PZT Thick-Film Actuators on Alumina Substrates," *Sensor. Actuat. A-Phys.*, **148**, 134-137 (2008).

[142] M. Kosec, H. Ursic, J. Holc, M. Hrovat, D. Kuscer, and B. Malic, "High-Performance PMN-PT Thick Films," *IEEE T. Ultrason. Ferr.*, **57**, 2205-2212 (2010).

[143] G. Natarajan and J.N. Humernik, "3D Ceramic Microfluidic Device Manufacturing," *J. Phys. Conference Series*, **34**, 533-539 (2006).

[144] J.H. Yoo, J.M. Hwang, S.H. Lee, K.H. Chung, and H.G. Lee, "Piezoelectric and Dielectric Characteristics of Low Temperature Sintering $Pb(Ni_{1/3}Nb_{2/3})O_3$-$Pb(Mn_{1/3}Nb_{2/3})O_3$-$Pb(Zr_{1/2}Ti_{1/2})O_3$ Ceramics for Multilayer Piezoelectric Actuator," *J. Electroceram.*, **17**, 525-529 (2006).

[145] J.H. Moon, H.M. Jang, and B.D. You, "Densification Behaviors and Piezoelectric Properties of MnO_2, SiO_2-Doped $Pb(Ni_{1/3}Nb_{2/3})O_3$-$PbTiO_3$-$PbZrO_3$ Ceramics," *J. Mater. Res.*, **8**, 3184-3191 (1993).

[146] S. Kaneko, D.Z. Dong, K. Murakami, "Effect of Simultaneous Addition of $BiFeO_3$ and $Ba(Cu_{0.5}W_{0.5})O_3$ on Lowering of Sintering Temperature of Pb(Zr, Ti)O_3 Ceramics," *J. Am. Ceram. Soc.*, **81**, 1013-1018 (1998).

[147] M. Hrovat, J. Holc, S. Drnovsek, D. Belavic, J. Bernard, M. Kosec, L. Golonka, A. Dziedzic, and J. Kita, "Characterization of PZT Thick Films Fired on LTCC Substrates," *J. Mate. Sci. Lett.*, **22**, 1193-1195 (2003).

[148] L.J. Golonka, M. Buczek, M. Hrovat, and D. Belavic, "Properties of PZT Thick Films Made on LTCC," *Microelectron. Int.*, **22**, 13-16 (2005).

[149] D. Belavic, M.S. Zarnik, J. Holc, M. Hrovat, M. Kosec, S. Drnovsek, J. Cilensek, and S. Macek, "Properties of Lead Zirconate Titanate Thick-Film Piezoelectric Actuators on Ceramic Substrates," *Int. J. Appl. Ceram. Technol.*, **3**, 448-454 (2006).

[150] H. Ursic, M. Lowe, M. Stewart, M. Hrovat, D. Belavic, J. Holc, M.S. Zarnik, M. Kosec, and M. Cain, "PZT Thick Films on Different Ceramic Substrates: Piezoelectric Measurements," *J. Electroceram.*, **20**, 11-16 (2008).

[151] D. Belavic, M. Hrovat, M.S. Zarnik, J. Holc, and M. Kosec, "An Investigation of Thick Films for Sensor Applications: A Case Study with Different Electrode Materials," *J. Electroceram.*, **23**, 1-5 (2009).

[152] A. Bochenek, B. Bober, A. Dziedzic, and L. Golonka, "Investigation of Assembly Properties of Conductive Layers in LTCC Circuits," *Microelectron. Int.*, **18**, 11-15 (2001).

[153] M. Hrovat, D. Belavic, J. Kita, J. Holc, S. Drnovsek, J. Cilensek, L. Golonka, and A. Dziedzic, "Thick-Film Strain and Temperature Sensors on LTCC Substrate," *Microelectron. Int.*, **23**, 33-41 (2005).

[154] T. Rabe, W.A. Schiller, T. Hochheimer, C. Modes, and A. Kipka, "Zero Shrinkage of LTCC by Self-Constrained Sintering," *Int. J. Appl. Ceram. Technol.*, **2**, 374-382 (2005).

[155] F. Lautzenhiser and E. Amaya, "Self-Constrained LTCC Tapes," *Am. Ceram. Soc. Bull.*, **81**, 27-32 (2002).

[156] M. Hrovat, D. Belavic, H. Ursic, J. Kita, J. Holc, S. Drnovsek, J. Cilensek, M. Kosec, and R. Moos, "An Investigation of Thick-Film Materials for Temperature and Pressure Sensors on Self-Constrained LTCC Substrates," Proceedings of 2nd Electronics System Integration Technology Conference, Greenwich, UK, September 1-4, 2008.

[157] N.J. Donnelly, T.R. Shrout and C.A. Randall, "Properties of (1-x)PZT-xSKN Ceramics Sintered at Low Temperature Using Li_2CO_3," *J. Am. Ceram. Soc.*, **91**, 2182-2188 (2008).

[158] S. Kemethmuller, M. Hagymasi, A. Stiegelschmitt, and A. Roosen, "Viscous Flow as the Driving Force for the Densification of Low Temperature Co-Fired Ceramics," *J. Am. Ceram. Soc.*, **90**, 64-70 (2007).

[159] M.N. Rahaman, *Ceramic Processing and Sintering*, Second Edition, 425-684, CRC Press, Taylor & Francis Group, LLC, Boca Raton, FL, 2003.

[160] W.D. Kingery, H.K. Bowen, and D.R. Uhlmann, *Introduction to Ceramics*, Second Edition, 469-490, John Wiley & Sons, Inc., New York, NY, 1976.

[161] R.L. Coble, "Sintering Crystalline Solids. I. Intermediate and Final State Diffusion Models," *J. Appl. Phys.*, **32**, 787-792 (1961).

[162] R.L. Coble, "Sintering Crystalline Solids. II. Experimental Test of Diffusion Models in Powder Compacts," *J. Appl. Phys.*, **32**, 793-799 (1961).

[163] D.L. Johnson, "New Method of Obtaining Volume, Grain-Boundary, and Surface Diffusion Coefficients from Sintering Data," *J. Appl. Phys.*, **40**, 192-200 (1969).

[164] W.D. Kingery and M. Berg, "Study of the Initial Stages of Sintering Solids by Viscous Flow, Evaporation-Condensation, and Self-Diffusion," *J. Appl. Phys.*, **26**, 1205-1212 (1955).

[165] G.C. Kuczynski, "Study of the Sintering of Glass," *J. Appl. Phys.*, **20**, 1160-1163 (1949).

[166] H.E. Exner, "Principles of Single-Phase Sintering," *Rev. Powder Metall. Ceram.*, **1**, 1-4 (1979).

[167] J. Svoboda and H. Riedel, "New Solutions Describing the Formation of Interparticle Necks in Solid-State sintering," *Acta Mater.*, **43**, 1-10 (1995).

[168] M.W. Barsoum, *Fundamentals of Ceramics*, 331-380, The McGraw-Hill Companies, Inc., New York, NY, 1997.

[169] D.L. Johnson, "Fundamentals of the Sintering of Ceramics," Processing of Crystalline Ceramics, eds. H. Palmour, R.F. Davis, and T.M. Hare. Plenum Press Inc., New York, NY, 137-149, 1978.

[170] W.S. Coblenz, J.M. Cannon, R.L. Coble, "Initial Stage Solid State Sintering Models: a Critical Analysis and Assessment," *Mater. Sci. Res.*, **13**, 141-157 (1980).

[171] D.L. Johnson, "A General Model for the Intermediate Stage of Sintering," *J. Am. Ceram. Soc.*, **53**, 574-577 (1970).

[172] T.A. Ring, *Fundamentals of Ceramic Powder Processing and Synthesis*, 777-874, Academic Press Inc., San Diego, CA, 1996.

[173] W.D. Kingery, "Densification during Sintering in the Presence of a Liquid Phase: I. Theory," *J. Appl. Phys.*, **30**, 301-306 (1959).

[174] W.D. Kingery and M.D. Narasimhan, "Densification during Sintering in the Presence of a Liquid Phase: II. Experimental," *J. Appl. Phys.*, **30**, 307-312 (1959).

[175] R.M. German, *Liquid Phase Sintering*, 65-151, Plenum Press Inc., New York, NY, 1985.

[176] J. Frenkel, "Viscous Flow of Crystalline Bodies under the Action of Surface Tension," *J. Phys. USSR*, **62**, 385–91 (1945).

[177] J.K. Mackenzie and R. Shuttleworth, "Phenomenological Theory of Sintering," *Proc. Phys. Soc.*, **62**, 833-852 (1949).

[178] G.W. Scherer, "Sintering Inhomogeneous Glasses: Application to Optical Waveguide," *J. Non-cryst. Solids*, **34**, 234-256 (1979).

[179] A. Mohanram, Co-Sintering of Integrated Ceramics: Fundamentals, Observation and Design Guidelines, Ph.D. Dissertation, Pennsylvania State University, 2005.

[180] K. G. Ewsuk, L. W. Harrision, and F. J. Walczak, "Sintering Glass-Filled Ceramic Composites; Effects of Glass Properties," *Ceram. Trans. Ceram. Powder Sci. II*, **1**, 969-77 (1987).

[181] K. G. Ewsuk, "Ceramic-Filled-Glass Composite Sintering," *Ceram. Trans. Mater. Processes Microelectr. Syst.*, **15**, 279-95 (1989).

[182] W.S. Hackenberger, Reduction of Sintering Damage and Differential Densification in a Low Temperature Cofired Electronic Substrate Using Rate Controlled Sintering, Ph.D. Dissertation, Pennsylvania State University, 1995.

[183] R.K. Bordia and G.W. Scherer, "On Constrained Sintering – I. Constitutive Model for a Sintering Body", *Acta. Metall.*, **36**, 2393-2397 (1988); R.K. Bordia and G.W. Scherer, "On Constrained Sintering – II. Comparison of Constitutive Models", *Acta. Metall.*, **36**, 2398-2410 (1988); R.K. Bordia and G.W. Scherer, "On Constrained Sintering – III. Rigid Inclusions", *Acta. Metall.*, **36**, 2411-2416 (1988).

[184] E.A. Olevsky, "Theory of Sintering: From Discrete to Continuum," *Mater. Sci. Eng. R.*, **23**, 41-100 (1998).

[185] R. Raj and R.K. Bordia, "Sintering Behaviors of Bi-Modal Powder Compacts," *Acta. Metall.*, **32**, 1003-1019 (1984).

[186] T. Cheng and R. Raj, "Flaw Generation During Constrained Sintering of Metal-Ceramic and Metal-Glass Multilayer Films," *J. Am. Ceram. Soc.*, **72**, 1649-1655 (1989).

[187] J.H. Jean and C.R. Chang, "Camber Development during Cofiring Ag-Based Low-Dielectric-Constant Ceramic Package," *J. Mater. Res.*, **12**, 2743-2750 (1997).

[188] A. Mohanram, S.H. Lee, G.L. Messing, and D.J. Green, "Constrained Sintering of Low-Temperature Co-Fired Ceramics," *J. Am. Ceram. Soc.*, **89**, 574-577 (2006).

[189] S.M. Lee and M.J. Yoo, "Near Zero Shrinkage of an Low-Temperature Co-Fired Ceramic Package by Constrained Sintering Using Screen Printed Alumina Paste," *Int. J. Appl. Ceram. Technol.*, **7**, E9-E15 (2010).

[190] P. Gravesen, J. Branebjerg, and O.S. Jensen, "Microfluidics – A Review," *J. Micromech. Microeng.*, **3**, 168-182 (1993).

[191] R.M. Von Dam, Solvent-Resistant Elastomeric Microfluidic Devices and Applications, Ph.D. Dissertation, California Institute of Technology, 2005.

[192] R. Zengerle and H. Sandmaier, "Microfluidics," Proceedings of the 7th International Symposium on Micro Machine and Human Science, Nagoya, Japan, October 2-4, 1996.

[193] S. Shoji and M. Masayoshi, "Microflow Devices and Systems," *J. Micromech. Microeng.*, **4**, 157-171 (1994).

[194] J. Wang, L. Ren, L. Li, W. Liu, J. Zhou, W. Yu, D. Tong, and S. Chen, "Microfluidics: A New Cosset for Neurobiology," *Lab Chip*, **9**, 644-652 (2009).

[195] EMMA Report 2009, *Emerging Market for Microfluidic Applications in Life Sciences and In-Vitro Diagnostics*, Yole Inc., Mahwah, NJ, 2009.

[196] J. Antencia and D.J. Beebe, "Controlled microfluidic interfaces," *Nature*, **437**, 648-655 (2005).

[197] H.A. Stone, A.D. Stroock, and A. Ajdari, "Engineering Flows in Small Devices: Microfluidics Toward a Lab-on-a-Chip," *Annu. Rev. Fluid Mech.*, **36**, 381-411 (2004).

[198] T. Thorsen, S.J. Maerkl, and S.R. Quake, "Microfluidic Large-Scale Integration," *Science*, **298**, 580-584 (2002).

[199] J.G. Smits, "Piezoelectric Micropump with Three Valves Working Peristaltically," *Sensor. Actuat. A-Phys.*, **21**, 203-206 (1990).
[200] P. Woias, "Micropumps – Summarizing the First Two Decades," *Proc. SPIE*, **4560**, 39-52 (2001).
[201] P. Woias, "Micropumps – Past, Progress and Future Prospects," *Sensor. Actuat. B-Chem.*, **105**, 28-38 (2005).
[202] D.J. Laser and J.G. Santiago, "A Review of Micropumps," *J. Micromech. Microeng.*, **14**, R35-R64 (2004).
[203] N.C. Tsai and C.Y. Sue, "Reviews of MEMS-Based Drug Delivery and Dosing Systems," *Sensor. Actuat. A-Phys.*, **134**, 555-564 (2007).
[204] A. Nisar, N. Afzulpurkar, B. Mahaisavariya, and A. Tuantranont, "MEMS-Based Micropumps in Drug Delivery and Biomedical Applications," *Sensor. Actuat. B-Chem.*, **130**, 917-942 (2008).
[205] L. Chen, S. Lee, J. Choo, and E.K. Lee, "Continuous Dynamic Flow Micropumps for Microfluid Manipulation," *J. Micromech. Microeng.*, **18**, 013001 (2008).
[206] Y.C. Hsu, J.L. Hsu, and N.B. Le, "An Experimental and Numerical Investigation into the Effects of the PZT Actuator Shape in Polymethylmethacrylate (PMMA) Peristaltic Micropumps," *Microsyst. Technol.*, **15**, 565-571 (2009).
[207] L.S. Jang and W.H. Kan, "Peristaltic Piezoelectric Micropump System for Biomedical Applications," *Biomed. Microdevices*, **9**, 619-626 (2007).
[208] J.S. Yoon, J.W. Choi, I.H. Lee, and M.S. Kim, "A Valveless Micropump for Bidirectional Applications," *Sensor. Actuat. A-Phys.*, **135**, 833-838 (2007).
[209] M. Pham, T.T. Nguyen, and N.S. Goo, "Development of a Peristaltic Micropump for Bio-Medical Applications Based on Mini LIPCA," Proceedings of International Conference on Intelligent Unmanned System (ICIUS 2007), Bali, Indonesia, October 24-25, 2007.
[210] D.S. Lee, J.S. Ko, and Y.T. Kim, "Bidirectional Pumping Properties of a Peristaltic Piezoelectric Micropump with Simple Design and Chemical Resistance," *Thin Solid Films*, **468**, 285-290 (2004).
[211] C.G.J. Schabmueller, M. Koch, M.E. Mokhtari, A.G.R. Evans, A. Brunnschweiler, and H. Sehr, "Self-Aligning Gas/Liquid Micropump," *J. Micromech. Microeng.*, **12**, 420-424 (2002).
[212] M. Richter, R. Linnemann, and P. Woias, "Robust Design of Gas and Liquid Micropumps," *Sensor. Actuat. A-Phys.*, **68**, 480-486 (1998).
[213] M. Koch, N. Harris, A.G.R. Evans, N.M. White, and A. Brunnschweiler, "A Novel Micromachined Pump Based on Thick-Film Piezoelectric Actuation," *Sensor. Actuat. A-Phys.*, **70**, 98-103 (1998).
[214] A. Olsson, P. Enoksson, G. Stemme, and E. Stemme, "Micromachined Flat-Walled Valveless Diffuser Pumps," *J. Microelectromech. Syst.*, **6**, 161-166, (1997).
[215] M. Stehr, S. Messner, H. Sandmaier, and R. Zengerle, "The VAMP: A New Device for Handling Liquids or Gases," *Sensor. Actuat. A-Phys.*, **57**, 153-157 (1996).
[216] A. Olsson, G. Stemme, and E. Stemme, "A Valve-Less Planar Fluid Pump with Two Pump Chambers," *Sensor. Actuat. A-Phys.*, **47**, 549-556 (1995).

[217] J. Xie, J. Shih, Q. Lin, B. Yang, and Y.C. Tai, "Surface Micromachined Electrostatically Actuated Micro-Peristaltic Pump," *Lab Chip*, **4**, 495-501 (2004).

[218] R. Zengerle, J. Ulrich, S. Kluge, M. Richter, and A. Richter, "A Bidirectional Silicon Micropump," *Sensor. Actuat. A-Phys.*, **50**, 81-86 (1995).

[219] B.T. Chia, H.H. Liao, and Y.J. Yang, "A Novel Thermo-Pneumatic Peristaltic Micropump with Low Temperature Elevation on Working Fluid," *Sensor. Actuat. A-Phys.*, **165**, 86-93 (2011).

[220] W. Mamanee, A. Tuantanont, N.V. Afzulpurkar, N. Porntheerapat, S. Rahong, and A. Wisitsoraat, "PDMS Based Thermopnuematic Peristaltic Micropump for Microfluidic Systems," *J. Phys.: Conf. Ser.*, **34**, 564-569 (2006).

[221] A. Wego and L. Pagel, "A Self-Filling Micropump Based on PCB Technology," *Sensor. Actuat. A-Phys.*, **88**, 220-226 (2001).

[222] W.K. Schomburg, J. Vollmer, B. Bustgens, J. Fahrenberg, H. Hein, and W. Menz, "Microfluidic Component in LIGA Technique," *J. Micromech. Microeng.*, **4**, 186-191 (1994).

[223] C.Y. Lee, H.T. Chang, and C.Y. Wen, "A MEMS-Based Valveless Impedance Pump Utilizing Electromagnetic Actuation," *J. Micromech. Microeng.*, **18**, 035044 (2008).

[224] S. Bohm, W. Olthuis, and P. Bergveld, "A Plastic Micropump Constructed with Conventional Techniques and Materials," *Sensor. Actuat. A-Phys.*, **77**, 223-228 (1999).

[225] W.H. Grover, A.M. Skelley, C.N. Liu, E.T. Lagally, and R.A. Mathies, "Monolithic Membrane Valves and Diaphragm Pumps for Practical Large-Scale Integration into Glass Microfluidic Devices," *Sensor. Actuat. B-Chem.*, **89**, 315-323 (2003).

[226] J.M. Berg, R.C. Anderson, M. Anaya, B. Lalouh, M. Holtz, and T. Dallas, "A Two Stage Discrete Peristaltic Micropump," *Sensor. Actuat. A-Phys.*, **104**, 6-10 (2003).

[227] K.S. Yun, I.J. Cho, J.U. Bu, C.J. Kim, and E. Yoon, "A Surface-Tension Driven Micropump for Low-Voltage and Low-Power Operations," *J. Microelectromech. Syst.*, **11**, 454-461 (2002).

[228] J. Darabi, M. Rada, M. Ohadi, and J. Lawler, "Design, Fabrication and Testing of an Electrohydrodynamic Ion-Drag Micropump," *J. Microelectromech. Syst.*, **11**, 684-690 (2002).

[229] S.H. Ahn and Y.K. Kim, "Fabrication and Experiment of a Planar Micro Ion Drag Pump," *Sensor. Actuat. A-Phys.*, **70**, 1-5 (1998).

[230] Q. Lu and G.E. Collins, "Lab on a Chip Packing of Submicron Particles for High Performance EOF Pumping," *J. Chromatogr. A*, **1217**, 7153-7157 (2010).

[231] P. Wang, Z. Chen, and H.C. Chang, "A New Electro-Osmotic Based on Silica Monoliths," *Sensor. Actuat. B-Chem.*, **113**, 500-509 (2006).

[232] C.H. Chen and J.G. Santiago, "A Planar Electroosmotic Micropump," *J. Microelectromech. Syst.*, **11**, 672-683 (2002).

[233] S.L. Zeng, C.H. Chen, J.C. Mikkelsen, and J.G. Santiago, "Fabrication and Characterization of Electroosmotic Micropumps," *Sensor. Actuat. B-Chem.*, **79**, 107-114 (2001).

[234] W.E. Gan, L. Yang, Y.Z. He, R.H. Zeng, M.L. Cervera, and M. de la Guardia, "Mechanism of Porous Core Electroosmotic Pump Flow Injection System and Its Application to Determination of Chromium (VI) in Waste-Water," *Talanta*, **51**, 667-675 (2000).

[235] P.H. Paul, D.W. Arnold, and D.J. Rakestraw, "Electrokinetic Generation of High Pressures Using Porous Microstructures," Proceedings of International Symposium on Micro-Total Analysis Systems (μ–TAS 98'), Banff, Canada, October 13-16, 1998.

[236] S.H. Chiua and C.H. Liu, "An Air-Bubble-Actuated Micropump for On-Chip Blood Transportation," *Lab Chip*, **9**, 1524-1533 (2009).

[237] H.J. Kang and B. Choi, "Development of the MHD Micropump with Mixing Function," *Sensor. Actuat. A-Phys.*, **165**, 439-446 (2011).

[238] J.S. Jang and S.S. Lee, "Theoretical and Experimental Study of MHD Micropump," *Sensors Actuat. A-Phys.*, **80**, 84-89 (2000).

[239] L. Huang, W. Wang, M.C. Murphy, K. Lian, and Z.G. Ling, "LIGA Fabrication and Test of a DC Type Magnetohydrodynamic (MHD) Micropump," *Microsyst. Technol.*, **6**, 235-240 (2000).

[240] B.D. Iverson and S.V. Garimella, "Experimental Characterization of Induction Electrohydrodynamics for Integrated Microchannel Pumping," *J. Micromech. Microeng.*, **19**, 055015 (2009).

[241] F. Trenkle, S. Haeberle, and R. Zengerle, "Normally Closed Peristaltic Micropump with Re-Usable Actuator and Disposable Fluid Chip," *Sensor. Actuat. B-Chem.*, **154**, 137-141 (2011).

[242] M. Zhu, P. Kirby, M. Wacklerle, M. Herz, and M. Richter, "Optimization Design of Multi-Material Micropump Using Finite Element Method," *Sensor. Actuat. A-Phys.*, **149**, 130-135 (2009).

[243] O.C. Jeong and S. Konishi, "Fabrication of a Peristaltic Micropump with Novel Cascaded Actuators," *J. Micromech. Microeng.*, **18**, 025022 (2008).

[244] O.C. Jeong and S. Konishi, "Fabrication of Peristaltic Micropump Driven by a Single-Phase Pneumatic Force," *Jpn. J. Appl. Phys.*, **49**, 056506 (2010).

[245] M.A. Unger, H.P. Chou, T. Thorsen, A. Scherer, and S.R. Quake, "Monolithic Microfabricated Valves and Pumps by Multilayer Soft Lithography," *Science*, **288**, 113-116 (2000)

[246] N.T. Nguyen and X. Huang, "Minature valveless Pumps Based on Printed Circuit Board Technique," *Sensor. Actuat. A-Phys.*, **88**, 104-111 (2001).

[247] L. Cao, S. Mantell, and D. Polla, "Design and Simulation of an Implantable Medical Drug Delivery System Using Mircoelectromechanical Systems Technology," *Sensor. Actuat. A-Phys.*, **94**, 117-125 (2001).

[248] Q. Lin, B. Yang, J. Xie, and Y.C. Tai, "Dynamic Simulation of a Peristaltic Micropump Considering Coupled Fluid Flow and Structural Motion," *J. Micromech. Microeng.*, **17**, 220-228 (2007).

[249] A. Tuantranont, W. Mamanee, T. Lomas, N. Porntheerapat, N.V. Afzulpurkar, and A. Wisitsoraat, "A Three-Stage Thermopneumatic Peristaltic Micropump for PDMS-Based Micro/Nanofluidic Systems," Proceedings of the 7th IEEE International Conference on Nanotechnology, Hong Kong, China, August 2-5, 2007.

[250] M.M. Teymoori and E.A. Sani, "Design and Simulation of a Novel Electrostatic Peristaltic Micromachined Pump for Drug Delivery," *Sensor. Actuat. A-Phys.*, **117**, 222-229 (2005).

[251] H. Lai and A. Folch, "Design and Dynamic Characterization of 'Single-Stroke' Peristaltic PDMS Micropumps," *Lab Chip*, **11**, 336–342 (2011).

[252] J. Goulpeau, D. Trouchet, A. Ajdari, and P. Tabeling, "Experimental Study and Modeling of Polydimethylsiloxane Peristaltic Micropumps," *J. Appl. Phys.*, **98**, 044914 (2005).

[253] L. Yobas, K.C. Tang, S.E. Yong, and E.K.Z. Ong, "A Disposable Planar Peristaltic Pump for Lab-on-a-Chip," *Lab Chip*, **8**, 660-662 (2008).

[254] N.T. Nguyen and S.T. Wereley, *Fundamentals and Applications of Microfluidics*, 293-343, Artech House Inc., Norwood, MA, 2002.

[255] C.H. Chen, S.H. Cho, F. Tsai, A. Erten, and Y.H. Lo, "Microfluidic Cell Sorter with Integrated Piezoelectric Actuator," *Biomed. Microdevices*, **11**, 1223-1231 (2009).

[256] T. Zhang and Q.M. Wang, "Performance Evaluation of a Valveless Micropump Driven by a Ring-Type Piezoelectric Actuator," *IEEE Trans. Ultrason. Ferroelectr. Freq. Control*, **53**, 463-473 (2006).

[257] L. Jang and Y. Yu, "Peristaltic Micropump System with Piezoelectric Actuators," *Microsyst. Technol.*, **14**, 241-248 (2008).

[258] Q. Cui, C. Liu, and X.F. Zha, "Study on a Piezoelectric Micropump for the Controlled Drug Delivery System," *Microfluid. Nanofluid.*, **3**, 377-390 (2007).

[259] C.G.J. Schabmueller, M. Koch, A.G.R. Evans, and A. Brunnschweiler, "Design and Fabrication of a Microfluidic Circuitboard," *J. Micromech. Microeng.*, **9**, 176-179 (1999).

[260] C.Y. Lee, G.B. Lee, J.L. Lin, F.C. Huang, and C.S. Liao, "Integrated Microfluidic Systems for Cell Lysis, Mixing/Pumping and DNA Amplification," *J. Micromech. Microeng.*, **15**, 1215-1223 (2005).

[261] Z. Xu, C. Zhong, Y. Guan, X. Chen, J. Wang, and Z. Fang, "A Microfluidic Flow Injection System for DNA Assay with Fluids Driven by An On-Chip Integrated Pump Based on Capillary and Evaporation Effects," *Lab Chip*, **8**, 1658-1663 (2008).

[262] Y. Tanaka, K. Morishima, T. Shimizu, A. Eikuchi, M. Yamato, T. Okano, and T. Kitamori, "An Actuated Pump On-Chip Powered by Cultured Cardiomyocytes," *Lab Chip*, **6**, 362-368 (2006).

[263] R. Yokokawa, T. Saika, T. Nakayama, H. Fujita, and S. Konishi, "On-Chip Syringe Pumps for Picoliter-Scale Liquid Manipulation," *Lab Chip*, **6**, 1062-1066 (2006).

[264] L. Rebenklau, K.J. Wolter, and S. Howitz, "Realization of Hybrid Microfluidic Systems Using Standard LTCC Process," Proceedings of the 50th Electronic Components and Technology Conference, Las Vegas, NV, May 21-24, 2000.

[265] A. Baker, M. Lanagan, C. Randall, E. Semouchkina, G. Semouchkin, K.Z. Rajab, R. Eitel, R. Mittra, S. Rhee, P. Geggier, C. Duschl, and G. Fuhr, "Integration Concepts for the Fabrication of LTCC Structure," *Int. J. Appl. Ceram. Technol.*, **2**, 514-520 (2005).

[266] N.S. Satarkar, W. Zhang, R.E. Eitel, and J.Z. Hilt, “Magnetic Hydrogel Nanocomposites as Remote Controlled Microfluidic Valves,” *Lab Chip*, **9**, 1773–1779 (2009).

[267] M. Sobocinski, J. Juuti, H. Jantunen, and L. Golonka, “Piezoelectric Unimorph Valve Assembled on an LTCC Substrate,” *Sensor. Actuat. A–Phys.*, **149**, 315–319 (2009).

[268] H. Klumbies, U. Partsch, A. Goldberg, S. Gebhardt, U. Keitel, and H. Neubert, “Actuators to be Integrated in Low Temperature Cofired Ceramics (LTCC) Microfluidic Systems,” Proceedings of the 32nd International Spring Seminar on Electronics Technology, Brno, Czech Republic, May 13-17, 2009.

[269] W. Zhang and R. Eitel, “Low Temperature Sintering and Properties of 0.98PZT–0.02SKN Ceramics with $LiBiO_2$ and CuO Addition,” *J. Am. Ceram. Soc.*, DOI: 10.1111/j.1551-2916.2011.04504.x.

[270] W. Zhang and R. Eitel, “Sintering Behavior, Properties, and Applications of Co-Fired Piezoelectric/Low Temperature Co-Fired Ceramic (PZT–SKN/LTCC) Multilayer Ceramics,” *Int. J. Appl. Ceram. Technol.*, Submitted.

[271] G. Helke, S. Seifert, and S.J. Cho, “Phenomenological and Structural Properties of Piezoelectric Ceramics Based on xPb(Zr, Ti)O_3-(1-x)Sr($K_{0.25}$, $Nb_{0.75}$)O_3 (PZT/SKN) Solid Solutions,” *J. Eur. Ceram. Soc.*, **19**, 1265-1268 (1999).

[272] T. Hayashi, T. Hasegawa, J. Tomizawa, and Y. Akiyama, “Low-Temperature Sintering of $LiBiO_2$-Coated $Pb(Mg_{1/3}Nb_{2/3})O_3$-$PbZrO_3$-$PbTiO_3$ Powders Prepared by Surface Chemical Modification Method and Their Piezoelectric Properties,” *Jpn. J. Appl. Phys.*, **42**, 6074-6080 (2003).

[273] X. Jiang, J. Liao, X. Wei, G. Li, D. Chen, and Q. Yin, “Intermediate Temperature Sintering of La-Modified $Pb(Zn_{1/3}Nb_{2/3})O_3$-$PbZrO_3$-$PbTiO_3$ Ceramics,” *J. Mater. Sci. Technol.*, **17**, 287-289 (2001).

[274] C.C. Tsai, S.Y. Chu, and C.K. Liang, “Low-Temperature Sintered PMnN-PZT Based Ceramics Using the B-site Oxide Precursor Method for Therapeutic Transducers,” *J. Alloy. Compd.*, **478**, 516-522 (2009).

[275] X. Chao, Z. Yang, C. Kang, and Y. Chang, “Effect of $BiFO_3$ on Electrical Properties and Temperature Stability of Low Temperature Sintered PZT-PFW-PMN Ceramics,” *Sensor. Actuat. A-Phys.*, **141**, 482-488 (2008).

[276] S. Zhang, R. Xia, and T.R. Shrout, “Low Temperature Sintering and Properties of Piezoelectric Ceramics PSNT-Mn with $LiBiO_2$ Addition,” *Mater. Sci. Eng. B*, **129**, 131-134 (2006).

[277] T. Hayashi, T. Inoue, and Y. Akiyama, “Low-Temperature Sintering and Properties of (Pb,Ba,Sr)(Zr,Ti,Sb)O_3 Piezoelectric Ceramics Using Sintering Aids,” *Jpn. J. Appl. Phys.*, **38**, 5549-5552 (1999).

[278] K. Chung, J. Yoo, C. Lee, D. Lee, Y. Jeong, and H. Lee, “Microstructural, Dielectric and Piezoelectric Properties of Low-Temperature Sintering $Pb(Co_{1/2}W_{1/2})O_3$-$Pb(Mn_{1/2}Nb_{2/3})O_3$-Pb(Zr, Ti)O_3 Ceramics with the addition of Li_2CO_3 and Bi_2O_3,” *Sensor. Actuat. A-Phys.*, **125**, 340-345 (2006).

[279] X.X. Wang, K. Murakami, O. Sugiyama, and S. Kaneko, “Piezoelectric Properties, Densification Behavior and Microstructural Evolution of Low-Temperature Sintered PZT Ceramics with Sintering Aids,” *J. Eur. Ceram. Soc.*, **21**, 1367-1370 (2001).

[280] T. Hayashi, T. Hasegawa, and Y. Akiyama, "Enhancement of Piezoelectric Properties of Low-Temperature-Fabricated $Pb(Mg_{1/3}Nb_{2/3})O_3$-$PbZrO_3$-$PbTiO_3$ Ceramics with $LiBiO_2$ Sintering Aids by Post-Annealing Process," *Jpn. J. Appl. Phys.*, **43**, 6683-6688 (2004).

[281] D. Wan, Q. Li, J.Y. Choi, J.W. Choi, Y. Yang, and S.J. Yoon, "Low-Temperature Sintered Pb(Zr, Ti)O_3–Pb(Mn, Sb)O_3–Pb(Zn, Nb)O_3 for Multilayer Ceramic Actuators," *Jpn. J. Appl. Phys.*, **49**, 071503 (2010).

[282] K. Murakami, D. Dong, H. Suzuki, and S. Kaneko, "Microanalysis of Grain Boundary on Low-Temperature Sintered Pb(Zr, Ti)O_3 Ceramics with Complex Oxide Additives," *Jpn. J. Appl. Phys.*, **34**, 5457-5461 (1995).

[283] J. Yoo, K. Kim, C. Lee, L. Hwang, D. Paik, H. Yoon, and H.W. Choi, "Electrical Properties of Low Temperature Sintering Multilayer Piezoelectric Transformer Using $Pb(Mn_{1/3}Nb_{2/3})O_3$-$Pb(Zn_{1/3}Nb_{2/3})O_3$-$Pb(Zr,Ti)O_3$ Ceramics," *Sensor. Actuat. A-Phys.*, **137**, 81-85 (2007).

[284] C.H. Nam, H.Y. Park, I.T. Seo, J.H. Choi, S. Hahm, and H.G. Lee, "Effect of CuO on the Sintering Temperature and Piezoelectric Properties of MnO_2-Doped $0.75Pb(Zr_{0.47}Ti_{0.53})O_3$-$0.25Pb(Zn_{1/3}Nb_{2/3})O_3$ Ceramics," *J. Alloy. Compd.*, **509**, 3686-3689 (2011).

[285] C.C. Tsai, S.Y. Chu, and C.H. Lu, "Doping Effects of CuO Additives on the Properties of Low-Temperature-Sintered PMnN-PZT-Based Piezoelectric Ceramics and Their Applications on Surface Acoustic Wave Devices," *IEEE Trans. Ultrason. Ferroelectr. Freq. Control*, **56**, 660-668 (2009).

[286] American National Standards Institute, *IEEE Standard on Piezoelectricity*, American National Standards Institute, Washington, DC, 1976.

[287] E.M. Levin and H.F. McMurdie, *Phase Diagrams for Ceramists*, Vol. III, 20-21, The American Ceramic Society, Westerville, Ohio, 1975.

[288] Y. Mao, G. Li, Y. Sun, and S. Feng, "Hydrothermal Synthesis and Characterization of $Bi_2Pb_2O_7$ with Pyrochlore Structure," *J. Solid State Chem.*, **149**, 314-319 (2000).

[289] K. Chung, D. Lee, J. Yoo, Y. Jeong, H. Lee, H. Kang, "Piezoelectric Properties of Low-temperature Sintering $Pb(Co_{1/2}W_{1/2})O_3$-$Pb(Mn_{1/3}Nb_{2/3})O_3$-$Pb(Zr_{0.48}Ti_{0.52})O_3$ Ceramics with the Sintering Temperature and the Amount of CuO Addition," *Sensor. Actuat. A-Phys.*, **121**, 142-147 (2005).

[290] H.G. Lee, J.H. Choi, and E.S. Kim, "Low-temperature Sintering and Electrical Properties of $(1-x)Pb(Zr_{0.5}Ti_{0.5})O_3$-$xPb(Cu_{0.33}Nb_{0.67})O_3$ Ceramics," *J. Electroceram.*, **17**, 1035-1040 (2006).

[291] Y. Jeong, K. Yoo, and J. Yoo, "Piezoelectric and Dielectric Characteristics of Low-Temperature-Sintering $Pb(Mg_{1/2}W_{1/2})O_3$-$Pb(Ni_{1/3}Nb_{2/3})O_3$-$Pb(Zr,Ti)O_3$ Ceramics According to the Amount of PNN Substitution," *J. Electroceram.*, **23**, 387-391 (2009).

[292] Y. Jeong, J. Yoo, S. Lee, and J. Hong, "Pizeoelectric Characteristics of Low Temperature Sintering $Pb(Mn_{1/3}Nb_{2/3})O_3$-$Pb(Ni_{1/3}Nb_{2/3})O_3$-$Pb(Zr_{0.50}Ti_{0.50})O_3$," *Sensor. Actuat. A-Phys.*, **135**, 215-219 (2007).

[293] X. Chao, Z. Yang, L. Xiong, and Z. Li, "Effect of Addition of $Ba(W_{0.5}Cu_{0.5})O_3$ in $Pb(Mg_{1/3}Nb_{2/3})O_3$-$Pb(Zn_{1/3}Nb_{2/3})O_3$-$Pb(Zr_{0.52}Ti_{0.48})O_3$ Ceramics on the Sintering Temperature, Electrical Properties and Phase Transition," *J. Alloy. Compd.*, **509**, 512-517 (2011).

[294] S. Hayano, R. Shike, K. Shoji, H. Ochiai, O. Kimura, and H. Maiwa, "Low-Temperature Sintering of $Pb(Ni_{1/3}Nb_{2/3})O_3$-$PbZrO_3$-$PbTiO_3$ Ceramics via Single-Step Calcination Process without Sintering Additives," *Jpn. J. Appl. Phys.*, **49**, 09MC08 (2010).

[295] X. Chao, Z. Yang, Y. Chang, and M. Dong, "Temperature Dependence Piezoelectric Properties of Low Temperature Sintered PZT-PFW-PMN Ceramics with Additive $LiSbO_3$," *J. Alloy. Compd.*, **477**, 243-249 (2009).

[296] X. Chao, Z. Yang, X. Huang, D. Ma, and J. Zeng, "Electrical Characteristics and Low-Temperature Sintering of $BiFeO_3$-Modified $Pb(Zr,Ti)O_3$-$Pb(Fe_{2/3}W_{1/3})O_3$-$Pb(Mn_{1/3}Nb_{2/3})O_3$ Ceramics with ZnO Addition," *Curr. Appl. Phys.*, **9**, 1283-1287 (2009).

[297] Z. Yang, X. Chao, C. Kang, and R. Zhang, "Low Temperature Sintering and Properties of Piezoelectric PZT-PFW-PMN Ceramics with $YMnO_3$ Addition," *Mater. Res, Bull.*, **43**, 38-44 (2008).

[298] H. Li, Z. Yang, L. Wei, and Y. Chang, "Effect of ZnO Addition on the Sintering and Electrical Properties of (Mn,W)-Doped PZT-PMS-PZN Ceramics," *Mater. Res, Bull.*, **44**, 638-643 (2009).

[299] H. Su and D.L. Johnson, "Master Sintering Curve: a Practical Approach to Sintering," *J. Am. Ceram. Soc.*, **79**, 3211-3217 (1996).

[300] D.Z. de Florio, V. Esposito, E. Traversa, R. Muccillo, and F.C. Fonseca, "Master Sintering Curve for Gd-Doped CeO_2 Solid Electrolytes," *J. Thermo. Anal. Calorim.*, **97**, 143-147 (2009).

[301] M.H. Teng, Y.C. Lai, and Y.T. Chen, "A Computer Program of Master Sintering Curve Model to Accurately Predict Sintering Results," *West. Pac. Earth Sci.*, **2**, 171-180 (2002).

[302] S. Kiani, J. Pan, and J. A. Yeomans, "A New Scheme of Finding the Master Sintering Curve," *J. Am. Ceram. Soc.*, **89**, 3393-3396 (2006).

[303] S.J. Park, J.M. Martin, J.F. Guo, J.L. Johnson, and R.M. German, "Densification Behavior of Tungsten Heavy Alloy Based on Master Sintering Curve Concept," *Metall. Mater. Trans. A*, **37A**, 2837-48 (2006).

[304] S.J. Park, P. Suri, E. Olevsky, and R.M. German, "Master Sintering Curve Formulated from Constitutive Models," *J. Am. Ceram. Soc.*, **92**, 1410-1413 (2009).

[305] S.J. Park, J.M. Martin, J.F. Guo, J.L. Johnson, and R.M. German, "Grain Growth Behavior of Tungsten Heavy Alloys Based on the Master Sintering Curve Concept," *Metall. Mater. Trans. A*, **37A**, 3337-3346 (2006).

[306] S.J. Park, S.H. Chung, J.M. Martin, J.L. Johnson, and R.M. German, "Master Sintering Curve for Densification Derived from a Constitutive Equation with Consideration of Grain Growth: Application to Tungsten Heavy Alloys," *Metall. Mater. Trans. A*, **39A**, 2941-2948 (2008).

[307] W. Zhu, K. Yao, and Z. Zhang, "Design and Fabrication of a Novel Piezoelectric Multilayer Actuator by Thick-Film Screen Printing Technology," *Sensor. Actuat. A-Phys.*, **86**, 149-153 (2000).

[308] R.N. Torah, S.P. Beeby, and N.W. Whiite, "Improving the Piezoelectric Properties of Thick-Film PZT: the Influence of Paste Composition, Powder Milling Process and Electrode Material," *Sensor. Actuat. A-Phys.*, **110**, 378-384 (2004).

[309] R. Kurchania and S.J. Milne, "Characterization of Sol-Gel $Pb(Zr_{0.53}Ti_{0.47})O_3$ Films in the Thickness Range 0.25-10 μm," *J. Mater. Res.*, **14**, 1852-1859 (1999).

[310] D.A. Barrow, T.E. Petroff, R.P. Tandon, and M. Sayer, "Characterization of Thick Lead Zirconate Titanate Films Fabricated Using a New Sol Gel Based Process," *J. Appl. Phys.*, **81**, 876-881, (1997).

[311] R.E. Mistler, "Tape Casting – The Basic Process for Meeting the Needs of the Electronics Industry," *Am. Ceram. Soc. Bull.*, **69**, 1022-1026 (1990).

[312] V. Vinothini, P. Singh, and M. Balasubramanian, "Optimization of Barium Titanate Nanopowder Slip for Tape Casting," *J. Mater. Sci.*, **41**, 7082-7087 (2006).

[313] J. Honkamo, H. Jantunen, G. Subodh, M.T. Sebastian, and P. Mohanan, "Tape Casting and Dielectric Properties of $Zn_2Te_3O_8$-Based Ceramics with an Ultra-Low Sintering Temperature," *Int. J. Appl. Ceram. Technol.*, **6**, 531-536 (2009).

[314] J.J. Choi, J.H. Lee, B.D. Hahn, W.H. Yoon, and D.S. Park, "Co-Firing of PZN-PZT/Ag Multilayer Actuator Prepared by Tape-Casting Method," *Mater. Res. Bull.*, **43**, 483-490 (2008).

[315] H. Amorin, I. Santacruz, J. Holc, M.P. Thi, M. Kosec, R. Moreno, and M. Alguero, "Tape-Casting Performance of Ethanol Slurries for the Processing of Textured PMN-PT Ceramics from Nanocrystalline Powder," *J. Am. Ceram. Soc.*, **92**, 996-1001 (2009).

[316] Y. Chou, Y. Ko, and M. Yan, "Fluid Flow Model for Ceramic Tape Casting," *J. Am. Ceram. Soc.*, **70**, C280-C282 (1987).

[317] A. Roosen, "Basic Requirements for Tape Casting of Ceramic Powders," Ceramic Transactions, Ceramic Powder Science II, Vol. 1, Part A-B, ed. G.L. Messing. American Ceramic Society, Westerville, OH, 675-692, 1988

[318] A. Mohanram, G.L. Messing, and D.J. Green, "Densification and Sintering Viscosity of Low-Temperature Co-Fired Ceramics," *J. Am. Ceram. Soc.*, **88**, 2681-2689 (2005).

[319] S.Y. Tzeng and J.H. Jean, "Stress Development during Constrained Sintering of Alumina-Glass-Alumina Sandwich Structure," *J. Am. Ceram. Soc.*, **85**, 335-340 (2002).

[320] K.L. Ekinci, Y.T. Yang, and M.L. Roukes, "Ultimate Limits to Inertial Mass Sensing Based upon Nanoelectromechanical Systems," *J. Appl. Phys.*, **95**, 2682-2689 (2004).

[321] B.P. Harrington, R. Abdolvand, A. Hajjam, J.C. Wilson, and S. Pourkamali, "Thin-Film Piezoelectric-on-Silicon Particle Mass Sensors," Proceedings of the 2010 IEEE International Frequency Control Symposium, Newport Beach, CA, June 1-4, 2010.

[322] R.H. Liu, J. Yang, R. Lenigk, J. Bonanno, and P. Grodzinski, "Self-Contained, Fully Integrated Biochip for Sample Preparation, Polymerase Chain Reaction Amplification, and DNA Microarray Detection," *Anal. Chem.*, **76**, 1824-1831 (2004).

[323] C.W. Lim, L.H. He, and A.K. Soh, "Three-Dimensional Electromechanical Response of a Parallel Piezoelectric Bimorph," *Int. J. Solid Structure.*, **38**, 2833-2849 (2001).

[324] A. Fernandes and J. Pouget, "Analytical and Numerical Approach to Piezoelectric Bimorph," *Int. J. Solid Structure.*, **40**, 4331-4352 (2003).

[325] N. J. Graf and M.T. Bowser, "A Soft-Polymer Piezoelectric Bimorph Cantilever-Actuated Peristaltic Micropump," *Lab Chip*, **8**, 1664-1670 (2008).

[326] L. Jang, K. Shu, Y. Yu, Y. Li, and C. Chen, "Effect of Actuation Sequence on the Flow Rates of Peristaltic Micropumps with PZT Actuators," *Biomed Microdevices*, **11**, 173-181 (2009).

[327] W. Yang, *Mechatronic reliability: electric failures, mechanical-electrical coupling, domain switching, mass-flow instabilities*, 219-239, Tsinghua University Press Inc., Beijing, China, 2002.

[328] A. Olsson, G. Stemme, and E. Stemme, "Diffuser-Elements Design Investigation for Valve–Less Micropumps," *Sensor. Actuat. A-Phys.*, **57**, 137-143 (1996).

[329] A. Olsson, G. Stemme, and E. Stemme, "Numerical and Experimental Studies of Flat-Walled Diffuser Elements for Valve–Less Micropumps," *Sensor. Actuat. A-Phys.*, **84**, 165-175 (2000).

[330] J. Judy D. Maynes, and B.W. Webb, "Characterization of Frictional Pressure Drop for Liquid Flows Through Microchannels," *Int. J. Heat Mass Transfer*, **45**, 3477-3489 (2002).

[331] T. Bayraktar and S. B. Pidugu, "Characterization of Liquid Flows in Microfluidic Systems," *Int. J. Heat Mass Transfer*, **49**, 815-824 (2006).

[332] L.S. Jang, Y.J. Li, S.J. Lin, Y.C. Hsu, W.S. Yao, M.C. Tsai, and C.C. Hou, "A Stand-Alone Peristaltic Micropump Based on Piezoelectric Actuation," *Biomed. Microdevices*, **9**, 185-194 (2007).

[333] M. Koch, A.G.R. Evans, and A. Brunnschweiler, "The Dynamic Micropump Driven with a Screen Printed PZT Actuator," *J. Micromech. Microeng.*, **8**, 119-122 (1998).

[334] D.L. Laser, A.M. Myers, S. Yao, K.F. Bell, K.E. Goddson, J.G. Santiago, and T.W. Kenny, "Silicon Electroosmotic Micropumps for Integrated Circuit Thermal Management," Proceedings of the 12th international Conference on Solid State Sensors, Actuators and Microsystems, Boston, MA, June 8-12, 2003.

[335] Y.C. Lin and J.H. Jean, "Constrained Densification Kinetics of Alumina/Borosilicate Glass + Alumina/Alumina Sandwich Structure," *J. Am. Ceram. Soc.*, **85**, 150-154 (2002).

[336] G. Liu, C. Shen, Z. Yang, X. Cai, and H. Zhang, "A Disposable Piezoelectric Micropump with High Performance for Closed-Loop Insulin Therapy System," *Sensor. Actuat. A-Phys.*, **163**, 291-296 (2010).

[337] A. Geipel, F. Goldschmidtboing, A. Doll, P. Jantscheff, N. Esser, U. Massing, and P. Woias, "An Implantable Active Microport Based on a Self-Priming High-Performance Two-Stage Micropump," *Sensor. Actuat. A-Phys.*, **145-146**, 414-422 (2008).

[338] W. Zhang, P. Wattamar, K. Cummins, T. Dziubla, and R.E. Eitel, "LTCC Based Microfluidic Structures for the Controlled Synthesis of Antioxidant Polymers," in Proceedings of the IMAPS 2008, 41st International Symposium on Microelectronics, Providence, RI, November 2-6, 2008.

[339] J. Poag, K. Anderson, T. Dziubla, and R.E. Eitel, "Endothelial Cell Culture in a Ceramic Microfluidic Device," in Proceedings of 2009 AlChE Annual Meeting, Nashville, TN, November 8-13, 2009.

[340] C. Yamahata, C. Vendevyver, F. Lacharme, P. Izewska, H. Vogel, R. Freitag, and M.A.M. Gijs, "Pumping of Mammalian Cells with a Nozzle-Diffuser Micropump," *Lab Chip*, **5**, 1083-1088 (2005).

Vita

Name: WENLI ZHANG

Date of birth: July 11, 1981 Place of birth: Beijing, China

Educational institutions attended and degrees already awarded:

- Master of Engineering, Materials Physics and Chemistry, Beijng University of Technology, Beijing, China, July 2006
- Bachelor of Engineering, Materials Science and Engineering, Beijng University of Technology, Beijing, China, July 2003

Professional positions held:

- Research Assistant, University of Kentucky, Jun. 2007 — present
- Teaching Assistant, University of Kentucky, Aug. 2006 — May 2007
- Research Assistant, Beijng University of Technology, Sept. 2003 — Jun. 2006

Scholastic and professional honors:

- Winner for Student Poster Competition Award
  2010 U.S. Navy Workshop on Acoustic Transduction Materials and Device, May 2010
- Research Challenge Trust Fund I Fellowship
  University of Kentucky, June 2007 — June 2008

Professional publications:

- **W. Zhang** and R.E. Eitel, "Sintering Behavior, Properties, and Applications of Co-Fired Piezoelectric/Low Temperature Co-Fired Ceramic (PZT–SKN/LTCC) Multilayer Ceramics," *Int. J. Appl. Ceram. Technol.*, Submitted.
- **W. Zhang** and R.E. Eitel, "Low Temperature Sintering and Properties of 0.98PZT-0.02SKN Ceramics with $LiBiO_2$ and CuO Addition," *J. Am. Ceram. Soc.*, DOI: 10.1111/j.1551-2916.2011.04504.x.
- **W. Zhang** and R.E. Eitel, "Biostability of LTCC Materials for Microfluidic and Biomedical Devices," *Int. J. Appl. Ceram. Technol.*, DOI: 10.1111/j.1744-7402.2010.02581.x.

- N.S. Satarkar, **W. Zhang**, R.E. Eitel, and J.Z. Hilt, “Magnetic Hydrogel Nanocomposites as Remote Controlled Microfluidic Valves,” *Lab Chip*, 2009, **9**, 1773-1779.
- Y. Ding, G. Chen, G. Liu, X. Zhu, **W. Zhang**, B. He, Z. Ma, D. He, “Double Effects of Atomic Hydrogen Anneal on the Microstructure of Hydrogenated Amorphous Silicon Films,” *Vacuum*, 2007, **82 [1]**, 105-108.
- X. Zhu, G. Chen, Y. Ding, Z. Ma, **W. Zhang**, B. He, Z. Gao, Z. Li, “Influence of Hot- wire on the Formation of Microcrystalline Silicon in MWECR-CVD System,” *Vacuum*, 2006, **80 [5]**, 421-425.
- X. Zhu, G. Chen, **W. Zhang**, Y. Ding, Z. Ma, Y. Hu, B. He, Y. Rong, “Study on Stability of Hydrogenated Amorphous Silicon Films,” *Chinese Phys.*, 2005, **14 [11]**, 2348-2351.
- Y. Hu, G. Chen, J. Zhou, Y. Rong, Y. Li, X. Song, **W. Zhang**, Y. Ding, X. Zhu, “Nanomorph Silicon Thin Films Prepared by Using an HW-MWECR CVD System,” *Chinese Phys. Lett.*, 2005, **22 [5]**, 1260-1263.